Imperial College London

School of Design Engineering

Modelling diffusion across solid-solid interfaces in electroceramic materials

Liam Yasin

Submitted in part fulfilment of the requirements

for the degree of Doctor of Philosophy at

Imperial College London, March 2024



I hereby declare that this thesis and the work reported herein was composed by and originated entirely from me. Information derived from the published and unpublished work of others has been acknowledged in the text and references are given in the list of sources.

Liam Yasin (2024)

The copyright of this thesis rests with the author. Unless otherwise indicated, its contents are licensed under a Creative Commons Attribution-Non Commercial-No Derivatives 4.0 International Licence (CC BY-NC-ND). Under this licence, you may copy and redistribute the material in any medium or format on the condition that; you credit the author, do not use it for commercial purposes and do not distribute modified versions of the work. When reusing or sharing this work, ensure you make the licence terms clear to others by naming the licence and linking to the licence text. Please seek permission from the copyright holder for uses of this work that are not included in this licence or permitted under UK Copyright Law.

Abstract

The performance and stability of Solid Oxide Cells (SOCs) is partially determined by the structure and evolution of the interfaces within them. New approaches to the modelling of multi-layer structures are outlined, enabling analysis of experimental data obtained from multi-layer SOC samples.

A new framework for modelling self-diffusion across multiple layers with an interface between them was derived. No existing model that is able to account for the changing diffusivities across a multi-layer structure has been developed previously. This is achieved by deriving a finite-difference-based numerical solution to the new system of equations that emerges. This enabled the quantification of interface blocking effects that were identified in previous experiments. Two different approaches are tested; one assumes the interface to exist in infinitesimal layer in space, while the other assumes an interface of finite thickness at the interface with diffusivities that are lower than other materials in the system. These models were tested against a series of experimental data, where $La_{0.6}Sr_{0.4}Co_{0.2}Fe_{0.8}O_{3-\delta}$ (LSCF) was deposited on yttria-stabilised zirconia (YSZ) substrates using pulsed laser deposition (PLD) followed by heat treatment before isotope exchange depth profiling (IEDP). The heat treatment resulted in progressively larger drops in isotopic fraction at the interface. This profile was fitted quantitatively with both multi-layer diffusion models, showing an increase in interface resistance with treatment temperature.

A different modelling approach looked into the rate-limiting reaction steps of the oxygen reduction reaction (ORR) in mixed ionic and electronic conductors (MIECs). COMSOL simulations of impedance spectra were systematically performed to investigate the effect of different ORR steps acting as rate-limiting and how these would be reflected in experimental data. The study recommends the testing of thin, dense films under different oxygen partial pressures as a method of determining the rate-limiting step in the ORR exhibited by different MIEC materials.

Acknowledgements

I must begin by thanking Dr. Sam Cooper for his inspiring supervision. I have felt a confidence in our approach to science from the very beginning, and without his steadfast support, incredible scientific thinking and trusting work environment, this thesis would have been impossible. I am also grateful for his always encouraging the cultivation of a critical and sometimes unconventional approach to science in the group. It has been a pleasure to see the tldr group grow and evolve over the years, always offering fun, insightful conversations and great humour. I am particularly grateful to them for always indulging in my opinionated monologues about all sorts of topics. The Design Engineering department provided a fascinating and dynamic community of people that continued to teach me new things about many diverse disciplines. They made me believe that academia can be a space for innovation and experimentation with new ideas and approaches.

My lab work benefited greatly from the help of Dr. Inyoung Jang, who graciously offered her experience and friendship to help me with the project during a time when progress appeared difficult. The Electroceramics group helped me continue on with lab work for many years, and the relaxed and supportive environment made things much easier each week. The Department of Materials has been a constant presence in my life for more than eight years, giving me many formative experiences. Without the support from facility managers and lab staff, the experimental work in this project could not exist. I feel proud to be able to call myself a materials scientist.

I would also like to thank Dr. Antonio Bertei and Prof. Alan Atkinson for the opportunity to work together, it was an enjoyable and rewarding process during a turbulent time in the world. I was inspired by the high level of scientific thinking that they displayed.

My friends offered an ever-present and much needed escape from the stressful periods, reminding me to keep enjoying life and not get lost in work. I am particularly grateful to my flatmates Ben and Yeona supporting me during the writing stage, making daily life so much easier by taking care of the household and providing calm surroundings that enabled me to keep going each day.

Finally, I thank my parents for always supporting me and my decisions, and my sister for being a role model both as a scientist and as a person.

الكون أصغر من جناح فراشة في ساحة القلب الكبير

The universe is smaller than a butterfly's wing in the courtyard of the heart

– Mahmoud Darwish محمود درويش –

Contents

Abstract **iii**

Acknowledgements **iv**

Nomenclature **xxii**

1 Introduction **2**

1.1 Filling in the gaps . . . 2

1.2 Solid Oxide Cells . . . 3

1.2.1 Alternative Fuel Cell and Electrolyser Technologies . . . 4

1.2.2 Material Interfaces . . . 4

1.2.3 Quantifying Interfaces . . . 6

1.3 Literature Review . . . 7

1.3.1 Materials science of SOFCs . . . 7

1.3.2 Interfaces in SOFCs . . . 13

1.4 Modelling diffusion in multi-layer materials . . . 20

1.4.1 Modelling diffusion in ceramics . . . 20

1.5 Identifiability of kinetic mechanisms at the gas-cathode interface . . . 22

1.6 Conclusions, Aims and Objectives . . . 25

References . . . 26

2 Identifiability of the mechanisms governing the reaction kinetics of MIEC electrodes in solid oxide cells **35**

2.1 Model development . . . 35

2.1.1 Defect Chemistry . . . 36

2.1.2 Electrochemical Reaction Steps . . . 36

2.1.3 Boundary Conditions . . . 39

2.1.4 Mass Transport . . . 39
2.1.5 Implementation . . . 40
2.2 Results . . . 45
2.2.1 Polarisation Curves . . . 46
2.2.2 Kinetic identification in dense films . . . 48
2.2.3 Porous electrodes . . . 52
2.3 Discussion . . . 55
2.3.1 Interpretation of experimental data on thin film electrodes . . . 55
2.3.2 Interpretation of experimental data on porous electrodes . . . 58
2.4 Conclusions . . . 59
References . . . 60

3 Modelling multi-layer diffusion systems 64
3.1 Modelling Multi-Layer Diffusion . . . 64
3.2 Interface Resistance Model . . . 65
3.2.1 Discretising the variable-D diffusion equation . . . 65
3.2.2 Boundary Conditions . . . 70
3.2.3 Matrix Implementation . . . 71
3.3 Triple Layer Model . . . 75
3.3.1 Behaviour of the triple layer model simulations . . . 75
3.4 Conclusion . . . 77
References . . . 78

4 Materials and Methods 79
4.1 Sample Preparation . . . 79
4.1.1 Ink Processing . . . 79
4.1.2 Thin Film Deposition . . . 81
4.2 Characterisation . . . 83
4.2.1 SEM . . . 83
4.2.2 XRD . . . 83
4.2.3 Diffusion Measurements . . . 83
4.2.4 Topography . . . 88
4.2.5 EIS . . . 88
References . . . 89

5 Experimental investigation of diffusion in LSCF-YSZ multilayers fabricated by pulsed laser deposition **91**

5.1 Measuring Interfacial Resistance . . . 91

5.2 PLD Sample Series . . . 93

5.2.1 PLD Fabrication . . . 93

5.2.2 Isotope Exchange on PLD Samples . . . 94

5.2.3 PLD SIMS . . . 95

5.2.4 Fitting with Interface Resistance Model . . . 98

5.2.5 Ion Signals . . . 108

5.2.6 Triple Layer Model Fit . . . 117

5.2.7 Comparison to Literature Values . . . 125

References . . . 128

6 Other interfaces and analysis techniques **130**

6.1 LSCF-GDC multilayer samples fabricated with PLD . . . 130

6.2 EDX Analysis . . . 132

6.2.1 Properties of potential reaction products . . . 134

6.2.2 Phase formation . . . 135

6.3 EIS Experiments and Results . . . 136

6.3.1 Low Temperature . . . 138

6.3.2 High Temperature . . . 139

6.4 Conclusion . . . 141

References . . . 142

7 Conclusions **144**

7.1 Future Work . . . 145

7.1.1 Sample Fabrication . . . 146

7.1.2 Characterisation Methods . . . 146

7.2 Dissemination . . . 147

7.2.1 Papers . . . 147

7.2.2 Conference Presentations . . . 147

A Further Experimental Data **A-1**

A.1 Topography Data . . . A-1

A.2 Grazing incidence XRD data A-2
A.3 EIS Data A-4
A.4 Ceramics Processing Samples A-5
A.4.1 Ceramics Processing A-5
A.4.2 Layer Thickness and Mechanical Stability A-7
A.4.3 SIMS ANALYSIS A-10

List of Tables

2.1 Fundamental model equations describing defect chemistry, ORR kinetics and charge transport in the p-type oxygen-deficient perovskite MIEC cathode under consideration. 42

2.2 Table S2 – Governing equations for the conservation of species in porous and dense MIEC cathodes. 43

2.3 Model Parameters 44

2.4 Kinetic parameters used to illustrate the four extreme kinetic scenarios 46

4.1 Table detailing the final ink composition chosen for the fabrication of LSCF layers on substrate pelelts. 80

5.1 Table compiling the upper and lower bounds of each variable that is relevant during the fitting of experimental multi-layer IEDP data. The bounds are determined by changing the target variable, keeping all others constant. 103

6.1 Table compiling the atomic percentage of the listed elements obtained from each point of the cross-section EDX analysis. The columns marked in blue represent the points from the darkened spots around the interface, while the columns marked in yellow were taken from the YSZ side. 134

6.2 Table summarising the conductivity and, where available, diffusivity at 460 °C of potential reaction products between LSCF and YSZ. 134

6.3 Table summarising the ohmic and polarisation resistance as well as capacitance values obtained from the EIS data. The resistance values are inferred from the start and end point of the semicircles, while the capacitance is calculated from the peak frequencies at each semicircle. 137

List of Figures

1.1 Schematic of a Solid Oxide Fuel Cell 5

1.2 Tracer diffusion profile obtained from a GDC-YSZ layer system with a SZO reaction layer in between the two. Shown are a) the full diffusion profile across the multilayer sample, including concentration drops at each interface and b) the fitting approach chosen by the authors to model the transport properties of the SZO-YSZ interface. Reprinted from Develos-Bagarinao *et al.*[39], Copyright 2017 Royal Society of Chemistry. 15

1.3 Tracer diffusion profile obtained from a multilayer sample consisting of LSCF deposited by PLD onto a single crystal GDC film which in turn was deposited on a YSZ substrate (partial diffusion profile shown here). The dashed lines indicate the region of fit chosen by the authors. Reprinted from Develos-Bagarinao *et al.*[42], Copyright 2016 Elsevier. 16

1.4 Elemental composition of the GDC-LSCF interface at co-sintering temperatures of a) 1100 ℃ and b) 1400 ℃. A relationship between sintering temperature and degree of cation interdiffusion can clearly be observed. Reprinted with permission from Li *et al.*[30], Copyright 2011 American Chemical Society. 17

2.1 Schematic representation showing the cross-section of the considered MIEC system including the oxygen reduction reaction steps. 37

2.2 Simulation results for a porous LSCF electrode at OCV, 600 °C, and p_{O2} = 0.21 atm, using the kinetic parameters of the four extreme scenarios reported in Table 2.4a) Nyquist plot for a 20 mm thick electrode; b) area-specific resistance as a function of electrode thickness. 46

2.3 Simulated polarisation curves for a 20 um-thick, porous LSCF electrode at pO_2 = 0.21 atm for the four kinetic scenarios reported in Table 2.4. The inset reports the corresponding ASR as a function of current 47

2.4 Simulated Nyquist plots for a 1 mm-thick dense LSCF film at 600 ℃ and 0.21 atm pO_2 for different values of the cathodic bias, considering the kinetic parameters of the four extreme scenarios reported in Table 2.4. The first plot reports in the inset a magnification of the spectra. The frequency of 0.1 Hz is marked with a black dot in each case. 48

2.5 a) Simulated ASR as function of pO_2 in a log-log plot for a 1 mm-thick dense LSCF film at 600 ℃ and OCV for the four extreme scenarios reported in Table 2.4. The triangle represents the slope -1/2 in the log-log plot. b) Equilibrium surface coverage of adsorbed oxygen for buffered (el-B and io-B, black solid line) and unbuffered (el-U and io-U, black dashed line) kinetic scenarios on the left axis, along with the equilibrium vacancy concentration (green solid line) on the right axis, as a function of pO_2 according to defect chemistry. 49

2.6 Simulated ASR as a function of pO_2 in a log-log plot for a 1 mm-thick dense LSCF film at 600 ℃ for different values of the cathodic bias hcat: a) 0.0 V, b) -0.1 V, c) -0.2 V. The kinetic parameters of the three extreme scenarios that can be identified by pO_2 changes, namely, el-B, io-B and io-U, as reported in Table 2.4, are considered. The triangles represent relevant slopes in the log-log plot. 51

2.7 Simulated ASR as function of pO_2 in a log-log plot for a 20 mm-thick porous LSCF electrode at 600 ℃ and OCV considering the kinetic parameters of the four extreme scenarios reported in Table 2.4. 53

2.8 Simulated EIS spectra of a porous 20 mm-thick LSCF electrode as a function of pO_2 at OCV. The insets report the full spectra at a larger scale when they do not fit within the selected plot area. 54

2.9 Flowchart outlining the procedure to identify the rate-determining kinetic mechanism in dense MIEC films. 55

2.10 Polarisation resistance as a function of cathodic overpotential at 700 ℃ in air for a) LSC and b) LSM thin films. c) Polarisation resistance as a function of oxygen partial pressure at 700 ℃ and open circuit conditions of LSM and LSC thin films. d) Visual representation of LSC and LSM within a map of extreme kinetic scenarios. The original experimental data are taken from Imanishi et al. [66] for thin films deposited on YSZ single crystal substrates having different orientations indicated. 56

2.11 The effect of overpotential (at $pO_2 = 10^{-2}$ bar) and oxygen partial pressure (at OCV) on the ASR of porous LSF electrode at 700 ℃ . The overpotential scale is adjusted so that it matches the equivalent pO_2 value according to the Nernst equation. Experimental data reproduced from Nenning et al. [65]. 58

3.1 Schematic representation of 1D diffusion across an interface using a series resistor analogy. Shown here are a) the conceptual set of 'resistor' elements related to each layer's diffusion coefficient, as well as the additional resistor element r representing interfacial resistance 68

3.2 A sample diffusion profile as generated by the code developed in this project. Note that although the line appears to run diagonally through the interface region, no data points are generated in this region, as the width of the interface corresponds to Δx, the step size in between two data points. 73

3.3 A series of generated diffusion profiles with exponentially increasing values of r plotted as a function of x' as defined in eq. 3.35, keeping all other parameters constant. The position of the interface is set at a) $x' = 0.5$ and b) $x' = 1$ in order to visualise the influence of interface position on the profile's behaviour across the full range of r values. 74

3.4 Set of simulated multi-layer diffusion profiles using the triple layer model, fixing the interlayer thickness L_{int} at 20nm and varying the interlayer diffusivity D_{int}. All other simulation parameters are kept constant. The series shows an increasing interface drop with lower interlayer diffusivity. 76

3.5 Set of simulated multi-layer diffusion profiles using the triple layer model, fixing the interlayer diffusivity D_{int} and varying the interlayer thickness L_{int} between 5 and 40 nm. All other simulation parameters are kept constant. The series shows an increasing interface drop with increased interlayer thickness, illustrating how both variables can significantly influence the shape of the overall profile. 77

4.1 Schematic illustrating the experimental procedure for the fabrication of micrometer-scale LSCF-Electrolyte multilayer samples using drop casting. 80

4.2 Sketch illustrating the experimental setup of a Pulsed Laser Deposition (PLD) machine. 82

4.3 Illustration of the isotope exchange rig enabling the annealing under controlled atmosphere. Reproduced from Cooper [8]. 84

4.4 Schematic showing the principle of obtaining isotopic fraction data from the ToF SIMS 86

4.5 The two different data acquisition methods for Isotope Exchange Depth Profiling. In depth profiling, a hole is sputtered into the sample with ion analysis at each step, while line scans are done over a cross-section. 87

5.1 XRD patterns of LSCF and YSZ powder mixed at a 1:1 weight ratio, pressed into a pellet and heated to varying temperatures for 6h. As the temperature increases, the signal for SZO increases in intensity just as the signal for LSCF is decreasing. 92

5.2 Cross-section image of a LSCF layer deposited onto a GDC pellet using PLD. The area in between the horizontal white lines shows the LSCF layer cross section, while the remaining signal below this is part of the substrate. The upper part of the image shows the surface topology of the LSCF layer. The cursor height provides an indication of the layer thickness, but should not be considered an accurate measurement due to the effects of tilting the sample for analysis and the unclear boundary between the layers. 94

5.3 Isotope fraction depth profiles of multi-layer LSCF on YSZ samples that were fabricated using PLD. Each sample was heat treated at the temperatures indicate in the top right for 4 hours prior to isotope exchange. All of these were conducted at 460 ℃ for 90 minutes after a preannealing process of 24 hours. The sharp drop in isotope fraction that is visible in the samples treated at 600 degrees and above denotes the transition between the LSCF and YSZ layers. 95

5.4 Isotope fraction graphs of the LSCF-YSZ PLD samples heat treated at temperatures of 800 ℃ or lower for 4 hours before isotope exchange. From the sample that did not undergo any additional heat treatment, these results show the progressively increasing drop in isotope fraction that takes place at the interface between LSCF and YSZ. While the samples have a different LSCF layer thickness at the point of analysis, the drop in isotopic fraction at the interface is nevertheless proportional to heat treatment temperature. 96

5.5 Isotope fraction graphs of the LSCF-YSZ PLD samples heat treated at temperatures of 800 ℃ and higher before isotope exchange. It can be observed that the interface drop does not increase significantly in magnitude beyond 900 ℃. In this range, the bulk isotopic fraction is low enough to be near the background concentration of ^{18}O, indicating a strong interface blocking effect. Each profile was obtained from a separate physical sample piece, which is why the LSCF layer thicknesses vary. 97

5.6 Fit of the LSCF-YSZ multi-layer sample that was heat treated at 800 ℃ obtained from the code that incorporated the multi-layer model with an interface resistance parameter. The values indicated on the rightmost part of the figure show the material properties obtained by the fitting algorithm, including the diffusion coefficients of each layer. . . 98

5.7 Variation in the fitting curve resulting from changing the interface resistance r while keeping all other values constant. A change in r of $0.15 * 10^{10}$ changes the curve such that the fit is no longer accurately capturing the shape of the data. This determines an approximate error range for the accuracy of the fitting algorithm when calculating the interface resistance parameter. 100

5.8 Variation in the fitting curve resulting from changing the interface resistance r and the surface exchange coefficient k^* simultaneously, with the goal of trying to keep the fit to the data as accurately as possible. While fitting the first layer remains possible with many combinations of values, the accuracy of the second layer's fit diminishes. This further illustrates the manner in which the interface resistance parameter captures the magnitude of the drop in isotopic fraction at the interface with high levels of accuracy. 101

5.9 Variation in the fitting curve resulting from changing the diffusion coefficient of the first layer (LSCF) D_1 while keeping all other variables constant. It can be seen that D_1 influences the gradient of the first layer's diffusion profile, which enables fitting to a degree of accuracy that is well below a full order of magnitude. 102

5.10 Variation in the fitting curve resulting from changing the diffusion coefficient of the second layer (YSZ) D_2 while keeping all other variables constant. D_2 determines the gradient of the curve in the bulk component of the multi-layer. Since the diffusion profile is nearly horizontal, implying fast diffusion, the accuracy of the value for D_2 is less clear on the upper bound. This means that D_2 can be increased by multiple orders of magnitude with small visible changes to the profile shape 102

5.11 Interface resistance model fit of the isotope exchange depth profile data obtained from a LSCF-YSZ multilayer sample annealed at 600 ℃ before exchange. 104

5.12 Interface resistance model fit of the isotope exchange depth profile data obtained from a LSCF-YSZ multilayer sample annealed at 700 ℃ before exchange. 104

5.13 Interface resistance model fit of the isotope exchange depth profile data obtained from a LSCF-YSZ multilayer sample annealed at 900 ℃ before exchange. 105

5.14 Interface resistance model fit of the isotope exchange depth profile data obtained from a LSCF-YSZ multilayer sample annealed at 900 ℃ before exchange. Note that this profile was obtained from a different sample than the previous 900 ℃ sample. 105

5.15 Interface resistance model fit of the isotope exchange depth profile data obtained from a LSCF-YSZ multilayer sample annealed at 1000 ℃ before exchange. 106

5.16 Interface resistance model fit of the isotope exchange depth profile data obtained from a LSCF-YSZ multilayer sample annealed at 1000 ℃ before exchange. Note that this profile was obtained from a different sample than the previous 1000 ℃ sample. 106

5.17 The value of the interface resistance parameter r obtained from the fitting of data obtained from LSCF-YSZ samples annealed at various temperatures. 107

5.18 Signals of various ion species obtained from a LSCF-YSZ PLD multi-layer sample with **no further heat treatment** by SIMS depth profiling. The SIMS is set to obtain negatively charged ions from the sample, as this gives the best data quality for oxygen, the main species. Keeping in mind that the ion counts are on a logarithmic scale, the species associated with LSCF diminish sharply around the same area that the ZrO from the YSZ substrate emerges, pinpointing the interface region between the two layers. . 108

5.19 Signals of various ion species obtained from a LSCF-YSZ PLD multi-layer sample heat treated at **600 ℃**. In addition to the interface location being shown by the characteristic species, the emergence of a drop in isotope fraction can be discerned from the sharp drop in ^{18}O ion counts around the interface area. 110

5.20 Signals of various ion species obtained from a LSCF-YSZ PLD multi-layer sample heat treated at **700 ℃**. In addition to the same interface transition information from the previous samples, this data shows the way in which the shape of the individual ion counts mirror that of the total ion counts, enabling the distinction between artefacts related to the ion species and artefacts originating from the physical sample itself. . . 111

5.21 Signals of various ion species obtained from a LSCF-YSZ PLD multi-layer sample heat treated at **800 ℃**. The dip in bulk isotopic fraction is mirrored in the total ion counts, indicating that this feature is a result of a locally lower ion yield in the bulk pellet as that point of the depth profile is reached. 112

5.22 Signals of various ion species obtained from the first LSCF-YSZ PLD multi-layer sample heat treated at **900 ℃**. The interface region here is extended compared to the previous samples that were heat treated at lower temperatures. It also contains artifacts and features of inconclusive origin, showing the increased complexity of the interface region at higher treatment temperatures. 113

5.23 Signals of various ion species obtained from the second LSCF-YSZ PLD multi-layer sample heat treated at **900 ℃**. Similarly, the interface region is extended and contains different features. While some of them follow the shape of the total ion count curve, others, such as FeO and ZrO, do not. This might indicate a combination of measurement artifacts due to sample quality and the expression of a more intermixed interface region due to high annealing temperatures. 113

5.24 Signals of various ion species obtained from the first LSCF-YSZ PLD multi-layer sample heat treated at **1000 ℃**. A notable feature that is different from other samples is the slight spike in SrO counts in the interface region, which runs counter to the total ion counts. This might either indicate measurement artifacts or a buildup of strontium in the interface. 114

5.25 Signals of various ion species obtained from the second LSCF-YSZ PLD multi-layer sample heat treated at **1000 ℃**, distinct from the previous sample treated at the same temperature. The total ion counts are slightly less consistent compared to other samples, particularly in the bulk region, where they increase steadily until plateauing at around 300-400 nm. This may indicate that the substrate pellet's fabrication quality is lower compared to other samples. 114

5.26 Width of the interface region derived from the SIMS data of FeO and ZrO species in a LSCF-YSZ multilayer sample, with associated errors. 116

5.27 LSCF-YSZ PLD sample heat treated at 800 ℃ and fit using the triple layer model. . . 117

5.28 Triple Layer Fit of the LSCF-YSZ sample heat treated at 800 ℃ at a constant value of interlayer diffusion coefficient and a thickness varying from 5 to 40nm. 118

5.29 Triple Layer Fit of the LSCF-YSZ sample heat treated at 800 ℃ at a constant interlayer thickness of 20nm with a variety of diffusion coefficient values. 118

5.30 Fits of the LSCF-YSZ sample heat treated at 800 ℃ using the triple layer model where a set of interlayer thicknesses L_{int} and interlayer diffusion coefficients D_{int} are chosen to reproduce an accurate fit. While producing the same magnitude drop with a combination of the two is possible, matching the gradient of the data in the interlayer region narrows the window of L_{int}. 119

5.31 Comparison of the fits for the LSCF-YSZ sample heat treated at 800 ℃ obtained via the interface resistance model and the triple layer model. While the size of the drop is the same with both methods, the triple layer fit captures the shape of the broad interface region more accurately. 120

5.32 Triple Layer Fit of the LSCF-YSZ sample heat treated at 600 ℃. 121

5.33 Triple Layer Fit of the LSCF-YSZ sample heat treated at 700 ℃. 121

5.34 Triple Layer Fit of the LSCF-YSZ sample heat treated at 900 ℃. 122

5.35 Triple Layer Fit of the LSCF-YSZ sample heat treated at 1000 ℃. 122

5.36 Compilation of values for D_{int} and L_{int} obtained using the triple layer fit from the LSCF-YSZ samples heat treated at various temperatures. The black points show the variation of interlayer diffusivity, while the red points show the variation in interlayer thickness. 123

5.37 Comparison of the values of the interface resistance parameter r as obtained through fitting the data from the model (red) and calculating from the variables in the triple layer model (black). 124

5.38 Tracer diffusion coefficients obtained from two different fitting methods for LSCF-YSZ samples heat treated at the indicated temperature and compared to the literature values of LSCF and YSZ shown in the dashed lines. The values for 900 and 1000 ℃ are obtained from two separate samples. 125

5.39 Surface exchange coefficients obtained from two different fitting methods for LSCF-YSZ samples heat treated at the indicated temperature and compared to the literature value of LSCF shown in the dashed line. The values for 900 and 1000 ℃ are obtained from two separate samples. 126

6.1 Isotopic fraction data obtained from a series of samples containing LSCF deposited on a YSZ substrate and subsequently heat treated at the indicated temperatures. As with the LSCF-YSZ samples, isotope exchanges were performed at 460 ℃ for 90 minutes. . 131

6.2 EDX images obtained from the cross-section of a sample consisting of LSCF deposited onto a YSZ substrate using the drop casting method. The cross-section focuses on the interface region between the two materials, displaying darker spots with distinct elemental characteristics. 132

6.3 EDX analysis obtained from a series of points along the interface of a sample consisting of LSCF deposited onto a YSZ substrate using the drop casting method. The points were chosen to fall within and between the darker spots, as well as away from the region. 133

6.4 Nyquist plots of all the multi-layer LSCF-YSZ samples fabricated with PLD and heat treated at the labelled temperatures. Note the logarithmic scale on both axes for the purpose of global comparison. 137

6.5 Impedance spectra comparing the response of the LSCF-YSZ PLD samples, one without additional heat treatment, the others heat treated at 700 and 800 ℃. 138

6.6 Bode plot comparing the imaginary response of the LSCF-YSZ PLD samples, one without additional heat treatment, the others heat treated at 700 and 800 ℃. 138

6.7 Impedance spectrum of the LSCF-YSZ PLD sample heat treated at 900 ℃. 140

6.8 Impedance spectrum of the LSCF-YSZ PLD sample heat treated at 1000 ℃. 140

6.9 Bode plot of the imaginary imedance by the LSCF-YSZ PLD sample heat treated at 900 ℃ 140

6.10 Bode plot of the imaginary imedance by the LSCF-YSZ sample heat treated at 1000 ℃. 140

A.1 3D Zygo topography map of the surface of a multi-layer sample where the LSCF layer was deposited using PLD on a sintered substrate. The crater seen is the result of the sputtering beam in the SIMS. A-1

A.2 Variation in surface position as determined by linear analysis of the Zygo surface topography data. The profile shows the depth of the sputtering crater caused by the SIMS. A-2

A.3 XRD patterns obtained from LSCF deposited on YSZ substrates and heat treated at different temperatures. A-3

A.4 Impedance spectra collected from a LSCF-YSZ PLD sample heat treated at 700 ℃, one without any DC bias and two with a positive and negative DC bias of 200mV, respectively. The spectrum obtained from a pure YSZ pellet is inserted for reference. . A-4

A.5 SEM images obtained from a multilayer samples of LSCF deposited using a terpineol-based ink painted onto a pre-sintered GDC substrate showing a) the cross section and b) a top-down view of the LSCF layer. While a good quality deposition of a layer of approximately 200 µm was achieved, this layer has a clearly porous microstructure, indicating that it has not completed sintering and is therefore not suitable for isotopic exchange experiments. A-6

A.6 SEM images obtained from a multilayer samples of LSCF deposited using a terpineol-based ink painted onto a GDC substrate showing a) the cross section and b) a top-down view of the LSCF layer. The GDC substrate was pre-fired at 800 ℃ before ink depositionA-6

A.7 Simplified respresentation and resulting SEM images of the processes occuring during co-sintering of a) pre-sintered GDC with an LSCF ink deposited on top and b) pre-fired, but not densified GDC with the same ink deposited on top. During the latter process, the intially dispersed layer of LSCF powder densifies along with the electrolyte substrate, whereas in a) the lack of sintering densification in the GDC introduces a tensile strain perpendicular to the interface which prevents full densification of the LSCF powder. . A-7

A.8 Oxygen isotopic fraction data of an LSCF layer deposited on a GDC substrate and annealed in Oxygen-18 atmosphere at 650 C for 1h obtained using cross-sectional SIMS A-8

A.9 Top surface images of an LSCF layer deposited onto a GDC pellet using an ink drop casting technique. These images focus in on the edge of the sample pellet, where the accumulation of ink during the deposition of many consecutive layers resulted in the cracks and tears seen. A-9

A.10 Top surface and cross-section image of an LSCF layer deposited onto a GDC pellet using ink drop casting. This sample shows minimal cracks and pores, while still having a thickness in the area of 30 microns. A-9

A.11 Oxygen isotopic fraction data of an LSCF layer deposited on a YSZ substrate and annealed in Oxygen-18 atmosphere at 600 C for 1h obtained using cross-sectional SIMS(right) and FeO ion signal data indicating the presence of an LSCF layer (left) . A-10

A.12 Cross-section SIMS isotopic fraction data from a LSCF-GDC multi-layer sample fabricated using the drop casting and co-sintering method. The sample was exchanged at 600 ℃ for 90 minutes. The right hand side of the image shows the LSCF layer delaminated from the GDC substrate, while the left hand side represents a different sample pellet glued to the multi-layer. A-12

A.13 SEM-EDX compound image of the iron signal in the cross-section of the LSCF-GDC multilayer sample obtained after the full polishing procedure and SIMS analysis. This cross section consists of two multi-layer samples glued to each other along the LSCF surface. The iron signal indicates the presence of LSCF. A-12

Nomenclature

List of Abbreviations

ASR Area Specific Resistance [$\Omega\,m^2$]

BTCS Backward-Time Central-Space

CFO $CoFe_2O_4$

CGO $Ce_{1-x}Gd_xO_{2-\delta}$

CN Crank-Nicolson method

EDX Energy Dispersive X-Ray Spectroscopy

EELS Electron Energy Loss Spectroscopy

EIS Electrochemical Impedance Spectroscopy

FTCS Forward-Time Central-Space

GIXRD Grazing Incidence X-Ray Diffraction

IEDP Isotopic Exchange Depth Profiling

IF Isotopic Fraction

LEIS Low Energy Ion Scattering

LSCF6428 $La_{0.6}Sr_{0.4}Co_{0.2}Fe_{0.8}O_{3-\delta}$

LZO $La_2Zr_{22}O_7$

ORR Oxygen Reduction Reaction

PEM Proton Exchange Membrane

PLD Pulsed Laser Deposition

SEM Scanning Electron Microscope

SIMS Secondary Ion Mass Spectrometer

SOEC Solid Oxide Electrolyser Cell

SOFC Solid Oxide Fuel Cell

SZO $SrZrO_3$

TEM Transmission Electron Microscope

ToF Time of Flight

YSZ Yttria-Stabilized Zirconia

Chapter 1

Introduction

1.1 Filling in the gaps

The global greenhouse gas emissions from all sectors including electricity, heat and industry, and agriculture need to be reduced as urgently as possible in order to minimise the effects of climate change. Recent years have seen increasing deployment of renewable electricity generation from wind and solar as well as an improvement in energy storage technologies, mainly batteries. This comes with an increased focus on electrification of many different processes. Directly deploying generated electricity in an application minimises waste heat and maximises energy efficiency, as opposed to combustion processes where the majority of available energy is dissipated as unused heat. Examples of this are electric vehicles and heat pumps, both of which have seen accelerated growth and become part of national decarbonisation strategies worldwide [1][2]. The combination of these technologies as well as low carbon renewable electricity generation offers a path to decarbonising the majority of emitting sectors.

While these developments are promising and seem to offer a path to decarbonise energy in the near-to-medium-term future, questions remain particularly on the sectors and processes that are harder to decarbonise. One example is long-haul heavy-duty transport, such as jet planes and cargo shipping, which need high energy densities that batteries cannot provide [3]. This is where hydrogen-derived fuels such as ammonia or synthetic gas could play a role, as it is possible to produce hydrogen at low emissions from water using electrolysis. Using pure hydrogen could also be useful, to produce steel without the carbon-emitting coke fuel currently in use, which both provides heat and reduces the iron ore for further processing. Another potential use case would be for long term duration energy storage, particularly in localities that have the ability to store large amounts of hydrogen gas cheaply. This

would be the case for any region which has underground cavern systems, either naturally occurring or as the result of human activity [4]. Due to the fact that no additional material or infrastructure is necessary to increase the total amount of hydrogen stored, such a system can act as a grid back-up for longer periods of time (weeks to months).
These use cases show the diverse potential utility of hydrogen technologies. Given the need to rapidly scale up decarbonising technologies on the one hand and the wider systematic issues that come with such a scaling process, much analysis points towards a heterogeneous approach that takes into consideration the optimal solutions for a particular sector or geography. In other words, while it is likely that some technologies will play the role of providing the 'baseload' decarbonisation, the development of alternative technologies remains of interest.

While the potential uses for hydrogen are varied, its sourcing or generation is a fundamental issue that first needs to be addressed. Today, the vast majority of hydrogen is generated as a byproduct of fossil fuel extraction from natural gas [5]. While there is some suggestion that hydrogen generated from natural gas with carbon capture technology (blue hydrogen) could be a feasible transitionary solution, if the continued exploration of fossil fuels is to be phased out, eventually the majority of hydrogen will have to be generated via electrolysis. While the renewable energy to power this could be available, the water splitting process is an energy intensive one associated with significant conversion losses. The same is the case for re-converting hydrogen into electricity using fuel cells, as might be the case in a long duration storage use case.

1.2 Solid Oxide Cells

If hydrogen is to play a significant role in the energy transition, developing the capacity to produce, convert and store hydrogen as efficiently and cheaply as possible is essential. Assuming that electrification will be ubiquitous and that most hydrogen will be created using electrolysis, the devices used to convert electricity to hydrogen and vice-versa need to fulfill these requirements. Solid Oxide Cells are a class of technology that seek to minimise the cost and energy intensity of producing and converting hydrogen. Since there is an intrinsic thermodynamic energy requirement to split water molecules, this process should be as efficient as possible for commercial viability. Similarly, converting the hydrogen into electricity is a challenge due to the losses occurring during this process. One method of achieving this is to burn the hydrogen to power a steam engine, as is done in conventional gas-fired power plants. This has the advantage of drawing upon technology that is already well-established in

industry. However, hydrogen combustion also entails large amount of waste heat and has a limited efficiency because of this, in addition to producing nitrous oxide emissions [6]. This is where fuel cells are particularly interesting, as they are theoretically more efficient due to the electrochemical nature of the conversion process. They also don't produce pollutants when run on pure hydrogen fuel and are maturing as a technology, therefore becoming more commercially viable. However, practical operating conditions such as gas flow rate, gas pressure and operating voltage also need to be optimised in order for the technology to be competitive. [7][8][9].

1.2.1 Alternative Fuel Cell and Electrolyser Technologies

Proton exchange membrane cells (PEM) are currently one of the most common commercially used type of technology used for the generation and conversion of hydrogen. PEM Fuel cells, however, require a high purity hydrogen gas stream to function properly, while SOCs are capable of not only operating without such a high purity, but also with other fuels such as natural gas or ammonia. PEM cells also typically require platinum and iridium catalysts both for fuel cells and electrolysers, which are both expensive and scarce, limiting the upscaling potential [10]. While many alternatives to such catalysts are being explored, there has not yet emerged a viable strategy to tackle this problem. SOCs function with ceramic oxide materials which are in general more common and less expensive. Finally, alkaline water electrolysis is the most mature hydrogen generation technology, but its potential is diminished by degradation due to its corrosive components as well as the cost being prohibitive to being a wide-reaching solution [11]. While the cost of SOCs could fall, currently the long-term stability of SOCs is a concern for commercial viability [7]. The higher operating temperatures (500-700 °C) enable various processes that are detrimental to long-term stability such as reactivity between cell materials, structural degradation of the cell materials and thermal cycling due to expansion and contraction of materials with different expansion coefficients. Materials selection is therefore a critical step in designing SOCs with long-term stability.

1.2.2 Material Interfaces

To further understand the factors influencing the performance of SOCs, it is instructive to look at the working mechanism of a SOFC as an illustrative example. The basic electrochemical processes in such a system are shown in Figure 1.1. In such a system, the reduction of oxygen on the cathode side as well as the transport of oxygen across the cell are two key properties that determine the cell performance. The higher the rate of oxygen that can be catalysed and transported, the more cell reactions to form steam can occur, and more electricity can be extracted from the cell.

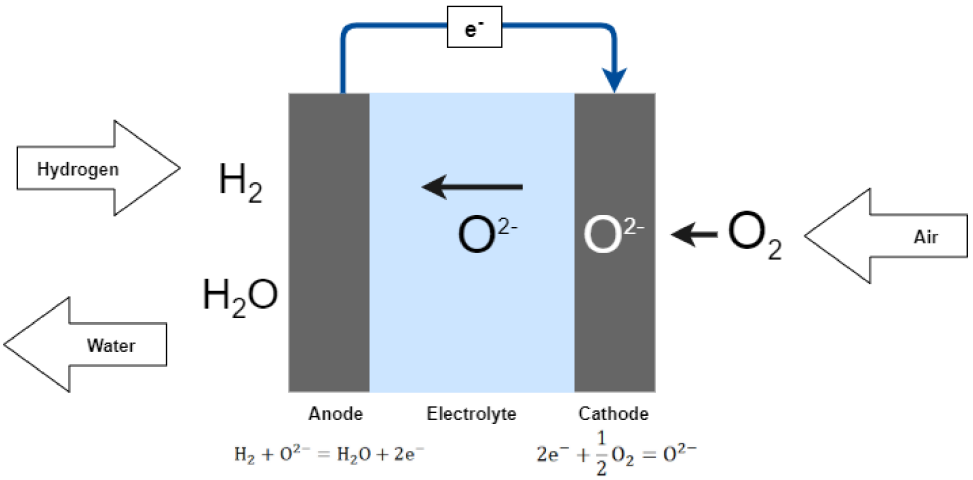

Figure 1.1: Schematic of a Solid Oxide Fuel Cell

The catalysis of the oxygen reduction reaction (ORR) has received much attention in research. In the first designs of SOFCs, the cathode consisted of a mostly pure electronic conductor that is able to catalyse the ORR, with the amount of triple phase boundaries (TPBs) between the gas, cathode and electrolyte essential in determining cell performance. The main example of these earlier materials is lanthanum strontium manganite (LSM), which when combined with an yttria-stabilised zirconia (YSZ) electrolyte forms triple phase boundaries (TPBs) that show good performance at high temperatures (800-1000 ℃). These high operating temperatures cause issues both with long-term stability and cell design. The higher energy environment enables many more degradation processes to take place in all parts of the cell, while also making it impossible to use metallic current collectors, increasing both the cost and sources of degradation in the cell [7]. This is why a reduction in cell operating temperature has been pursued, spurring on a development of mixed ionic and electronic conducting (MIEC) cathodes.

These MIEC materials are able to transport oxygen within their own lattices, extending the active catalysis regions from the TPBs to the entire cathode surface. This increased capacity enables the reduction of operating temperatures without losing performance, making it possible to operate the cell around 500-700 ℃ instead. This reduces the input energy needed, enables the use of cheaper steel interconnects, and reduces degradation risk. One of the most commonly used MIEC materials is the $La_{0.6}Sr_{0.4}Co_{0.2}Fe_{0.8}O_{3-\delta}$ (LSCF) system, which presents the issue of being chemically reactive with the conventionally used YSZ electrolytes [12]. This has resulted in the emergence of gadolinium-doped ceria (GDC) electrolytes as the main choice for intermediate temperature SOFCs, as it appears stable in conjunction with LSCF while still showing good oxygen diffusion properties. In the more application-focused development of these cells, many multi-layer architectures have emerged, where a

combination of GDC and YSZ as well as other materials are deposited as interlayers. These structures balance out the different benefits of the materials, such as the chemical stability of GDC and the lower electronic conductivity of YSZ.

This means that within any SOC, there will be at least 2, if not more, interfaces between different materials with different properties. Interfaces are often the source of degradation. Mechanical delamination becomes possible due to the physical mismatch between the two crystal structures. This is exacerbated by thermal expansion and compression of layers with different thermal expansion coefficients [7]. The formation of chemical reaction products can become thermodynamically favourable under certain conditions, particularly when the operating temperature is high, as is the case with SOCs. Some of these reaction products might be unfavourable to the transport of oxygen ions within the lattice, reducing overall performance. Characterising and quantifying these interfaces could therefore be an important tool to further understand the degradation processes taking place in SOC materials, as well as their effect on performance.

1.2.3 Quantifying Interfaces

There are various experimental tools that help characterise the materials in electrochemical systems. This can either be done by assembling a cell that can be tested as a whole, or by characterising the individual components. Methods to test the performance of whole cells under operating conditions are well-established, mainly electrochemical impedance spectroscopy (EIS). It provides information about various aspects of the frequency response of the cell, including some interface-related processes [13]. EIS can be used for a variety of samples. One option is to assemble a whole cell containing an anode, cathode and electrolyte with a rig providing an appropriate gas stream and operating temperature. This puts the cell under operating conditions, particularly useful for investigating the electrochemical processes occurring. A half-cell structure or single material pellet can also be helpful in characterising the intrinsic properties of cell components, rather than just under operating conditions. Interface transfer processes can produce a low-frequency impedance response visible in the spectra. However, the information obtained from this is undifferentiated and captures the combined behaviour of all cell components, rather than decisively describing one interface.

To obtain the material properties of the cell components individually, isotope exchange depth profiling (IEDP) is a useful technique that allows the self-diffusion coefficient D to be extracted. D is the measure of how capable a material is to allow oxygen diffusion within its solid lattice, which determines

the overall cell performance. While this gives a picture of the intrinsic material properties by visualising the diffusion of oxygen through a material, it is only an approximation of the conditions the material would find itself in when built into a full cell.

In particular, the technique would not be able to capture the influence of a degraded interface that might block ion transport, since IEDP assumes constant diffusion properties throughout the material. Combining the accurate measurements that IEDP offers with a sample that is closer to a real SOC might elucidate the role of material interfaces further. For this reason, the goal of this project is to develop a modelling framework that enables the use of the IEDP technique to visualise oxygen diffusion across multiple layers of materials, including an interface between these materials. This more refined model can then be compared with EIS data to further elucidate the role of interfaces in SOC systems.

1.3 Literature Review

In order to understand what influences the efficiency and lifetime of SOFCs, it is necessary to first understand the materials science behind them. Knowing which materials to use and how to process them is important to fabricate high-quality samples suitable for IEDP. It is also essential to be aware of existing work in literature on multi-layer solid oxide samples, particularly if IEDP was used for characterisation. Finally, the nature of chemical interaction between solid oxide cell materials can provide guidance on potential mechanistic explanations for the processes taking place on the interface and the effect they have on the cell as a whole.

1.3.1 Materials science of SOFCs

Performance metrics and materials properties

The following is a short overview of the metrics that are commonly used to quantify the quality and performance of solid oxide cell materials.

SOFC Efficiency

Efficiency will often be one of the most accessible and commonly cited indicators of the performance of a fuel cells. There are several ways to think about the efficiency of a fuel cell system. One metric is fuel utilisation, i.e. the amount of hydrogen converted into water. SOFCs can, in theory, achieve 100% fuel utilisation. This does not, however, translate to the overall system performance. High fuel utilisation can increase losses associated with concentration polarisation and further cause

oxidation on the fuel electrode side, reducing lifetime. Furthermore, higher fuel utilisation will not necessarily directly relate to a higher system efficiency. A fully operational SOFC system has to consider gas pressures and operating temperatures of both the cell and support systems [9][8]. Depending on the stack design, lower fuel utilisation might be desirable, as the excess fuel can be recycled or burned off to keep the system temperature high.
For these reasons, efficiency is often defined as the ratio of the power drawn from the system relative to the energy available from the fuel consumed, i.e. 'electrical efficiency. This depends on the output power, mass flow rate and reaction enthalpy and produces efficiencies in the range of 45-65 %. If the thermal efficiency of the system is added (i.e. the reaction energy embodied in the produced water that could be captured), the overall 'efficiency' can in theory be higher than 80 % [14][15]. This means that, when talking about SOFC efficiency, close attention must be paid to the context and methodology in which such a value was obtained.

Focusing on purely the performance at cell level, the thermodynamic limitations in SOFCs must be considered. By calculating the free energy of water formation, assuming no losses, the open circuit voltage of the cell can be obtained. The relationship between the actual and open circuit cell voltage, multiplied by fuel utilisation, gives a measure of the ideal cell efficiency. The next step is to introduce losses in cell voltage due to polarisation mechanisms. Briefly, these include the intrinsic ohmic resistance of the electrolyte, the activation polarisation due to sluggish reaction kinetics and the concentration polarisation due to gas transport losses. While the ohmic losses are solely dependent on the ionic conductivity and thickness of the electrolyte (as well as the electronic losses at the electrodes), the electrode losses are more complex. Since concentration polarisation is described by gas transport (and there are various models employed to model this), a porous electrode structure that optimises gas diffusion is needed. When considering activation polarisation on the other hand, charge transfer kinetic models based on the Butler-Volmer equation are often used [16]. Combining these insights and models gives an idea of the factors involved in loss of performance. While many different factors play into the total efficiency of an SOFC, from a materials property perspective, the most notable quantities are the ionic conductivity and the surface reaction kinetics.

Ionic conductivity

The ionic conductivity of a material is the most fundamental property that determines suitability to a solid oxide cell, as it describes the ability to conduct oxygen ions through the cell. It can be

related to its diffusion properties using the Nernst-Einstein equation.

$$\sigma_{\text{ion}} = \left(\frac{z_i^2 e^2 C_{\text{carrier}}}{k_{\text{B}} T} \right) D \tag{1.1}$$

where z_i is the valence of the mobile ion; e is the charge on an electron; C_{carrier} is the concentration of available charge carriers; k_{B} is the Boltzmann constant; and T is the absolute temperature. The concentration of charge carriers in a solid oxide cell refers to the concentration of oxygen vacancies. It is important at this point to emphasize that the diffusivity in this equation is a generalised term, whereas experimental processes specifically measure only a type of diffusivity depending on the mechanism of transport. When applying an external electric field or a change in the chemical environment, the movement of oxygen vacancies depends on these factors. When no external stimulus is applied and only the movement of isotopes is measured, this is referred to as self-diffusion. Depending on the experimental setup, different values of D are obtained. These values are related and conversion between them is possible using thermodynamic/chemical factors. The isotope exchange technique measures the self-diffusion properties of a material, therefore from this point onwards, D always refers to self-diffusion.

Surface reaction kinetics

Referring to the Butler-Volmer based description of charge transfer kinetics, the material property that is most relevant for activation polarisation at the cathode is the surface exchange coefficient k. This describes a material's ability to exchange oxygen between the gas phase and the lattice. This is another key metric where materials selection is an important factor. Since this property is only relevant for the electrode materials, it can be accurately characterised using a single material sample. For the purpose of modelling multi-layer diffusion, k will be a necessary part of the model to capture the whole system's behaviour. However it is likely not a relevant variable that describes or quantifies the processes at the interface. The value of k will instead be useful for comparison with literature values, confirming if the properties of the electrode in the multi-layer sample match those obtained from a single material sample.

SOFC materials and degradation mechanisms

The following is a quick overview of the most commonly used materials in SOFC systems and which ones will be relevant for this project. Further, the degradation mechanisms that these materials can be involved in are discussed.

Electrolyte

Many solid oxides have been investigated for their ionic conductivity properties over the decades. In addition to the electrochemical performance, thermal and mechanical stability is of high importance, since the cell operates at high temperatures and experiences thermal cycling on start up and shut down. This not only places limitations on the electrolyte material in isolation, but also its compatibility with the electrode materials, particularly compatibility with regards to chemical reactions and thermal expansion. The most commonly considered materials in commercial or close to commercial systems are yttria-stabilised zirconia (YSZ) and gadolinium-doped ceria (GDC). They have a cubic crystal structure which through the introduction of dopants form oxygen vacancies in the lattice, improving the ability to transport oxygen. YSZ has been the electrolyte material of choice for a long time and was amongst the first solid oxide materials to be investigated.

GDC is a material that has received an increased amount of attention in recent times, mainly because it exhibits higher ionic conductivity at lower temperatures (< 800 ℃), opening a pathway for intermediate temperature SOFCs. This is balanced against the higher levels of electronic conductivity, which can become an issue under some operating conditions [17][18]. This is why multi-layer structures incorporating both GDC and YSZ have also been investigated and might present a relevant scenario for the modelling of diffusion across different materials.

Another issue in both GDC and YSZ systems is that silica impurities in the structure can affect the performance through aggregation at the grain boundaries, forming an amorphous network that negatively affects performance [19][20][21]. This has to be considered when evaluating characterisation and performance results.

Anode/Fuel Electrode

The anode materials need to be capable of catalysing the oxidation of hydrogen. Beyond this, an important requirement is the stability even under the high temperatures as well as the reducing atmosphere that hydrogen provides. This problem becomes significantly more complex when the SOFC is operated using carbonaceous fuels [7]. The material most commonly used today is a composite of nickel and the electrolyte material (Ni-YSZ and Ni-GDC most commonly). Much of the research in optimising anodes centres around microstructural optimisation, enabling the best possible gas flow and mechanical stability. Since the focus of this project is to investigate the solid transport processes in

and around interfaces, the anode side of the cell structure will not need to be considered.

Cathode/Air Electrode

Cathode materials have differing requirements depending on the intended application. Traditionally, cathodes consisted of electronic conductors capable of catalysing the oxygen reduction reaction and then allowing the incorporation into the electrolyte lattice at triple phase boundary (TPB) points. This has limited SOFCs to operation at very high temperatures (around 1000 ℃). The degradation and lifetime issues (among others) associated with this have inspired the search for cathodes capable of operating at lower temperatures. One successful approach for this is to employ mixed ionic and electronic conductors (MIECs). This extends the range of chemically active regions to the whole cathode surface rather than just the TPBs, thereby reducing activation polarisation and operating temperature. The most commonly used such MIEC cathode is lanthanum strontium cobalt ferrite (LSCF), which will also be the main material of choice in this project. LSCF has a perovskite ABO_3 structure of $La_{1-x}Sr_xCo_{1-y}Fe_yO_{3-\delta}$, where La and Sr occupy the A- and Co and Fe the B-site, respectively. The introduction of divalent Sr into the trivalent La A-site leads to the additional formation of oxygen vacancies due to the compensation on the oxygen site following such a substitution, improving the diffusion properties [22]. The ratio of B-site cations is chosen to offer the best combination of structural stability and electronic properties. While cobalt appears to contribute significantly to the catalytic ability to reduce oxygen, the introduction of iron stabilises the crystal structure, reduces the thermal expansion coefficient and increases electronic conductivity at high temperatures [23]. These factors mean that the ratio of the cations on each site can be varies in order to enhance or reduce certain properties. $La_{0.6}Sr_{0.4}Co_{0.2}Fe_{0.8}O_{3-\delta}$, or LSCF6428, offers a balance between performance properties and stability.

SOFC Degradation

There are many different factors in various cell components that contribute to degradation in SOFCs. They can broadly be categorised into physical/mechanical and chemical degradation [7].

Physical degradation

Most physical degradation mechanisms in SOFCs can be traced back to volume changes. The high operating temperatures induce significant enough thermal expansion of all cell components. This

becomes particularly problematic when considering the multi-layer nature of the cell, as a mismatch of thermal expansion between the cell components can lead to significant cracking and delamination. Another way in which volume changes can happen is due to redox cycling. This is a particular issue at the anode side, as often there will be an *in situ* reduction of NiO to Ni that might need to be repeated several times over the cell's lifetime. This comes with a significant enough volume change that it could present issues, such as agglomeration of nickel to reduce the TPBs available or expansion-related stresses.

Chemical degradation

Chemical degradation can roughly be split into intrinsic degradation and degradation resulting from interactions with the gases used to operate the cell. The latter includes trace gases in natural air on the cathode side and various carbonaceous fuels and their trace gases on the anode side.
Intrinsic degradation describes the cell materials in isolation undergoing a degradation process, reducing the performance properties of the material. This is again facilitated by the high operating temperatures. The same circumstance also enables chemical reactions between the cell components, potentially forming compounds that impede the function of the cell. One prominent example of this is LSCF (a newer, lower temperature cathode material) and YSZ (the most studied used electrolyte historically) reacting to form various new compounds, which will be discussed in more detail later.
Finally, other components in the stack, such as the interconnects, can react with the functional cell materials. One common issue in high-temperature cells without a MIEC cathode is the poisoning from chromium vapours that originate in cell interconnects and block the TPBs needed to perform the cell reactions. This illustrates further reasons why a shift towards intermediate temperature cells, which can use steel interconnects that are cheaper and do not provide sources of chemical degradation, is targeted.

Processing Multi-Layer SOFC Materials

After understanding the materials involved in solid oxide cells and how they can degrade both individually and at a cell level, the processing techniques to fabricate multi-layer samples out of these materials are investigated. The fabrication of multi-layer samples of SOFC materials can be broadly subdivided into two main categories: thin film deposition techniques (such as pulsed laser deposition or PLD) and ink processing techniques such as screen printing and tape casting.
Thin film deposition is useful for producing dense layers in the nanometer to low-micrometer range, and does not require temperatures in excess of 1000 ℃ during the fabrication process. This is because the

laser hitting the PLD target provides enough energy to ablate the target and initiate deposition onto the substrate, although the resulting microstructure is highly dependent on the substrate temperature, among other factors [24] [25]. If there is not enough energy available for diffusion on the substrate surface, the ablated and deposited pieces of target material will clump on the surface, resulting in a porous microstructure. Furthermore, the composition and partial pressure of the gas that is fed in before the deposition process can significantly change the deposition process, particularly if the pO_2 is too high [26]. In such a scenario, the ablated particles of target material begin to cluster as they move through the oxygen gas, which similarly causes the deposition process to occur from clumps of target material aggregating on the substrate surface [27]. This also results in a porous and disconnected microstructure. Finally, the growth process during PLD occurs on top of the substrate microstructure, meaning that the grains themselves will act as growth sites for the deposited layer, while the grain boundaries remain as gaps. This means that the thin film grain structure will likely be reproduced from the substrate, which has to be considered when designing experiments [28].

The initial challenge in this project is to fabricate dense layers of LSCF on top of an electrolyte substrate. This is a process that is well-established in literature for thin film deposition methods. Since in real-life applications, cathodes are fabricated to be porous, there is not much literature on using ink-based processing techniques to deposit dense layers of LSCF. For electrolyte materials such as YSZ as well as porous LSCF, however, there are many different approaches including terpineol-based ink [29][30] and more complex ethanol/toluene-based inks using various additives[31], among many others. These will be used as a basis for methods used in this project. Another important factor to consider for processing is the co-sintering. Cation interdiffusion can become an issue that has to be taken into account at higher sintering temperatures and thinner layers. The balance between thermal expansion and densification is another subject of study [31]. The unique properties of each layer have to be balanced out to ensure no cracking, delamination or incomplete sintering occurs.

1.3.2 Interfaces in SOFCs

In a complex, multi-layer device such as a solid oxide fuel cell, there are a wide variety of what can be considered interfaces. The contact between the electrodes and the gaseous environment forms one such interface, which is extensively described by electrochemical models for oxidation and reduction processes. The principal interface of interest in this project will be the solid-solid interface between the air electrode and the electrolyte materials, as this system can be investigated in detail with tracer diffusion experiments, as will be discussed in this section.

Apart from these interfaces between different materials entirely, grain boundaries also fulfil many of the definitions of an interface, being a distinct transition region between two phases that possesses properties specific to it. This has led to much study on the effect of grain boundaries in electroceramic materials, with different effects observed across materials and experimental conditions [32][33][34][35]. While no fully conclusive descriptions have emerged, the general trend of study indicates that grain boundaries can offer a fast diffusion path in materials with low bulk ionic conductivity, while they act in a more resistive manner in materials with high bulk ionic conductivity [36]. This has been hypothesised to be related to the formation of space charge regions within the boundaries, coupled to the charged oxygen vacancies in solid oxide materials [37]. Such descriptions centred around atomistic and space charge mechanisms have been developed to describe solid-solid interfaces in general, and offer potential mechanistic explanations for the behaviour of interfaces. While these models may be helpful in describing the cause of interface blocking effects, the main goal of this project is to develop a quantification method that can easily be verified with experimental data, particularly tracer diffusion.

Many studies have been done to investigate the properties of SOFC material interfaces, primarily focusing on cation interdiffusion, secondary phase formation and lattice mismatch with resulting strains. Some of these could contribute to degradation mechanisms that could reduce the lifetime of the cells significantly.

Tracer diffusion across an interface

Since the aim of this project is to use tracer diffusion methods for the characterisation of multi-layer samples, the first step is to analyse the work already done using this method.
Horita *et al.* conducted tracer diffusion experiments on an LSCF-GDC-YSZ multilayer sample that had been exchanged under an applied potential [38]. This acted as a pump for the oxygen ions to diffuse through the layers, putting this system under different conditions than the self-diffusion used in this project, as it introduces an electrical driving force for diffusion, rather than the self-diffusion obtained by tracer experiments. The diffusion behaviour around the interface regions was examined, although no attempt was made to extract any material parameters such as the tracer diffusion coefficient D^*. In these types of multi-layer samples, a common problem is the high reactivity between YSZ and LSCF to form $SrZr(Y)O_3$ (SZO) layers. This layer has been found to potentially have ion-blocking properties [39]. Even when applying a GDC interlayer, the same reaction can still take place due to the diffusion of cations across the interlayer [40]. Tracer diffusion analysis seemed to show that the SZO phase itself

may be subject to modification due to various species diffusing into it from other layers, potentially creating multiple types of SZO with different degrees of ion blocking [41]. Develos-Bagarinao *et al.* attempted to use tracer diffusion experiments to further elucidate this blocking effect going from an SZO to a YSZ phase [39]. A multilayer sample consisting of GDC, SZO and YSZ was analysed using isotope exchange experiments, with the resulting diffusion profile shown in Figure 1.2a.

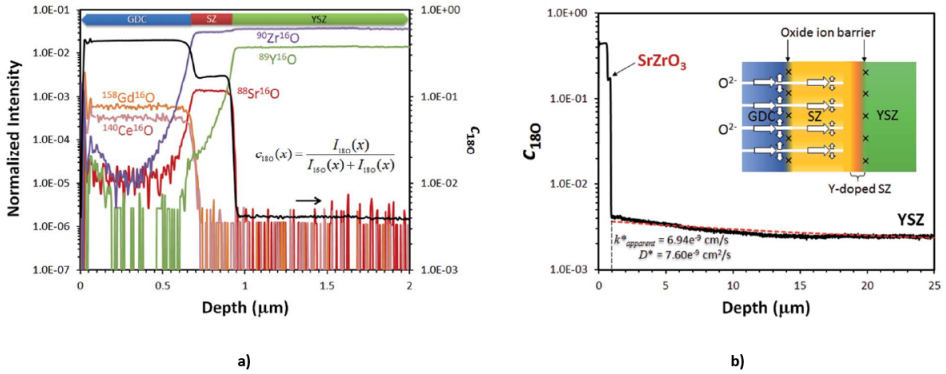

Figure 1.2: Tracer diffusion profile obtained from a GDC-YSZ layer system with a SZO reaction layer in between the two. Shown are a) the full diffusion profile across the multilayer sample, including concentration drops at each interface and b) the fitting approach chosen by the authors to model the transport properties of the SZO-YSZ interface. Reprinted from Develos-Bagarinao *et al.*[39], Copyright 2017 Royal Society of Chemistry.

This profile showed a drop in isotopic fraction at the GDC/SZO as well as the SZO/YSZ interface, while the SZO region itself showed a flat diffusion profile. The authors interpreted this data to mean that the ion blocking effect is not due to the intrinsic properties of SZO, but rather the properties of the interfaces themselves. This opens up the question of whether the interface blocking effect is related to a process intrinsic to the transfer from one layer to another, or purely determined by diffusion properties. This question will be explored further in this project.

An approach was chosen to model the system by fitting the data to Crank's 1D solution in a semi-infinite medium with a surface exchange boundary condition. The SZO-YSZ interface was modelled as the 'apparent surface' of the exchange, extracting D^* for YSZ and a k^*_{apparent} which was meant to represent the ability of oxygen ions to diffuse across the interface, as shown in Figure 1.2b. This approach has the following issues that undermine the validity of the extracted parameters. For one, diffusion across a solid-solid interface cannot be modelled using a gas-solid analogy, as the surface exchange process does not underlie the same boundary conditions as solid ionic transport. The gas phase is assumed to be a source of constant concentration, while the solid phase preceding the interface is part of the diffusion region and therefore does not present constant source conditions. In a similar manner, modelling an

interface in this way does not take into account any of the diffusion profile of the previous layers, which in turn is dependent on the actual oxygen exchange at the cathode surface. The system has to be considered holistically, since variations in one part of the profile will have an impact on all other parts.

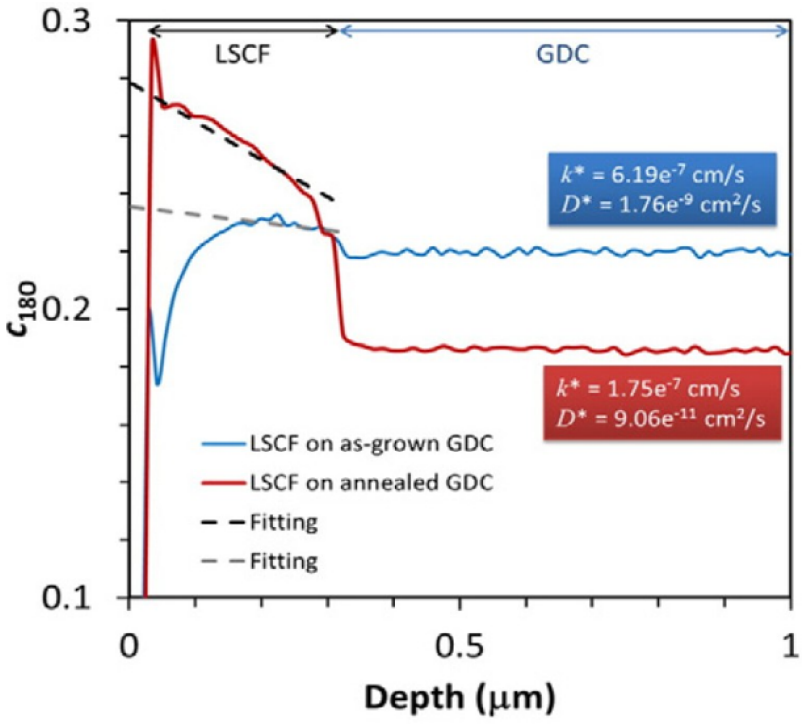

Figure 1.3: Tracer diffusion profile obtained from a multilayer sample consisting of LSCF deposited by PLD onto a single crystal GDC film which in turn was deposited on a YSZ substrate (partial diffusion profile shown here). The dashed lines indicate the region of fit chosen by the authors. Reprinted from Develos-Bagarinao *et al.*[42], Copyright 2016 Elsevier.

In a paper by the same group, the effect of LSCF microstructure on surface exchange and tracer diffusion properties was investigated [42]. LSCF thin films were grown on a GDC-YSZ multilayer sample with various differing processing parameters. Isotopic exchange experiments were once again conducted. In this case, an attempt was made to fit only the LSCF part of the SIMS profile to Crank's solution, as seen in Figure 1.3. The ability of the GDC part to diffuse oxygen has a knock-on effect on the isotopic fraction observed in the LSCF layer. If, for example, the GDC had poor oxygen diffusion properties, this would increase the isotopic fraction closer to the surface. A higher surface concentration in the data will in turn lead to an apparent higher surface exchange coefficient obtained from the fit. The intrinsic interconnectedness of the fitting parameters show the necessity for a model that can capture diffusion across multiple layers in a mathematically sound manner. Beyond finding a mathematical description, understanding the chemical mechanisms that occur in the systems of interest is necessary to develop an understanding of why interface blocking could happen.

Cation Interdiffusion and Reactivity

An SOFC consists of a wide variety of interfaces between electrode, electrolyte and interconnect materials. Here the focus is on three classes of materials: the LSCF cathode and the GDC and YSZ electrolytes and their interaction. It has long been known that YSZ reacts with La-based cathode materials (such as LSCF) to form insulating interlayers such as $SrZrO_3$ (SZO) or $La_2Zr_2O_7$ [12][43]. GDC does not form such reaction products, which prompted research into using it as an interlayer as well as to replace YSZ entirely. It also exhibits a higher oxygen diffusion coefficient at lower temperatures whilst having some issues with developing electronic conductivity under certain reducing conditions, such as can be found at the SOFC anode. This can be managed by using YSZ as an interlayer at the anode side [44][45]. The interfaces between GDC-YSZ, LSCF-GDC, and a triple layer of all three materials are therefore important to consider.

Interaction between LSCF-GDC

Li *et al.* conducted a study on the effect of sintering temperatures on the interface of an LSCF-GDC multilayer sample [30]. While it was found that no secondary phase formation due to chemical reactions occurs, temperature-dependent cation interdiffusion is significant. This is not limited to any particular type of element, and the diffusion length is roughly the same for each species. This creates a 'diffusion zone' where intermixing between all of the species occurs, as detailed in Figure 1.4.

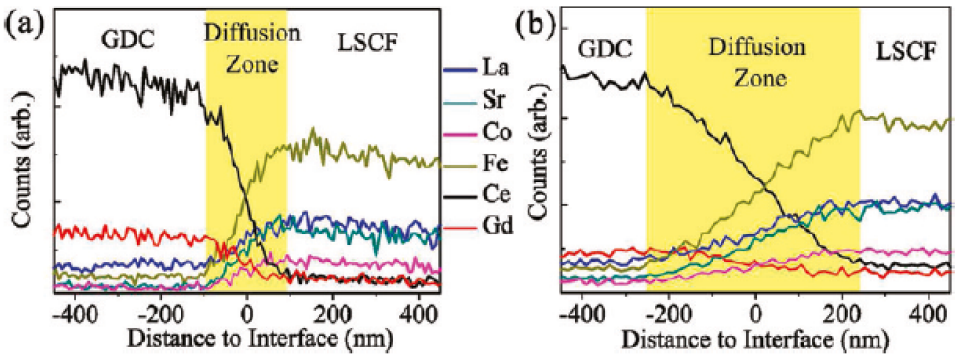

Figure 1.4: Elemental composition of the GDC-LSCF interface at co-sintering temperatures of a) 1100 ℃ and b) 1400 ℃. A relationship between sintering temperature and degree of cation interdiffusion can clearly be observed. Reprinted with permission from Li *et al.*[30], Copyright 2011 American Chemical Society.

Electron Energy Loss Spectroscopy (EELS) analysis revealed changes in valence states in this diffusion zone. Furthermore, microstructural changes were also identified and related to a change in oxygen vacancy ordering in the diffusion zone. These effects are considered to be detrimental to

cell performance, and using the lowest possible sintering temperature during cell fabrication was thus suggested. The significance of this effect on the interfacial resistance as defined in this project will be an interesting factor to investigate.

Another notable way in which GDC and LSCF can interact during co-sintering was observed by Szasz *et al.* during a study of the LSCF-GDC-YSZ system[40]. When a porous GDC interlayer that had been screen printed onto a dense YSZ substrate was co-sintered with LSCF, the cations in the latter appeared to act as a sintering aid to the GDC, further promoting densification. Another key finding from the study is that controlling the composition of the diffusion zone between GDC and YSZ partially prevents the undesirable formation of SZO at this interface.

Interaction between LSCF and YSZ

Precursors to the LSCF system (mainly various cobaltites) have been under investigation since at least the 1980s [46]. As YSZ and its ionic conductivity was known and studied as a material for SOC applications, much of the materials discovery research was focused around investigating the compatibility and performance of many different compounds. It was found early on that some of the LSCF-type compounds tended to react with YSZ electrolytes to form new phases. The phase that emerged most prominently out of the XRD data in such system is that of $SrZrO_3$, with $La_2Zr_2O_7$ also found. Yamamoto *et al.* found that cobalt and strontium-containing compounds would react with the zirconia electrolyte to form $La_2Zr_2O_7$ and Sr_2ZrO_4, respectively, and that this resulted in an increased overpotential [46]. Later studies refined this further and specifically with LSCF6428, indicating $SrZrO_3$ as the dominant phase [43][47][12]. These reaction products present two major issues. Firstly, these reaction products could potentially show worse electrochemical properties by themselves, having lower ionic conductivity due to potentially different crystal structures and defect properties. This structural difference could also exacerbate the issues related to thermal cycling and mismatch of thermal expansion properties in the multi-layer structure. Finally, the favourability of the reaction itself suggests a chemical instability window at operating temperatures. This could lead to the continued reaction between LSCF and YSZ that degrades each of these components to the point where their performance diminishes. All of these potential mechanisms will be considered when investigating interface effects in this project.

Interaction between YSZ and GDC

Bi-layer electrolytes consisting of YSZ and GDC have long been a subject of investigation. Both of these materials have the fluorite structure and are therefore capable of forming a solid solution. This can become an issue at high co-sintering temperatures of around 1400 ℃ , as the interdiffusion process can form interlayers that reduce the ionic conductivity by up to two orders of magnitude [48]. Lowering the firing temperature has been proven to minimise interdiffusion sufficiently [49]. This effect is unlikely to occur during operating temperatures, as the activation energy for the self-diffusion of Zr in the 8YSZ (ZrO_2 doped with 8 mol % Y) lattice is too high [7]. This could, however, be an effect that lends itself to investigation using the interfacial resistance studies undertaken in this project.

Interfacial Strain

Apart from the chemistry of the interface, the lattice structure has also been the subject of much investigation, as it provides an alternative way to potentially improve performance and reduce operating temperatures of SOFCs. From a fundamental point of view, an interface is the conjunction of two different crystals with potentially different lattice parameters that form bonds. This mismatch of lattice parameters will lead to an interfacial strain. How this strain will affect the cell performance is of great interest. Garcia-Barriocanal *et al.* reported an increase in ionic conductivity in YSZ grown on strontium titatanate (STO) epitaxial films of up to 8 orders of magnitude [50]. This effect was ascribed to a combination of interfacial strain and an increase in mobile carrier concentration at the heterostructure. Schichtel *et al.* continued investigation into this effect, suggesting that the large increase in measured conductivity by Garcia-Barriocanal *et al.* was caused by an increase in electronic conductivity at the interface due to a free electron space[51]. A detailed investigation into the effects of lattice strain on ionic conductivity was undertaken. The conclusion was that under certain conditions where the lattice is strained at the interface, ionic transport can be enhanced due to a 'dilatative strain' which leaves more space in the lattice structure for oxygen vacancies to migrate. This effect can, according to the authors, account for an increase in conductivity of up to 2.5 orders of magnitude at the most.

Han *et al.* suggested that lattice strain decreases the energy of formation for oxygen vacancies, allowing it to be used as a tool to find the amount of lattice strain which maximises the enhancement of conductivity [52]. Wen *et al.* later expanded this description to develop a quantitative model for the effect of lattice strain on ionic conductivity, finding an optimal lattice strain of 3.46 % for the STO-YSZ system, resulting in an increase in conductivity of 2.7 order of magnitude [53]. The same author in a later review noted that this effect is more noticeable in and relevant to thin film devices,

and the interface region does not physically constitute a significant amount of the whole multilayer sample and the enhanced conductivity might not be noticeable[54]. Nevertheless, this effect could be an interesting factor to consider when investigating interfacial resistance effects in different types of multi-layer samples.

1.4 Modelling diffusion in multi-layer materials

As indicated previously, many approaches have been developed with the purpose of describing and understanding the mechanisms of solid-solid interfaces generally [37][55].
While these approaches offer useful ways to understand interface behaviour and potentially enable the simulation of multi-layer materials, no other experimental method is as capable of measuring diffusion in as direct a manner as IEDP. Fitting the data obtained from these experiments is therefore the priority of the modelling work in this project, which is why it is essential to understand how diffusion modelling of IEDP data works and how this can be used as a basis for further exploration.

1.4.1 Modelling diffusion in ceramics

The electrochemical performance of a material can be quantified in a variety of different ways depending on the function that is intended. In solid state, electrochemically active materials, the intrinsic crystal and defect structure will determine how it behaves. Electroceramics in particular are often designed to induce a particular type of defect that will benefit performance in some form. This is the case for oxygen conducting materials such as those used in Solid Oxide Cells, where lattice substitution induced oxygen vacancies, enabling a conductivity of oxygen atoms through the crystal. The higher a material's ability to allow oxygen to move through its lattice, the higher the corresponding ionic conductivity would be. This is dependent on a variety of constants related to thermodynamics and crystallography as well as the diffusivity [56].

Diffusivity and Fick's Laws

Diffusivity can be described as a constant that relates the flux of a given species through a material to the concentration gradient of that species in space [57]. This means that diffusive flux is driven by differences in concentration, which ultimately creates a Gibbs free energy or chemical potential driving movement. The degree to which this movement (or flux) can occur is related to a material's intrinsic ability to allow species to randomly jump between different positions in the crystal. This ability is

summarised in the diffusivity as defined by Fick's first law of diffusion

$$J = -D\frac{\partial C}{\partial x} \tag{1.2}$$

Extending this concept to a system where there is not only a concentration gradient, but it also changes over time, Fick's second law of diffusion can be derived. It takes the form of a partial differential equation.

$$\frac{\partial C}{\partial t} = -\frac{\partial J}{\partial x} \tag{1.3}$$

These types of equations can be solved by introducing boundary conditions in the system, which can then be solved using either with an analytical solution or a numerical one. As diffusion describes a significant number of transport processes in nature, the amount of different boundary conditions that can be introduced to describe different systems is vast. This is what motivated Crank to write an entire book containing only different diffusion systems and their solutions [58]. Included in this work is a semi-infinite diffusion system with a surface exchange boundary condition, a setup that can be approximated experimentally to measure oxygen diffusivity in electroceramic materials.

The conventional method of mathematically modelling tracer diffusion experiments is by considering a one-dimensional, semi-infinite medium as follows

$$\begin{cases} \partial_t C' = D\partial_{xx} C' & \text{on } (0,\infty)\times[0,\infty), \\ C'|_{t=0} = 0 & \forall x \geq 0, \\ C'|_{x=0} = 1 + \frac{D}{k}\partial_x C'|_{x=0} & \forall t > 0, \\ \lim_{x\to\infty}(C') = 0 & \forall t > 0. \end{cases} \tag{1.4}$$

This system enforces Fick's second law of diffusion throughout the whole material and furthermore introduces boundary conditions in space as well as an initial condition in time. C' refers to the normalised concentration of the diffusant, which is a function of both time and space. D here is the system's diffusion coefficient, while k describes the surface exchange coefficient. This parameter measures the material's ability to exchange the diffusing object with an outside source.

This system has an explicit analytical solution, first published by Carslaw and Jaeger in 1959 [59], and later more famously by Crank in 1975 [58]. One name given to this solution is Crank's solution in a one-dimensional, semi-infinite medium with an exchange boundary, henceforth referred to as just

'Crank's solution'.

$$C'_{\text{Crank}}(t,x) = \text{erfc}\left\{\frac{x}{2\sqrt{D^*t}}\right\} - \exp\left\{\frac{k^*x}{D^*} + \frac{k^{*2}t}{D^*}\right\}\text{erfc}\left\{\frac{x}{2\sqrt{D^*t}} + k^*\sqrt{\frac{t}{D^*}}\right\} \tag{1.5}$$

This equation has formed the foundation of fitting IEDP data in experiments involving electroceramics. Before Cooper standardised the fitting process by developing the MATLAB application TraceX, experimentalists manually fit their obtained data to Crank's solution [60]. For this reason, a model that is capable of fitting diffusion data across multiple layers has not been developed until this point. As TraceX was developed partially to standardise the fitting process and partially to enable the fitting of samples that underwent back-exchange processes, the software did not simply match the data to Crank's solution, but rather numerically solved the set of equations in order to calculate the diffusion profiles separately. This principle will be used as the basis of the multi-layer diffusion model outlined in chapter 3.

1.5 Identifiability of kinetic mechanisms at the gas-cathode interface

While the bulk of this project focuses on quantifying solid-solid interfaces, the gas-solid interface is another essential component of fuel cells that has significant effect on the performance. For this reason, it is important to have consistent methods of modelling and quantifying the different aspects of the cell that play a role.

One key way of improving the performance of solid oxide cells (SOCs) is by maximising the ability of the electrodes to carry out electrochemical reactions [61][62][63]. While the macroscopic effects of the electrochemistry can be understood relatively clearly as a conversion of chemical species (such as hydrogen and oxygen to water), the actual details of these reaction mechanisms are not fully clear. Much research is dedicated to better understanding these mechanisms and, on this basis, improve and optimise the design of the electrodes [64][65][66][67]. In SOCs, the relevant phases are those present in the solid electrode material (which may be a composite or single material) as well as the gas phase containing the species involved in the overall cell reaction. When modelling this system, two main categories of electrodes have emerged, which are referred to by the dominant reaction mechanism governing the system [68][69]. The triple phase boundary (TPB) systems carry out reactions mainly at the point where the gas phase, the electrode phase and the electrolyte phase of the cell meet [70][71]. Electrodes which are capable of both conducting electrons as well as ions are referred to as mixed ionic and electronic conductors (MIEC). Since these materials are capable of both catalysing the

electrochemical reaction at the gaseous surface as well as incorporating and transporting the species from the gas phase, the reaction sites are no longer limited to single points but, in theory, across the whole surface [72][73][74]. In practice, many materials contain a mixture of both behaviours and cannot necessarily be classified as exclusively one or the other [75][76][77].

When considering various SOC systems to look at in order to better understand the reaction mechanism, a single phase MIEC oxygen electrode emerges as a suitable candidate due to the fact that only one material's properties need to be accounted for in the model. It is already known in literature that the surface oxygen reduction reaction is coupled to the bulk ion diffusion processes in a MIEC material, meaning that the ability of the electrode to perform its function is dependent on both factors simultaneously [78][79][80]. Distinguishing between these two processes could help make clear which one of them is rate-limiting in the reaction and by extension the entire cell performance.

One of the most common experimental methods used to further understand these steps is electrochemical impedance spectroscopy (EIS), which measures the material's response to a frequency-variable applied voltage and models it as an equivalent circuit that can be mathematically analysed [13][81]. This method aims to distinguish charge transfer processes (as can be seen in the solid/gas surface reactions) from other relevant mechanisms, such as diffusion of ions in the bulk [82]. These processes can be modelled as different elements in the equivalent circuit, the sum of which will produce the impedance plots that can be read from doing an EIS experiment.
The first attempt at doing this in a porous MIEC electrode is the so-called ALS model first published by Adler, Lane and Steele in 1996 [83]. It assumes a thick electrode where diffusion and charge transfer work only in 1D with no external bias being applied. While the inter-pore gas diffusion is assumed to be fast, meaning that gas transport does not limit the reaction rate, rather than modelling the microstructure explicitly, the porosity is represented by an equivalent homogeneous medium. Incorporating these assumptions into the calculations yields an EIS curve with various unique features. The contributions made by the porous electrode can be described by a Gerischer element, an equivalent circuit component representing irreversible chemical reactions. This element can be involved in the EIS response over a wide range of frequencies because in MIEC materials, the oxygen non-stoichiometry can vary a great degree with the partial pressure of the oxygen in the gaseous phase. This is represented by the so-called 'chemical capacitance', which can become a significant factor in the impedance response, sometimes making it difficult to distinguish between individual reaction steps [84][85]. The final mechanism that is considered is the ion transfer at the interface between the MIEC electrode and the electrolyte.

It shows up relatively straightforwardly as a high frequency semi-circle, as it is in series with the electrode impedance [86]. The ALS model aims to show a system which is only dependent on the oxygen transfer at the gas/solid interface as well as the bulk ion diffusion in the MIEC, the main issue being the fact that these processes are coupled to each other and can therefore difficult to distinguish [87].

One of the most prominent MIEC electrode materials is $La_{0.6}Sr_{0.4}Co_{0.2}Fe_{0.8}O_{3-\delta}$ (LSCF). Due to its good balance of properties it is often the air electrode of choice in SOC systems both in research and in industry. For this reason, there is a rich body of work where EIS characterisation of LSCF took place [74][88]. As alluded to earlier, many different characteristics of a porous electrode make the identifiability of the individual reaction steps through EIS difficult. While fast gas diffusion is assumed in most models, some systems can still exhibit noticeable gas diffusion resistance both in the porous network of the material itself and the external apparatus supplying the gas [80][89][90]. Another issue is the variability of the electrochemical reaction pathways depending on microstructural peculiarities. If the particles in the electrode are very coarse, a significant amount of TPBs with the MIEC and the electrolyte can become significant and offer an alternative reaction path. This effect was studied in some detail by Laurencin et al. [91][92], who used more detailed microstructural models to elucidate the change in behaviour. One key finding of this series of papers is that under conditions where the MIEC's vacancy concentration (and thereby its ionic conductivity) becomes small, alternative reaction pathways such as those at the TPBs become dominant. These conditions are reached under anodic bias or under high oxygen partial pressure. These conclusions are supported by various other pieces of work applying different modelling approaches [93][90][77].

All of this seems to suggest that porous electrodes inherently introduce several variables that make clear elucidation of reaction steps difficult. As a logical conclusion, some work has been done on dense LSCF and other perovskite materials which do not present the issues caused by the pore network [94][95][96][97][98]. While this makes the system that is analysed less realistic and further away from a real cell, the well-defined geometry of a dense film should make it easier to distinguish the surface reaction step. Dense LSCF can be fabricated using thin film deposition techniques such as pulsed laser deposition (PLD). While some established experimental procedures for thin film LSCF have emerged, there is still considerable inconsistency in the results between studies. This is usually ascribed to changes in the surface of the MIEC such as morphology or composition [95][42], while these properties in the current collector can also influence results [99][100]. This body of work makes it clear that even in a controlled geometry thin film setup, the clear elucidation of reaction steps and their associated

values remains difficult.

This work is an attempt to help make the interpretation of experimental data easier by modelling a thin film system under a variety of applied biases and oxygen partial pressures. By examining one system and its EIS response to these scenarios, some consistent trends might emerge. To achieve this, a model for the oxygen reduction reaction (ORR) and its reaction steps must be developed. This process is complex and still not fully understood, but much work has been dedicated to understanding the individual steps in the reaction through modelling and sometimes fitting to real EIS data [79][101]. The intention here is not to develop a model that can be fitted to real data, but rather breaking down the process to its minimum relevant reaction steps in order to get a simplified, one dimensional continuum model. This model would simulate the EIS response under different bias/partial pressure and potentially reveal conditions where a clear rate limiting step can be identified.

1.6 Conclusions, Aims and Objectives

Hydrogen-based technologies could play an important role in decarbonising hard-to-abate sectors. Solid oxide cells are a technology that could play a key role within the hydrogen industry as methods of generating and converting hydrogen at large scales and high efficiencies. The main concern around SOCs is their long term stability, having many risk points in the materials and cell structure that could cause performance degradation under operating conditions. The interfaces between different materials in the cell can play a particularly prominent role in these degradation processes, potentially inhibiting the ion transport across the cell that determines performance. While diffusion models in single materials exist, there has not yet been a thorough mathematical description of diffusion across a multi-layer system with internal interfaces. The aim of this project is to develop such a model and test it against experimental data of multi-layer samples of SOFC materials. An increased synergy and coordination between modelling and experimental work is essential especially in today's scientific methodology, where every experimentalist must be able to consistently use theoretical methods to contextualise their data. This project explores two primary methods that aim to help guide experimentalists and result in more consistent data fitting methodology. Firstly, by exploring the identifiability of the kinetic steps in the oxygen reduction reaction using simulations, guidelines for designing experiments that are as insightful as possible are investigated. Secondly, by developing a model for diffusion across solid-solid interfaces, extending the isotope exchange depth profiling technique to analysis of multi-layer samples, the scope of this technique may be expanded.

References

[1] IEA. Electric vehicles. *International Energy Agency*, 2023.

[2] IEA. The future of heat pumps. *International Energy Agency*, 2023.

[3] N. Gray, S. McDonagh, R. O'Shea, B. Smyth, and J. D Murphy. Decarbonising ships, planes and trucks: An analysis of suitable low-carbon fuels for the maritime, aviation and haulage sectors. *Advances in Applied Energy*, 1:100008, 2021.

[4] D. Zivar, S. Kumar, and J. Foroozesh. Underground hydrogen storage: A comprehensive review. *International Journal of Hydrogen Energy*, 46(45):23436–23462, 2021.

[5] IEA. Hydrogen Report. *International Energy Agency*, 2021.

[6] A. C. Lewis. Optimising air quality co-benefits in a hydrogen economy: a case for hydrogen-specific standards for nox emissions. *Environ. Sci.: Atmos.*, 1:201–207, 2021.

[7] Brandon N.P. Cooper, S.J. *Solid Oxide Fuel Cell Lifetime and Reliability.* Elsevier, 2017.

[8] P. Vijay, A. K. Samantaray, and A. Mukherjee. Constant Fuel Utilization Operation of a SOFC System: An Efficiency Viewpoint. *Journal of Fuel Cell Science and Technology*, 7(4), 2010.

[9] Q. Fang, L. Blum, R. Peters, M. Peksen, P. Batfalsky, and D. Stolten. SOFC stack performance under high fuel utilization. *International Journal of Hydrogen Energy*, 40(2):1128–1136, 2015.

[10] C. Minke, M. Suermann, B. Bensmann, and R. Hanke-Rauschenbach. Is iridium demand a potential bottleneck in the realization of large-scale PEM water electrolysis? *International Journal of Hydrogen Energy*, 46(46):23581–23590, 2021.

[11] R.M. Navarro, R. Guil, and J.L.G. Fierro. Introduction to hydrogen production. In *Compendium of Hydrogen Energy*, pages 21–61. Elsevier, 2015.

[12] L Kindermann. Chemical compatibility of the $LaFeO_3$ base perovskites $(La_{0.6}Sr_{0.4})_zFe_{0.8}M_{0.2}O_3$ (z = 1, 0.9; M = Cr, Mn, Co, Ni) with yttria stabilized zirconia. *Solid State Ionics*, 89(3-4):215–220, 1996.

[13] E Barsoukov and J. Macdonald, editors. *Impedance Spectroscopy: Theory, Experiment, and Applications.* Wiley, 2005.

[14] R. M. Dell, P. T. Moseley, and D.A.J. Rand. Hydrogen, Fuel Cells and Fuel Cell Vehicles. In *Towards Sustainable Road Transport*, pages 260–295. Elsevier, 2014.

[15] J. Zhou, Z. Wang, M. Han, Z. Sun, and K. Sun. Optimization of a 30 kW SOFC combined heat and power system with different cycles and hydrocarbon fuels. *International Journal of Hydrogen Energy*, 47(6):4109–4119, 2022.

[16] D.A. Noren and M.A. Hoffman. Clarifying the Butler–Volmer equation and related approximations for calculating activation losses in solid oxide fuel cell models. *Journal of Power Sources*, 152:175–181, 2005.

[17] H Inaba. Ceria-based solid electrolytes. *Solid State Ionics*, 83(1-2):1–16, 1996.

[18] B. Steele. Appraisal of $Ce_{1y}Gd_yO_{2y/2}$ electrolytes for IT-SOFC operation at 500°C. *Solid State Ionics*, 129(1-4):95–110, 2000.

[19] R. Gerhardt, A. S. Nowick, M. E. Mochel, and I. Dumler. Grain-Boundary Effect in Ceria Doped with Trivalent Cations: II, Microstructure and Microanalysis. *Journal of the American Ceramic Society*, 69(9):647–651, 1986.

[20] R. Gerhardt and A. S. Nowick. Grain-Boundary Effect in Ceria Doped with Trivalent Cations: I, Electrical Measurements. *Journal of the American Ceramic Society*, 69(9):641–646, 1986.

[21] T. Andersen, K. V. Hansen, M. Mogensen, and I. Chorkendorff. Electrochemical removal of segregated silicon dioxide impurities from yttria stabilized zirconia surfaces at elevated temperatures. *Solid State Ionics*, 190(1):60–66, 2011.

[22] L Tai. Structure and electrical properties of $La_{1-x}Sr_xCo_{1-y}Fe_yO_3$ Part 2. The system $La_{1-x}Sr_xCo_{0.2}Fe_{0.8}O_3$. *Solid State Ionics*, 76(3-4):273–283, 1995.

[23] L Tai. Structure and electrical properties of $La_{1-x}Sr_xCo_{1-y}Fe_yO_3$ Part 1. The system $La_{0.8}Sr_{0.2}Co_{1-y}Fe_yO_3$. *Solid State Ionics*, 76(3-4):259–271, 1995.

[24] P. Plonczak, A. Bieberle-Hütter, M. Søgaard, T. Ryll, J. Martynczuk, P. V. Hendriksen, and L. J. Gauckler. Tailoring of $La_xSr_{1-x}Co_yFe_{1-y}O_3$ Nanostructure by Pulsed Laser Deposition. *Advanced Functional Materials*, 21(14):2764–2775, 2011.

[25] J. Schou. Physical aspects of the pulsed laser deposition technique: The stoichiometric transfer of material from target to film. *Applied Surface Science*, 255(10):5191–5198, 2009.

[26] D Waller. The effect of pulse duration and oxygen partial pressure on $La_{0.7}Sr_{0.3}CoO_3$ and $La_{0.7}Sr_{0.3}Co_{0.2}Fe_{0.8}O_3$ films prepared by laser ablation. *Solid State Ionics*, 134(1-2):119–125, 2000.

[27] W Marine, L Patrone, B Luk'yanchuk, and M Sentis. Strategy of nanocluster and nanostructure synthesis by conventional pulsed laser ablation. *Applied Surface Science*, 154-155:345–352, 2000.

[28] J A Thornton. High Rate Thick Film Growth. *Annu. Rev. Mater. Sci.*, 7(1):239–260, 1977.

[29] Y. Zhang, X. Huang, Z. Lu, Z. Liu, X. Ge, J. Xu, X. Xin, X. Sha, and W. Su. A study of the process parameters for yttria-stabilized zirconia electrolyte films prepared by screen-printing. *Journal of Power Sources*, 160(2):1065–1073, 2006.

[30] Z. P. Li, M. Toshiyuki, G. J. Auchterlonie, J. Zou, and D. John. Mutual diffusion occurring at the interface between $La_{0.6}Sr_{0.4}Co_{0.8}Fe_{0.2}O_3$ cathode and Gd-doped ceria electrolyte during IT-SOFC cell preparation. *ACS Appl Mater Interfaces*, 3(7):2772–8, 2011.

[31] C. Seok, J. Moon, M. Park, J. Hong, H. Kim, J. Son, J. Lee, B. Kim, H. Lee, and K. Yoon. Low-temperature co-sintering technique for the fabrication of multi-layer functional ceramics for solid oxide fuel cells. *Journal of the European Ceramic Society*, 36(6):1417–1425, 2016.

[32] A Atkinson. Diffusion along grain boundaries and dislocations in oxides, alkali halides and carbides. *Solid State Ionics*, 12:309–320, 1984.

[33] R. A. De Souza, M. J. Pietrowski, U. Anselmi-Tamburini, S. Kim, Z. A. Munir, and M. Martin. Oxygen diffusion in nanocrystalline yttria-stabilized zirconia: the effect of grain boundaries. *Phys. Chem. Chem. Phys.*, 10(15):2067, 2008.

[34] X. Guo, W. Sigle, and J. Maier. Blocking Grain Boundaries in Yttria-Doped and Undoped Ceria Ceramics of High Purity. *Journal of the American Ceramic Society*, 86(1):77–87, 2003.

[35] R. J. Chater, A. Cavallaro, R. D. Bayliss, S. N. Cook, B. D. Esser, D. W. McComb, and J. A. Kilner. Fast grain boundary oxygen ion diffusion in the -phase of Bi_2O_3. *Solid State Ionics*, 299:89–92, 2017.

[36] J. M. Polfus, B. Yildiz, and H. L. Tuller. Origin of fast oxide ion diffusion along grain boundaries in Sr-doped LaMnO $_3$. *Phys. Chem. Chem. Phys.*, 20(28):19142–19150, 2018.

[37] G. Gregori, R. Merkle, and J. Maier. Ion conduction and redistribution at grain boundaries in oxide systems. *Progress in Materials Science*, 89:252–305, 2017.

[38] T. Horita, M. Nishi, T. Shimonosono, H. Kishimoto, K. Yamaji, M. E. Brito, and H. Yokokawa. Visualization of oxide ionic diffusion at SOFC cathode/electrolyte interfaces by isotope labeling techniques. *Solid State Ionics*, 262:398–402, 2014.

[39] K. Develos-Bagarinao, H. Yokokawa, H. Kishimoto, T. Ishiyama, K. Yamaji, and T. Horita. Elucidating the origin of oxide ion blocking effects at GDC/SrZr(Y)O_3/YSZ interfaces. *Journal of Materials Chemistry A*, 5(18):8733–8743, 2017.

[40] J. Szász, F. Wankmüller, V. Wilde, H. Störmer, D. Gerthsen, N. H. Menzler, and E. Ivers-Tiffée. Nature and Functionality of $La_{0.58}Sr_{0.4}Co_{0.2}Fe_{0.8}O_3$/ $Gd_{0.2}Ce_{0.8}O_2$/ $Y_{0.16}Zr_{0.84}O_2$ Interfaces in SOFCs. *Journal of The Electrochemical Society*, 165(10):F898–F906, 2018.

[41] M. Nishi, H. Yokokawa, H. Kishimoto, K. Yamaji, and T. Horita. Oxygen Ion Diffusion in Dense $SrZrO_3$ Layer on YSZ. *Solid Oxide Fuel Cells 13 (Sofc-Xiii)*, 57(1):1957–1967, 2013.

[42] K. Develos-Bagarinao, H. Kishimoto, J. De Vero, K. Yamaji, and T. Horita. Effect of $La_{0.6}Sr_{0.4}Co_{0.8}Fe_{0.2}O_3$ microstructure on oxygen surface exchange kinetics. *Solid State Ionics*, 288:6–9, 2016.

[43] F Willy Poulsen and N Van Der Puil. Phase relations and conductivity of Sr- and La-zirconates. *Solid State Ionics*, 53-56:777–783, 1992.

[44] H. Choi, G. Y. Cho, and S. Cha. Fabrication and Characterization of Anode Supported YSZ/GDC Bilayer Electrolyte SOFC Using Dry Press Process. *International Journal of Precision Engineering and manufacturing - Green Technology*, 1(2):95–99, 2014.

[45] A. Tsoga, A. Gupta, A. Naoumidis, D. Skarmoutsos, and P. Nikolopoulos. Performance of a Double-Layer CGO/YSZ Electrolyte for Solid Oxide Fuel Cells. *Ionics*, 4(3-4):234–240, 1998.

[46] O Yamamoto. Perovskite-type oxides as oxygen electrodes for high temperature oxide fuel cells. *Solid State Ionics*, 22(2-3):241–246, 1987.

[47] H Yokokawa, N Sakai, T Kawada, and M Dokiya. Thermodynamic stabilities of perovskite oxides for electrodes and other electrochemical materials. *Solid State Ionics*, 52(1-3):43–56, 1992.

[48] A Tsoga, A Naoumidis, and D Stover. Total electrical conductivity and defect structure of ZrO_2-CeO_2-Y_2O_3-Gd_2O_3 solid solutions. *Solid State Ionics*, 135(1-4, SI):403–409, 2000.

[49] Z. Gao, V. Y. Zenou, D. Kennouche, L. Marks, and S. A. Barnett. Solid oxide cells with zirconia/ceria Bi-Layer electrolytes fabricated by reduced temperature firing. *Journal of Materials Chemistry A*, 3(8):9955–9964, 2015.

[50] J. Garcia-Barriocanal, A. Rivera-Calzada, M. Varela, Z. Sefrioui, E. Iborra, C. Leon, S. J. Pennycook, and J. Santamaria. Colossal ionic conductivity at interfaces of epitaxial ZrO_2 : Y_2O_3/$SrTiO_3$ heterostructures. *Science*, 321(5889):676–680, 2008.

[51] N. Schichtel, C. Korte, D. Hesse, and J. Janek. Elastic strain at interfaces and its influence on ionic conductivity in nanoscaled solid electrolyte thin films-theoretical considerations and experimental studies. *Physical Chemistry Chemical Physics*, 11(17):3043–3048, 2009.

[52] J. W. Han and B. Yildiz. Mechanism for enhanced oxygen reduction kinetics at the (La,Sr)CoO_3-delta/(La,Sr)$_2CoO_{4+delta}$ hetero-interface. *Energy and Environmental Science*, 5(9):8598–8607, 2012.

[53] K. C. Wen, W. Q. Lv, and W. D. He. Interfacial lattice-strain effects on improving the overall performance of micro-solid oxide fuel cells. *Journal of Materials Chemistry A*, 3(40):20031–20050, 2015.

[54] K. C. Wen, K. H. L. Zhang, W. Wang, J. H. Lin, W. Q. Lv, B. Wang, Z. M. Wang, J. H. Dickerson, X. Guo, and W. D. He. Physical justification for ionic conductivity enhancement at strained coherent interfaces. *Journal of Power Sources*, 285:37–42, 2015.

[55] D. Wolf and S. Yip. *Materials interfaces: atomic-level structure and properties*. Chapman & Hall, London Glasgow New York [etc.], 1992.

[56] M. Barsoum and M.W Barsoum. *Fundamentals of Ceramics*. CRC Press, 2002.

[57] A. Fick. Ueber Diffusion. *Annalen der Physik*, 170(1):59–86, 1855.

[58] J. Crank. *The mathematics of diffusion*. Clarendon Press, Oxford, 1976.

[59] H. S. Carslaw and J. C. Jaeger. *Conduction of heat in solids*. Oxford science publications. Clarendon Press, Oxford, 1959.

[60] S.J. Cooper. PhD thesis, Imperial College London, 2015.

[61] S. J. Cooper and N. P. Brandon. An Introduction to Solid Oxide Fuel Cell Materials, Technology and Applications. In *Solid Oxide Fuel Cell Lifetime and Reliability*, pages 1–18. Elsevier, 2017.

[62] F. Tariq, E. Ruiz-Trejo, A. Bertei, P. Boldrin, and N. P. Brandon. Microstructural Degradation. In *Solid Oxide Fuel Cell Lifetime and Reliability*, pages 79–99. Elsevier, 2017.

[63] M. Liu, M. E. Lynch, K. Blinn, F. M. Alamgir, and Y. Choi. Rational SOFC material design: new advances and tools. *Materials Today*, 14(11):534–546, 2011.

[64] H. Zhu, R. J. Kee, V. M. Janardhanan, O. Deutschmann, and D. G. Goodwin. Modeling Elementary Heterogeneous Chemistry and Electrochemistry in Solid-Oxide Fuel Cells. *Journal of The Electrochemical Society*, 152(12):A2427, 2005.

[65] W. G. Bessler, S. Gewies, and M. Vogler. A new framework for physically based modeling of solid oxide fuel cells. *Electrochimica Acta*, 53(4):1782–1800, 2007.

[66] A. Bertei, M.P. Carpanese, D. Clematis, A. Barbucci, M.Z. Bazant, and C. Nicolella. Understanding the electrochemical behaviour of LSM-based SOFC cathodes. Part II - Mechanistic modelling and physically-based interpretation. *Solid State Ionics*, 303:181–190, 2017.

[67] F. R. Bianchi, B. Bosio, A. Baldinelli, and L. Barelli. Optimization of a Reference Kinetic Model for Solid Oxide Fuel Cells. *Catalysts*, 10(1):104, 2020.

[68] S. B. Adler. Factors governing oxygen reduction in solid oxide fuel cell cathodes. *Chemical Reviews*, 104(10):4791–4843, 2004.

[69] A. Weber and E. Ivers-Tiffée. Materials and concepts for solid oxide fuel cells (SOFCs) in stationary and mobile applications. *Journal of Power Sources*, 127(1-2):273–283, 2004.

[70] M Mogensen. Kinetic and geometric aspects of solid oxide fuel cell electrodes. *Solid State Ionics*, 86-88:1151–1160, 1996.

[71] D. Clematis M.P. Carpanese A. Barbucci C. Nicolella N.P. Brandon A. Bertei, E. Ruiz-Trejo. A perspective on the role of the three-phase boundary in solid oxide fuel cell electrodes. *Bulgarian Chemical Communications. 50 (2018) 31–38.*

[72] W. Li, B. Guan, T. Yang, N. Zhang, X. Zhang, and X. Liu. On the bulk transport process and its impact on the electrode behavior of mixed conducting electrodes for SOFCs. *Physical Chemistry Chemical Physics*, 19(34):23218–23228, 2017.

[73] C. Chen, D. Chen, W. C. Chueh, and F. Ciucci. Modeling the impedance response of mixed-conducting thin film electrodes. *Physical Chemistry Chemical Physics*, 16(23):11573, 2014.

[74] S. Jiang. Development of lanthanum strontium cobalt ferrite perovskite electrodes of solid oxide fuel cells – A review. *International Journal of Hydrogen Energy*, 44(14):7448–7493, 2019.

[75] M. Gong, R. S. Gemmen, D. S. Mebane, K. Gerdes, and X. Liu. Simulation of Surface-Potential Driven ORR Kinetics on SOFC Cathode with Parallel Reaction Pathways. *Journal of The Electrochemical Society*, 161(3):F344–F353, 2014.

[76] A. Banerjee and O. Deutschmann. Elementary kinetics of the oxygen reduction reaction on LSM-YSZ composite cathodes. *Journal of Catalysis*, 346:30–49, 2017.

[77] A. Donazzi, G. Cordaro, A. Baricci, Z. Ding, and M. Maestri. A detailed kinetic model for the reduction of oxygen on LSCF-GDC composite cathodes. *Electrochimica Acta*, 335:135620, 2020.

[78] F. Ciucci, W. C. Chueh, D. G. Goodwin, and S. M. Haile. Surface reaction and transport in mixed conductors with electrochemically-active surfaces: a 2-D numerical study of ceria. *Phys. Chem. Chem. Phys.*, 13(6):2121–2135, 2011.

[79] A. Donazzi, M. Maestri, and G. Groppi. A multistep model for the kinetic analysis of the impedance spectra of a novel mixed ionic and electronic conducting cathode. *Electrochimica Acta*, 222:1029–1044, 2016.

[80] L. Almar, J. Szász, A. Weber, and E. Ivers-Tiffée. Oxygen Transport Kinetics of Mixed Ionic-Electronic Conductors by Coupling Focused Ion Beam Tomography and Electrochemical Impedance Spectroscopy. *Journal of The Electrochemical Society*, 164(4):F289–F297, 2017.

[81] M. E. Orazem and B. Tribollet. *Electrochemical Impedance Spectroscopy*. Wiley, 2008.

[82] M.J.L. Østergård and M. Mogensen. ac Impedance study of the oxygen reduction mechanism on La1xSrxMnO3 in solid oxide fuel cells. *Electrochimica Acta*, 38(14):2015–2020, 1993.

[83] S. B. Adler, J. A. Lane, and B. C. H. Steele. Electrode Kinetics of Porous Mixed-Conducting Oxygen Electrodes. *Journal of The Electrochemical Society*, 143(11):3554–3564, 1996.

[84] J. Jamnik and J. Maier. Generalised equivalent circuits for mass and charge transport: chemical capacitance and its implications. *Physical Chemistry Chemical Physics*, 3(9):1668–1678, 2001.

[85] W. Lai and S. M. Haile. Impedance Spectroscopy as a Tool for Chemical and Electrochemical Analysis of Mixed Conductors: A Case Study of Ceria. *Journal of the American Ceramic Society*, 88(11):2979–2997, 2005.

[86] S.B. Adler. Mechanism and kinetics of oxygen reduction on porous La1Sr CoO3 electrodes. *Solid State Ionics*, 111(1-2):125–134, 1998.

[87] S Adler. Limitations of charge-transfer models for mixed-conducting oxygen electrodes. *Solid State Ionics*, 135(1-4):603–612, 2000.

[88] C. Fu, K. Sun, N. Zhang, X. Chen, and D. Zhou. Electrochemical characteristics of LSCF–SDC composite cathode for intermediate temperature SOFC. *Electrochimica Acta*, 52(13):4589–4594, 2007.

[89] A. Häffelin, J. Joos, M. Ender, A. Weber, and E. Ivers-Tiffée. Time-Dependent 3D Impedance Model of Mixed-Conducting Solid Oxide Fuel Cell Cathodes. *Journal of The Electrochemical Society*, 160(8):F867–F876, 2013.

[90] V. Yurkiv, R. Costa, Z. Ilhan, A. Ansar, and W. G. Bessler. Impedance of the Surface Double Layer of LSCF/CGO Composite Cathodes: An Elementary Kinetic Model. *Journal of The Electrochemical Society*, 161(4):F480–F492, 2014.

[91] J. Laurencin, M. Hubert, K. Couturier, T. Le Bihan, P. Cloetens, F. Lefebvre-Joud, and E. Siebert. Reactive Mechanisms of LSCF Single-Phase and LSCF-CGO Composite Electrodes Operated in Anodic and Cathodic Polarisations. *Electrochimica Acta*, 174:1299–1316, 2015.

[92] M. Hubert, J. Laurencin, P. Cloetens, J.C. Da Silva, F. Lefebvre-Joud, P. Bleuet, A. Nakajo, and E. Siebert. Role of microstructure on electrode operating mechanisms for mixed ionic electronic conductors: From synchrotron-based 3D reconstruction to electrochemical modeling. *Solid State Ionics*, 294:90–107, 2016.

[93] A. Donazzi, S. De Pascali, F. Garavaglia, and M. Bracconi. A quasi 2D model for the interpretation of impedance and polarization of a planar solid oxide fuel cell with interconnects. *Electrochimica Acta*, 365:137346, 2021.

[94] K. Dumaisnil, D. Fasquelle, M. Mascot, A. Rolle, P. Roussel, S. Minaud, B. Duponchel, R.-N. Vannier, and J.-C. Carru. Synthesis and characterization of $La_{0.6}Sr_{0.4}Co_{0.8}Fe_{0.2}O_3$ films for solid oxide fuel cell cathodes. *Thin Solid Films*, 553:89–92, 2014.

[95] T. C. Geary, D. Lee, Y. Shao-Horn, and S. B. Adler. Nonlinear Impedance Analysis of $La_{0.6}Sr_{0.4}Co_{0.8}Fe_{0.2}O_3$ Thin Film Oxygen Electrodes. *Journal of The Electrochemical Society*, 163(9):F1107–F1114, 2016.

[96] R. Radhakrishnan, A. V. Virkar, and S. C. Singhal. Estimation of Charge-Transfer Resistivity of $La_{0.8}Sr_{0.2}MnO_3$ Cathode on $Y_{0.16}Zr_{0.84}O_2$ Electrolyte Using Patterned Electrodes. *Journal of The Electrochemical Society*, 152(1):A210, 2005.

[97] F. S. Baumann, J. Fleig, G. Cristiani, B. Stuhlhofer, H.-U. Habermeier, and J. Maier. Quantitative Comparison of Mixed Conducting SOFC Cathode Materials by Means of Thin Film Model Electrodes. *Journal of The Electrochemical Society*, 154(9):B931, 2007.

[98] N.J. Simrick, A. Bieberle-Hütter, T.M. Ryll, J.A. Kilner, A. Atkinson, and J.L.M. Rupp. An investigation of the oxygen reduction reaction mechanism of $La_{0.6}Sr_{0.4}Co_{0.8}Fe_{0.2}O_3$ using patterned thin films. *Solid State Ionics*, 206:7–16, 2012.

[99] B. A. Boukamp, N. Hildenbrand, P. Nammensma, and D. H.A. Blank. The impedance of thin dense oxide cathodes. *Solid State Ionics*, 192(1):404–408, 2011.

[100] B. A. Boukamp, N. Hildenbrand, H. J.M. Bouwmeester, and D. H.A. Blank. Impedance of thin film cathodes: Thickness and current collector dependence. *Solid State Ionics*, 283:81–90, 2015.

[101] L. Ma, P. Priya, and N. R. Aluru. A Multiscale Model for Electrochemical Reactions in LSCF Based Solid Oxide Cells. *Journal of The Electrochemical Society*, 165(14):F1232–F1241, 2018.

Chapter 2

Identifiability of the mechanisms governing the reaction kinetics of MIEC electrodes in solid oxide cells

The following chapter is adapted from a paper published in 2023 by the author and collaborators [1]. The author's contribution to the paper included performing COMSOL calculations, evolving the discussion of the model's results, as well as producing the figures. The model itself (formulation and bringing together of the set of equations as well as assumptions regarding the kinetic steps) was developed by Dr. Antonio Bertei, while further feedback and discussion was provided by Professor Alan Atkinson and Dr. Sam Cooper. The majority of this work was undertaken in 2020 and early 2021, when lockdown and social distancing regulations limited the access to lab equipment.

2.1 Model development

The model is implemented using COMSOL multiphysics and consists of three main processes as expressed by equations. The first is the bulk defect chemistry of the MIEC material, which can be computed from the crystal and defect structure in LSCF6428. The second are the reaction mechanism of the ORR as broken down into fundamental reaction steps. The third is the transport of charge-carrying species. Using the principles of non-equilibrium thermodynamics [2] with some simplifications, a series of expressions is derived which compute the conservation of species. While this study focuses on LSCF explicitly, it is a general representation of any p-type perovskite material which derives its properties from oxygen deficiency. The general ABO_3 unit cell formula is modified through doping on the A site, creating oxygen vacancies as well as electron holes on the B-site. Although the real perovskite will

show more complex behaviour at the B-site, whereby a disproportionation into holes and electrons can to take place [3], for simplicity of the model this mechanism is not taken into account, making holes the only electronic charge carriers of significance, as has been suggested previously [4].

2.1.1 Defect Chemistry

When the surface of this MIEC perovskite is exposed to air, the following oxygen reduction reaction occurs:

$$R_{ORR} : \frac{1}{2}\mathrm{O}_{2(g)} + \mathrm{V}_{\mathrm{O}}^{\bullet\bullet} + 2\mathrm{B}_{\mathrm{B}}^{x} \rightleftharpoons \mathrm{O}_{\mathrm{O}}^{x} + 2\mathrm{B}_{\mathrm{B}}^{\bullet} \tag{2.1}$$

Where $\mathrm{V_O}^{\bullet\bullet}$ represents the oxygen vacancies in the material and $\mathrm{B_B}^{\bullet}$ the B-site electron hole induced by the A-site doping. This reaction is captured by the equilibrium reaction constant $\mathrm{K_{ORR}}$ as expressed by:

$$K_{\mathrm{ORR}} = \frac{1}{\sqrt{\hat{p}_{O_2}}} \left(\frac{1 - \hat{c}_{\mathrm{V}_{\mathrm{O}}^{\bullet\bullet}}}{\hat{c}_{\mathrm{V}_{\mathrm{O}}^{\bullet\bullet}}} \right)^{\frac{1}{3}} \left(\frac{\hat{c}_{\mathrm{B}_{\mathrm{B}}^{\bullet}}}{1 - \hat{c}_{\mathrm{B}_{\mathrm{B}}^{\bullet}}} \right)^{2}$$

where the activities of each species pair are computed with respect to the number of crystallographic sites they occupy in the unit cell (i.e. 3 for the oxygen and 1 for the B-site). The standard potential of the reactions can then be related to $\mathrm{K_{ORR}}$ by:

$$\frac{RT}{F} \ln K_{ORR} = E_{eltr}^{\Theta} + E_{iotr}^{\Theta}$$

By finally considering local electroneutrality between the two species

$$\hat{c}_{\mathrm{B}_{\mathrm{B}}^{\bullet}} + 2\hat{c}_{\mathrm{V}_{\mathrm{O}}^{\bullet\bullet}} = y$$

where y is the doping fraction of the perovskite, all the conditions necessary to compute the equilibrium concentration of holes and oxygen vacancies with respect to the oxygen partial pressure $\hat{p}_{O_2}$. This set of equations can be modified for any type of MIEC material.

2.1.2 Electrochemical Reaction Steps

The goal is to take the global oxygen reduction reaction and segmenting it into a sequence of elementary electrochemical reaction steps. These steps are still not decisively understood, and a wide variety of

complex mechanisms have been proposed in the literature [5][6][7]. To achieve a method of distinguishing behaviours using experimental analysis, a simplified sequence of ORR steps that takes into account only the electron transfer during oxygen dissociation and oxygen ion transfer into the vacancy sites is considered. They are described by the following reaction equations:

$$R_{\text{eltr}}: \quad \mathrm{O}_{2(g)} + 2\mathrm{F_S} + 2\mathrm{B_B^x} \rightleftharpoons 2\mathrm{O_S^-} + 2\mathrm{B_B^\bullet} \tag{2.2}$$

$$R_{\text{iotr}}: \quad \mathrm{O_S^-} + \mathrm{B_B^x} + \mathrm{V_O^{\bullet\bullet}} \rightleftharpoons \mathrm{F_S} + \mathrm{B_B^\bullet} + \mathrm{O_O^x} \tag{2.3}$$

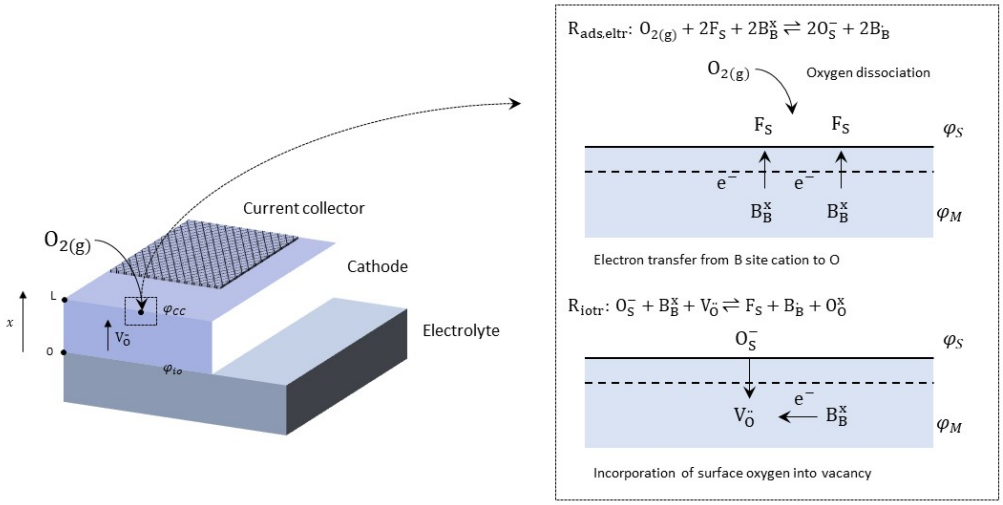

Figure 2.1: Schematic representation showing the cross-section of the considered MIEC system including the oxygen reduction reaction steps.

When a gaseous oxygen molecule meets the surface of the MIEC, it transfers electrons to the oxygen upon dissociation of the molecule into free surface sites (F_S), creating two charged oxygen atoms on these sites. It is two electrons from the B site that enable this to happen. Since this dissociation steps involves the transfer of electrons, it is referred to as the electron transfer step (eltr) from this point onwards. Once the oxygen ions are adsorbed onto the surface, the next reaction step involves transferring this species into an oxygen vacancy in the MIEC's crystal structure, from which point onwards it will enter the ion transport processes in the bulk. It is assumed that during this process a second electron is transferred to the oxygen anion from the B site in order to balance the two positive charges in the oxygen vacancy. The key rate limiting process in this reaction is the incorporation of the oxygen ion, which is modeled as a transfer across a surface double layer created by the negative

adsorbed oxygen and positive counter charge in the MIEC [8]. Therefore, this second reaction step will be called the ion-transfer step (iotr).

The sum of the ion-transfer and the electron transfer steps yields the global ORR. Since R_{eltr} contains two charges being transferred while R_{iotr} only involves one charge, the total R_{ORR}, is the sum of $\frac{1}{2}R_{eltr}$ + R_{iotr}. These concepts are represented visually in Figure 2.1. The reaction steps are assumed to be quantifiable using a Butler-Volmer-type set of equations [2][9]:

$$\hat{r}_{\text{eltr}} = k^p_{\text{eltr}} \left\{ \exp\left[-\alpha_{\text{eltr}} \frac{2F}{RT} \eta_{\text{eltr}} \right] - \exp\left[(1-\alpha_{\text{eltr}}) \frac{2F}{RT} \eta_{\text{eltr}} \right] \right\} \tag{2.4}$$

$$\hat{r}_{\text{iotr}} = k^p_{\text{iotr}} \cdot \left\{ \exp\left[-\alpha_{\text{iotr}} \frac{F}{RT} \eta_{\text{iotr}} \right] - \exp\left[(1-\alpha_{\text{iotr}}) \frac{F}{RT} \eta_{\text{iotr}} \right] \right\} \tag{2.5}$$

where η_{iotr} and η_{eltr} are the activation overpotentials, and α the transfer coefficients, T is temperature, while F the Faraday and R the universal gas constant. The activation overpotentials are a result of a difference in electrical potentials between the surface and the bulk as well as the local equilibrium redox potentials as described by the Nernst equation [6][7][8]. As discussed previously, the surface can be modelled as an electric double layer caused by the adsorbed oxygen species, therefore the coverage of surface sites with oxygen anions plays a major role in determining the potential difference between the surface and the bulk [10][11][12][7][8]. It can be modelled as a plate capacitor

$$\phi_M - \phi_S = \frac{F\Gamma_S}{C_S} \hat{\theta}_{\mathrm{O}^-_S}$$

where C_S is the MIEC surface capacitance and Γ_S is the density of available surface sites per unit area.

The k^p_{iotr} and k^p_{eltr} terms contain within it the kinetic reaction constants as well as species concentrations, surface coverage of oxygen species, and oxygen partial pressure [2]. This is expressed in the following equations:

$$k^p_{\text{eltr}} = k_{\text{eltr}} \left(\hat{p}_{O_2} (1-\hat{\theta}_{\mathrm{O}^-_S})^2 (1-\hat{c}_{\mathrm{B}^\bullet_{\mathrm{B}}})^2 \right)^{1-\alpha_{\text{eltr}}} \left(\hat{\theta}^2_{\mathrm{O}^-_S} \hat{c}^2_{\mathrm{B}^\bullet_{\mathrm{B}}} \right)^{\alpha_{\text{eltr}}} \tag{2.6}$$

$$k^p_{\text{iotr}} = k_{\text{iotr}} \left(\hat{\theta}_{\mathrm{O}^-_S} (1-\hat{c}_{\mathrm{B}^\bullet_{\mathrm{B}}}) \left(\frac{\hat{c}_{\mathrm{V}^{\bullet\bullet}_{\mathrm{O}}}}{3} \right) \right)^{1-\alpha_{\text{iotr}}} \left((1-\hat{\theta}_{\mathrm{O}^-_S}) \hat{c}_{\mathrm{B}^\bullet_{\mathrm{B}}} \left(1 - \frac{\hat{c}_{\mathrm{V}^{\bullet\bullet}_{\mathrm{O}}}}{3} \right) \right)^{\alpha_{\text{iotr}}} \tag{2.7}$$

2.1.3 Boundary Conditions

To obtain a complete description of the kinetic processes in the system, two more reactions have to be incorporated, representing either end of the cell. When the oxygen ions reach the physical end of the MIEC, they will transfer to the electrolyte, the rate of which this is happening will have an influence on the transfer processes at the surface also. It is expressed by:

$$R_{\text{oxtr}}: \quad \mathrm{O}_O^x + \mathrm{V}_\mathrm{O}^{\bullet\bullet} \rightleftharpoons \mathrm{V}_\mathrm{O}^{\bullet\bullet} + \mathrm{O}_\mathrm{O}^x \tag{2.8}$$

Where the subscript (ey) serves to distinguish the oxygen sites in the MIEC from that of the electrolyte. The electrolyte's oxygen vacancy concentration is assumed to be independent of the gaseous oxygen concentration and applied bias. Finally, the contact between the MIEC surface and the current collector mesh is considered. Since the current collector is metallic and a source of electrons, it is assumed to quickly compensate the electron holes on the B site of the MIEC, as can be expressed by:

$$B_\mathrm{B}^\bullet + e_\mathrm{CC}^- \rightleftharpoons B_\mathrm{B}^x \tag{2.9}$$

This results in the following expression for the boundary condition at the current collector upon the application of an overpotential

$$\phi_M = \eta_{\text{cat}} + \phi_{\text{ey}} + E_{\text{oxtr}}^\Theta + \frac{RT}{2F}\ln(K_{\text{ORR}}\hat{p}_{O_2}^{0.5}) + \frac{RT}{F}\ln\left(\frac{1-\hat{c}_{\mathrm{B}_\mathrm{B}^\bullet}}{\hat{c}_{\mathrm{B}_\mathrm{B}^\bullet}}\right)$$

2.1.4 Mass Transport

After obtaining a set of equations to describe the reaction steps of the electrochemical processes, the bulk transport of the charged species have to be quantified. Firstly, it is assumed that the surface species do not diffuse horizontally after adsorption. In the bulk, the two main transport processes are diffusion (transport driven by chemical potential) and migration (transport driven by electrical potential). These can be described by non-equilibrium thermodynamics, for which much literature exists [6][13][14][2][9][15]. Here, the molar flux of each species is written as

$$N_{V_\mathrm{O}^{\bullet\bullet}} = -\frac{\epsilon_M}{\tau_M}\left[D_{V_\mathrm{O}^{\bullet\bullet}}\rho_M\frac{\partial\hat{c}_{V_\mathrm{O}^{\bullet\bullet}}}{\partial x} + \frac{2F}{RT}D_{V_\mathrm{O}^{\bullet\bullet}}\rho_M\hat{c}_{V_\mathrm{O}^{\bullet\bullet}}\left(1-\frac{\hat{c}_{V_\mathrm{O}^{\bullet\bullet}}}{3}\right)\frac{\partial\phi_M}{\partial x}\right]$$

$$N_{B_{\mathrm{B}}^{\bullet}} = -\frac{\epsilon_M}{\tau_M}\left[D_{B_{\mathrm{B}}^{\bullet}}\rho_M\frac{\partial \hat{c}_{B_{\mathrm{B}}^{\bullet}}}{\partial x} + \frac{F}{RT}D_{B_{\mathrm{B}}^{\bullet}}\rho_M\hat{c}_{B_{\mathrm{B}}^{\bullet}}\left(1-\hat{c}_{B_{\mathrm{B}}^{\bullet}}\right)\frac{\partial \phi_M}{\partial x}\right]$$

Where ρ_M is the molar density of the MIEC and D refers to the diffusion coefficients of each charged species, which are assumed to be constant at a given temperature. The first term of the sum in the brackets describes diffusion, while the second describes migration.

Some of the calculations will involve modelling a porous electrode, which introduces considerations of gas transport and the associated material properties. The method chosen here is using a macro-homogeneous model whereby the volume fraction of the MIEC relative to the pores as well as its tortuosity factor are the properties dictating behaviour [16][17][18]. This ignores any local microstructural features and assumes one bulk phase where the gas transport is infinitely fast and there are no local variations in oxygen partial pressure. This is a simplified approach which is chosen because the primary goal of this model is to study the MIEC electrochemical kinetics, not the effect of gas transport.

2.1.5 Implementation

These expressions for fundamental material defect chemistry, the kinetics of the ORR and the transport of charged species are then fed into the equations describing the molar balance of the adsorbed oxygen ions, oxygen vacancies and electron holes as reported in Table 2.1. The cathode-electrolyte interface is set at $x = 0$ and the MIEC surface (and current collector) at $x = L$ where L is the cathode thickness. At the interface, the flux of electron holes is assumed to be zero, as the electrolyte material generally does not enable electronic conduction. At the current collector, the flux of oxygen vacancies stops, and the electrical potential at the surface is applied. The current collector also entails an electronic current flowing out of the cathode. The details of the equations vary depending on whether the system is modelled with a porous or a dense cathode. In the dense cathode, only the surface provides reaction sites. In a porous system, the whole thickness of the layer contains sites for gaseous oxygen to adsorb onto the surface, meaning the reaction steps are enabled for the whole material. The material-specific properties that become relevant for such a scenario are the specific surface area per unit volume of the cathode material and the concentration of crystallographic sites per unit area that are available for adsorption.

All of the equations described until this point compute within the time domain of sequential electrochemical reactions. Since the goal of this model is to simulate how different scenarios would show up

in experimental data, the time domain has to be transformed into the frequency domain in order to model impedance spectra. To do this, the equations first have to be solved at steady-state at a given applied bias, and then transformed into frequency domain using a Taylor expansion under sinusoidal perturbation [19][20]. The result is the ability to compute EIS spectra under different applied voltages and oxygen partial pressures.

The parameters for the execution of the model are listed in Table 2.3. The parameters are supposed to be representative of a generic p-type oxygen-deficient perovskite, resembling LSCF. In particular, the doping fraction, y, and the MIEC molar density, ρ_M, are chosen to represent $La_{0.52}Sr_{0.48}Co_{0.18}Fe_{0.82}O_{3\text{-d}}$ (mass density equal to 6000 kg m^{-3}), while the value of the ORR equilibrium constant, K_{ORR} is set to get an oxygen deficiency of $\delta = 0.02$ at 0.21 bar. In order to define the extreme kinetic scenarios, the kinetic constants k_{eltr} and k_{iotr} are set to represent the four extreme kinetic scenarios, while the value of k_{oxtr} is chosen so that the oxygen-ion transfer resistance is equal to $1/10^{\text{th}}$ of the ASR of a porous MIEC electrode. The phenomenological capacitance C_{oxtr} is set to zero to remove any capacitive response to the oxygen-ion transfer reaction at the MIEC/electrolyte interface. The surface capacitance of the MIEC, C_S is chosen so that the maximum potential difference between the MIEC bulk and surface is equal to 3 V [16], where a representative value of 10^{-5} mol m^{-2} is assumed for the density of available surface sites per unit area. The microstructural properties of the porous electrode are representative of an electrode with 35% porosity made of MIEC particles having a diameter of 1 micron [21][22].

Table 2.1: Fundamental model equations describing defect chemistry, ORR kinetics and charge transport in the p-type oxygen-deficient perovskite MIEC cathode under consideration.

Description	**Equation**	**No.**
Equilibrium constant of the ORR (R1)	$K_{\mathrm{ORR}} = \frac{1}{\sqrt{\hat{p}_{O_2}}} \left(\frac{1-\hat{c}_{\mathrm{V}_{\mathrm{O}}^{\bullet\bullet}}}{\hat{c}_{\mathrm{V}_{\mathrm{O}}^{\bullet\bullet}}} \right)^{\frac{1}{3}} \left(\frac{\hat{c}_{\mathrm{B}_{\mathrm{B}}^{\bullet}}}{1-\hat{c}_{\mathrm{B}_{\mathrm{B}}^{\bullet}}} \right)^{2}$	(S1a)
	$\frac{RT}{F} \ln K_{ORR} = E^{\Theta}_{eltr} + E^{\Theta}_{iotr}$	(S1b)
Local MIEC electro-neutrality	$\hat{c}_{\mathrm{B}_{\mathrm{B}}^{\bullet}} + 2\hat{c}_{\mathrm{V}_{\mathrm{O}}^{\bullet\bullet}} = y$	(S2)
Kinetics of electron-transfer step (R2)		(S3a)
	$\hat{r}_{\mathrm{eltr}} = k^{p}_{\mathrm{eltr}} \left\{ \exp\left[-\alpha_{\mathrm{eltr}} \frac{2F}{RT} \eta_{\mathrm{eltr}} \right] - \exp\left[(1-\alpha_{\mathrm{eltr}}) \frac{2F}{RT} \eta_{\mathrm{eltr}} \right] \right\}$	
	$k^{p}_{\mathrm{eltr}} = k_{\mathrm{eltr}} \left(\hat{p}_{O_2} (1-\hat{\theta}_{\mathrm{O}_{\bar{S}}^{-}})^2 (1-\hat{c}_{\mathrm{B}_{\mathrm{B}}^{\bullet}})^2 \right)^{1-\alpha_{\mathrm{eltr}}} \left(\hat{\theta}^2_{\mathrm{O}_{\bar{S}}^{-}} \hat{c}^2_{\mathrm{B}_{\mathrm{B}}^{\bullet}} \right)^{\alpha_{\mathrm{eltr}}}$	(S3b)
	$\eta_{\mathrm{eltr}} = \phi_M - \phi_S - \Delta\phi^{\mathrm{eq}}_{\mathrm{eltr}}$	
	$\Delta\phi^{\mathrm{eq}}_{\mathrm{eltr}} = E^{\Theta}_{\mathrm{eltr}} - \frac{RT}{2F} \ln \left(\frac{1}{\hat{p}_{O_2}} \left(\frac{\hat{\theta}_{\mathrm{O}_{\bar{S}}^{-}}}{1-\hat{\theta}_{\mathrm{O}_{\bar{S}}^{-}}} \right)^2 \left(\frac{\hat{c}_{\mathrm{B}_{\mathrm{B}}^{\bullet}}}{1-\hat{c}_{\mathrm{B}_{\mathrm{B}}^{\bullet}}} \right)^2 \right)$	(S3c)
		(S3d)
Kinetics of ion-transfer step (R3)		(S4a)
	$\hat{r}_{\mathrm{iotr}} = k^{p}_{\mathrm{iotr}} \cdot \left\{ \exp\left[-\alpha_{\mathrm{iotr}} \frac{F}{RT} \eta_{\mathrm{iotr}} \right] - \exp\left[(1-\alpha_{\mathrm{iotr}}) \frac{F}{RT} \eta_{\mathrm{iotr}} \right] \right\}$	
	$k^{p}_{\mathrm{iotr}} = k_{\mathrm{iotr}} \left(\hat{\theta}_{\mathrm{O}_{\bar{S}}^{-}} (1-\hat{c}_{\mathrm{B}_{\mathrm{B}}^{\bullet}}) \left(\frac{\hat{c}_{\mathrm{V}_{\mathrm{O}}^{\bullet\bullet}}}{3} \right) \right)^{1-\alpha_{\mathrm{iotr}}} \left((1-\hat{\theta}_{\mathrm{O}_{\bar{S}}^{-}}) \hat{c}_{\mathrm{B}_{\mathrm{B}}^{\bullet}} \left(1-\frac{\hat{c}_{\mathrm{V}_{\mathrm{O}}^{\bullet\bullet}}}{3} \right) \right)^{\alpha_{\mathrm{iotr}}}$	(S4b)
	$\eta_{\mathrm{iotr}} = \phi_S - \phi_M - \Delta\phi^{\mathrm{eq}}_{\mathrm{iotr}}$	
	$\Delta\phi^{\mathrm{eq}}_{\mathrm{iotr}} = E^{\Theta}_{\mathrm{iotr}} - \frac{RT}{F} \ln \left(\frac{(1-\hat{\theta}_{\mathrm{O}_{\bar{S}}^{-}})/\hat{\theta}_{\mathrm{O}_{\bar{S}}^{-}}}{\hat{c}_{\mathrm{B}_{\mathrm{B}}^{\bullet}}/(1-\hat{c}_{\mathrm{B}_{\mathrm{B}}^{\bullet}})} \cdot \frac{(1-\hat{c}_{\mathrm{V}_{\mathrm{O}}^{\bullet\bullet}})/3}{\hat{c}_{\mathrm{V}_{\mathrm{O}}^{\bullet\bullet}}/3} \right)$	(S4c)
		(S4d)
Kinetics oxygen transfer at MIEC/electro-lyte interface (R4)		(S5a)
	$\hat{r}_{\mathrm{oxtr}} = k^{p}_{\mathrm{oxtr}} \left\{ \exp\left[-\alpha_{\mathrm{oxtr}} \frac{2F}{RT} \eta_{\mathrm{oxtr}} \right] - \exp\left[(1-\alpha_{\mathrm{oxtr}}) \frac{2F}{RT} \eta_{\mathrm{oxtr}} \right] \right\}$	
	$k^{p}_{\mathrm{oxtr}} = k_{\mathrm{oxtr}} \left(1-\frac{\hat{c}_{\mathrm{V}_{\mathrm{O}}^{\bullet\bullet}}}{3} \right)^{1-\alpha_{\mathrm{oxtr}}} \left(\frac{\hat{c}_{\mathrm{V}_{\mathrm{O}}^{\bullet\bullet}}}{3} \right)^{\alpha_{\mathrm{oxtr}}}$	(S5b)
	$\eta_{\mathrm{oxtr}} = \phi_M - \phi_{\mathrm{ey}} - \Delta\phi^{\mathrm{eq}}_{\mathrm{oxtr}}$	
	$\Delta\phi^{\mathrm{eq}}_{\mathrm{oxtr}} = E^{\Theta}_{\mathrm{oxtr}} - \frac{RT}{2F} \ln \left(\frac{\hat{c}_{\mathrm{V}_{\mathrm{O}}^{\bullet\bullet}}/3}{1-\hat{c}_{\mathrm{V}_{\mathrm{O}}^{\bullet\bullet}}/3} \right)$	(S5c)
		(S5d)
Overpotential MIEC/current collector interface (R5)	$\phi_M = \eta_{\mathrm{cat}} + \phi_{\mathrm{ey}} + E^{\Theta}_{\mathrm{oxtr}} + \frac{RT}{2F} \ln(K_{\mathrm{ORR}} \hat{p}^{0.5}_{O_2}) + \frac{RT}{F} \ln \left(\frac{1-\hat{c}_{\mathrm{B}_{\mathrm{B}}^{\bullet}}}{\hat{c}_{\mathrm{B}_{\mathrm{B}}^{\bullet}}} \right)$	(S6)
MIEC surface-bulk double layer	$\phi_M - \phi_S = \frac{F\Gamma_S}{C_S} \hat{\theta}_{\mathrm{O}_{\bar{S}}^{-}}$	(S7)
Molar flux of oxygen vacancies	$N_{\mathrm{V}_{\mathrm{O}}^{\bullet\bullet}} = -\frac{\epsilon_M}{\tau_M} \left[D_{\mathrm{V}_{\mathrm{O}}^{\bullet\bullet}} \rho_M \frac{\partial \hat{c}_{\mathrm{V}_{\mathrm{O}}^{\bullet\bullet}}}{\partial x} + \frac{2F}{RT} D_{\mathrm{V}_{\mathrm{O}}^{\bullet\bullet}} \rho_M \hat{c}_{\mathrm{V}_{\mathrm{O}}^{\bullet\bullet}} \left(1-\frac{\hat{c}_{\mathrm{V}_{\mathrm{O}}^{\bullet\bullet}}}{3} \right) \frac{\partial \phi_M}{\partial x} \right]$	(S8)
Molar flux of electron holes	$N_{B_{\mathrm{B}}^{\bullet}} = -\frac{\epsilon_M}{\tau_M} \left[D_{B_{\mathrm{B}}^{\bullet}} \rho_M \frac{\partial \hat{c}_{B_{\mathrm{B}}^{\bullet}}}{\partial x} + \frac{F}{RT} D_{B_{\mathrm{B}}^{\bullet}} \rho_M \hat{c}_{B_{\mathrm{B}}^{\bullet}} \left(1-\hat{c}_{B_{\mathrm{B}}^{\bullet}} \right) \frac{\partial \phi_M}{\partial x} \right]$	(S9)

Table 2.2: Table S2 – Governing equations for the conservation of species in porous and dense MIEC cathodes.

Description	**Equation**	**No.**
Molar balance of oxygen vacancies	$\epsilon_M \rho_M \frac{\partial \hat{c}_{V_{\mathrm{O}}^{\bullet\bullet}}}{\partial t} + \frac{\partial N_{V_{\mathrm{O}}^{\bullet\bullet}}}{\partial x} = \begin{cases} -s_M \Gamma_S \hat{r}_{\mathrm{iotr}} & \text{(porous)} \\ 0 & \text{(dense)} \end{cases}$	(S10)
Molar balance of electron holes	$\epsilon_M \rho_M \frac{\partial \hat{c}_{B_{\mathrm{B}}^{\bullet}}}{\partial t} + \frac{\partial N_{B_{\mathrm{B}}^{\bullet}}}{\partial x} = \begin{cases} s_M \Gamma_S (2\hat{r}_{\mathrm{eltr}} + \hat{r}_{\mathrm{iotr}}) & \text{(porous)} \\ 0 & \text{(dense)} \end{cases}$	(S11)
Molar balance of adsorbed oxygen species	$\Gamma_S \frac{\partial \hat{\theta}_{\mathrm{O}_S^-}}{\partial t} = \Gamma_S \left(2\hat{r}_{\mathrm{eltr}} - \hat{r}_{\mathrm{iotr}}\right)$ applied in $\begin{cases} 0 \leq x \leq L & \text{(porous)} \\ x = L & \text{(dense)} \end{cases}$	(S12)
Boundary conditions at electrolyte interface ($x = 0$)	$\mathrm{N}_{V_{\mathrm{O}}^{\bullet\bullet}} = -\frac{\epsilon_M C_{\mathrm{oxtr}}}{2F} \frac{\partial(\phi_M - \phi_{\mathrm{ey}})}{\partial t} + \epsilon_M \Gamma_M \hat{r}_{\mathrm{oxtr}}$	(S13a)
	$\mathrm{N}_{B_{\mathrm{B}}^{\bullet}} = 0$	(S13b)
Boundary conditions at current collector interface ($x = L$)	$N_{V_{\mathrm{O}}^{\bullet\bullet}} = \begin{cases} 0 & \text{(porous)} \\ \Gamma_S \hat{r}_{\mathrm{iotr}} & \text{(dense)} \end{cases}$	(S14a)
	$\phi_M = \eta_{\mathrm{cat}} + \phi_{\mathrm{ey}} + E^{\Theta}_{\mathrm{oxtr}} + \frac{RT}{2F} \ln(K_{\mathrm{ORR}} \hat{p}_{O_2}^{0.5}) + \frac{RT}{F} \ln\left(\frac{1-\hat{c}_{B_{\mathrm{B}}^{\bullet}}}{\hat{c}_{B_{\mathrm{B}}^{\bullet}}}\right)$	(S14b)
Evaluation of current at current collector interface ($x = L$)	$i_{\mathrm{cat}} = \begin{cases} F N_{B_{\mathrm{B}}^{\bullet}} & \text{(porous)} \\ F N_{B_{\mathrm{B}}^{\bullet}} + F \Gamma_S (2\hat{r}_{\mathrm{eltr}} + \hat{r}_{\mathrm{iotr}}) & \text{(dense)} \end{cases}$	(S15)

Table 2.3: Model Parameters

Parameter	**Value**
Doping fraction, y	0.48
MIEC molar density, ρ_M	28392 mol m^{-3}
Diffusivity of oxygen vacancies, $D_{V_O^{\bullet\bullet}}$	$1.010^{-9}m^2s^{-1}$
Diffusivity of electron holes, $D_{B_B^{\bullet}}$	$2.5\times10^{-}6m^2s^{-1}$
Equilibrium constant of ORR reaction, K_{ORR}	201.35
Standard potential of the electron-transfer reaction, E^{Θ}_{eltr}	2.5451 V (el-B, io-B) -0.2749 V (el-U, io-U)
Standard potential of the oxygen-ion transfer reaction, E^{Θ}_{oxtr}	0 V
Transfer coefficients of charge-transfer reactions, $\alpha_{\text{eltr}} = \alpha_{\text{iotr}} = \alpha_{\text{oxtr}}$	0.5
Kinetic constant of the electron-transfer reaction, k_{eltr}	$1.25\times10^3s^{-1}$(el-B) $2.07\times10^4s^{-1}$(el-U) $5.55\times10^7s^{-1}$(io-B) $2.22\times10^8s^{-1}$(io-U)
Kinetic constant of the ion-transfer reaction, k_{iotr}	$1.25\times10^7s^{-1}$(el-B) $2.07\times10^8s^{-1}$(el-U) $5.55\times10^3s^{-1}$(io-B) $2.22\times10^4s^{-1}$(io-U)
Kinetic constant of the oxygen-ion transfer reaction, k_{oxtr}	$3.3\times10^5s^{-1}$
Phenomenological capacitance of oxygen-ion transfer, C_{eltr}	0 F m^{-2}
Surface capacitance of the MIEC, C_{S}	0.3216 F m^{-2}
Density of available surface sites per unit area, Γ_{S}	1×10^{-5}mol m^{-2}
Concentration of MIEC crystallographic sites per unit area, Γ_{M}	$1.10^2 \times 10^{-}5$mol m^{-2}
Volume fraction of MIEC phase, ϵ_{M}	0.65 (porous) 1.00 (dense)
Tortuosity factor of MIEC phase, τ_{M}	2.493 (porous) 1.000 (dense)
Specific surface area of the MIEC phase per unit volume, s_{M}	$3.448\times10^6m^{-1}(porous)$
Electrode thickness, L	20 $\mu m(porous)$ 1 $\mu m(dense)$
Operating temperature, T	600 ℃
Oxygen partial pressure, p_{O_2}	0.21 bar

2.2 Results

The model described in the previous section is capable of simulating EIS spectra for a given set of conditions. The materials properties of the system are modelled on an LSCF MIEC cathode at 600 ℃. This material's particular features are captured through the non-stoichiometry and charge carrier diffusivities, as well as the crystallographic parameters LSCF possesses. This was chosen as LSCF is the most common intermediate temperature cathode which is very well studied in literature, and 600 ℃ a targeted operating temperature for such devices.

In practice, fuel cell cathodes are porous and tend to be around 20 microns in thickness, which is why this type of system was first chosen to be simulated. Such a cathode typically has a porosity of around 35% and the open-circuit area-specific resistance (ASR) in the order of 0.1 Ωcm^2 at atmospheric oxygen partial pressure [23]. This value is used as a guide, where the kinetic parameters of the ORR steps (R2 and R3) are varied to always produce an ASR of 0.1 Ωcm^2. While in theory an infinite set of these parameters can produce this ASR value, selecting them to represent extreme system scenarios allows for a relationship to be inferred. Specifically, the rate-limiting reaction step is expressed by setting the kinetic parameter for the other step to be four orders of magnitude larger. In addition, the surface coverage of adsorbed oxygen species is varied to two extreme cases, resulting in either an 'unbuffered' or a 'buffered' surface as defined by Fleig [8]. The surface being **buffered** indicates that the surface coverage does not vary significantly as a result of an applied overpotential. This can only be the case when the surface coverage is already high, meaning most of the available adsorption sites on the surface are filled. In the **unbuffered** case, many sites remain available, and thus it is more likely for the overpotential having a significant effect on the amount of adsorbed surface species.

Four representative extreme scenarios, with the kinetic parameters (k_{eltr} and k_{iotr} for reactions (R2) and (R3)) and the equilibrium fractional occupancy of oxygen surface adsorption sites considered, are produced. They are characterised through being either electron transfer or ion transfer dominated (el-, or io-) and either buffered or unbuffered (-B, –U). This is summarised in Table 2.4. Taking these scenarios and producing EIS spectra from which the ASR can be taken results in the curves seen in Figure 2.2. They are calculated at OCV and ambient oxygen partial pressure (0.21 atm). What can be seen in the impedance spectra is that each of the four scenarios produces an identical response, not only in terms of the ASR value but also in the shape of the curves. A 45 degree initial slope followed by a semicircle at lower frequencies is consistent with the Gerischer element from the ALS model [5][24]

and is indicative of a MIEC material. Since the ALS model does not consider the different reaction steps and instead contains effective kinetic and diffusion coefficients, the different scenarios produce the same results under ambient conditions. Figure 2.2b shows how the ASR value changes with electrode thickness, keeping all other parameters constant. An optimum at around 20 microns can be observed where the minimal amount of material is required to produce the lowest possible ASR.

Table 2.4: Kinetic parameters used to illustrate the four extreme kinetic scenarios

Scenario	$k_{eltr}[s^{-1}]$	$k_{iotr}[s^{-1}]$	$\hat{\Theta}^{eq}_{O_S^-}$	Description
el-B	1.25×10^{3}	1.25×10^{7}	80	eltr rate-determining, buffered surface
el-U	2.07×10^{4}	2.07×10^{8}	1	eltr rate-determining, unbuffered surface
io-B	5.55×10^{7}	5.55×10^{3}	80	iotr rate-determining, buffered surface
io-U	2.22×10^{8}	2.22×10^{4}	1	iotr rate-determining, unbuffered surface

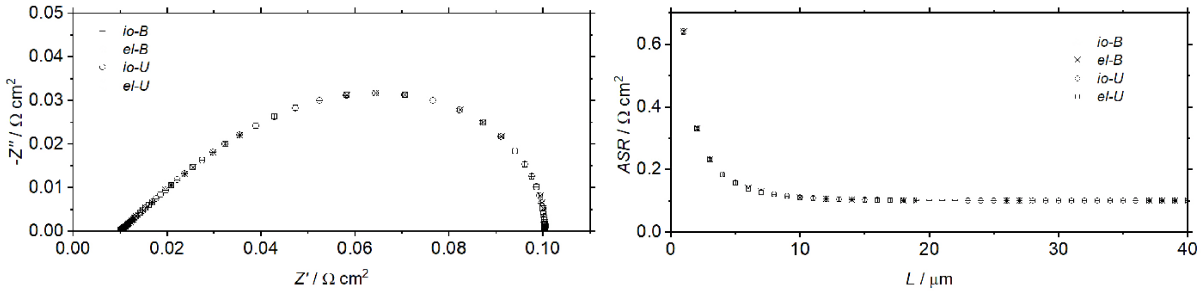

Figure 2.2: Simulation results for a porous LSCF electrode at OCV, 600 °C, and $p_{O2} = 0.21$ atm, using the kinetic parameters of the four extreme scenarios reported in Table 2.4a) Nyquist plot for a 20 mm thick electrode; b) area-specific resistance as a function of electrode thickness.

As is clear from the identical shape of the curves, identifying the specific components of the ORR (and which of them is rate-determining) is impossible in such a system. This serves to express that EIS under ambient conditions on its own is not capable of any sort of kinetic identifiability for the ORR.

2.2.1 Polarisation Curves

As we have seen that ambient conditions do not help elucidating the ORR, the next step is to study the polarisation behaviour under cathodic bias, i.e. the current density response. This is plotted in Figure 2.3. Here an increase in cathodic current with applied potential can be observed and some differences between the four different kinetic scenarios emerge. While the other three scenarios show slightly different absolute values, only the el-U (unbuffered surface, electron transfer rate determining) parameters qualitatively differ in shape. It appears to have a limiting current density on the order of

about 3 A cm^{-2}, whereas the other three seem to have no such limitation. This reflects in a different behaviour when plotting the change of ASR with current density as seen in the inset of Figure 2.3. The el-U scenario shows an increase in ASR shortly after the limiting current density is reached, while the other three monotonically decline.

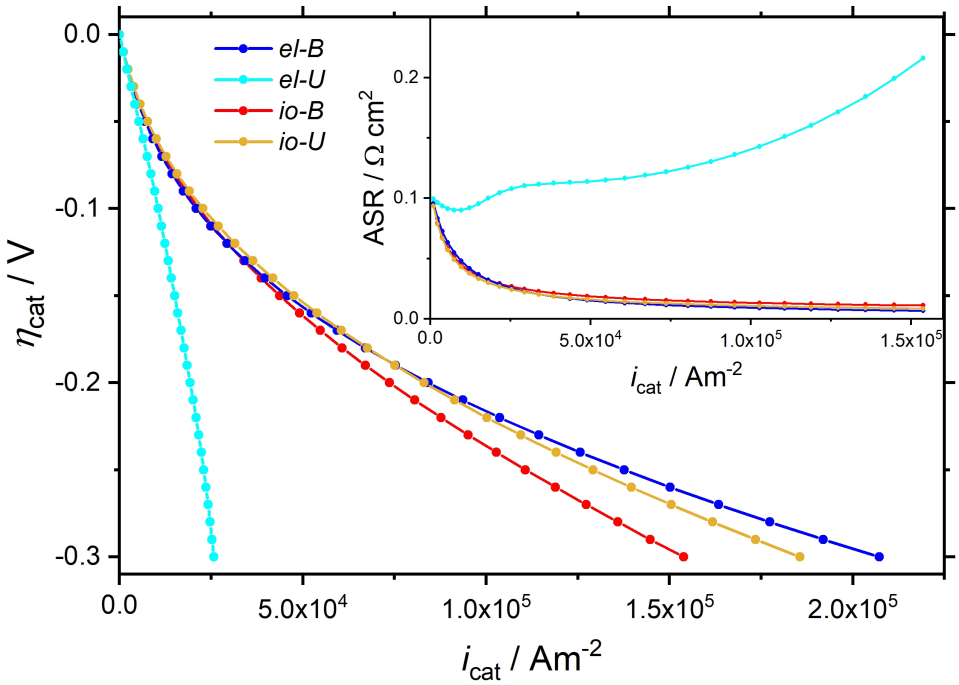

Figure 2.3: Simulated polarisation curves for a 20 um-thick, porous LSCF electrode at $pO_2 = 0.21$ atm for the four kinetic scenarios reported in Table 2.4. The inset reports the corresponding ASR as a function of current

The reason for this behaviour can be traced back to the relationship between the cathodic bias and the surface coverage of oxygen adatoms. In the buffered scenarios io-B and el-B, increasing the bias will not have a significant effect on the overall kinetics, as the surfaces are already buffered and will therefore not experience any significant changes in surface coverage, which could in turn influence kinetics. A steady decrease in ASR with bias is observed in these scenarios. When the cathode surface is unbuffered as in el-U and io-U, the change in surface coverage will have a measurable effect on the overall kinetics. Applying bias will therefore have an effect on the surface coverage in these scenarios, which means that increased bias will have an effect on the overall kinetics on top of the standard Butler-Volmer behaviour. The kinetic variables depend on the oxygen surface coverage as follows:

$$k^p_{\text{iotr}} \approx \left(\hat{\theta}_{\text{O}^-_S}\right)^{1-\alpha_{\text{iotr}}} \left(1-\hat{\theta}_{\text{O}^-_S}\right)^{\alpha_{\text{iotr}}} \approx \left(\hat{\theta}_{\text{O}^-_S}\right)^{1-\alpha_{\text{iotr}}}$$

$$k^p_{\text{eltr}} \approx \left(\hat{\theta}^2_{\text{O}^-_S}\right)^{\alpha_{\text{eltr}}} \left((1-\hat{\theta}_{\text{O}^-_S})^2\right)^{1-\alpha_{\text{eltr}}} \approx \left(\hat{\theta}^2_{\text{O}^-_S}\right)^{\alpha_{\text{eltr}}}$$

When the electron transfer and oxygen dissociation step is the rate-determining one, an increase in cathodic bias will lead to a decrease in surface coverage as the ion transfer can occur at a higher rate under bias. This decrease will decrease the reaction step factor, resulting in an increase in ASR. This results in the anomalous behaviour of the el-U scenario that can be observed in Figure 2.3. In the io-U scenario on the other hand, the surface coverage increases with bias, which in turn increases the reaction factor of the ion transfer, making it quicker and thereby reducing the overall ASR.

2.2.2 Kinetic identification in dense films

The previous section has shown the identifiability issues associated with porous electrodes. Since the goal is to investigate kinetic processes in as much isolation as possible, a dense, thin film cathode model presents the optimal platform. To achieve this, a 1 micron dense MIEC film at 600 ℃ was simulated using the model whilst varying both bias and oxygen partial pressure. The EIS curves produced by keeping the pO_2 at atmospheric level and varying the bias are shown in Figure 2.4.

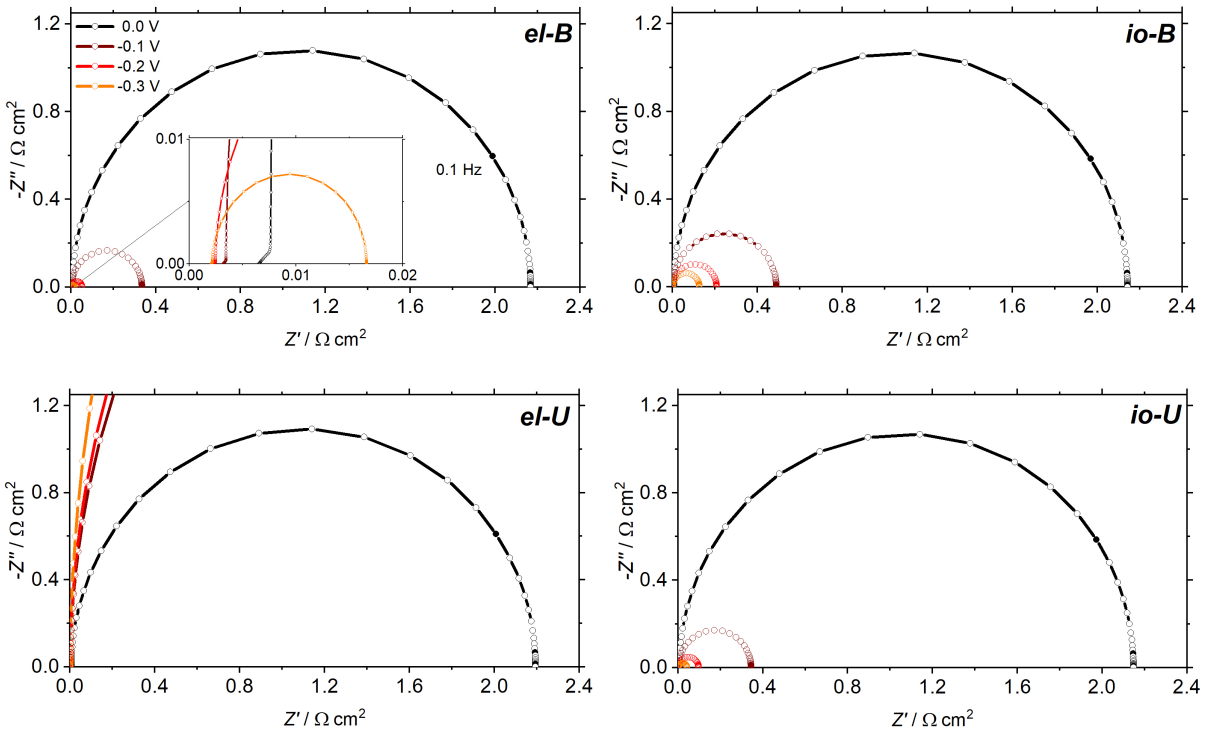

Figure 2.4: Simulated Nyquist plots for a 1 mm-thick dense LSCF film at 600 ℃ and 0.21 atm pO_2 for different values of the cathodic bias, considering the kinetic parameters of the four extreme scenarios reported in Table 2.4. The first plot reports in the inset a magnification of the spectra. The frequency of 0.1 Hz is marked with a black dot in each case.

It can be observed that the shape of the impedance curves presents as a simple semi-circle rather than the hedgehog shape observed in the porous EIS as seen in Figure 2.2. This is indicative of a R//C element in the equivalent circuit [20], where the resistance R corresponds to the rate-limiting step in the ORR while the capacitance C represents the chemical capacitance of the film [25][14][26]. This chemical capacitance is an intrinsic material property of the films, and therefore contains no information about processes occurring at the surface (i.e. ORR kinetics). Therefore, the R element (i.e. the ASR), which can be read by the real axis intercept, provides the information relevant for the study.

The inset in Figure 2.4a in the el-B graph shows two further features apart from the semi-circle; a small initial 45 degree slope in the high-frequency area, and an offset in the same region which decreases with applied bias. The slope can be explained as a finite-length Warburg behaviour induced by the transport of oxygen vacancies through the film [20], while the offset is caused by the ion transfer resistance across the MIEC/Electrolyte interface. While these features present in the graph, their influence on the overall analysis can be considered to be negligible when compared with the changes in the semi-circle with applied bias.

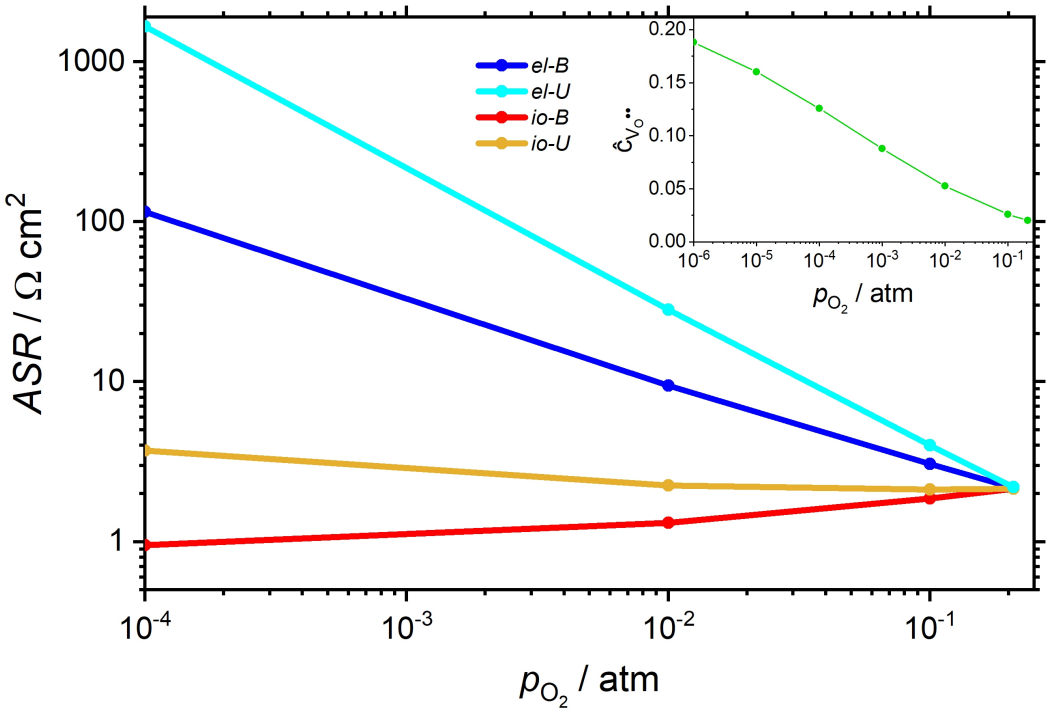

Figure 2.5: a) Simulated ASR as function of pO_2 in a log-log plot for a 1 mm-thick dense LSCF film at 600 ℃ and OCV for the four extreme scenarios reported in Table 2.4. The triangle represents the slope -1/2 in the log-log plot. b) Equilibrium surface coverage of adsorbed oxygen for buffered (el-B and io-B, black solid line) and unbuffered (el-U and io-U, black dashed line) kinetic scenarios on the left axis, along with the equilibrium vacancy concentration (green solid line) on the right axis, as a function of pO_2 according to defect chemistry.

The EIS curves in Figure 2.4 follow the same trends as already observed in the polarisation curves in Figure 2.3, namely that the el-U scenario behaves distinctly differently from the others, making it uniquely identifiable. However, this still leaves the other three scenarios ambiguous. Varying the thickness of the dense film does not have a significant impact on ASR as the rate-limiting kinetics take place at the surface. Varying the operating temperature would change intrinsic defect chemistry, surface coverage and kinetics at the same time, making it difficult to elucidate any information. This leaves oxygen partial pressure as the variable to change, the results are shown in Figure 2.5.

Io-B Identifiability

The ASR values as obtained from the EIS curves are plotted against different $p\mathrm{O}_2$ in a log-log scale. These show various behaviours that indicate identifiability. Firstly, the io-B scenario shows a slight decrease in ASR with lower $p\mathrm{O}_2$, in contrast to all other cases. Considering the reaction equilibrium for the ion transfer step

$$R_{\text{iotr}}: \quad \mathrm{O}_{\mathrm{S}}^{-} + \mathrm{B}_{\mathrm{B}}^{x} + \mathrm{V}_{\mathrm{O}}^{\bullet\bullet} \rightleftharpoons \mathrm{F}_{\mathrm{S}} + \mathrm{B}_{\mathrm{B}}^{\bullet} + \mathrm{O}_{\mathrm{O}}^{x} \tag{2.10}$$

A dependence on the oxygen vacancy concentration, hole concentration and surface coverage is exhibited. When reducing the $p\mathrm{O}_2$, the concentration of oxygen vacancies increases significantly, which will then be balanced out by a decrease in electron hole concentration, resulting in more neutral B-sites. Since the io-B scenario contains a buffered surface, the coverage of adsorbed oxygen is not significantly affected by changes in $p\mathrm{O}_2$. This results in a shift in the kinetics that expresses as a decreased ASR. This yields both an observation as well as a mechanistic explanation, which enable the identification of one unique kinetic scenario.

El-B and Io-U Identifiability

The other three scenarios in Figure 2.5a instead generally show an increased ASR with lower $p\mathrm{O}_2$. Since the qualitative difference is difficult to establish, a closer look at the quantitative behaviour of the slopes is needed. The el-B scenario shows a slope of -1/2 in the log-log plot, which can be explained by looking at the pre-exponential factor of the kinetic step in an electron-transfer dominated case:

$$k_{\text{eltr}}^{p} = k_{\text{eltr}} \left(\hat{p}_{O_2} (1 - \hat{\theta}_{\mathrm{O}_S^-})^2 (1 - \hat{c}_{\mathrm{B}_{\mathrm{B}}^{\bullet}})^2 \right)^{1-\alpha_{\text{eltr}}} \left(\hat{\theta}_{\mathrm{O}_S^-}^2 \hat{c}_{\mathrm{B}_{\mathrm{B}}^{\bullet}}^2 \right)^{\alpha_{\text{eltr}}} \tag{2.11}$$

Assuming α to be 0.5, a slope of -1/2 when plotting the slope of ASR vs. $p\mathrm{O}_2$ can be observed. The

el-B scenario therefore can be identified by varying the pO_2 and analysing the value of the slope in a log-log plot.

The io-U scenario shows less straightforward behaviour. In general, it can be observed that there seems to be only a weak dependence of the ASR on pO_2. In particular, the ASR only slightly increases at p_{O2} ¡ 10^{-2} atm, while it stays constant above this value. This weak dependence can be seen as a unique fingerprint of this case, even if no clear quantitative or qualitative behaviour can be observed.

To mechanistically explain why this is the case, it is necessary to look at the changes in adsorbed oxygen species and the concentration of oxygen vacancies. In an unbuffered case such as this one, the oxygen surface coverage is small and decreases further with decreasing pO_2. As already discussed previously, a low pO_2 will increase the concentration of vacancies. As both of these variables are on the left hand side of the ion transfer reaction R3, their respective changes mostly balance out, which is reflected in the effective kinetic constant and the ASR not changing much. Summarising these findings, varying the oxygen partial pressure whilst keeping the bias constant appears to be a useful method to identify unique behaviour for the other three kinetic scenarios that were ambiguous after varying just the bias.

Bias and pO_2 combined

While the conclusions in the previous section are useful, some ambiguity still remains. This reveals itself in particular when varying both the applied bias and the oxygen partial pressure at the same time. The results from this analysis are shown in Figure 2.6.

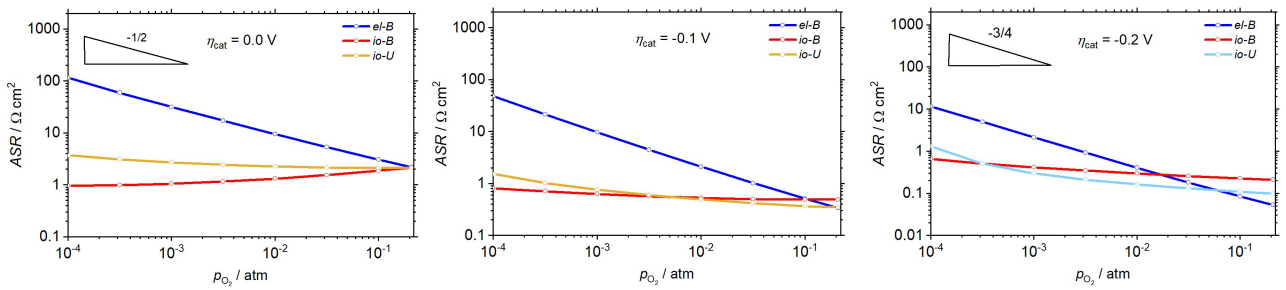

Figure 2.6: Simulated ASR as a function of pO_2 in a log-log plot for a 1 mm-thick dense LSCF film at 600 °C for different values of the cathodic bias hcat: a) 0.0 V, b) -0.1 V, c) -0.2 V. The kinetic parameters of the three extreme scenarios that can be identified by pO_2 changes, namely, el-B, io-B and io-U, as reported in Table 2.4, are considered. The triangles represent relevant slopes in the log-log plot.

While the el-U scenario continues to exhibit increasing ASR with decreasing pO_2 even when applying

a bias, the other two cases change their behaviour. Where previously the io-B curve was characterised by increasing with partial pressure, the trend is reversed under applied bias. These changes when combining $p\mathrm{O}_2$ and applied bias are not unexpected as many intrinsic variables are changed by such an environment. This affects the ion-transfer step limited scenarios in particular, since these show strong dependence on the oxygen vacancy and electron hole concentration. The rate-determining kinetic constant for the ion-transfer process is given by:

$$k^p_{\mathrm{iotr}} = k_{\mathrm{iotr}} \left(\hat{\theta}_{\mathrm{O}^-_S} (1 - \hat{c}_{\mathrm{B}^\bullet_\mathrm{B}}) \left(\frac{\hat{c}_{\mathrm{V}^{\bullet\bullet}_\mathrm{O}}}{3} \right) \right)^{1-\alpha_{\mathrm{iotr}}} \left((1 - \hat{\theta}_{\mathrm{O}^-_S}) \hat{c}_{\mathrm{B}^\bullet_\mathrm{B}} \left(1 - \frac{\hat{c}_{\mathrm{V}^{\bullet\bullet}_\mathrm{O}}}{3} \right) \right)^{\alpha_{\mathrm{iotr}}}$$

As mentioned previously, the increase in oxygen vacancies is balanced out by a decrease in electron holes, in this scenario $\hat{c}_{\mathrm{B}^\bullet_\mathrm{B}}$ approaches 0. Assuming again that $\alpha = 0.5$, this results in k^p_{iotr} scaling approximately by a power of 0.5. Since this decreases with $p\mathrm{O}_2$, the result will be an increase in ASR, as can be observed in Figure 2.6. This behaviour is observed both in io-B, where the trend reverses compared to OCV, as well as in io-U, where the previously weak dependence on $p\mathrm{O}_2$ grows stronger at low values and higher bias. At $\mathrm{h_{cat}}$ = -0.2 V, the slope of io-B approaches -3/4, making it increasingly difficult to distinguish even from the el-B case. All of these trends show that varying both bias and $p\mathrm{O}_2$ is not a suitable method to further advance identifiability of the kinetic regimes. Instead, these results indicate that care must be taken in such experiments to not mistakenly attribute certain results to a particular step being rate-determining. To summarise, dense films show a way to identify extreme kinetic regimes by varying bias and $p\mathrm{O}_2$ separately, combining both quantitative and qualitative analysis. Combining the two external variables only further complicates the picture and highlights how easily experimental data can be dominated by contradictory mechanistic processes. This will be investigated even further in the next section studying porous electrodes.

2.2.3 Porous electrodes

In most experimental studies that investigate the properties of SOC cathodes, porous electrode structures will be used, as these most closely resemble real cells. Even without explicitly modelling such a system, it can be asserted that the deconvolution of individual kinetic processes is more challenging than in a dense film, since the role of gas transport introduces significant complexity.

As already touched upon previously, the polarisation curve in Figure 2.3, which models a 20-micron porous cathode, allows for the distinguishing of the el-U scenario. This behaviour can therefore be described as being identical to that of a dense film, where variable bias enables unambiguous identifiability.

ASR vs pO_2 in porous samples

Moving on the variation of oxygen partial pressure, the ASR is plotted in Figure 2.7.

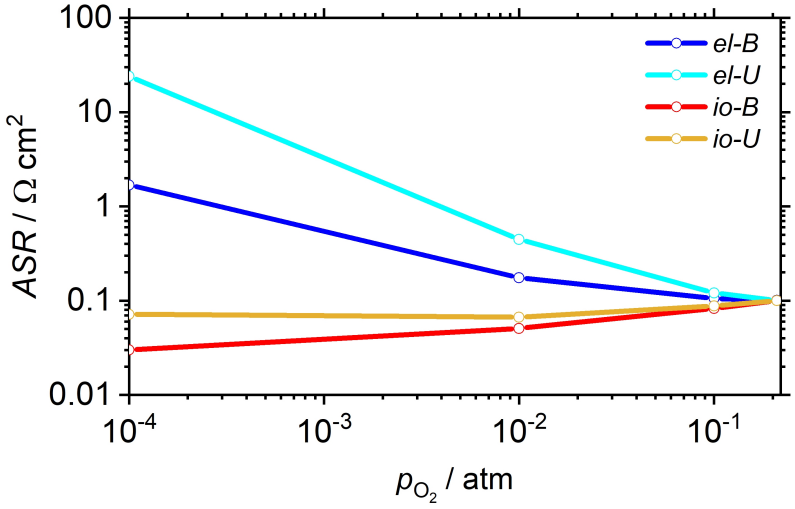

Figure 2.7: Simulated ASR as function of pO_2 in a log-log plot for a 20 mm-thick porous LSCF electrode at 600 ℃ and OCV considering the kinetic parameters of the four extreme scenarios reported in Table 2.4.

As before, the el scenarios show an increase in ASR with lower pO_2. The io scenarios, however, show subtly different behaviour, mainly that they both show decreasing ASR at lower pO_2. This means that the io-B scenario is no longer the only case that exhibits such a trend, removing identifiability. In a porous cathode therefore varying the pO_2 only allows for the qualitative distinction between eltr-dominated and iotr-dominated processes. While the behaviour particularly of io-U and io-B does show some features that are distinct from one another (such as the slope changes), they are unlikely to be clear in an experimental scenario. This is particularly the case in low pO_2 experiments, where uncertainties in the EIS measurements become more prominent, if such a setup is capable of going to values as low as 10^{-4} atm at all.

Returning to looking at the full Nyquist plots in Figure 2.8, it can be seen that at atmospheric pressure, all scenarios show the same Gerischer behaviour shape where the initial 45 degree slope transitions into a semi-circle, yielding the characteristic Hedgehog shape. When this shape changes to a 45 degree slope followed by a large semi-circle (as can be seen in el-U and el-B with decreasing pO_2), it is indicative of finite-length Gerischer behaviour with limiting kinetics [27][28]. In such scenarios, the porous cathode behaves as a quasi-dense film with full utilisation of the MIEC surface where bulk transport does not play a significant limiting role. The ORR kinetics and charge transport become consecutive processes, which is not the case in a hedgehog curve.

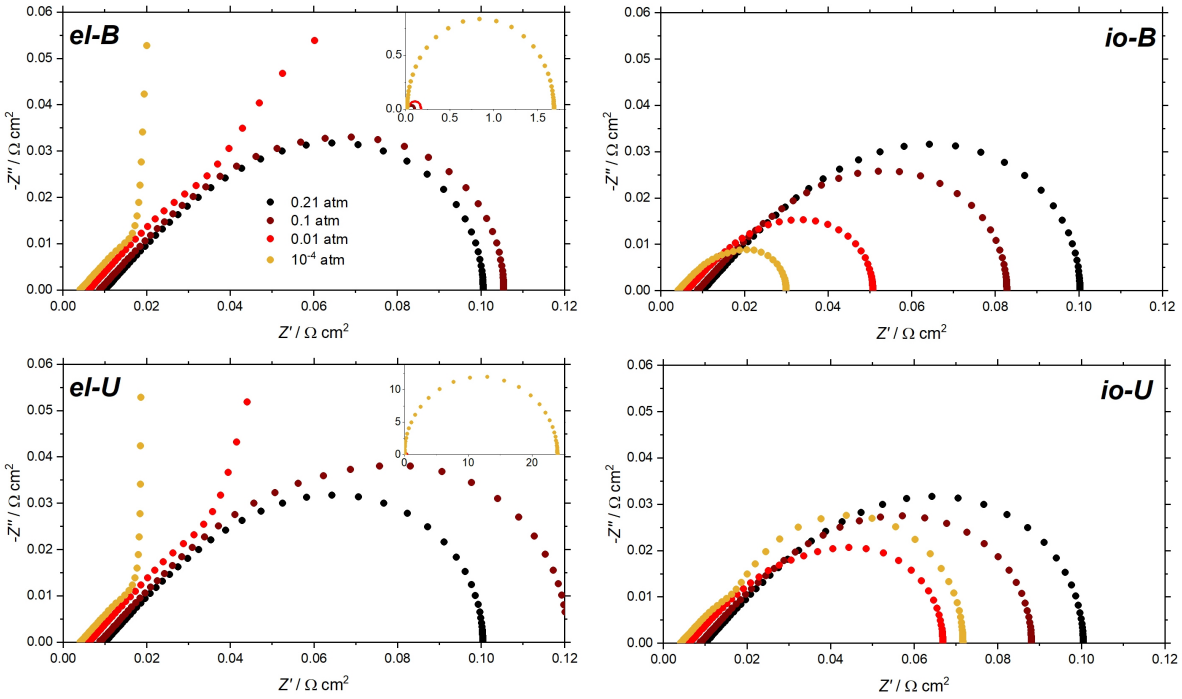

Figure 2.8: Simulated EIS spectra of a porous 20 mm-thick LSCF electrode as a function of pO_2 at OCV. The insets report the full spectra at a larger scale when they do not fit within the selected plot area.

Returning to the io-B and io-U scenarios, it is possible to explain why the ASR decreases at low p_{O2} as shown in Figure 2.7. When the ion-transfer process is rate-determining, the main effect of a low p_{O2} is an increase in oxygen vacancy concentration (see Figure 2.5b). This influences chemical capacitance and improves kinetics of the iotr step as it does in the dense film, but it also enhances vacancy transport. This means that, even though in the io-U scenario the adsorbed oxygen surface coverage decreases at low p_{O2} (Figure 2.5b), the increase in enhances both the ORR kinetics and the transport of vacancies, resulting in the ASR globally decreasing with low p_{O2}. Thus, in contrast to the dense film case, where the opposing and trends balance out, in a porous electrode the positive effect of vacancy transport upsets the balance of the two kinetic trends, resulting in a decrease in ASR as p_{O2} decreases also for the io-U scenario. It can be concluded that this is a clear blurring effect of charge transport across the porous electrode thickness that masks the intrinsic behaviour of the ORR surface, indicating that kinetic identification in porous electrodes is more ambiguous and challenging to accomplish than in dense films.

2.3 Discussion

In the previous sections, it was established that porous cathodes show some distinct trends between kinetic scenarios, but still remain too ambiguous for clear identifiability. Dense films are more useful for this; a sequential investigation of these, where first the bias and then the partial pressure are varied during the EIS measurements, enables a certain level of distinction. This process is visually summarised in the flowchart in Figure 2.9.

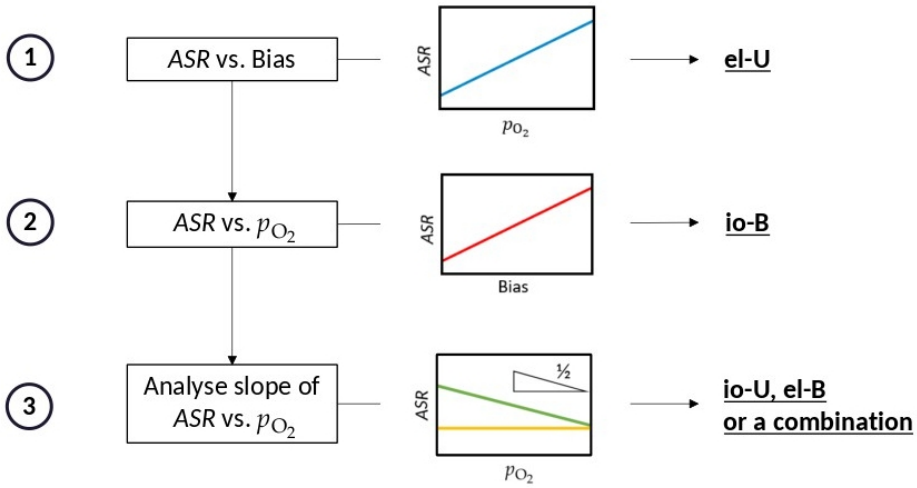

Figure 2.9: Flowchart outlining the procedure to identify the rate-determining kinetic mechanism in dense MIEC films.

In a hypothetical scenario where experiments would be run in an attempt to identify the kinetic process dominant in a particular material, the flowchart provides a guide to narrow down possibilities. If no clear qualitatively distinctive trend with either bias or pO_2 can be established, then quantitative analysis in the pO_2 study must be applied.

2.3.1 Interpretation of experimental data on thin film electrodes

The next step after establishing this approach is to apply it to data from the literature, which provides experimental data for thin film, dense p-type perovskites. The work by Imanishi et al. [29] is particularly useful for this, as it involves collecting EIS data for LSM and LSC films under independently varied bias and partial pressure. These films were grown on a single crystal YSZ substrate using laser ablation and were around 30nm in thickness. Pt counter and reference electrodes as well as current collector meshes were used for the EIS measurements.

The equivalent circuit chosen by the authors to fit the data consisted of a series resistance (r1), and three resistance elements in parallel. In order of decreasing frequency, the elements were ion transfer

at the MIEC-YSZ interface (r2), the ORR at the surface (r3) and the vacancy diffusion through the film (r4). The interpretation of r3 and r4 is in contrast to the model developed here, as a 30nm film is not expected to have a separate resistance contribution due to the speed of vacancy diffusion in such dimensions. Furthermore, the distinction between the two semi-circles in the data is already uncertain. Based on the model developed here, it is decided to combine r3 and r4 into a single response, called the polarisation resistance from here on. By digitising the EIS results from the original work and interpreting the low frequency semicircle as polarisation resistance, the real axis intercept can once again provide a quantity for this.

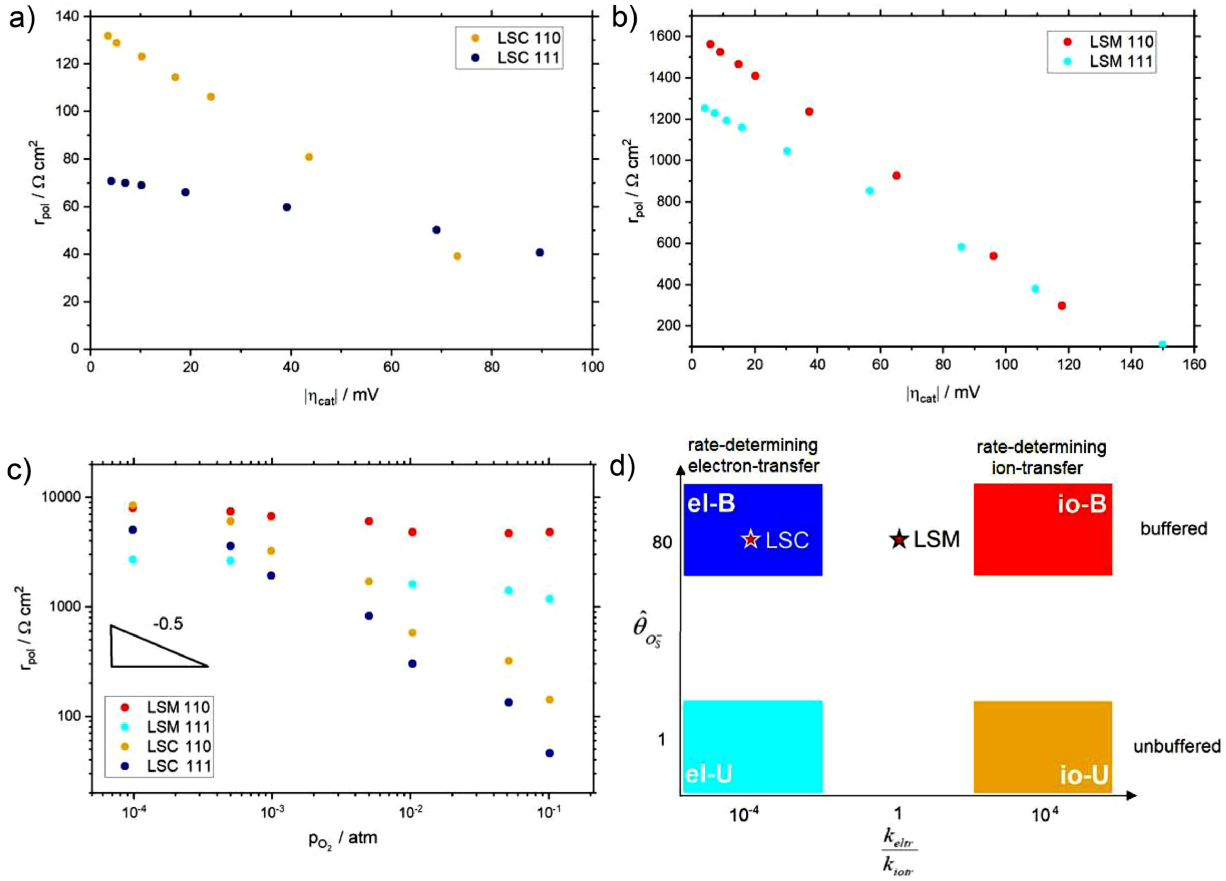

Figure 2.10: Polarisation resistance as a function of cathodic overpotential at 700 °C in air for a) LSC and b) LSM thin films. c) Polarisation resistance as a function of oxygen partial pressure at 700 °C and open circuit conditions of LSM and LSC thin films. d) Visual representation of LSC and LSM within a map of extreme kinetic scenarios. The original experimental data are taken from Imanishi et al. [66] for thin films deposited on YSZ single crystal substrates having different orientations indicated.

The resulting plot is shown in Figure 2.10c, and the results depend both on the difference between LSM and LSC as well as the crystal orientation that the film developed as a result of the deposition. While the crystal orientation result is interesting in its own right, as it suggests different crystal faces have different ability to perform the ORR, the focus here is on the difference in slope between the two materials. It is clear that the polarisation resistance in LSC decreases more significantly with

increasing pO_2, with a slope of around -0.65, which is not far off -1/2.

While the authors did not produce EIS measurements as a function of cathodic bias, it presented DC current density as a function of cathodic overpotential. Differentiating the DC polarisation curve allows for the evaluation of the small signal polarisation resistance by digitising the plot and fitting it to a 4th order polynomial with zero intercept, then differentiating this polynomial and subtracting the interfacial resistance r2. The resulting polarisation resistance and its dependence on applied overpotential is shown in Figure 2.10a for LSC and 10b for LSM. They both show a decrease in resistance with increased bias. Taking the decision tree in Figure 2.9 as a guide, the change in polarisation resistance with overpotential is examined. It can be seen that in both materials, there is a reduction in resistance with increasing bias, excluding the el-U scenario from being relevant. Figure 2.10c shows the polarisation resistance with partial pressure, where it can be observed that rpol increases the lower the pO_2 becomes. This limits the discussion to the el-B or the io-U scenario, and to further investigate from this point, quantitative analysis has to be done.

LSC

The slope of the LSC is close enough to -1/2 to consider this material to be dominated by the el-B scenario, as shown in Figure 2.10c. In LSC therefore, the electron transfer step in the ORR is rate-determining with buffered oxygen surface coverage. A similar conclusion was reached by Adler [30] from a series of non-linear EIS experiments on thin film electrodes while investigating strontium segregation.

LSM

Looking at the LSM data, the slope, i.e. the exponent of rpol, is lower than -1/2, being around -0.11. This behaviour can partially be explained by a codependency on different kinetic limitations. Since the scenarios in this study are extreme ones which clearly show one dominant behaviour, it is not unreasonable to assume that in a real material, the behaviour can be more complex. In this case, LSM is exhibiting a behaviour that indicates a kinetic mechanism somewhere in between the strong pO_2 dependency of el-B and other, less sensitive scenarios (such as io-B and io-U).
LSM is a well studied SOC electrode and known to be an exceptional triple phase boundary catalyst, through combination with an ionic conducting material. Given this, it is more likely to have a buffered

oxygen surface coverage, meaning the io-B scenario is more likely to play a role. It can therefore be assumed that LSM is co-limited by both the ion and electron transfer steps with a buffered surface. As it is known that LSC has a higher oxygen vacancy concentration than LSM [5][31], making ion transfer more facile, explaining the electron transfer-limited behaviour. The oxygen vacancy concentration in LSM will increase as pO_2 is lowered, facilitating ion transfer more, resulting in a mild dependency compared with LSC.

These conclusions are summarised in Figure 2.10d. This chart is not meant to be quantitative, but rather an indicative illustration for following the flow chart. As mentioned previously, the real dynamics of the oxygen reduction reaction are likely to be much more complex than the extreme scenarios outlined in this study. Further, a MIEC with a different crystal structure and defect chemistry might not show the same behaviours as this LSCF-like model.

2.3.2 Interpretation of experimental data on porous electrodes

Having already mentioned the difficulty of interpreting data from porous cathodes, it is worth looking at some work in the literature to further underline this. Nenning et al. [32] produced a study of porous $La_{0.6}Sr_{0.4}O_{3-d}$ (LSF) electrodes under varying oxygen partial pressures. The relationship between ASR and pO_2 are reproduced in Figure 2.11.

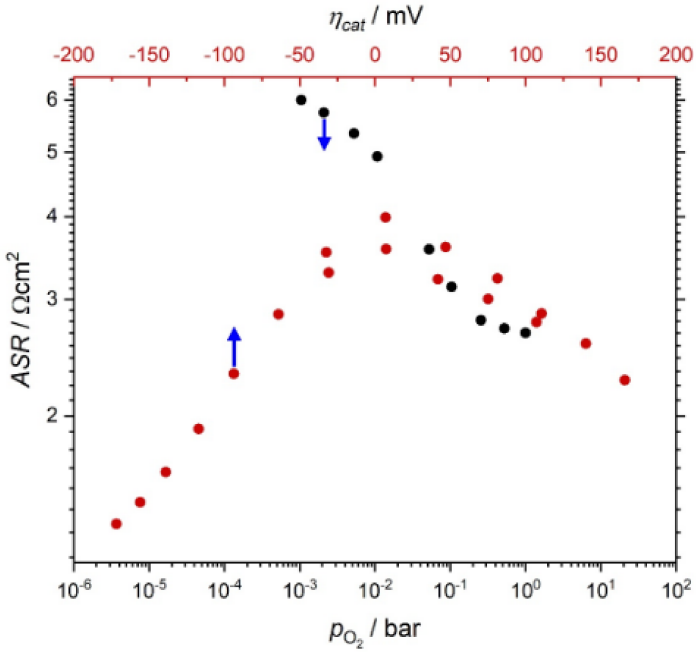

Figure 2.11: The effect of overpotential (at $pO_2 = 10^{-2}$ bar) and oxygen partial pressure (at OCV) on the ASR of porous LSF electrode at 700 °C . The overpotential scale is adjusted so that it matches the equivalent pO_2 value according to the Nernst equation. Experimental data reproduced from Nenning et al. [65].

An increase in ASR with lower oxygen partial pressure can be observed, with a relatively small p_{O2} exponent of ASR (-0.14 ± 0.03). Referring back to Figure 2.7, this is indicative of a kinetic behaviour that is limited by the electron-transfer step. Knowing this, and knowing that the el-U step can be distinguished from the el-B step by examining the change in ASR with applied overpotential. Figure 2.11 shows a decrease in ASR under applied negative bias, making el-B the most likely scenario. Given the relatively weak pO_2 dependence, it is possible that the ion transfer is not entirely facile and could still contribute to the ASR in a minor way. This illustrates that the extreme kinetic scenarios presented here are a useful guide, but often do not exactly correspond to experimental data, as real materials show more complex behaviour, particularly when porous.

Using the thin film literature data discussed in the previous section, it could be shown that LSC shows a kinetic behaviour that is mostly dominated by an el-B scenario, while LSM appeared to lie in between io-B and el-B. LSF from previous research is understood to be in between LSM and LSC in terms of its defect chemistry and resulting materials properties [32], therefore an assumption can be made that the ORR kinetics behaviour follows a similar trend, with LSF being closer to el-B than LSM. However, this interpretation is only possible due to the previous knowledge obtained from the thin film samples and could not be derived from porous experimental data alone.

2.4 Conclusions

This study introduced a physics-based model to analyse the oxygen reduction reaction (ORR) kinetics in mixed ionic-electronic conductors(MIEC) p-type cathodes. The model integrated bulk defect chemistry, elementary kinetics, and charge transport in dense and porous oxygen-deficient perovskite electrodes. The ORR was divided into two charge-transfer steps: electron-transfer (el) and ion-transfer (io). The study considered different MIEC surface conditions (buffered or unbuffered) and explored four kinetic scenarios (el-B, el-U, io-B, io-U) using electrochemical impedance spectroscopy (EIS) as a function of oxygen partial pressure (pO_2) and cathodic bias.

Simulation results revealed that, after eliminating blurring effects, the EIS response of a thin dense MIEC film exhibited a semi-circle in the Nyquist plot, indicating vacancy transport and dominant ORR kinetics. A strategy for kinetic identification based on analysis of area-specific resistance (ASR) dependence on pO_2 and cathodic bias was proposed. However, identification, especially in porous MIEC electrodes, proved challenging due to convoluted vacancy transport effects.

Application of the kinetic identification strategy to literature EIS data of LSC and LSM dense films and LSF porous electrodes suggested potential ORR scenarios. The dense LSC film likely followed the el-B scenario, while LSM showed co-limitation by both electron-transfer and ion-transfer steps with buffered oxygen surface coverage. Porous LSF data had higher uncertainty, indicating challenges in kinetic identification for porous electrodes.

The study concluded that relying solely on EIS data for kinetic identification is challenging, particularly for porous electrodes. The presented modelling tool served as a valuable platform for testing hypotheses and defining identification strategies for MIEC electrodes in different configurations. Future work aims to extend the model to diverse MIEC materials and account for non-ideal behaviour in transport and reaction phenomena.

References

[1] L. Yasin, A. Atkinson, S. J. Cooper, and A. Bertei. Identifiability of the mechanisms governing the reaction kinetics of miec electrodes in solid oxide cells. *Electrochimica Acta*, 472:143418, 2023.

[2] M. Z. Bazant. Theory of Chemical Kinetics and Charge Transfer based on Nonequilibrium Thermodynamics. *Accounts of Chemical Research*, 46(5):1144–1160, 2013.

[3] M. Prestat, J. Koenig, and L. J. Gauckler. Oxygen reduction at thin dense La0.52Sr0.48Co0.18Fe0.82O3– electrodes: Part I: Reaction model and faradaic impedance. *Journal of Electroceramics*, 18(1-2):87–101, 2007.

[4] S Wang. High temperature properties of La0.6Sr0.4Co0.8Fe0.2O3 phase structure and electrical conductivity. *Solid State Ionics*, 159(1-2):71–78, 2003.

[5] S. B. Adler. Factors governing oxygen reduction in solid oxide fuel cell cathodes. *Chemical Reviews*, 104(10):4791–4843, 2004.

[6] A. Donazzi, G. Cordaro, A. Baricci, Z. Ding, and M. Maestri. A detailed kinetic model for the reduction of oxygen on LSCF-GDC composite cathodes. *Electrochimica Acta*, 335:135620, 2020.

[7] V. Yurkiv, R. Costa, Z. Ilhan, A. Ansar, and W. G. Bessler. Impedance of the Surface Double Layer of LSCF/CGO Composite Cathodes: An Elementary Kinetic Model. *Journal of The Electrochemical Society*, 161(4):F480–F492, 2014.

[8] J. Fleig. On the current–voltage characteristics of charge transfer reactions at mixed conducting electrodes on solid electrolytes. *Phys. Chem. Chem. Phys.*, 7(9):2027–2037, 2005.

[9] L.R. Faulkner A.J. Bard. *Electrochemical methods: fundamentals and applications*. Wiley, New York, 2001.

[10] M. Gong, R. S. Gemmen, D. S. Mebane, K. Gerdes, and X. Liu. Simulation of Surface-Potential Driven ORR Kinetics on SOFC Cathode with Parallel Reaction Pathways. *Journal of The Electrochemical Society*, 161(3):F344–F353, 2014.

[11] A. Banerjee and O. Deutschmann. Elementary kinetics of the oxygen reduction reaction on LSM-YSZ composite cathodes. *Journal of Catalysis*, 346:30–49, 2017.

[12] A. Donazzi, M. Maestri, and G. Groppi. A multistep model for the kinetic analysis of the impedance spectra of a novel mixed ionic and electronic conducting cathode. *Electrochimica Acta*, 222:1029–1044, 2016.

[13] F. Ciucci, W. C. Chueh, D. G. Goodwin, and S. M. Haile. Surface reaction and transport in mixed conductors with electrochemically-active surfaces: a 2-D numerical study of ceria. *Phys. Chem. Chem. Phys.*, 13(6):2121–2135, 2011.

[14] W. Lai and S. M. Haile. Impedance Spectroscopy as a Tool for Chemical and Electrochemical Analysis of Mixed Conductors: A Case Study of Ceria. *Journal of the American Ceramic Society*, 88(11):2979–2997, 2005.

[15] F. Ciucci, Y. Hao, and D. G. Goodwin. Impedance spectra of mixed conductors: a 2D study of ceria. *Physical Chemistry Chemical Physics*, 11(47):11243, 2009.

[16] W. G. Bessler, S. Gewies, and M. Vogler. A new framework for physically based modeling of solid oxide fuel cells. *Electrochimica Acta*, 53(4):1782–1800, 2007.

[17] H. Zhu and R. J. Kee. Modeling Distributed Charge-Transfer Processes in SOFC Membrane Electrode Assemblies. *Journal of The Electrochemical Society*, 155(7):B715, 2008.

[18] A. Bertei, J. Mertens, and C. Nicolella. Electrochemical Simulation of Planar Solid Oxide Fuel Cells with Detailed Microstructural Modeling. *Electrochimica Acta*, 146:151–163, 2014.

[19] A. Bertei, G. Arcolini, J.P. Ouweltjes, Z. Wuillemin, P. Piccardo, and C. Nicolella. Physically-based deconvolution of impedance spectra: interpretation, fitting and validation of a numerical model for

lanthanum strontium cobalt ferrite-based solid oxide fuel cells. *Electrochimica Acta*, 208:129–141, 2016.

[20] A. Lasia. *Electrochemical Impedance Spectroscopy and its Applications*. Springer New York, New York, NY, 2014.

[21] M Mogensen. Kinetic and geometric aspects of solid oxide fuel cell electrodes. *Solid State Ionics*, 86-88:1151–1160, 1996.

[22] D. Clematis M.P. Carpanese A. Barbucci C. Nicolella N.P. Brandon A. Bertei, E. Ruiz-Trejo. A perspective on the role of the three-phase boundary in solid oxide fuel cell electrodes. *Bulgarian Chemical Communications. 50 (2018) 31–38.*

[23] Z. Gao, L. V. Mogni, E. C. Miller, J. G. Railsback, and S. A. Barnett. A perspective on low-temperature solid oxide fuel cells. *Energy & Environmental Science*, 9(5):1602–1644, 2016.

[24] S. B. Adler, J. A. Lane, and B. C. H. Steele. Electrode Kinetics of Porous Mixed-Conducting Oxygen Electrodes. *Journal of The Electrochemical Society*, 143(11):3554–3564, 1996.

[25] J. Jamnik and J. Maier. Generalised equivalent circuits for mass and charge transport: chemical capacitance and its implications. *Physical Chemistry Chemical Physics*, 3(9):1668–1678, 2001.

[26] J. Fleig, A. Schmid, G. M. Rupp, C. Slouka, E. Navickas, L. Andrejs, H. Hutter, L. Volgger, and A. Nenning. The Chemical Capacitance as a Fingerprint of Defect Chemistry in Mixed Conducting Oxides. *Acta Chimica Slovenica*, pages 509–518, 2016.

[27] Y. Fu, S. Poizeau, A. Bertei, C. Qi, A. Mohanram, J.D. Pietras, and M.Z. Bazant. Heterogeneous electrocatalysis in porous cathodes of solid oxide fuel cells. *Electrochimica Acta*, 159:71–80, 2015.

[28] G. Paasch, K. Micka, and P. Gersdorf. Theory of the electrochemical impedance of macrohomogeneous porous electrodes. *Electrochimica Acta*, 38(18):2653–2662, 1993.

[29] N Imanishi, T Matsumura, Y Sumiya, K Yoshimura, A Hirano, Y Takeda, D Mori, and R Kanno. Impedance spectroscopy of perovskite air electrodes for SOFC prepared by laser ablation method. *Solid State Ionics*, 174(1-4):245–252, 2004.

[30] S. B. Adler. Applications of Nonlinear Electrochemical Impedance Spectroscopy (NLEIS). *ECS Transactions*, 58(3):101–108, 2013.

[31] S. Jiang. A comparison of O2 reduction reactions on porous (La,Sr)MnO3 and (La,Sr)(Co,Fe)O3 electrodes. *Solid State Ionics*, 146(1-2):1–22, 2002.

[32] A. Nenning, S. Reuter, R. Schlesinger, H. Summerer, R. Ramehsan, L. Lindenthal, M. Holzmann, T. M. Huber, C. Rameshan, J. Fleig, and A. K. Opitz. Surface and Defect Chemistry of Porous La $_{0.6}$ Sr $_{0.4}$ FeO $_3$ Electrodes on Polarized Three-Electrode Cells. *Journal of The Electrochemical Society*, 169(9):094508, 2022.

Chapter 3

Modelling multi-layer diffusion systems

Considering only diffusion along one dimension, the change of concentration at any point in space is defined as the gradient of the flux as follows:

$$\frac{\partial C}{\partial t} = -\frac{\partial J}{\partial x} \tag{3.1}$$

where

$$J = -D\frac{\partial C}{\partial x} \tag{3.2}$$

In a multi-layer system, D is now a function of x, as it will be different for each material and interface involved. Thus the product rule has to be applied during the differentiation, yielding a new form of Fick's second law

$$\frac{\partial C}{\partial t} = \frac{\partial}{\partial x}\left(D(x)\frac{\partial C}{\partial x}\right) = \frac{\partial^2 C}{\partial x^2}D(x) + \frac{\partial D(x)}{\partial x}\frac{\partial C}{\partial x} \tag{3.3}$$

The second term on the right hand side of this equation will be zero for most cases in the system, as the gradient of the diffusion coefficient will be zero. This is assuming that each layer is distinct has a constant diffusivity throughout.

3.1 Modelling Multi-Layer Diffusion

The expansion of Fick's second law as described in the previous section provides a mathematical framework for calculating diffusion in a system with multiple materials with different diffusion properties. With D being a function of distance, a decision then has to be made on how to describe the system mathematically. One approach is to assume that the interface region can be simplified to a region of a

single space step, and that the ion transfer between two different phases can be summarised by the description of this single step, henceforth referred to as 'Interface Resistance Model'. A more complex approach would instead assume the creation of a thin interlayer of distinct diffusivity, where the layer thickness and D determine the shape of the profile in this region, rather than a drop across a single space step. This approach will be referred to as 'Triple Layer Model'. Both approaches will be outlined and investigated.

3.2 Interface Resistance Model

This model assumes a one-dimensional interface with a drop from the last point of the first layer to the first point of the second layer. The size of this drop is determined by an intrinsic resistance of this particular system to ion transfer across multiple phases. This description results in the following system of equations adapted from the system describing a single material's diffusion behaviour under semi-infinite and surface exchange boundary conditions.

$$\begin{cases} \partial_t C' = D(x)\partial_{xx}C' + \partial_x C'\partial_x D(x) & \text{on } (0,\infty)\times[0,\infty), \\ C'|_{t=0} = 0 & \forall x \geq 0, \\ C'|_{x=0} = 1 + \frac{D}{k}\partial_x C'|_{x=0} & \forall t > 0, \\ \lim_{x\to\infty}(C') = 0 & \forall t > 0, \\ D(x) = \begin{cases} D_1 & 0 \leq x < L_1 \\ D_{\text{int}} & L_1 \leq x < L_1 + \Delta x \\ D_2 & L_1 + \Delta x \leq x < \infty \end{cases} \end{cases} \tag{3.4}$$

Apart from each layer's diffusion coefficient, the interface region of width Δx is assigned its own coefficient D_{int}, which summarises the interface's ability to allow ion movement. An analytical solution to such a system does not appear to exist at this time and would likely be computationally intensive. A discretised approach to solving the diffusion equation is therefore necessary.

3.2.1 Discretising the variable-D diffusion equation

First, the principles of discretisation must be illustrated using the conventional form of Fick's second law. After understanding how to solve differential equations of this type, modifications to account for the variability of the diffusion coefficient over multiple layers can be applied.

Series Expansion

In order to solve a differential equation numerically, a commonly applied family of methods is the finite difference discretisation [1]. This works by first taking the system and sectioning it into nodes which are separated by a base length with the unit of the simulation domain (i.e. differentials with respect to time or space in this case, Δx or Δt). On this basis, a Taylor series expansion of the differentials is possible, describing the relationship of each node with its neighbours. Consider the basic form of a Taylor expansion about a given point in the system as seen in eq. 3.5.

$$f(x+\Delta x) = f(x) + \Delta x f'(x) + \frac{\Delta x^2}{2} f''(x) + \frac{\Delta x^3}{6} f'''(x) + \frac{\Delta x^4}{24} f^{(4)}(x) + O(\Delta x^5) \tag{3.5}$$

This expression can be rearranged to solve for the first derivative, resulting in the form of eq. 3.6, where the gradient between the current point and one step ahead of the current point is simulated, called the *forward approximation* or *Forward Euler* method [2]. This can be equally done by considering the previous node instead, as in eq. 3.7, which is then referred to as the *backward approximation*.

$$f'(x) = \frac{f(x+\Delta x) - f(x)}{\Delta x} - \left(\frac{\Delta x}{2} f''(x) + \frac{\Delta x^2}{6} f''(x) + \frac{\Delta x^3}{24} f^{(4)}(x) + ... \right) \tag{3.6}$$

$$f'(x) = \frac{f(x) - f(x-\Delta x)}{\Delta x} + \left(\frac{\Delta x}{2} f''(x) - \frac{\Delta x^2}{6} f''(x) + \frac{\Delta x^3}{24} f^{(4)}(x) - ... \right) \tag{3.7}$$

Rearranging the equations in this way enables the other parts of the sum to be summarised in one term as seen in the brackets. Since the Δx term gets raised to a higher power with each increasing term (and is assumed to be a small value), the terms in the brackets form an error for each approximation on the order of magnitude of the lowest term, i.e. Δx. The rest of the terms allows for an approximation of the gradient of the function between the values of the function at x and its neighbour $x + \Delta x$. Summing eq.s 3.7 and 3.6 results in the *central difference approximation* as seen in eq. 3.8. Similarly, subtracting the forward from the backward difference can be used to construct the second derivative as seen in eq. 3.9.

$$f'(x) = \frac{f(x+\Delta x) - f(x-\Delta x)}{2\Delta x} - \left(\frac{\Delta x^2}{6} f''(x) - \frac{\Delta x^4}{120} f^{(5)}(x) + ... \right) \tag{3.8}$$

$$f''(x) = \frac{f(x+\Delta x) - 2f(x) + f(x-\Delta x)}{\Delta x^2} - \left(\frac{\Delta x^2}{12} f^{(4)}(x) + ... \right) \tag{3.9}$$

Conventional Diffusion Equation

Fick's second law of diffusion is a differential equation with one space and one time derivative. Applying the principles of Taylor expansion and finite difference calculation as outlined previously yields eqs 3.10 and 3.11. Here, the time differential was discretised using the forward approximation while the space differential uses the central difference approximation.

$$\frac{\partial C}{\partial t} = D\frac{\partial^2 C}{\partial x^2} \tag{3.10}$$

$$\frac{C_i^{n+1} - C_i^n}{\Delta t} = D\frac{C_{i-1}^n - 2C_i^n + C_{i+1}^n}{\Delta x^2} + O(\Delta t) + O(\Delta x^2) \tag{3.11}$$

The equation contains two error terms in the sum dependent on the time and space steps, respectively. The superscript n refers to the number of time steps, while the subscript i describes the nodes in space. Rearranging this yields eq. 3.12

$$C_i^{n+1} = (1 - 4\sigma)C_i^n + 2\sigma C_{i-1}^n + 2\sigma C_{i+1}^n \tag{3.12}$$

where,

$$\sigma = \frac{D\Delta t}{2\Delta x^2} \tag{3.13}$$

This solution is susceptible to instability during the calculation process when the values of σ reach a certain range. While this could be circumvented by always selecting Δx and Δt accordingly, it limits the flexibility of the simulation conditions. In order to mitigate this, the *Crank-Nicolson* method is employed.

The Crank-Nicolson (CN) method

The Crank-Nicolson method can be thought of as a mathematical trick which stabilises the final calculation of the linear equations that result from the discretisation process [3]. It works by imagining a 'half-node' in between the real time steps of n and $n + 1$ and enforcing the diffusion equation at this point. Selecting this half-node, which lies halfway in between n and $n + 1$, allows for the central difference approximation to be used for the time differential as well. This reduces the error resulting from the Taylor expansion to be on the order of magnitude of Δt^2. The half-node differential approximation takes the form seen in eq. 3.14.

$$\frac{\partial C_i^{n+1/2}}{\partial t} \approx \frac{C_i^{n+1} - C_i^n}{\Delta t} \tag{3.14}$$

This concept can be extended to the space derivatives using $\hat{C}_{i-1}^{n+1/2}$, $\hat{C}_i^{n+1/2}$ and $\hat{C}_{i+1}^{n+1/2}$. Since the half-node concentration values, denoted with a circumflex, depend only upon real terms when differentiated, they disappear from the final equation. Calculating the differential form results in the solution seen in eq. 3.15

$$\frac{\partial^2 C_i^{n+1/2}}{\partial x^2} \approx \frac{C_{i-1}^{n+1/2} - 2C_i^{n+1/2} + C_{i+1}^{n+1/2}}{\Delta x^2} \tag{3.15}$$

to give the form of the diffusion equation as

$$\frac{C_i^{n+1} - C_i^n}{\Delta t} \approx D\frac{C_{i-1}^{n+1/2} - 2C_i^{n+1/2} + C_{i+1}^{n+1/2}}{\Delta x^2} \tag{3.16}$$

Finally, by considering the value of the half-node concentration as

$$\hat{C}_i^{n+1/2} = \frac{C_i^{n+1} + C_i^n}{2} \tag{3.17}$$

this expression can be inserted into eq. 3.16 to give the ultimate solution in eq. 3.18, which no longer references the half-nodes and only contains known points.

$$(1 + 2\sigma)C_i^{n+1} - \sigma C_{i-1}^{n+1} - \sigma C_{i+1}^{n+1} = (1 - 2\sigma)C_i^n + \sigma C_{i-1}^n + \sigma C_{i+1}^n \tag{3.18}$$

Discretising the variable-D diffusion equation

The final step is to derive an expression that incorporates both variable diffusion coefficients and an interface resistance factor as specified in new system of equations outlined in eq. 3.36. To achieve this, it is possible to imagine diffusion as a series of resistors between nodes as shown in Figure 3.1.

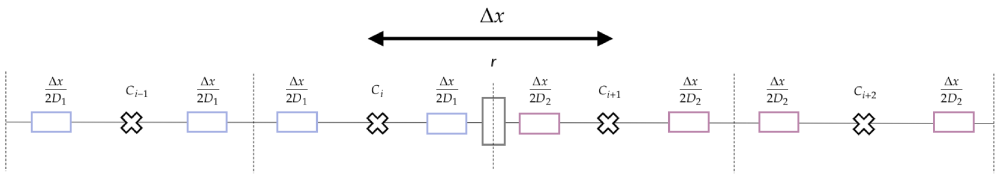

Figure 3.1: Schematic representation of 1D diffusion across an interface using a series resistor analogy. Shown here are a) the conceptual set of 'resistor' elements related to each layer's diffusion coefficient, as well as the additional resistor element r representing interfacial resistance

The component D_{int} is made up of three constituent parts; the bulk diffusion coefficients of either material as well as an additional factor – the interfacial resistance r. This variable represents the interface's particular resistance to cross-interface diffusion.

D_{int} can be seen as a series resistor sum of these components. If the resistance of a single resistor is equivalent to

$$R = \frac{\Delta x}{2D} \tag{3.19}$$

then we can quantify the total resistance D_{int} as a resistor sum consisting of the diffusivities of both bulk material as well as the interfacial resistance r.

$$\frac{\Delta x}{D_{\text{int}}} = \frac{\Delta x}{2D_1} + \frac{\Delta x}{2D_2} + r \tag{3.20}$$

Rearranging for r yields

$$r = \frac{\Delta x}{D_{\text{int}}} - \frac{\Delta x}{2D_1} - \frac{\Delta x}{2D_2} = \frac{\Delta x}{2}\left(\frac{2}{D_{\text{int}}} - \frac{1}{D_1} - \frac{1}{D_2}\right) \tag{3.21}$$

r can thereby be related to the materials properties of each component layer. This parameter will become the metric for the quality of any given interface. An increase in r after exposure to certain conditions could indicate interface degradation and will result in a loss of cell performance.

If the diffusion coefficient is defined as existing in half-nodes in between two spatial nodes (as seen in Figure 3.1, then at a physical node D will be the average:

$$D_i = \frac{D_{i+1/2} + D_{i-1/2}}{2} \tag{3.22}$$

And using central difference for the spatial gradient yields:

$$\frac{\mathrm{d}D_i}{\mathrm{d}x} \approx \frac{D_{i+1/2} - D_{i-1/2}}{\Delta x} \tag{3.23}$$

If we then apply central difference discretisation to the first and second spatial derivative of the

concentration, Fick's second law becomes:

$$\frac{C_i^{n+1} - C_i^n}{\Delta t} = \frac{D_{i+1/2} + D_{i-1/2}}{2} \frac{C_{i-1} - 2C_i + C_{i+1}}{\Delta x^2} + \frac{D_{i+1/2} + D_{i-1/2}}{\Delta x} \frac{C_{i+1} - C_{i-1}}{2\Delta x} \tag{3.24}$$

This simplifies to

$$C_i^{n+1} - C_i^n = \frac{\Delta t}{2\Delta x^2} \left(D_{i+1/2}(C_{i-1} + C_i) + D_{i+1/2}(C_i + C_{i+1}) \right) \tag{3.25}$$

As before, this can be evaluated using the Crank-Nicolson method at the half-nodes. Doing this for the time derivative at the half-nodes, where

$$\hat{C}_i^{n+1/2} = \frac{C_i^{n+1} - C_i^n}{2} \tag{3.26}$$

and

$$\frac{\Delta t}{2\Delta x^2} D_{i-1/2} = \sigma_- \tag{3.27}$$

$$\frac{\Delta t}{2\Delta x^2} D_{i+1/2} = \sigma_+ \tag{3.28}$$

ultimately obtaining

$$-\sigma_- C_{i-1}^{n+1} + (1 + (\sigma_- + \sigma_+)) C_i^{n+1} - \sigma_+ C_{i-1}^{n+1} = \sigma_- C_{i-1}^n + (1 - (\sigma_- + \sigma_+)) C_i^n + \sigma_+ C_{i-1}^n \tag{3.29}$$

This will result in a set of linear equations which have to be solved in order to obtain a solution.

3.2.2 Boundary Conditions

The final step before evaluating the newly derived system is to define the boundary conditions for the calculation.

Surface Exchange Boundary Condition

At the surface of this system, a boundary exists which enables the incorporation of diffusant from an external phase. This depends on the material's ability to incorporate and subsequently diffuse the species. These properties are expressed by the surface exchange coefficient k and the diffusion coefficient D, respectively. The ratio k/D is often summarised as h. While in this study, the diffusant

species is oxygen gas, the principle of this boundary condition extends to many other processes such as evaporation or radiation from a surface. The boundary condition is expressed in eq. 3.30.

$$\left.\frac{\partial C(t,x)}{\partial x}\right|_{x=0} = h\left(C(t,0) - C_{\text{gas}}\right) \tag{3.30}$$

This can be discretised by using the concept of the ghost node $\hat{C}^n_{-1}$ (which exists 'before' the surface) once again, enabling the use of the central difference approximation and thus a lower final error. Applying the discretisation yields eq. 3.31 which can be rearranged in terms of the ghost node, again resulting in the final result after differentiation containing only real nodes, as seen in 3.32.

$$\frac{C^n_1 - \hat{C}^n_{-1}}{2\Delta x} = h\left(C^n_0 - C_{\text{gas}}\right) \tag{3.31}$$

$$(1 + 2\Delta x h\sigma + 2\sigma)C^{n+1}_0 - 2\sigma C^{n+1}_1 = (1 - 2\Delta x h\sigma - 2\sigma)C^n_0 + 2\sigma C^n_1 + 4\Delta x h\sigma C_{\text{gas}} \tag{3.32}$$

This expression describes the first line of the matrix and gives it initial values of concentration that the subsequent time steps will be based upon.

Semi-Infinite Boundary Condition

The idea behind the semi-infinite boundary condition is that the concentration value at large distances away from the surface can be approximated without having to explicitly calculate it. This is done to save computational cost. Two of the commonly used methods are the direct Dirichlet boundary condition (which defines a specific value at the semi-infinite boundary) and the mirror boundary condition (where the gradient at the semi-infinite boundary is set to 0). In an oxygen diffusion system, the Dirichlet condition sets the boundary to be equal to the background isotope concentration. It was found that an average of these two methods most accurately captures the behaviour experimentally observed in tracer diffusion experiments [2].

3.2.3 Matrix Implementation

As this is now a system of linear equations, it becomes a matrix problem involving a tridiagonal matrix. These are easily invertible and are thus well suited for an iterative calculation, requiring the following matrix equation to be solved

$$\mathbf{A}^{n+1}\mathbf{C}^{n+1} = \mathbf{A}^{n}\mathbf{C}^{n} + \mathbf{G} \tag{3.33}$$

with

$$A^{n+1} = \begin{pmatrix} 1+\sum\sigma(1+\Delta xh) & -2\sigma & 0 & 0 & \dots & & & 0 \\ -\sigma & 1+\sum\sigma & -\sigma & 0 & & & & \\ 0 & -\sigma & 1+\sum\sigma & -\sigma & & & & \vdots \\ 0 & 0 & -\sigma & 1+\sum\sigma & \ddots & & & \\ & & & & \ddots & & & \\ & & & \ddots & 1+\sum\sigma & -\sigma & 0 & 0 \\ \vdots & & & & -\sigma & 1+\sum\sigma & -\sigma & 0 \\ & & & & 0 & -\sigma & 1+\sum\sigma & -\sigma \\ 0 & & \dots & & 0 & -\sigma & 2\sigma & 1-\sigma \end{pmatrix}$$

$$A^{n} = \begin{pmatrix} 1-\sum\sigma(1+\Delta xh) & 2\sigma & 0 & 0 & \dots & & & 0 \\ \sigma & 1-\sum\sigma & \sigma & 0 & & & & \\ 0 & \sigma & 1-\sum\sigma & \sigma & & & & \vdots \\ 0 & 0 & \sigma & 1-\sum\sigma & \ddots & & & \\ & & & & \ddots & & & \\ & & & \ddots & 1-\sum\sigma & \sigma & 0 & 0 \\ \vdots & & & & \sigma & 1-\sum\sigma & \sigma & 0 \\ & & & & 0 & \sigma & 1-\sum\sigma & \sigma \\ 0 & & \dots & & 0 & \sigma & -2\sigma & 1+\sigma \end{pmatrix}$$

where

$$\sum\sigma = \sigma_+ + \sigma_- \tag{3.34}$$

$$\mathrm{G} = \begin{pmatrix} 4\Delta x\sigma hC_{gas} \\ 0 \\ \vdots \\ 0 \end{pmatrix} \qquad \mathrm{C}^{n+1} = \begin{pmatrix} C_0^{n+1} \\ C_1^{n+1} \\ \vdots \\ C_{l-1}^{n+1} \\ C_l^{n+1} \end{pmatrix} \qquad C^{n} = \begin{pmatrix} C_0^{n} \\ C_1^{n} \\ \vdots \\ C_{l-1}^{n} \\ C_l^{n} \end{pmatrix}$$

In order to build the simulation for a system containing an interface, the values of σ have to be

adjusted according to the diffusion coefficient D of each component. In the nodes corresponding to the length of the first layer L_1, the value of D is set to be equal to that of the first material. The same is done for the second layer, and can be extended to any given number of layers. At the interface, the most central two nodes are changed based on the difference in σ as detailed in equation 3.29. This then produces the following configuration in the matrices at the interface nodes, i.e. from i=L_1-1 to i=L_1+2:

$$A^n_{\mathrm{int}} = \begin{pmatrix} \sigma_1 & 1-2\sigma_1 & \sigma_1 & \dots & & \\ \vdots & \sigma_1 & 1-(\sigma_1+\sigma_{\mathrm{int}}) & \sigma_{\mathrm{int}} & & \\ & & \sigma_{\mathrm{int}} & 1-(\sigma_{\mathrm{int}}+\sigma_2) & \sigma_2 & \\ & & & \sigma_2 & 1-2\sigma_2 & \sigma_2 \end{pmatrix}$$

MATLAB is well suited for solving iterative matrix calculations and was therefore chosen, although the same type of calculation could be implemented using other methods such as Python. The code works by generating an updated concentration vector, containing the values at each spatial node throughout the whole system, based on the concentration vector at the current timestep as well as the constant matrices.

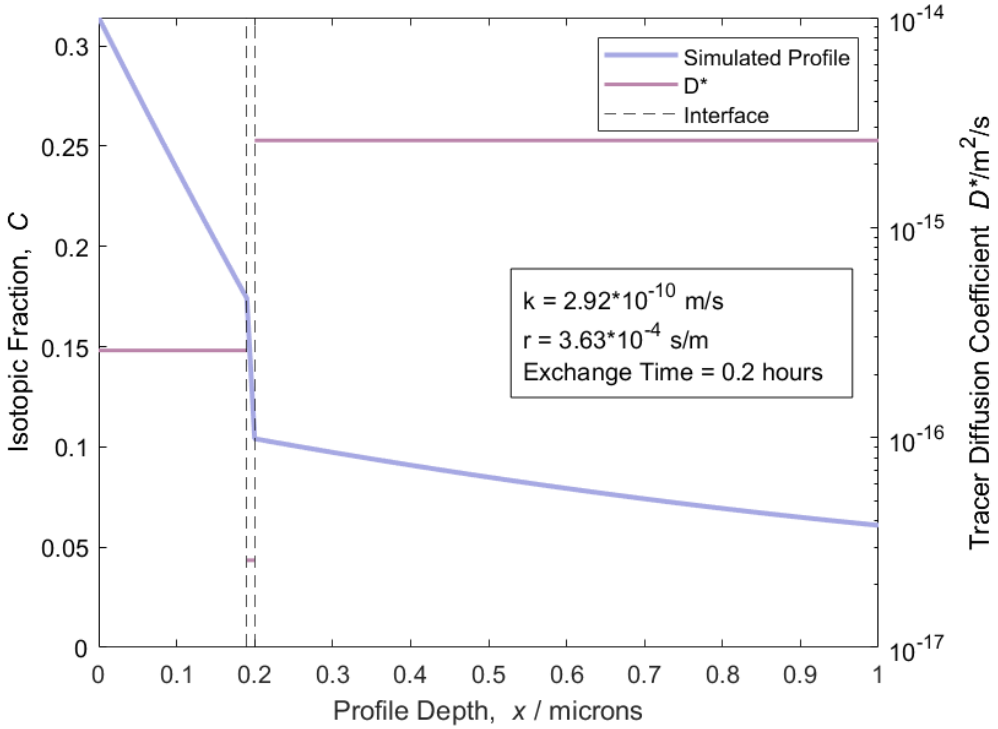

Figure 3.2: A sample diffusion profile as generated by the code developed in this project. Note that although the line appears to run diagonally through the interface region, no data points are generated in this region, as the width of the interface corresponds to Δx, the step size in between two data points.

An example output of this code is illustrated in Figure 3.2, which used the diffusion coefficients of

each layer, as well as the interface resistance parameter, r, to simulate exchange profiles for a given time and temperature.

To better understand the influence of r in a multi-layer system, plots showing the generated diffusion profile with fixed and equal diffusion coefficients while varying r are shown in Figure 3.3. In both graphs, the magnitude of the interfacial concentration step increases with r, showing an asymptotic behaviour at either extreme. When r tends to 0, the profile takes the shape of a regular, one-dimensional diffusion profile as describes by Crank's equation.

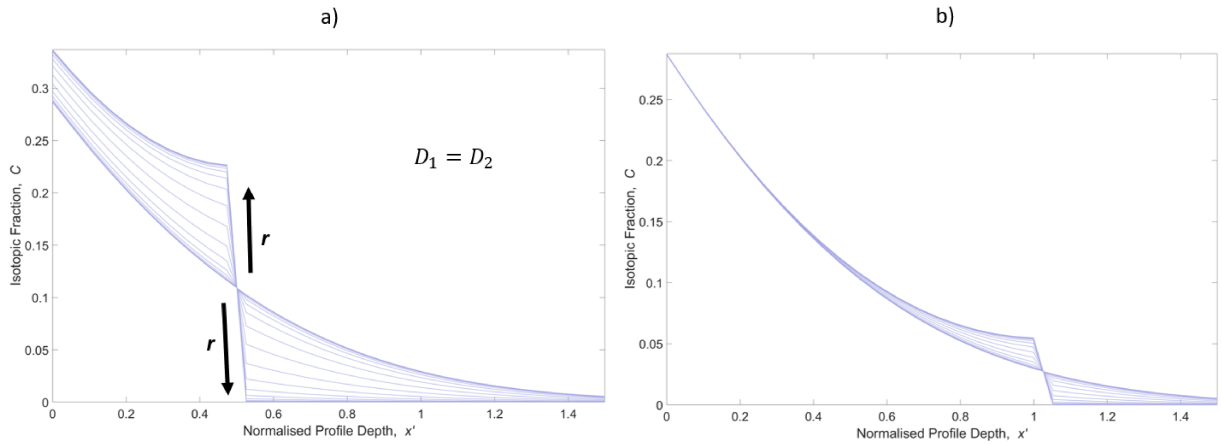

Figure 3.3: A series of generated diffusion profiles with exponentially increasing values of r plotted as a function of x' as defined in eq. 3.35, keeping all other parameters constant. The position of the interface is set at a) $x' = 0.5$ and b) $x' = 1$ in order to visualise the influence of interface position on the profile's behaviour across the full range of r values.

Another interesting property that is shown here is the influence of the interface's position on the overall diffusion profile. In particular, the influence of r on the profile shape is significantly higher when the interface is positioned at a lower normalised profile depth, as shown in Figure 3.3. The normalised profile depth is given by

$$x' = \frac{x}{2\sqrt{Dt}} \tag{3.35}$$

These results will be used to design experiments most suitable for measuring the interface resistance r.

3.3 Triple Layer Model

The previous section explained the mathematical steps necessary to describe a diffusion system of multiple layers with different material properties and an interface, as well as the steps needed to enable the discretisation and numerical calculation of such a system. The mathematical principles regarding the implementation are the same when assuming an interlayer with a defined thickness, the same methods for discretisation and calculation are used. The main difference is that the interface resistance parameter r, which is meant to summarise the properties into one factor, is extended by a third layer that now depends on two variables; the diffusion coefficient of the interlayer D_2 and its thickness L_{int}. The system of equations accordingly can be defined as follows:

$$\begin{cases} \partial_t C' = D(x)\partial_{xx} C' + \partial_x C' \partial_x D(x) & \text{on } (0,\infty)\times[0,\infty), \\ C'|_{t=0} = 0 & \forall x \geq 0, \\ C'|_{x=0} = 1 + \frac{D}{k}\partial_x C'|_{x=0} & \forall t > 0, \\ \lim_{x\to\infty}(C') = 0 & \forall t > 0, \\ D(x) = \begin{cases} D_1 & 0 \leq x < L_1 \\ D_{int} & L_1 \leq x < L_1 + L_{int} \\ D_3 & L_1 + L_{int} \leq x < \infty \end{cases} \end{cases} \tag{3.36}$$

The set-up for the matrices and boundary condition vectors as outlined in the interface resistance model section do not change; the calculations are performed in the same way. Instead of fitting for the interface resistor r to describe the drop, the diffusion coefficient of the second layer being significantly lower than the others provides the basis for the drop.

3.3.1 Behaviour of the triple layer model simulations

As described in the previous section, the triple layer model approach considers two main variables; the thickness of the interface region and the diffusivity of the same region. In order to study the evolution of the interface drop in the triple layer model, a series of simulations were run that changed each variable of interest (L_{int} and D_{int}) keeping all others constant. As the surface exchange coefficient as well as the diffusivities of each layer remain the same, this makes it possible to explore to what degree the assumed thickness of the interface layer affects the steepness of the isotopic fraction drop at a given interface diffusivity, and vice versa. This helps in understanding how sensitive the model is to

small changes in each of these values, and therefore how reliable a potential fit of experimental data would be in estimating these physical properties.

The results are summarised in Figures 3.4 and 3.5. The specific values of L_{int} and D_{int} here were chosen in order to produce a visible evolution in the drop in isotopic fraction. In other words, if either variable were significantly higher or lower in magnitude, then either the interface drop would be so large that there is no bulk diffusion whatsoever, or so small that the interface drop does not appear at all. In both cases, the same behaviour as in the interface resistance model can be observed; a progressively increasing interface drop that corresponds with a higher surface and lower bulk concentration. This illustrates the two ways in which the triple layer model can provide an explanation for the drop. Fundamentally, a significantly lower diffusion coefficient in this region will cause resistance to transport, resulting in a steep downwards diffusion profile. The thicker this layer is, the longer the region of low transport ability, and the more significant the drop. The fundamental difference between the two variables is that a thicker interlayer will result in a progressively lower gradient at the interface. The gradient of the drop therefore becomes a quantifiable feature, which would be useful for experimental data that does not follow a perfectly steep drop but rather a broader decrease across an interface region.

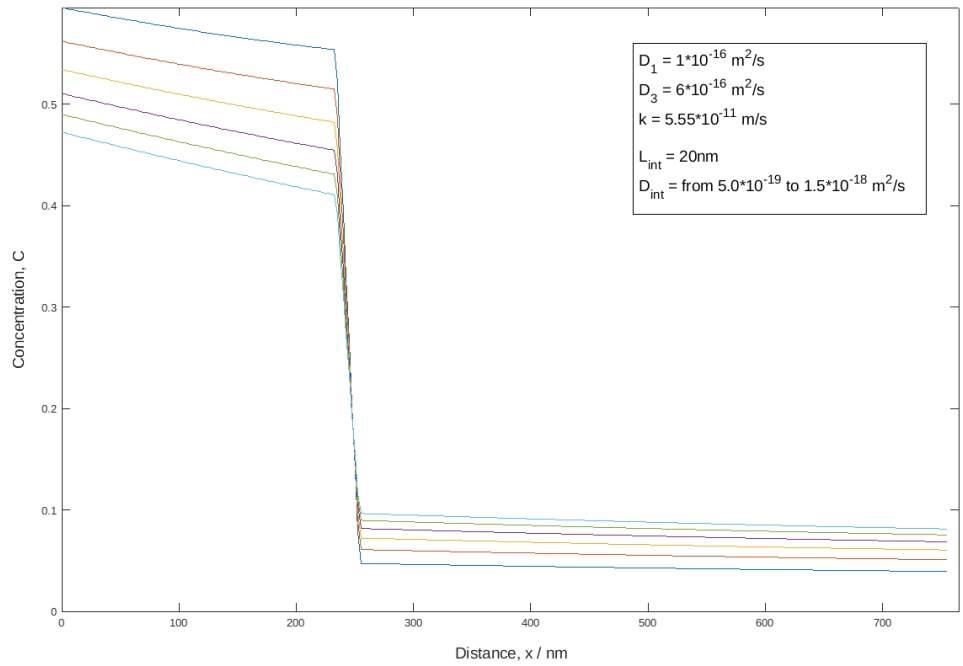

Figure 3.4: Set of simulated multi-layer diffusion profiles using the triple layer model, fixing the interlayer thickness L_{int} at 20nm and varying the interlayer diffusivity D_{int}. All other simulation parameters are kept constant. The series shows an increasing interface drop with lower interlayer diffusivity.

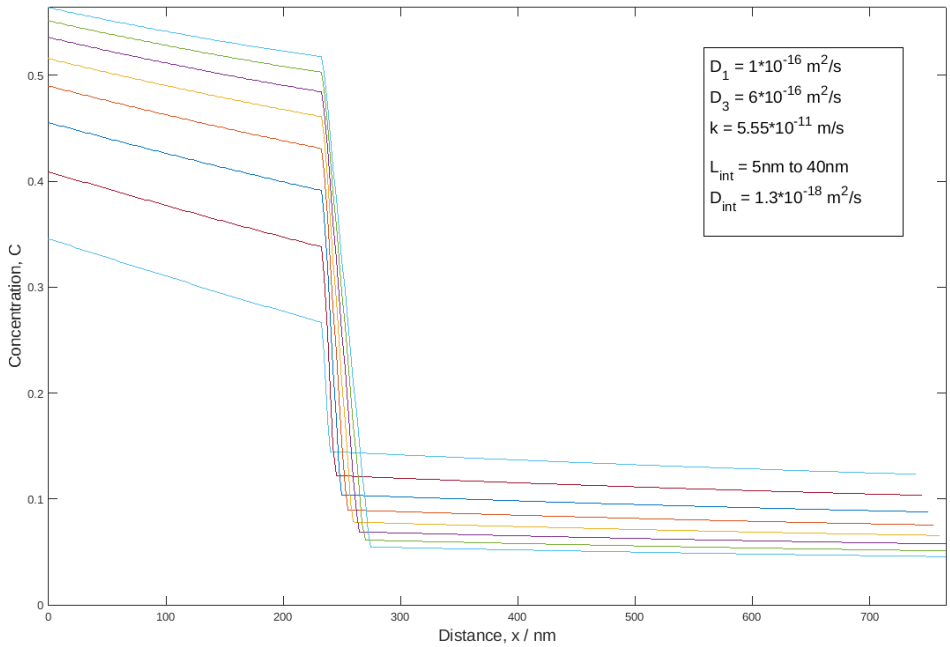

Figure 3.5: Set of simulated multi-layer diffusion profiles using the triple layer model, fixing the interlayer diffusivity D_{int} and varying the interlayer thickness L_{int} between 5 and 40 nm. All other simulation parameters are kept constant. The series shows an increasing interface drop with increased interlayer thickness, illustrating how both variables can significantly influence the shape of the overall profile.

3.4 Conclusion

In this chapter, the mathematical and practical approaches to modelling diffusion across a multi-layer system have been presented. Firstly, the conventional Fick's second law of diffusion was re-written with a non-uniform diffusion coefficient that depends on depth. This new differential equation was then discretised, and a numerical solution developed. Along with the incorporation of boundary conditions specific to this type of diffusion system, an implementable framework for calculating diffusion across multiple layers was formed. In order to capture the behaviour of a steep, nearly vertical drop in isotope fraction seen in literature, two models for the interface transport were presented.

The first simplified model assumes a one-dimensional interface region which contains a blocking effect quantified by the interfacial resistance variable r. This single parameter is able to capture and quantify different types of multi-layers with different resistances to cross-layer transport, while computing the drop to be between two data points in space. This means that no data points from inside the interface region are fit, and instead only the relationship between two points in space on either side of the interface is defined. A more complex modelling approach foregoes the summary of

interface blocking into one parameter, and instead assumes the formation of an extended interface region with its own properties and dimensions. The resistance to transport instead is then captured by the diffusion coefficient of the interlayer along with its thickness. The goal of this work is to pursue experimental routes which may validate either or both of these approaches.

References

[1] G. D. Smith. *Numerical solution of partial differential equations: finite difference methods*. Oxford applied mathematics and computing science series. Clarendon Pr, Oxford, 1979.

[2] S.J. Cooper. PhD thesis, Imperial College London, 2015.

[3] J. Crank and P. Nicolson. A practical method for numerical evaluation of solutions of partial differential equations of the heat-conduction type. *Mathematical Proceedings of the Cambridge Philosophical Society*, 43(1):50–67, 1947.

Chapter 4

Materials and Methods

The aim of the work is to produce multi-layer samples of an electrolyte pellet with a layer of LSCF cathode deposited on top. Both of these layers must be as dense as possible in order to enable high-quality IEDP analysis. Two main processing routes were pursued to achieve this; one ink-based ceramics processing route and a thin film deposition route. Ink processing is used in the industrial fabrication of SOFCs, making samples fabricated with this method closer to the conditions a real fuel cell might be under. While thin film deposition can be considered a more controlled and less realistic process, it produces consistent and high-quality films that can be valuable for characterisation purposes. The characterisation techniques need to ascertain the density and general quality of the sample and its layers, show the material properties of the multi-layer, and provide additional information for the mechanistic and chemical processes that can occur at interfaces.

4.1 Sample Preparation

4.1.1 Ink Processing

The conventional processes most commonly used in industry to fabricate SOFCs are screen printing and tape casting using a bespoke ink. The main issue for the purposes of this project is that these inks are optimised to produce cathodes of high porosity in order to maximise the surface area, providing more reaction sites and facilitating gas flow. Since the goal is to produce a dense cathode that is suitable for IEDP analysis, it is not possible to simply use commercial inks for sample fabrication. Such inks often contain pore-forming compounds, which would be counterproductive here. A custom method therefore has to be developed.

The requirements for this ink are to suspend LSCF powder and keep it well dispersed in order to prevent clustering which might not result in samples that are as flat and even as possible. This can be done with inks of higher viscosity, as would be used in screen printing or tape casting, which are designed to be used for mass production and easier handling. Producing these well-defined films required significant fine tuning of the ink compounds and ink processing itself. After trying many different fabrication methods, it was decided that optimising the ink in such a way was not necessary to achieve the desired result, and instead a simplified drop casting method was used.

Drop Casting

The drop casting method starts by fabricating a pellet of electrolyte material (YSZ8-TC or GDC10-TC, fuelcellmaterials, Ohio, USA). This is done by uniaxially pressing powder in a 13 mm pellet die (0.8 g of GDC and 0.6 g of YSZ to produce similar dimensions) at around 3 tons of pressure.

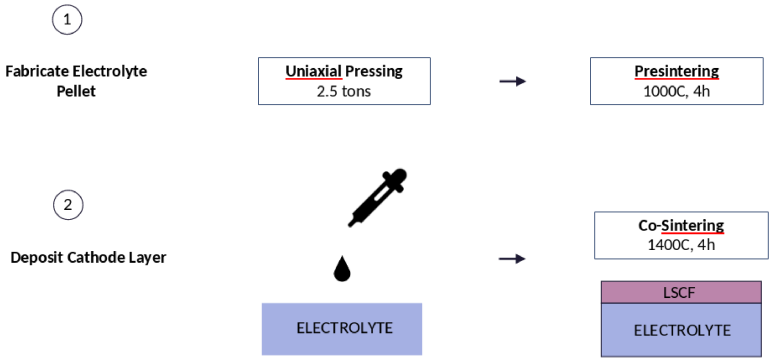

Figure 4.1: Schematic illustrating the experimental procedure for the fabrication of micrometer-scale LSCF-Electrolyte multilayer samples using drop casting.

These pressed pellets are then pre-sintered at 1000 °C for 4 h in a furnace. This is done because fully densifying the electrolyte would cause issues during the co-sintering process later, as the mismatch of shrinkage between the electrolyte and LSCF prevents densification, as will be discussed in more detail in a later chapter.

The $(La_{0.60}Sr_{0.40})_{0.95}Co_{0.2}Fe_{0.8}O_{3-\delta}$ powder (LSCF-P, fuelcellmaterials, Ohio, USA) is suspended in an ink consisting of the solvents shown in Table 4.1.

Table 4.1: Table detailing the final ink composition chosen for the fabrication of LSCF layers on substrate pelelts.

Compound	LSCF	Toluene	IPA	Fish Oil	Terpineol
Weight (g)	2	10	4	3 drops	1

The solvents were chosen for their general ability to carry the powder and evaporation properties. Conventional ink processing wisdom appears to dictate that mixing two solvents produces a better degree of mixing [1]. The dispersants were chosen based on convention for similar materials [2][3].
This mixture results in a well-dispersed ink of low viscosity that can be deposited in a controlled manner using an Eppendorf pipette. Approximately 0.2 ml per drop was then deposited onto the pre-sintered pellet which is pre-heated on a hotplate at 90 ℃. Heating the substrate resulted in a faster evaporation process which produced more evenly deposited LSCF powder layers. When the ink evaporates too slowly, the LSCF powder particles settle and form clusters around the edge of the sample, resulting in an uneven layer. This likely is caused by the 'coffee ring effect', whereby ink at the edge of the sample evaporates faster than in the interior, resulting in a replenishment of the ink around the edges from the centre. This replenishment carries LSCF particles from the centre to the edges, causing the formation of clusters.
The more drops of ink are deposited onto the substrate, the thicker the LSCF layer ends up being. It was found that 7 drops of ink produces a thickness of around 30 microns while minimising cracks in the structure. This will also be discussed in more detail in a later chapter. Once the ink has dried, the sample is then co-sintered at 1400 ℃ for 6 hours in a furnace to produce the final sample, with a heating rate of 5 ℃/min and a cooling rate of 2 ℃/min.

Preparation for Analysis

These samples can be used as they come out of the furnace for the isotope exchange process. After this is done, they are cut using a diamond saw, exposing the cross-section, and mounted in an epoxy resin, which is then left to harden overnight. This cross-section is then polished to a mirror finish, starting with SiC paper and ending up with diamond suspension polishing using a submicron particle size. The grinding process started with P600 SiC paper at 200 RPM, followed by P800, P1200 and P2400, representing successively smaller particle sizes. Diamond suspensions at 9 μm, 6 μm, 3 μm, 1 μm and 1/4 μm particle sizes were successively used for polishing with a Struers RotoPOl-15 Autopolisher at 100 RPM. Once the polishing process is complete, the epoxy-mounted samples can be cut to a convenient shape for SIMS analysis.

4.1.2 Thin Film Deposition

The thin film samples also start with the fabrication of the electrolyte pellet. Since the thin film deposition is able to produce dense layers without the need for co-sintering, the pellets do not need to

be pre-sintered, and can instead be fully sintered at 1400 ℃ after pressing. A 25 mm die was chosen to make YSZ and GDC pellets using approximately 2 g of powder each. The reason for the bigger die diameter is the ability to deposit LSCF on a larger area which can later be cut into many pieces. This enables many more samples to be fabricated in one deposition, making the process much quicker, and furthermore guaranteeing that the samples are as similar to each other as possible, having been deposited at the same time.

Pulsed Laser Deposition

The method chosen for thin film deposition was Pulsed Laser Deposition (PLD). It functions by firing a high-energy laser at a target pellet, which ablates material from this surface, creating a plume of vapour, as seen in Figure 4.2. The target pellet is fabricated using commercial LSCF powder, pressed and sintered at 1400 ℃ for 6 h to a diameter of 20 mm and a thickness of 5 mm.

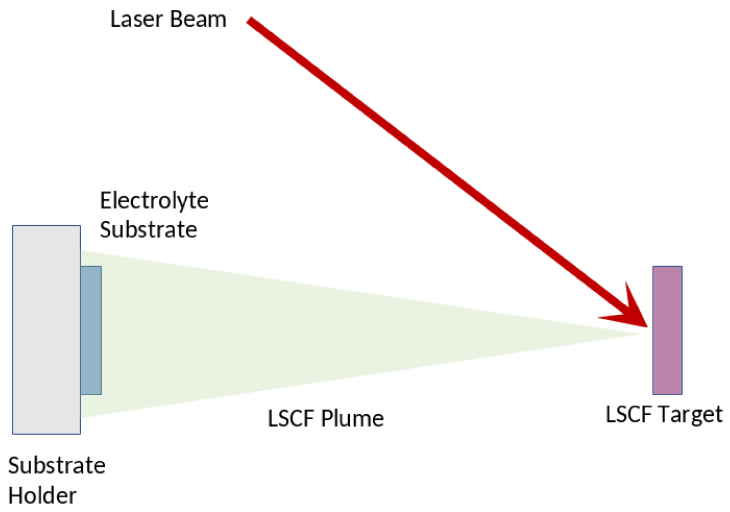

Figure 4.2: Sketch illustrating the experimental setup of a Pulsed Laser Deposition (PLD) machine.

The substrate is mounted opposite the target, and an oxygen atmosphere in the deposition chamber ensures that the stoichiometry of the ceramic oxide is kept as closely as possible to that of the target material. The number of laser pulses, which corresponds to the total deposition time, will determine the thickness of the film. The reason PLD was chosen is because it is a method that is particularly suitable for oxide materials, produces relatively reliable results, and has been used extensively in the field to deposit LSCF in particular [4][5]. The films fabricated here were deposited at 10 Hz laser frequency for 18,000 pulses, resulting in 30 minutes deposition time. The laser energy was set to 350 mJ. The oxygen pressure during deposition was set to 5 mTorr or 6.66 mbar. According to literature investigations, these conditions would result in films of approximately 200-300 nm thickness. While

fabricating thicker films than this is possible by extending the deposition time, the laser construction could overheat and would potentially require the temporary interruption of the deposition process. After deposition, the pellet is cut into multiple pieces for further analysis. As these films are 300nm or less in thickness, it is possible to analyse them using the depth profiling function of the SIMS. The samples therefore do not need any further processing or polishing to be ready for analysis after isotope exchange.

4.2 Characterisation

4.2.1 SEM

Before moving on to IEDP analysis, the density and structural integrity of the samples has to be ascertained. For the ink processing samples, SEM analysis of the surface and cross-section was used. The surface analysis shows whether the powder has densified fully and how many, if any, pores or voids are present. High-resolution SEM can also be used to characterise density and thickness of the thin film layers by imaging the cross-section. Furthermore, SEM-EDX is a useful technique for elemental analysis of the region around the interface, potentially giving clues about the chemical reactions and other processes taking place. The instruments used in this project were mainly the JEOL-6010LA and the Zeiss Sigma 300.

4.2.2 XRD

X-Ray Diffraction is a powerful technique for obtaining information about the crystal structure of a material. The positions of the diffraction peaks provide characteristic information about a specific phase, while the intensity of the peaks can indicate the quantitative relationships between different phases in a given sample. This is useful to determine the reaction mechanisms and formation of new phases when common SOC materials come into contact. For phase identification, a Bruker D2 desktop instrument was used using an incident wavelength of 1.54 Angstrom.

4.2.3 Diffusion Measurements

Isotope Exchange

The Isotope Echange (IE) technique was first developed by Kilner *et al.* as a method of directly measuring the self-diffusivity and surface exchange properties of solid oxide materials [6]. It relies upon the core principle that isotopes of oxygen (and other elements) exhibit a different mass due to extra

neutrons, but do not show a difference in their overall chemical behaviour. For a solid oxide material, this means that the mass difference is not assumed to significantly affect its ability to exchange and diffuse oxygen. By annealing a sample at operating temperature in an atmosphere of 99.9% pure isotope, the ^{18}O from the gas that enters the material can clearly be distinguished from the native lattice ^{16}O present in the sample using SIMS analysis. In order to achieve this, samples must be of the highest and most consistent quality possible. The two main factors that are important to consider are the surface roughness and the sample porosity. A rough surface can affect both the signal obtained from SIMS analysis (due to its surface sensitivity) and also have an influence the surface exchange ability of the material [7]. If the material has a significant number of interconnected pores, the gas diffusion through these pores will inevitably be much faster than the solid diffusion within the host lattice. This would result in a non-constant diffusion front that no longer matches theoretical description and make material property determination impossible. In the case of non-interconnected pores, these would present an 'obstacle' to diffusion and distort the isotopic fraction profile as well.

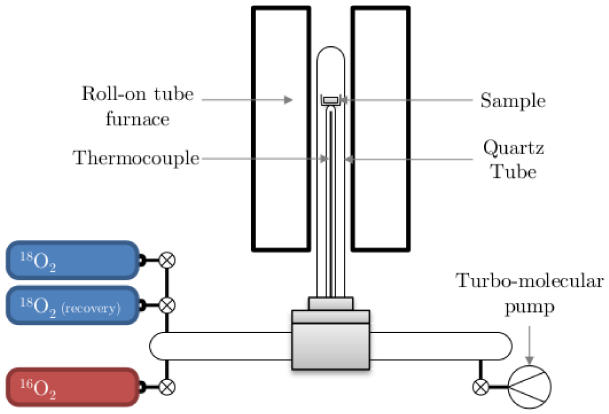

Figure 4.3: Illustration of the isotope exchange rig enabling the annealing under controlled atmosphere. Reproduced from Cooper [8].

The IE experiment setup is illustrated in Figure 4.3. The sample is held in a vacuum tube which enables precise control of the atmosphere around it, while a furnace lowered around the tube determines the temperature. A thermocouple just below the sampleholder measures as precisely as possible the real temperature the sample is exposed to. Knowing this value is important when later analysing the diffusion data, as variations in temperature can have a significant effect on the material's self-diffusivity and surface exchange properties.

Initially, a pre-annealing step at the exchange temperature with pure ^{16}O gas is done in order to ensure the equilibriation of oxygen vacancy concentration and stoichiometry within the sample.

This is important to ensure consistency between samples. The pre-annealing step is conventionally done for around 10 times longer than the planned ^{18}O exchange step [9]. The ^{16}O is then removed using a vacuum pump, and the ^{18}O introduced into the tube for the final step. Ensuring a high-quality vacuum for this ^{18}O annealing step in particular is important in order to minimise any potential chemical interactions with the sample surface that impurities in the gas stream could induce, ensuring consistency between samples. After the experiment has finished, the ^{18}O gas is recovered using a molecular sieve by cooling the reservoir and creating a pressure difference that drives the gas back from the vacuum tube once the connection between the two is opened. This is done both for cost-saving and to keep the ^{18}O gas pure from humidity and other contaminants, as the molecular sieve filters out components as well.

The most significant measurement uncertainty associated with the IE process is the accuracy of the temperature and the annealing time. The sample will need on average 10-15 minutes to reach operating temperature, and a similar amount of time to cool down once the exchange has finished. During these times, it is difficult to estimate how much exchange and diffusion is actually occurring. The Killoran correction method is commonly used to mathematically approximate this [10], but the best practical solution to this issue is to have the isothermal annealing time be significantly longer than the heating and cooling stages. For this reason, all exchanges undertaken in this project were done for 90 minutes.

SIMS Analysis

Secondary Ion Mass Spectrometry (SIMS) involves firing a high-energy primary ion beam (usually a liquid metal source, in this project a bismuth gun was used) at a sample surface, which will destructively interact there. Some of the surface species will transfer the collision energy throughout the material, entering deeper into it, while others will be knocked out of the surface and the material altogether. These can take the form of both neutral and charged (ion) species, the latter of which are then called Secondary Ions. These secondary ions, due to their charged nature, can then be separated according to their mass-to-charge ratio in a mass spectrometer and analysed. To enable probing further into the material, a caesium sputter beam is used to deepen the crater, which can then be analysed using the primary ion beam. Caesium in particular is used to enhance the sputtering of negative ions, which makes it suitable for the analysis of oxygen species [11][12]. Secondary ion yield is defined by the following equation:

$$I_s^m = I_p y_m \alpha^{\pm} \Theta_m \eta$$

Where I_s^m is the secondary ion current (yield) of species m, I_p is the primary ion flux, y_m is the sputter yield, α is the ionisation probability of the charged particle (positive or negative), Θ_m is the fractional concentration of species m in the surface layer and η is the transmission factor describing the ion extraction efficiency of the analysis system. While this equation offers an approximate quantification of the ion signal, there exists significant variety between different types of samples. This is influenced, among other factors, by the electronic properties and structure of the target material. In this project, the main ion signals of interest are the ^{16}O and ^{18}O species, which are chemically and electronically identical, leading to the same value of α. Regardless of the material property, the ratio of ^{18}O to ^{16}O should be the same in the secondary ions, meaning that further quantitative analysis is not necessary.

Time-of-Flight SIMS (ToF-SIMS)

The SIMS equipment used in this project is TOF-SIMS 5 (ION-TOF GmbH, Münster, Germany), TOF standing for time-of-flight. As the name suggests, the method for distinguishing different species in the mass spectrometer is by measuring the time each ion needs to reach the detector, and calculating the mass from this value. This is achieved by first decelerating the secondary ions and then accelerating them again with a predetermined electric field, giving all species the same kinetic energy. The ions then pass through a space free from any electric field, where the time of flight then differs based on the ion's mass according to the kinetic energy equation.

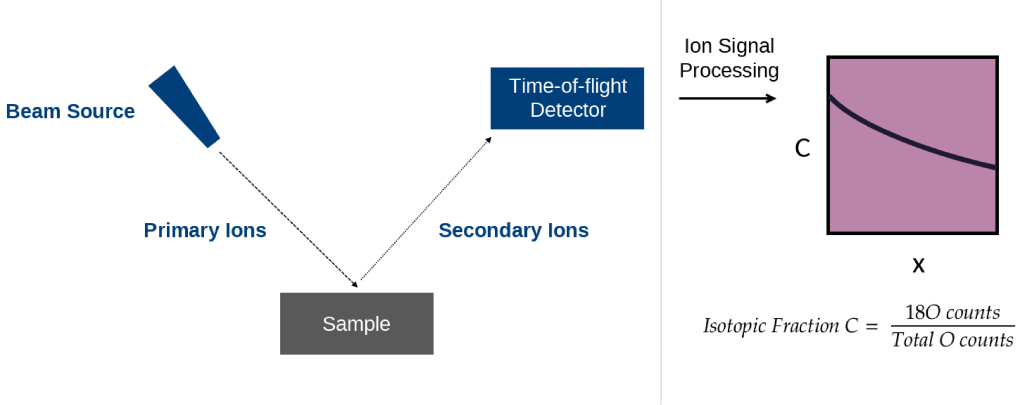

Figure 4.4: Schematic showing the principle of obtaining isotopic fraction data from the ToF SIMS

This process has the advantage of enabling simultaneous measurement of all ion species, therefore allowing not only the oxygen isotope ratio, but also the other relevant ions from the material to be

detected. This is particularly important for the analysis of a multi-layer sample, as it gives another way to measure the thickness of each layer and the transition points between them at the interface. This can be achieved by mapping the signature elements of each layer (such as Fe for LSCF and Zr for YSZ, for example) across the whole cross section and observing the dimensions of the high-concentration areas.

Depth Profiles

When analysing a depth in the nanometer range, as is the case for a sample deposited using PLD, ToF-SIMS is able to measure the entire relevant depth across a multi-layer sample by using a sputter beam. Each sputtering pulse is followed by an analysis beam, which then provides a value of ion species across the average of this sputtering depth, resulting in a depth profile as a function of sputtering time. The final depth of the sputtering crater has to be measured in order to convert sputtering time into real spatial depth.

When performing depth profiles, it is important to sputter a significantly larger area than is analysed with the ion beams. This is done both to prevent obscuring the ion signal with data from the edges of the crater, and furthermore to prevent re-deposited material from the sputtering process being analysed. The depth profile process is sensitive to surface roughness, which is why the electrolyte substrate pellet in these experiments was polished to a mirror finish prior to the LSCF PLD, ensuring as flat a surface and interface as possible. The mirror finish is achieved by using 0.25 micron diamond suspension paste until the appearance of the surface is smooth and highly reflective.

Line Scans

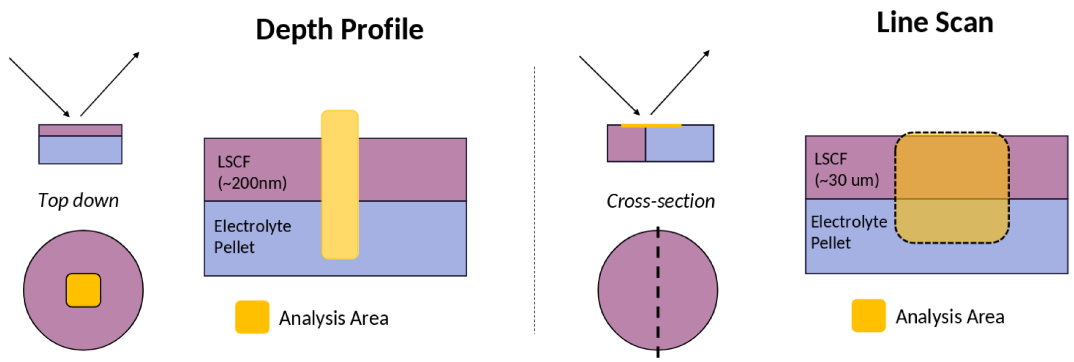

Figure 4.5: The two different data acquisition methods for Isotope Exchange Depth Profiling. In depth profiling, a hole is sputtered into the sample with ion analysis at each step, while line scans are done over a cross-section.

Another method for analysis is a line scan, i.e. a cross-sectional imaging process. This is suitable for the analysis of thicker layers, as is the case with the ink processing samples, where the area of interest will be on the order of 100 microns. The multi-layer samples have to be cut to reveal the cross-section, and subsequently polished in order to minimise the effects of surface roughness. Setting the analysis area to be around 150-250 microns squared then captures both layers of material as well as a diffusion profile of sufficient length.

4.2.4 Topography

As has been mentioned multiple times, the surface roughness of the samples plays a significant role in the SIMS analysis. Furthermore, for SIMS depth profiling, measuring the sputtering crater depth is essential for correlating sputtering time with actual distance. For both of these, White Light Interferometry is a well-suited technique.
The equipment used here was a Zygo New View 200. It functions by splitting an incident light beam between the sample surface and a reference material, receiving reflections from both surfaces that are directed towards a CCD camera. Due to the fact that the two light beams have different path lengths, they will be out of phase with each other, creating interference patterns. Guiding these interference patterns to the area of interest, such as a sputtering crater from SIMS depth profiling, enables the MetroPro11 software to calculate the surface topography to a resolution of around 2 nm, based on the path length difference at each point.

4.2.5 EIS

Electrochemical Impedance Spectroscopy (EIS) is one of the most commonly used experimental methods in electrochemistry. It works by applying an AC voltage or current of varying frequency to a sample and measuring the current at each point, from which the impedance can be derived. Impedance provides information about the resistance, but also more complex processes modelled through capacitance, inductance and further elements [13]. This makes it a useful tool for the study of electrochemical systems, where many complex processes coexist. This versatility and relative ease of sample preparation has made EIS the principal tool to characterise the performance and properties of Solid Oxide Cells.

The main purpose of EIS in this project is to provide a conventional reference point to the SIMS data, potentially confirming conclusions or revealing additional behaviours. Particularly, EIS can show processes associated with interface transfer mechanisms that may display a unique frequency range.

The thin film samples that were fabricated were prepared for analysis with EIS after having been analysed in the SIMS first. To do this, each side of the pellet was painted with a thin layer of silver paint, which was then fired at 500 ℃ for 4 h in a furnace. This removes the organic solvent compounds of the paint and creates a porous silver structure that serves as an electrode whilst still enabling gas diffusion. These samples were then placed into a ceramic tube with platinum meshes on either side of the sample to serve as the electrical contacts, and then heated to operating temperature (460 ℃) in a tube furnace. A frequency sweep from 0.01 Hz to 1 GHz was performed on a Solartron 1260 impedance analyser.

References

[1] R. E. Mistler and E. R. Twiname. *Tape casting: theory and practice*. American Ceramic Society, Westerville, Ohio, 2000.

[2] Y. Zhang, X. Huang, Z. Lu, Z. Liu, X. Ge, J. Xu, X. Xin, X. Sha, and W. Su. A study of the process parameters for yttria-stabilized zirconia electrolyte films prepared by screen-printing. *Journal of Power Sources*, 160(2):1065–1073, 2006. Type: Journal Article.

[3] Z. P. Li, M. Toshiyuki, G. J. Auchterlonie, J. Zou, and D. John. Mutual diffusion occurring at the interface between $La_{0.6}Sr_{0.4}Co_{0.8}Fe_{0.2}O_3$ cathode and Gd-doped ceria electrolyte during IT-SOFC cell preparation. *ACS Appl Mater Interfaces*, 3(7):2772–8, 2011.

[4] P. Plonczak, A. Bieberle-Hütter, M. Søgaard, T. Ryll, J. Martynczuk, P. Hendriksen, and L. J. Gauckler. Tailoring of La $_{x}$ Sr $_{1-x}$ Co $_{y}$ Fe $_{1-y}$ O $_{3-}$ Nanostructure by Pulsed Laser Deposition. *Advanced Functional Materials*, 21(14):2764–2775, 2011.

[5] S. Jiang. Development of lanthanum strontium cobalt ferrite perovskite electrodes of solid oxide fuel cells – A review. *International Journal of Hydrogen Energy*, 44(14):7448–7493, 2019.

[6] J Kilner, B Steele, and L Ilkov. Oxygen self-diffusion studies using negative-ion secondary ion mass spectrometry (SIMS). *Solid State Ionics*, 12:89–97, 1984.

[7] M. J. Pietrowski, R. A. De Souza, M. Fartmann, R. Ter Veen, and M. Martin. Oxygen Isotope Transport Properties of Yttria-Stabilized Zirconia (YSZ) in O $_{2}$ - and H $_{2}$ O-Containing Atmospheres. *Fuel Cells*, 13(5):673–681, 2013.

[8] S.J. Cooper. PhD thesis, Imperial College London, 2015.

[9] R.J. Chater, S. Carter, J.A. Kilner, and B.C.H. Steele. Development of a novel SIMS technique for oxygen self-diffusion and surface exchange coefficient measurements in oxides of high diffusivity. *Solid State Ionics*, 53-56:859–867, 1992.

[10] D. R. Killoran. The Effective Duration of a Linear Slow-Cool. *Journal of The Electrochemical Society*, 109(2):170, 1962.

[11] V. E. Krohn. Emission of Negative Ions from Metal Surfaces Bombarded by Positive Cesium Ions. *Journal of Applied Physics*, 33(12):3523–3525, 1962.

[12] G. Doucas. Energy distribution of negative ions sputtered from caesiated surfaces. *International Journal of Mass Spectrometry and Ion Physics*, 25(1):71–87, 1977.

[13] E. Barsoukov and J. R. Macdonald, editors. *Impedance Spectroscopy: Theory, Experiment, and Applications*. Wiley, 2005.

Chapter 5

Experimental investigation of diffusion in LSCF-YSZ multilayers fabricated by pulsed laser deposition

5.1 Measuring Interfacial Resistance

Having established methods for fabricating samples both in the nanometer and the micrometer range, as well as having developed a theoretical model that enables the analysis and quantification of diffusion data in multi-layer samples, a series of experiments that induce variable interface resistance is needed. This will allow the interfacial resistance parameter, r, to be used as a quantitative measure for ion-blocking properties.

Literature already shows the formation of an ion blocking layer when LSCF and YSZ are in contact in a high-temperature environment [1][2][3]. A clear mechanistic explanation for why this results in bad ion transport has not yet emerged, however there is some indication that the formation of a strontium zirconate (SZO) interlayer might play a role. To pursue this further, a set of experiments was run to indicate the temperature-dependence of SZO formation. For this, an equal wt% LSCF and YSZ powder were mixed in a pestle and mortar and fired at various temperatures. The XRD results of these samples are shown in Figure 5.1.

It can be observed that a minor amount of SZO formation occurs at 800 ℃, showing up as distinctive

peaks among the standard LSCF and YSZ peaks. With increasing temperature, this phase evolves, eventually showing a similar peak intensity to the YSZ signal and completely displacing any perovskite LSCF signal. The formation of a $CoFe_2O_4$ phase also becomes visible alongside the SZO, although at lower peak intensities. As the highest temperature sample (1400 °C for 6 h) corresponds to the sintering program mostly used to fabricate samples, it can safely be assumed that depositing an LSCF layer on a YSZ sample and then co-sintering the two will produce SZO and other reaction products.

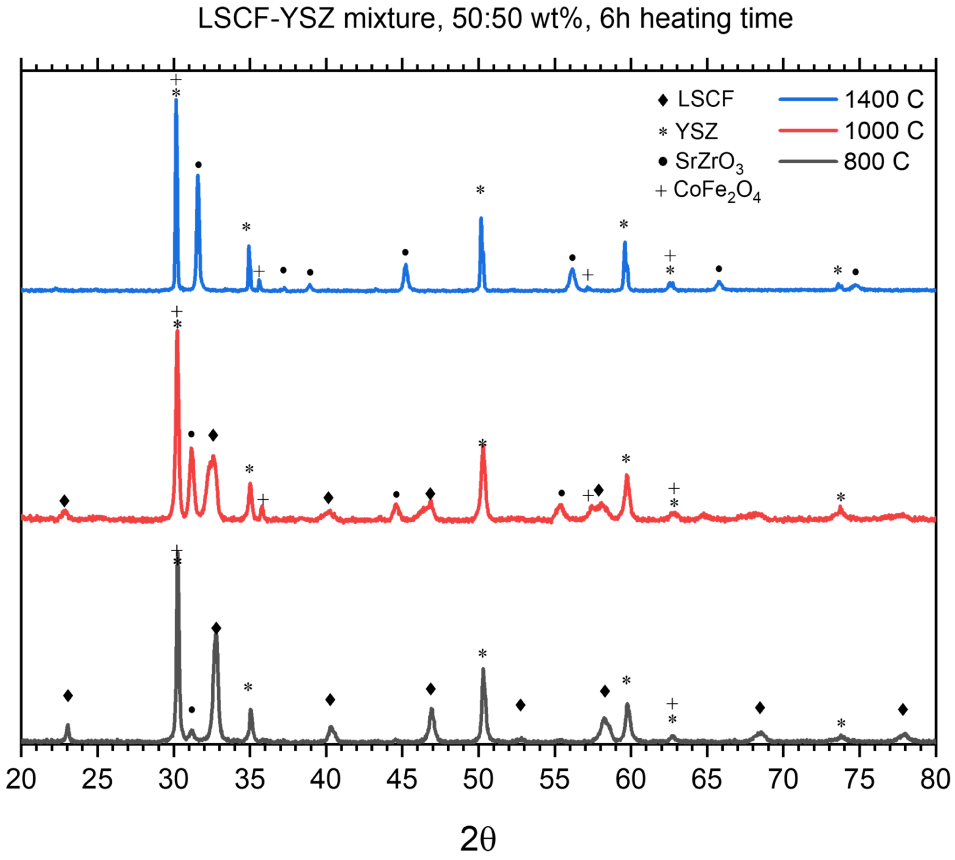

Figure 5.1: XRD patterns of LSCF and YSZ powder mixed at a 1:1 weight ratio, pressed into a pellet and heated to varying temperatures for 6h. As the temperature increases, the signal for SZO increases in intensity just as the signal for LSCF is decreasing.

These results open up the possibility of annealing the samples after sintering in order to actively induce the formation of an interlayer consisting of these reaction products. The XRD data gives some guidance about the range of temperatures that might be reasonable for an annealing process. It was decided to explore the range between no annealing and 1000 °C for the formation and evolution of a potential interface resistance. By keeping the temperature and other conditions of Isotope Exchange analysis identical and only varying the annealing temperature prior to the exchange, no other factors apart from the heat treatment-induced interface degradation should be significant.

5.2 PLD Sample Series

For the purpose of studying the fundamental properties of SOFC materials, thin film deposition is often used. This family of methods produces dense, well-defined films of any target material. Pulsed Laser Deposition (PLD) is one of the principal thin film deposition techniques used for ceramic oxides. For these reasons, much research in the area has focused on using thin film deposition techniques to grow the cathode layer. This has the advantage of not only being able to produce a dense layer, even on a pre-sintered sample, but also keeps the temperatures during the whole process significantly lower than with the ink processing routes. While the latter requires co-sintering temperatures in excess of 1400 ℃, the substrate temperature for PLD deposition can be as low as 600 ℃ and below [4]. According to the XRD data in Figure 5.1, this should be low enough not to induce a significant amount of reactions between LSCF and YSZ. This well-functioning layer can then be heat treated in order to induce further such reactions and worsen the interface quality.

5.2.1 PLD Fabrication

In order to obtain some experimental data for a multi-layer sample with an interface, a series of samples were fabricated. In order to exploit the reaction between LSCF and YSZ, YSZ pellets of 25 mm diameter were pressed uniaxially and sintered at 1400 ℃ for 6 h. These pellets were then mounted in an epoxy mixture which was left overnight to harden. This stub was then ground and polished to a mirror finish using SiC paper and diamond suspension on polishing pads, using the same sequence already described in the Materials and Methods chapter. This polished YSZ pellet was then mounted in a PLD chamber, after which LSCF was deposited using a laser at 10 Hz pulsing frequency and 350 mJ energy and at an oxygen pressure of 10 mTorr. The total number of pulses was set to 18000, resulting in a deposition time of 30 minutes. The YSZ substrate was heated to 600 ℃. These parameters were chosen based on literature investigations, showing that these laser conditions and substrate temperature produce dense LSCF layers of around 200-300nm [4]. The same exact method was also used to produce LSCF layers on a GDC substrate as a comparison series. The results from these samples are summarised in the Appendix.

The closest way of determining the thickness of the LSCF layer is from the SIMS depth profile data in conjunction with Zygo interferometry, as this probes the depth of the sample at exactly the point of analysis. However, to get an idea of the thickness and general condition of the layer, cross-section SEM at high resolutions is also a useful method. One such image is shown in Figure 5.2. At nanometer length scales, getting a sharp, high-resolution image of the LSCF layer is not trivial,

but the general features can be observed. It appears to have a mostly dense microstructure with a reasonably flat surface that is between 200-300 nm in thickness, depending on which part of the sample is imaged. It should be noted that this thickness is only indicative rather than a precise measurement, mainly due to the fact that the sample stage in the SEM had to be carefully tilted to allow the capture of the LSCF layer. Furthermore, the exact interface position between LSCF and electrolyte substrate contains some level of uncertainty.

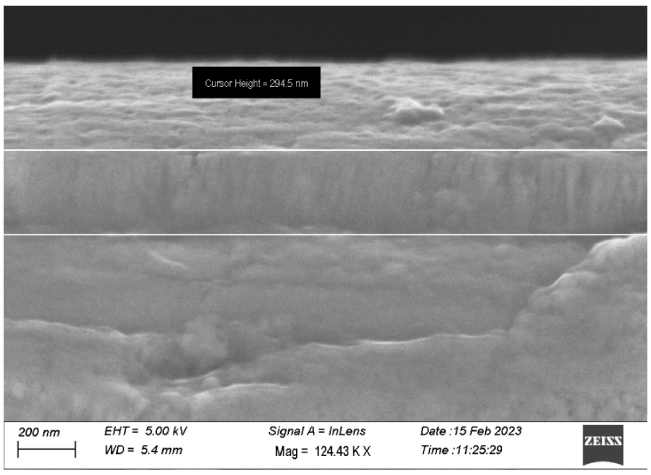

Figure 5.2: Cross-section image of a LSCF layer deposited onto a GDC pellet using PLD. The area in between the horizontal white lines shows the LSCF layer cross section, while the remaining signal below this is part of the substrate. The upper part of the image shows the surface topology of the LSCF layer. The cursor height provides an indication of the layer thickness, but should not be considered an accurate measurement due to the effects of tilting the sample for analysis and the unclear boundary between the layers.

To further confirm the appropriate deposition of the LSCF from the target onto the substrate, grazing incidence x-ray diffraction (GIXRD) was used, these results are further discussed in the supplementary material.

5.2.2 Isotope Exchange on PLD Samples

After deposition, the multi-layer sample was cut into multiple pieces. One of these was exchanged in the isotope exchange rig without further treatment, while the others were heat treated under ambient atmosphere at temperatures ranging from 600-1000 ℃ for 4 hours each. All samples were preannealed for 20-24 hours in 16O for equilibration. The heating and cooling rate were both set to 5 ℃/min. All the samples were annealed in ^{18}O at the same time and temperature; 460 ℃ for 90 minutes using the procedures specified in the experimental methods section. Once this was done, the samples were ready for analysis using SIMS without any further processing.

5.2.3 PLD SIMS

Each sample was then probed in the SIMS using a 1 kV Cs sputter beam and a Ga LMIG ion beam using Burst Alignment mode. The profile was monitored until a satisfactory depth to capture enough of the multi-layer profile for fitting and analysis was reached. The depth and flatness of the surface was then confirmed using Zygo surface topography analysis, further shown in the appendix. This showed that the surface shows minimal variation in roughness across the area covered by the sputtering and analysis beams. The isotopic fraction obtained from these experiments is summarised in Figure 5.3. Two features stand out in this set of data; the relatively large variation in the first layer thickness and the inconsistent shapes of the curves in the second layer. The different layers and their approximate thicknesses can be gauged from the point at which the drop in isotopic fraction occurs. These will be further explored in a later section exploring the ion signal data as shown in Figures 5.18 and onwards. Since that data enables the clear identification of species belonging to each layer, it is more suited to a detailed examination.

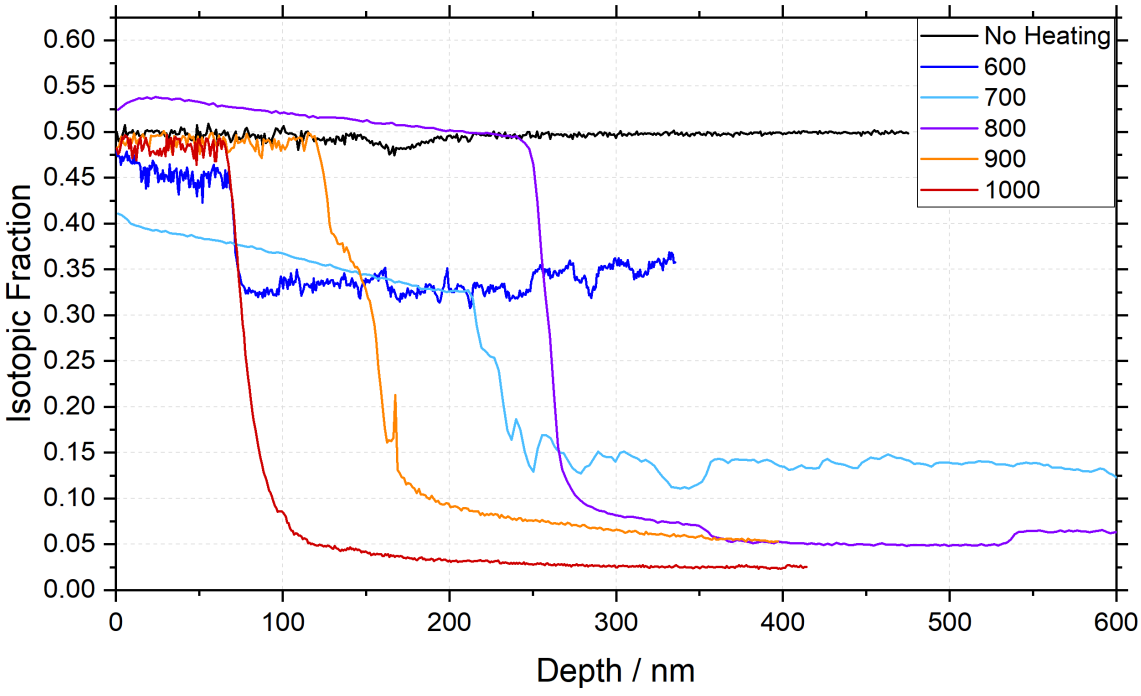

Figure 5.3: Isotope fraction depth profiles of multi-layer LSCF on YSZ samples that were fabricated using PLD. Each sample was heat treated at the temperatures indicate in the top right for 4 hours prior to isotope exchange. All of these were conducted at 460 °C for 90 minutes after a preannealing process of 24 hours. The sharp drop in isotope fraction that is visible in the samples treated at 600 degrees and above denotes the transition between the LSCF and YSZ layers.

The inconsistency in the LSCF layer thickness is undesirable for a higher degree of comparability

between samples, and repeat experiments would help refine and solidify the interface resistance values obtained for each treatment temperature. However, the models described in Chapter 3 provide quantification for all variables necessary to describe the shape and magnitude of the curve (D, k, r, exchange time and layer thickness). This enables a complete comparison between all values of the samples that can be considered when analysing the magnitude of the interface drop. The results show a clear trend of an increasing drop in isotopic fraction at the interface between LSCF and YSZ. In the sample that did not undergo any heat treatment, no drop in isotopic fraction is visible, and the value stays mostly constant throughout the whole sample. This is consistent with expectations from model simulations, as the literature values for both LSCF and YSZ at 460 ℃ would be sufficiently large to enable fast diffusion in the nanometer length scale, resulting in a relatively flat diffusion profile. This was confirmed using simulations using literature values and will be discussed in more detail at a later stage. The slight dip around the interface region is consistent with the transition in the SIMS from LSCF to YSZ. Each material has different hardness and electrical properties, making it possible for the total ion counts to be influenced. This will be discussed in more detail in a later section looking at the remaining ion data.

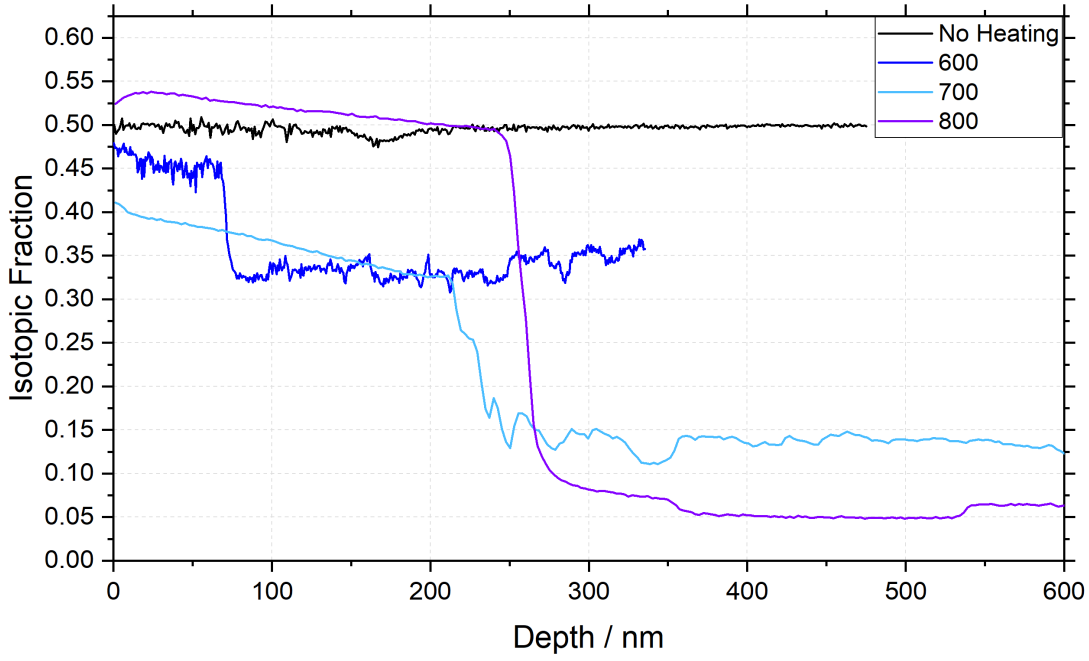

Figure 5.4: Isotope fraction graphs of the LSCF-YSZ PLD samples heat treated at temperatures of 800 ℃ or lower for 4 hours before isotope exchange. From the sample that did not undergo any additional heat treatment, these results show the progressively increasing drop in isotope fraction that takes place at the interface between LSCF and YSZ. While the samples have a different LSCF layer thickness at the point of analysis, the drop in isotopic fraction at the interface is nevertheless proportional to heat treatment temperature.

As the treatment temperature increases to 600, 700 and 800 ℃, a sharp drop in isotopic fraction is observed, the magnitude of which increases with treatment time. This drop is predicted in the model as a result of a resistance to ion transfer across a material interface. Figure 5.4 looks at the 600-800 ℃ regime in isolation in order to further illustrate the magnitude changes in this drop. Without any quantitative analysis, the gap between the final point before the rapid decrease in isotopic fraction and the average level to which it drops noticeably increases with higher treatment temperature. This occurs even though the LSCF layer thicknesses between the three samples vary considerably. There is also a noticeable change in surface concentration, particularly when comparing the 600 and 700 ℃ samples. This is due to a shift in the surface exchange coefficient which will be discussed later.

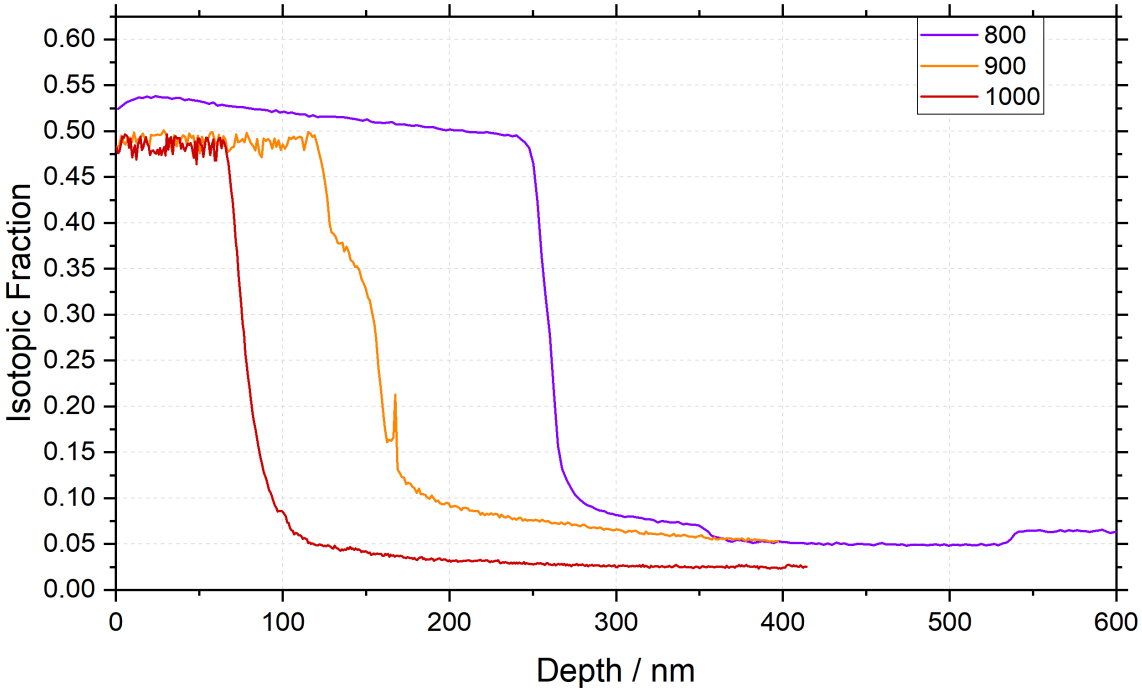

Figure 5.5: Isotope fraction graphs of the LSCF-YSZ PLD samples heat treated at temperatures of 800 ℃ and higher before isotope exchange. It can be observed that the interface drop does not increase significantly in magnitude beyond 900 ℃. In this range, the bulk isotopic fraction is low enough to be near the background concentration of ^{18}O, indicating a strong interface blocking effect. Each profile was obtained from a separate physical sample piece, which is why the LSCF layer thicknesses vary.

While the heat treatment up to 800 degrees results in an observable trend, the temperatures higher than this are less clear. This is shown in Figure 5.5, which compares the samples treated at 800, 900 and 1000 degrees. While some slight variations can be observed, and the thicker LSCF layer of the 800 ℃ sample yields slightly different behaviour, it is difficult to decisively determine an increase in the magnitude of the interface drop. All samples show surface concentrations of a similar value, which also holds true for the bulk concentration going into the YSZ substrate. Without doing any quantitative

analysis or fitting, this already suggests that 800 ℃ heat treatment represents a plateau point for interfacial resistance after which steady quantitative increases appear unlikely. In order to further investigate the behaviour of these samples and quantify the interfacial resistance, the data is fitted to the interface resistance model described in Chapter 2.

5.2.4 Fitting with Interface Resistance Model

The TraceX software, which was previously developed to fit single material and back exchange data from isotope exchange experiments [5] was adapted to enable fitting multi-layer material data that includes interfacial resistance, r. While for these conventional data sets it is possible to use the integrated fitting function, which uses *fminsearch* to find the variables that produce the minimum squared difference between the data and the fitted curve, manual adjustment of the parameters was used in most cases. This is due to two main features in most datasets that are illustrated in Figure 5.6.

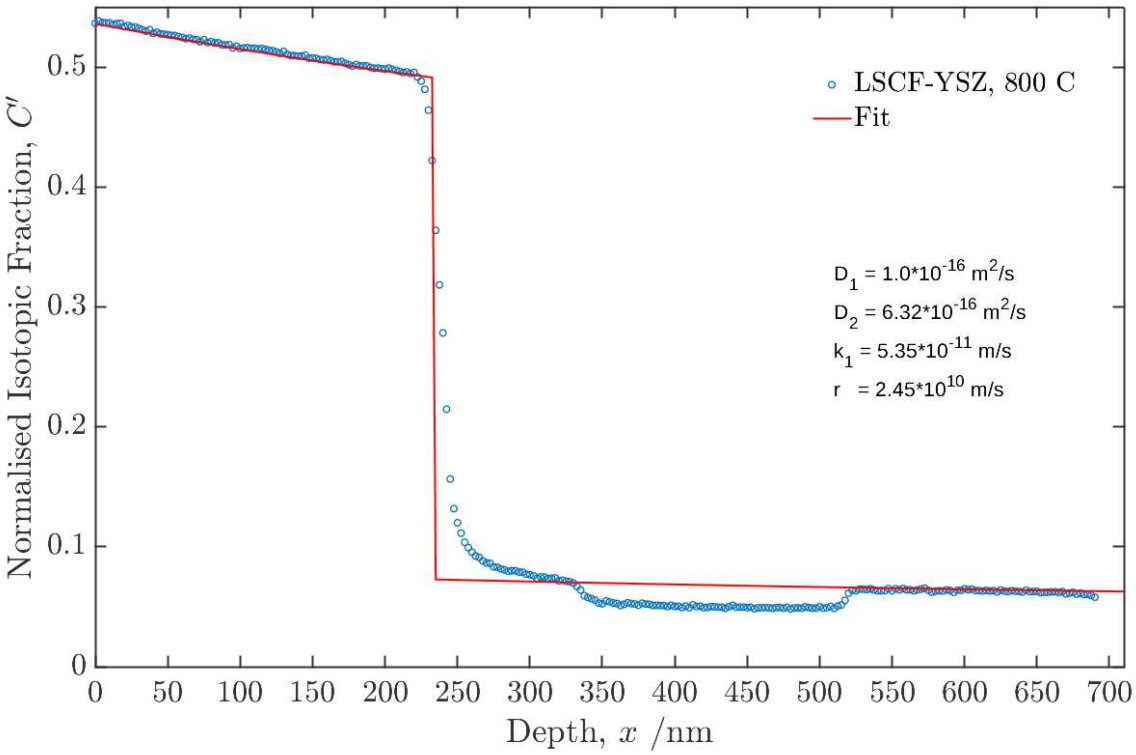

Figure 5.6: Fit of the LSCF-YSZ multi-layer sample that was heat treated at 800 ℃ obtained from the code that incorporated the multi-layer model with an interface resistance parameter. The values indicated on the rightmost part of the figure show the material properties obtained by the fitting algorithm, including the diffusion coefficients of each layer.

The first noticeable feature is that the interface itself is not perfectly sharp, but rather a region extending over several nanometers. The width of this interface will be studied in more detail in the following section. The main issue this feature presents with fitting the data is that the drop with a lower gradient in isotopic fraction cannot be captured by the sharp drop written into the model. For this reason, the interface drop was always set at the first point that deviates from the mean fit of the first layer.

The second reason why manual adjustment of the fitting values was necessary is due to artefacts in the data, particularly the YSZ layer, creating irregular patterns that the fitting algorithm struggles to account for. An attempt was made during the fitting process to represent the overall trend of the isotopic fraction in the second layer as accurately as possible. An example of this challenge is illustrated in Figure 5.6, where a peculiar dip in isotopic fraction in the YSZ bulk is present. The causes of this artefact will be discussed further at a later stage. Regardless of the mechanism causing this behaviour, it creates a section of the data that deviates in an irregular way from the profile that can be simulated with the model. Running the fminsearch algorithm on this data and the model would not make it possible to minimise the difference between them gradually through the adjustment of fitting parameters. In other words, the algorithm doesn't aim to capture the overall profile as appears reasonable, but purely on a mathematical basis. In the data seen in Figure 5.6, the algorithm tries to fit the dip in isotopic fraction as well, and will aim for fitting parameters that minimise the difference on this basis. Since the model cannot capture these irregular features, the other fitting parameters will also not be optimised. For this reason, a fit that captures the overall behaviour of the profile, including the bulk diffusion shape, has to be created through manual fitting.

Fitting Error

The accuracy of the values obtained from the fit shown in Figure 5.6 can be investigated using the fitting software, by changing each variable and observing the effect on the fit. This means looking at key indicators in the profile that can act as boundaries for acceptable values. These indicators include capturing the first layer's gradient and surface position properly, as well as the second layer's bulk concentration. Starting with the interface resistance, the variability is shown in Figure 5.7.

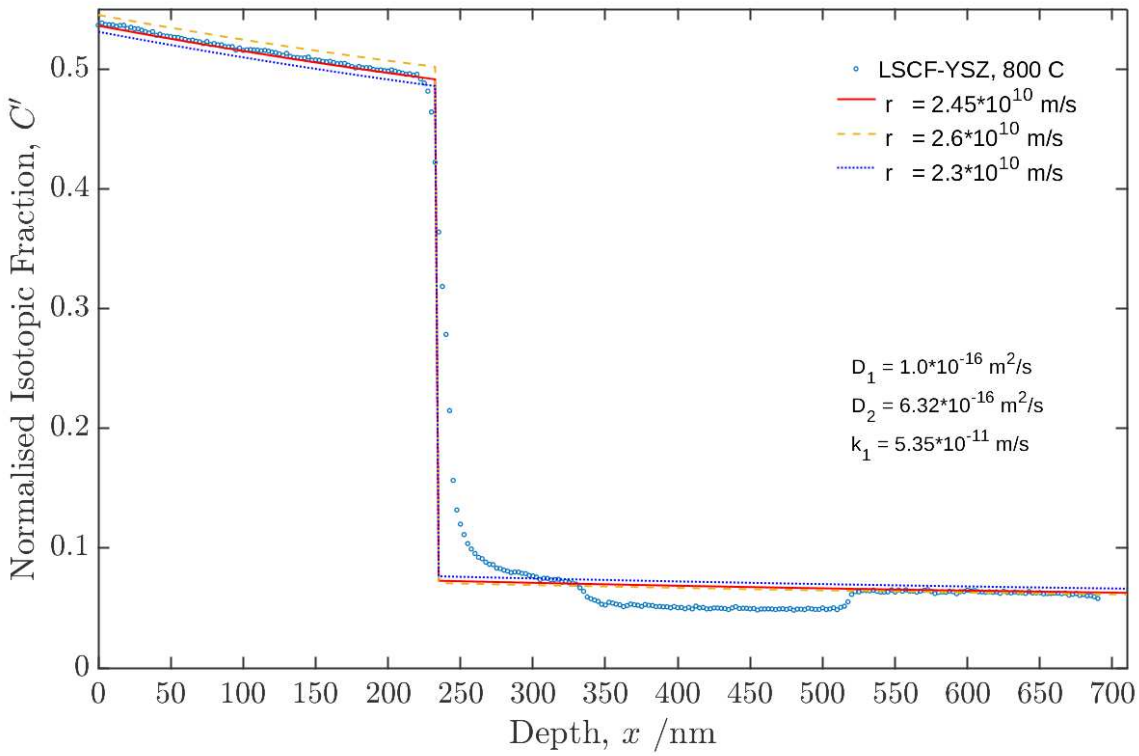

Figure 5.7: Variation in the fitting curve resulting from changing the interface resistance r while keeping all other values constant. A change in r of $0.15 * 10^{10}$ changes the curve such that the fit is no longer accurately capturing the shape of the data. This determines an approximate error range for the accuracy of the fitting algorithm when calculating the interface resistance parameter.

This test reveals a relatively narrow window of variability - only considering the change in r, the fit is accurate to within less than $\pm 0.15 \times 10^{10}$ s/m. This is because r directly influences the size of the interface drop, making it quickly too small or too large such that the rest of the curve no longer accurately captures the data. Here it has to be considered that the surface exchange coefficient k is directly related to the isotope fraction at the surface, and subsequently the whole profile. This means that an increase in r, which would shift the surface concentration to a higher point, can be balanced out by decreasing k. This means the total window of possible windows for both k and r is larger than if each variable is varied individually while fixing all others.

This fact makes it worth studying the relationship between the variables more closely, as shown in Figure 5.8. As can be observed, the interface resistance can be varied to a slightly larger degree when the surface exchange coefficient is varied in tandem to produce an accurate fit. Fitting the first layer's shape in particular remains possible due to the counteracting effects of the variables. However, this exercise shows the inherent connectivity of the whole profile across the entire sample with its

multiple layers through the decreasing fit quality in the second layer.

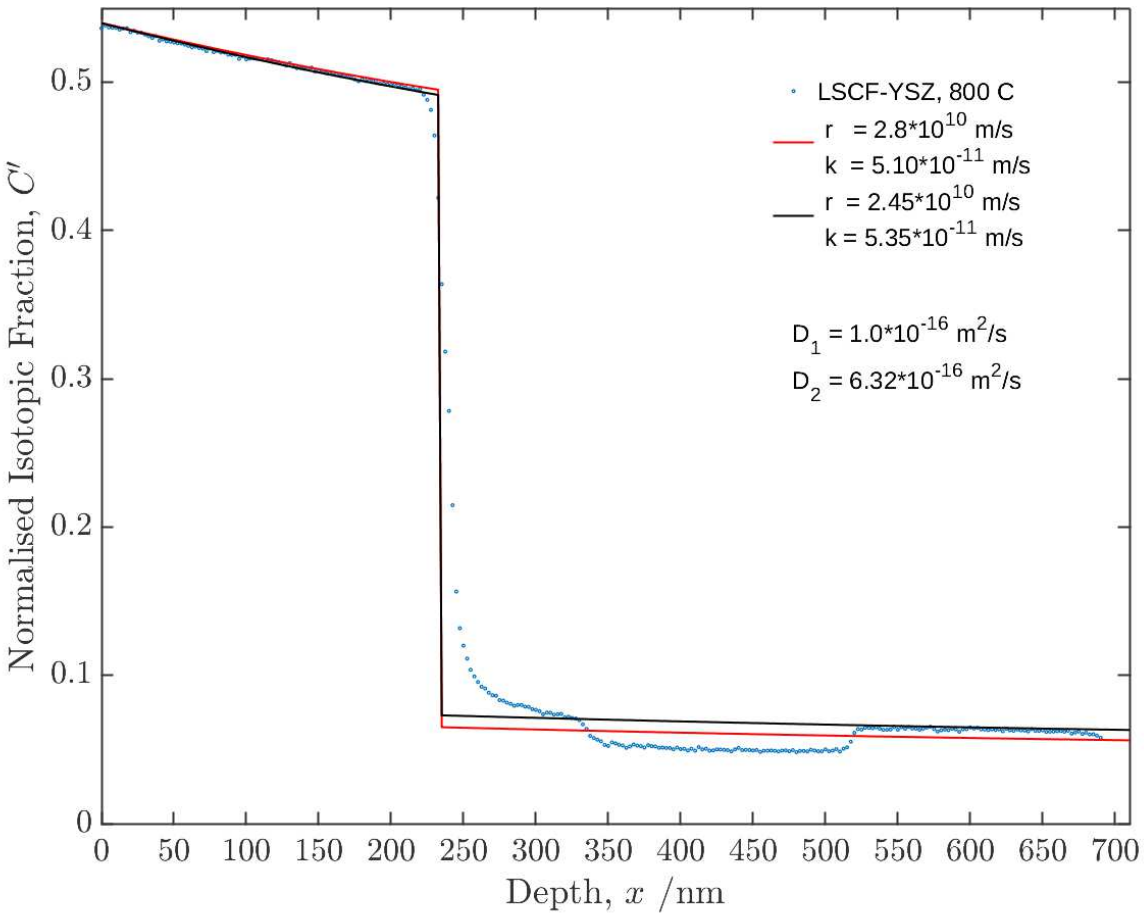

Figure 5.8: Variation in the fitting curve resulting from changing the interface resistance r and the surface exchange coefficient k^* simultaneously, with the goal of trying to keep the fit to the data as accurately as possible. While fitting the first layer remains possible with many combinations of values, the accuracy of the second layer's fit diminishes. This further illustrates the manner in which the interface resistance parameter captures the magnitude of the drop in isotopic fraction at the interface with high levels of accuracy.

Even if r can be increased up to 2.8×10^{10} s/m with a corresponding decrease in k^*, the fit in the second layer is no longer accurate. This happens because the resistance to transfer across the interface is higher, reducing the amount of oxygen that can diffuse through. Without varying k^*, this would also result in a higher surface concentration, as the isotope is 'backed up' to the first layer by the higher interface resistance. If the surface exchange ability is slightly reduced in such a scenario, the surface concentration lowers, but the ability to transfer across the interface remains low, resulting in the curve we see in Figure 5.8. This gives a roughly defined boundary for the accuracy of fit for both r and k^*. Doing similar investigations for the tracer diffusion coefficient of each layer, D_1 and D_2, produces ranges of accuracy for the fit, as shown in Figures 5.9 and 5.10.

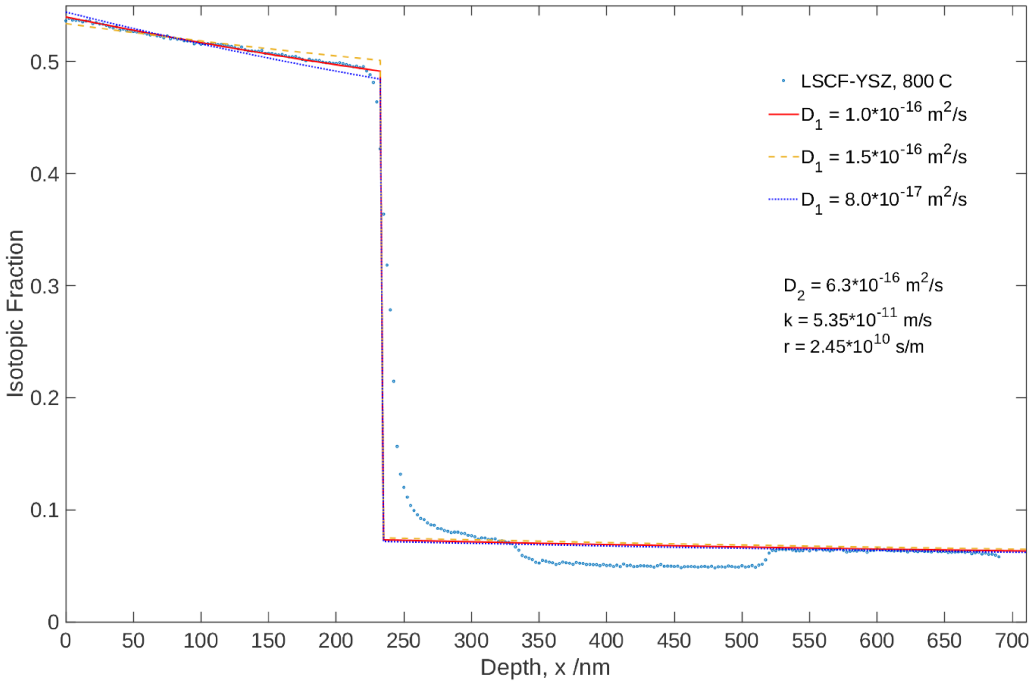

Figure 5.9: Variation in the fitting curve resulting from changing the diffusion coefficient of the first layer (LSCF) D_1 while keeping all other variables constant. It can be seen that D_1 influences the gradient of the first layer's diffusion profile, which enables fitting to a degree of accuracy that is well below a full order of magnitude.

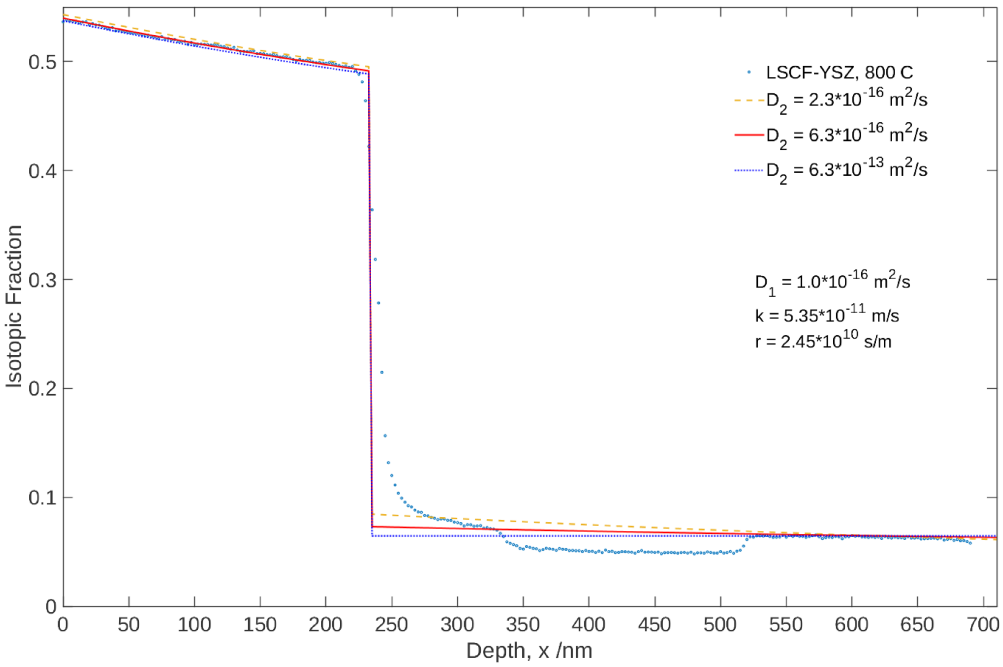

Figure 5.10: Variation in the fitting curve resulting from changing the diffusion coefficient of the second layer (YSZ) D_2 while keeping all other variables constant. D_2 determines the gradient of the curve in the bulk component of the multi-layer. Since the diffusion profile is nearly horizontal, implying fast diffusion, the accuracy of the value for D_2 is less clear on the upper bound. This means that D_2 can be increased by multiple orders of magnitude with small visible changes to the profile shape

The first layer's diffusion coefficient D_1 influences the gradient of the diffusion profile in the LSCF layer. Since this gradient is usually well-defined, the fit for D_1 can be considered to be reasonably accurate, as can be seen by the variation in values being within a narrow window. This is in contrast to D_2, where the upper bound particularly is difficult to clearly define. In a good oxygen conductor such as YSZ at 460 ℃, fast diffusion is expected into a semi-infinite bulk, creating a nearly horizontal profile shape. While there are subtle further decreases in bulk fraction gradient as D_2 increases, Figure 5.10 shows that even a jump over three orders of magnitude to 10^{-13} m^2/s only subtly changes the shape of the overall fit. The lower bound is easier to define, as a gradual reduction in D_2 will move the curve away from a flat horizontal shape and towards a shape more similar to a conventional diffusion profile. The value for D_2 that was ultimately chosen tracks the profile in the bulk the most closely, matching up from about 300 nm onwards. The region prior to this can be considered to be part of the extended interface area, and therefore difficult to model accurately with this method.

The results of these error analyses are summarised in Table 5.1. They show that while there is some variation in the values that result in an appropriate fit of the data, such variation is generally contained within one order of magnitude at least and sometimes within a decimal place at best. Even though all of the variables interact and have an effect on the total profile, for each variable there is a range of values that could produce a fit that captures the data. Values outside of this range will not be able to capture the profile shape even if all the other variables are adjusted to account for this.

Table 5.1: Table compiling the upper and lower bounds of each variable that is relevant during the fitting of experimental multi-layer IEDP data. The bounds are determined by changing the target variable, keeping all others constant.

Variable	$D_1(m^2/s)$	$D_2(m^2/s)$	$k(m/s)$	$r(s/m)$
Best Fit	$1*10^{-16}$	$6.3*10^{-16}$	$5.35*10^{-11}$	$2.45*10^{10}$
Upper Error	$1.5*10^{-16}$	-	$5.45*10^{-11}$	$2.7*10^{10}$
Lower Error	$8*10^{-17}$	$2.3*10^{-16}$	$5.10*10^{-11}$	$2.3*10^{10}$

For the fitting of diffusion coefficients, values within the same order of magnitude can be considered typical, due to the significant variation that can occur due to varying experimental conditions as well as slight changes in material stoichiometry and other properties. This method is extended to the other samples; all of the fits using the interface resistance model are shown in Figures 5.11-5.16.

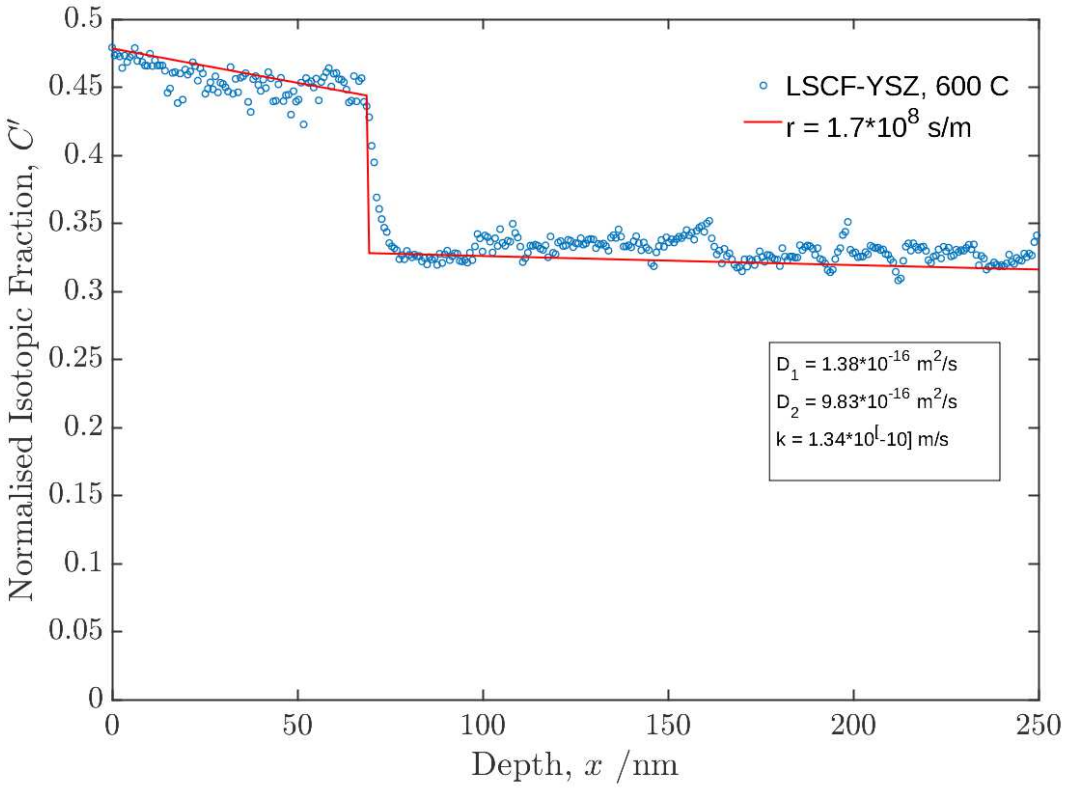

Figure 5.11: Interface resistance model fit of the isotope exchange depth profile data obtained from a LSCF-YSZ multilayer sample annealed at 600 ℃ before exchange.

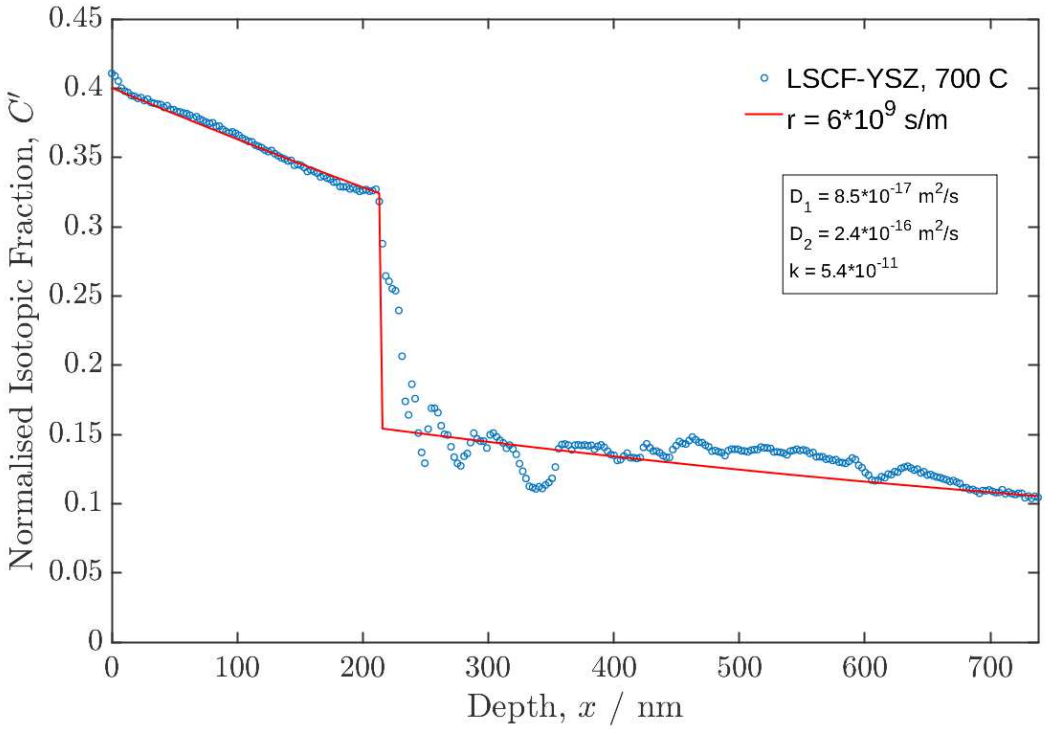

Figure 5.12: Interface resistance model fit of the isotope exchange depth profile data obtained from a LSCF-YSZ multilayer sample annealed at 700 ℃ before exchange.

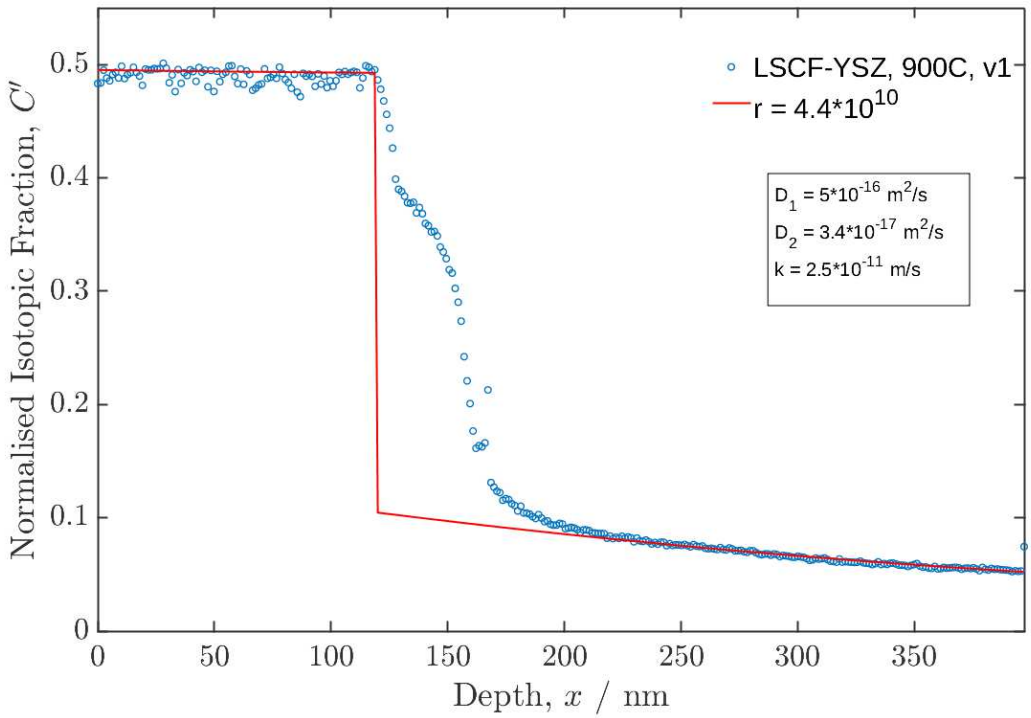

Figure 5.13: Interface resistance model fit of the isotope exchange depth profile data obtained from a LSCF-YSZ multilayer sample annealed at 900 ℃ before exchange.

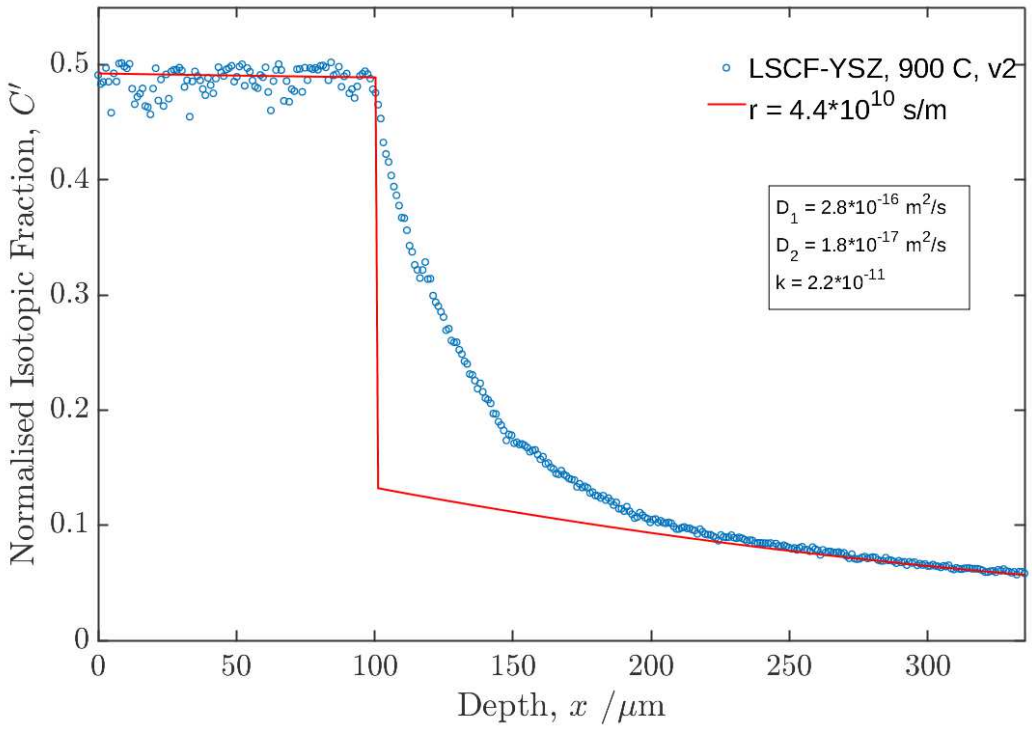

Figure 5.14: Interface resistance model fit of the isotope exchange depth profile data obtained from a LSCF-YSZ multilayer sample annealed at 900 ℃ before exchange. Note that this profile was obtained from a different sample than the previous 900 ℃ sample.

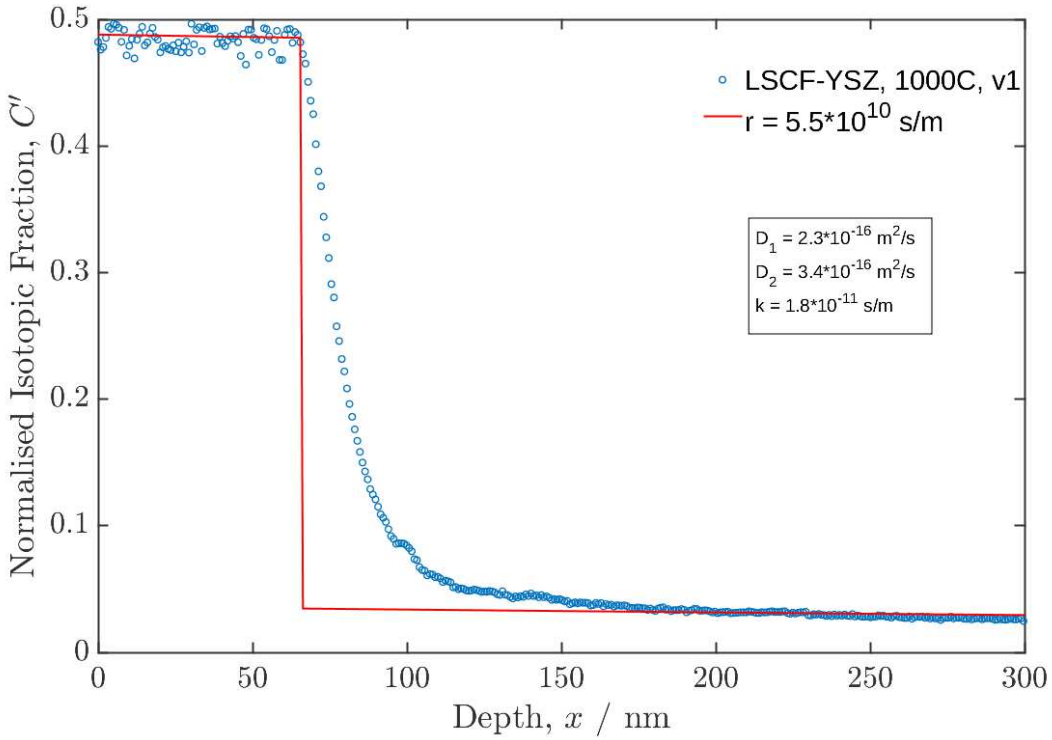

Figure 5.15: Interface resistance model fit of the isotope exchange depth profile data obtained from a LSCF-YSZ multilayer sample annealed at 1000 ℃ before exchange.

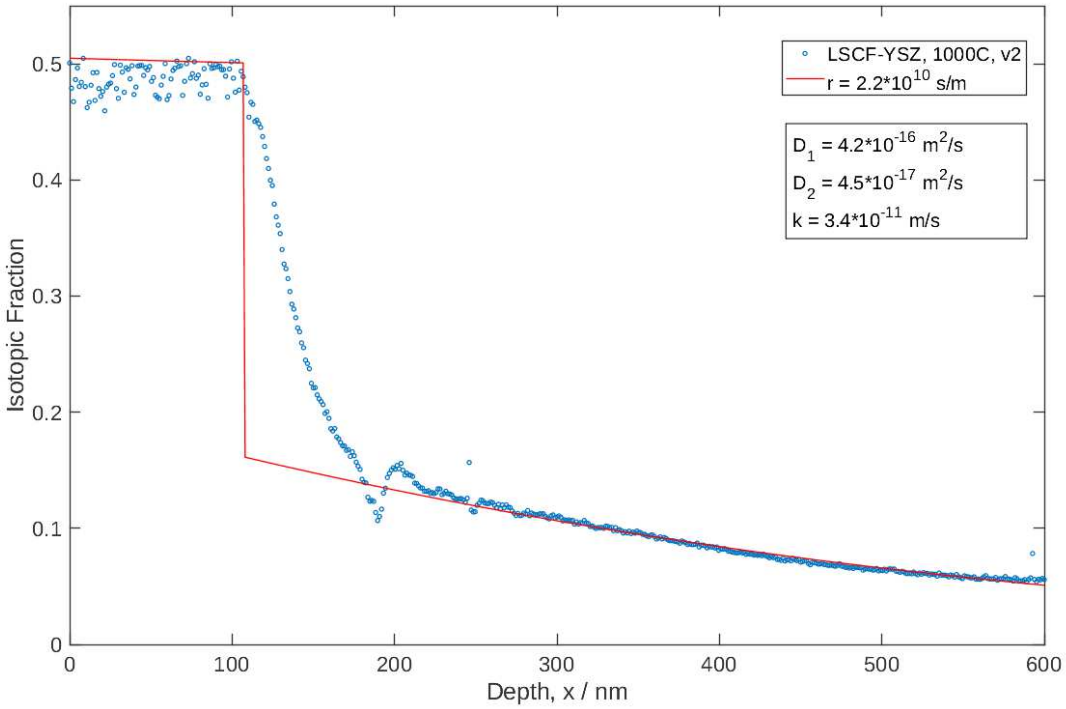

Figure 5.16: Interface resistance model fit of the isotope exchange depth profile data obtained from a LSCF-YSZ multilayer sample annealed at 1000 ℃ before exchange. Note that this profile was obtained from a different sample than the previous 1000 ℃ sample.

The SIMS data shows some irregular features that do not match the theoretical model description, particularly the fluctuation of isotope fraction around the bulk. This will be further discussed when looking at the ion signal data of other species. The fits also show significant broadening of the interface region at higher treatment temperatures. This broadening might be caused by an extended region of interdiffusion between LSCF and YSZ which might also form another phase. This is where some of the limitations of the interface resistance model become apparent. The assumption of a single step interface does not capture the behaviour of the data in the interface-adjacent region particularly accurately. The value of r does, however, enable fitting the overall shape of the profile. The generated curve in the first layer up until the interface and in the bulk generally follow the data. Furthermore, the magnitude of the interface drop corresponds closely to the value of r, as discussed earlier.

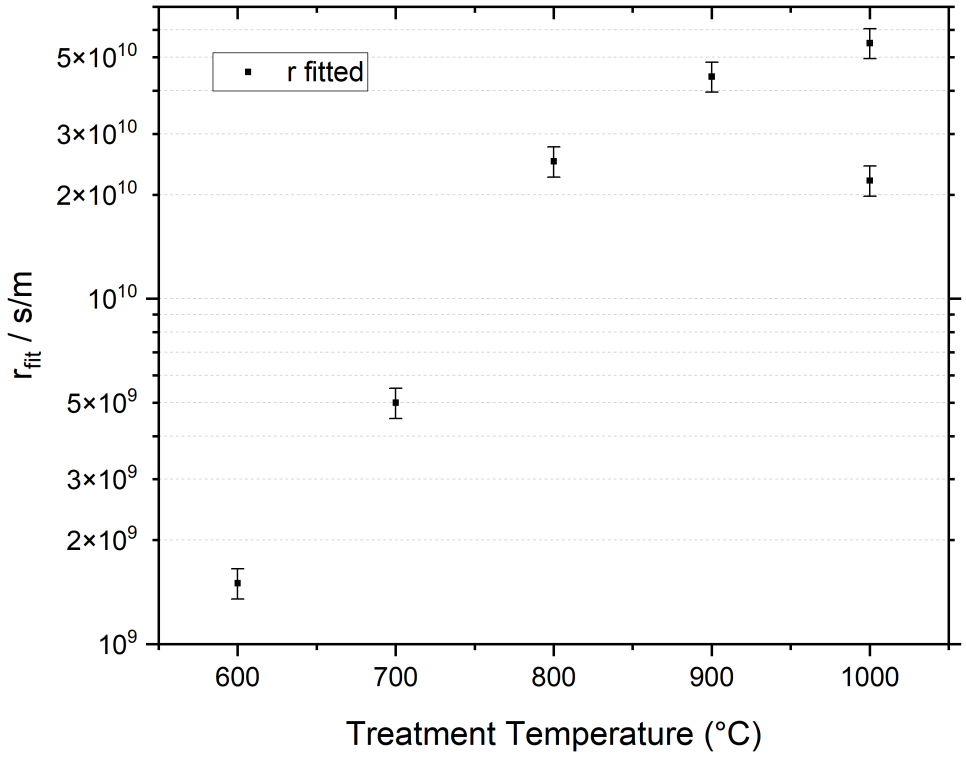

Figure 5.17: The value of the interface resistance parameter r obtained from the fitting of data obtained from LSCF-YSZ samples annealed at various temperatures.

Looking at the graph of the values of r as shown in Figure 5.17, the same trends that were qualitatively observed in the isotope exchange profiles can be seen. Between 600 and 900 ℃, a steady increase in r can be seen. The values at 900 ℃ are obtained from two different samples and remain consistent. This is in contrast to the samples treated at 1000 ℃, as they show unusually large variation. The profiles in Figures 5.15-5.16 illustrate where this difference originates, namely the larger magnitude

drop in Figure 5.15 which leads to a lower bulk concentration. Apart from this, the two profiles differ in LSCF thickness (around 65 nm vs around 100 nm) as well as interface width. In general, such differences in layer thickness to not significantly change the value of r given all other materials properties and experimental conditions are constant. Instead, the effect may originate from a physical effect in these particular samples that produced an interface region that is particularly good at blocking diffusion.

Despite some of the model's limitations becoming clear, the interface resistance parameter r nonetheless appears to be a useful parameter for quantifying the diffusion blocking effect at the LSCF-YSZ interface. It also becomes clear that further analysis of the physical mechanisms in the interface region is necessary.

5.2.5 Ion Signals

The previous section analysed the isotopic fraction properties of the series of samples, studying the behaviour of oxygen in particular. In these profiles, inconsistencies in the overall appearance of the data emerge, particularly in the signals around the interface region and in the bulk. In order to further analyse how representative the data is for quantitative analysis and what it can reveal about the sample conditions, the signals of other ion species obtained from the same SIMS depth profile can be studied.

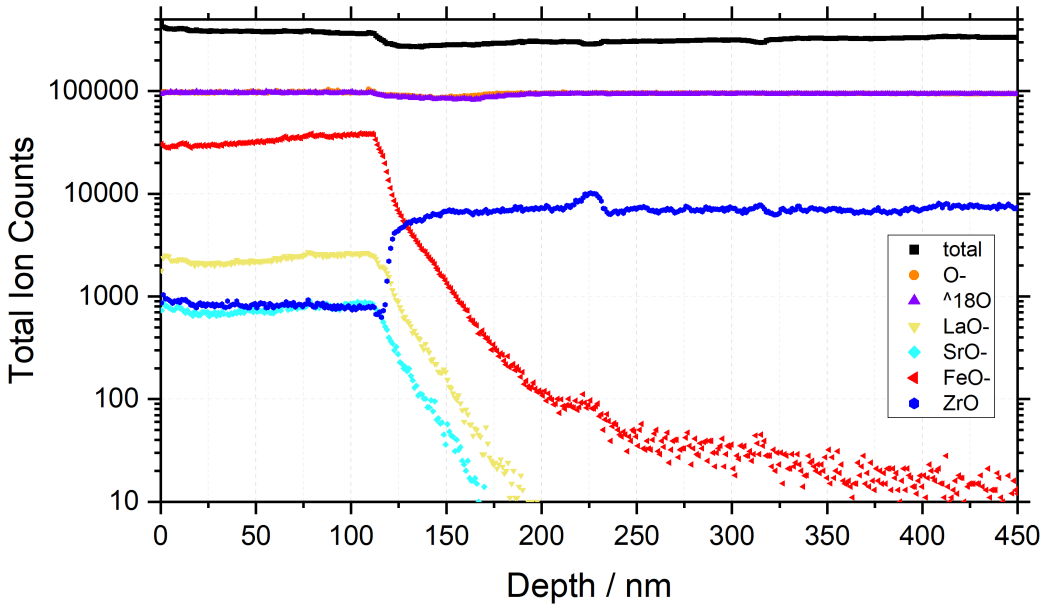

Figure 5.18: Signals of various ion species obtained from a LSCF-YSZ PLD multi-layer sample with **no further heat treatment** by SIMS depth profiling. The SIMS is set to obtain negatively charged ions from the sample, as this gives the best data quality for oxygen, the main species. Keeping in mind that the ion counts are on a logarithmic scale, the species associated with LSCF diminish sharply around the same area that the ZrO from the YSZ substrate emerges, pinpointing the interface region between the two layers.

Figure 5.18 shows the ion signal of the sample that did not undergo any additional heat treatment. LaO, SrO and FeO are the signals originating from the LSCF layer, the ZrO and YO signals from the YSZ substrate. These ion signals are a useful way of discerning the layers from each other, as well as what the transition region between the two looks like. This can be seen in the sharp drop-off in the FeO signal in particular, happening in conjunction with the rise of the ZrO signal. The first notable feature can be discerned from the total ion counts, which show a sudden drop-off around the interface region. This could be explained by the insulating properties of YSZ as well as the different ion sputtering properties that YSZ and LSCF have.

Since YSZ is an insulator, it can undergo charging from the ion beam during the sputtering process. This can affect the overall ion yield, as the local charge buildup can divert the ion beams and prevent the collection of some signals. This effect is normally mitigated by the application of an electron flood gun that compensates charge buildup on the surface. However, each material has different properties and correspondingly needs a different amount of charge compensation. When the analysis beam reaches the transition region between LSCF and YSZ, the flood gun settings might not be optimised anymore. This could explain the drop in total ion counts observed starting at the interface and continuing into the YSZ layer, as well as the fluctuations observed in the individual ion counts.

The ion yield of a given species depends on the Relative Sensitivity Factor (RSF) of a species, which differs depending on whether positive or negative ions are collected [6][7]. All of the measurements in this project were made using a negative ion setup. In this regime, iron and zirconium have a lower RSF than strontium and lanthanum, which results in a higher ion yield. This can also be observed in the total ion count trends between these species. The buildup of charge as well as the different RSFs for each species could explain the quality variation of the data. As the sputtering crater gets deepened by the ion beam, effects other than the sputtering of secondary ions might occur. There could be intermixing, where the sputtering beam moves species around instead of removing them from the lattice. Another effect that can occur is redeposition, where some of the secondary ions that get removed from the sample do not make it to the detector, but rather 're-deposit' in a different area on the sample. All of these effects can influence the ion signals.

The interface region, while relatively sharp, does contain a few data points within it that could suggest a broader region with multiple ion species that underwent diffusion. No additional heat treatment was done to this sample, but it still experienced exposure to high temperatures during

deposition and exchange. The exchange temperature was set to 460 ℃, which may be below the activation energy for diffusion, but the long duration of this exposure during the pre-annealing process in particular (12-20 hours) could play a role. The substrate temperature during PLD deposition is 600 ℃, which is needed for the LSCF to properly densify. The layer is grown for a period of 30 minutes, followed by a relaxation period of 10 minutes, and then cooled down under ambient conditions, rather than through quenching. This means that the sample is exposed to temperatures between 550-600 ℃ for a period of at least an hour, making it possible for some interdiffusion to happen during this time.

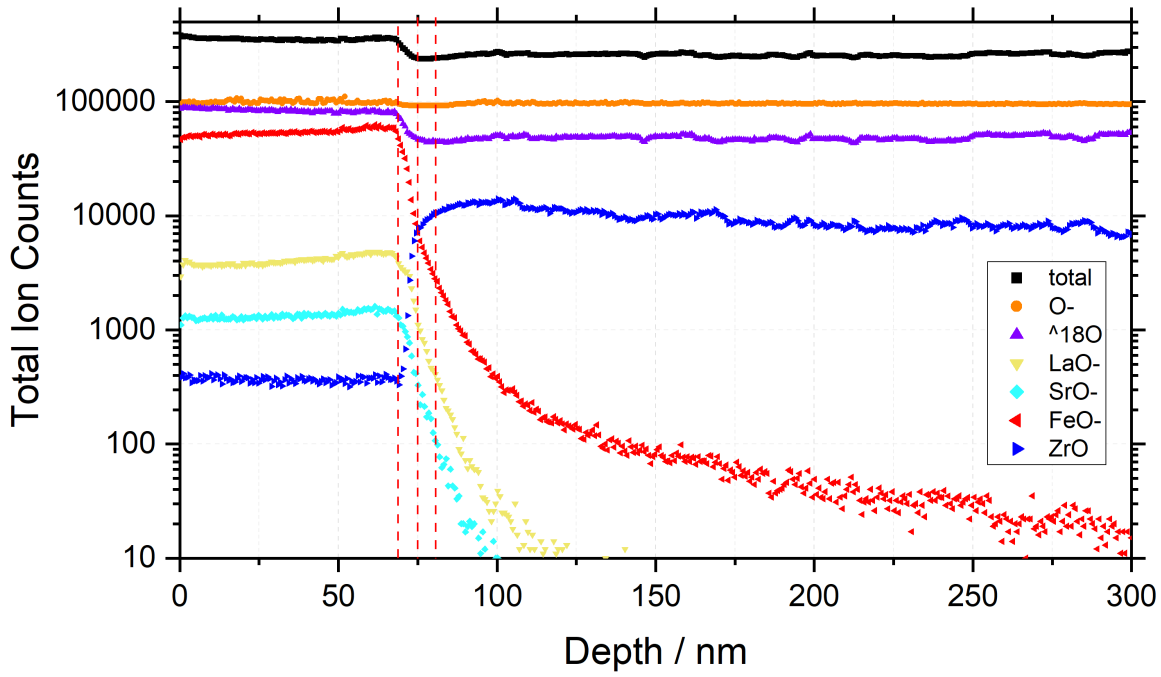

Figure 5.19: Signals of various ion species obtained from a LSCF-YSZ PLD multi-layer sample heat treated at **600 ℃**. In addition to the interface location being shown by the characteristic species, the emergence of a drop in isotope fraction can be discerned from the sharp drop in ^{18}O ion counts around the interface area.

Figure 5.19 shows the data obtained from the sample that was heat treated at 600 ℃. The same features as noted previously appear, mainly the slight drop-off in the total ion counts at the interface, as well as the sharp delineation of the interface region through the FeO and ZrO signals. Given the inconsistent nature of the isotope exchange curve shape as seen in Figure 5.4, it is worth examining the relationship between the total ion counts and the individual ion signals. Some artefacts (such as sudden spikes or dips in the data) translate directly from the total ion counts, excluding explanations that could potentially be related to the specific signal. These variations in the total ion counts are likely due to the charge buildup effects and variations in sensitivity factors as mentioned earlier.

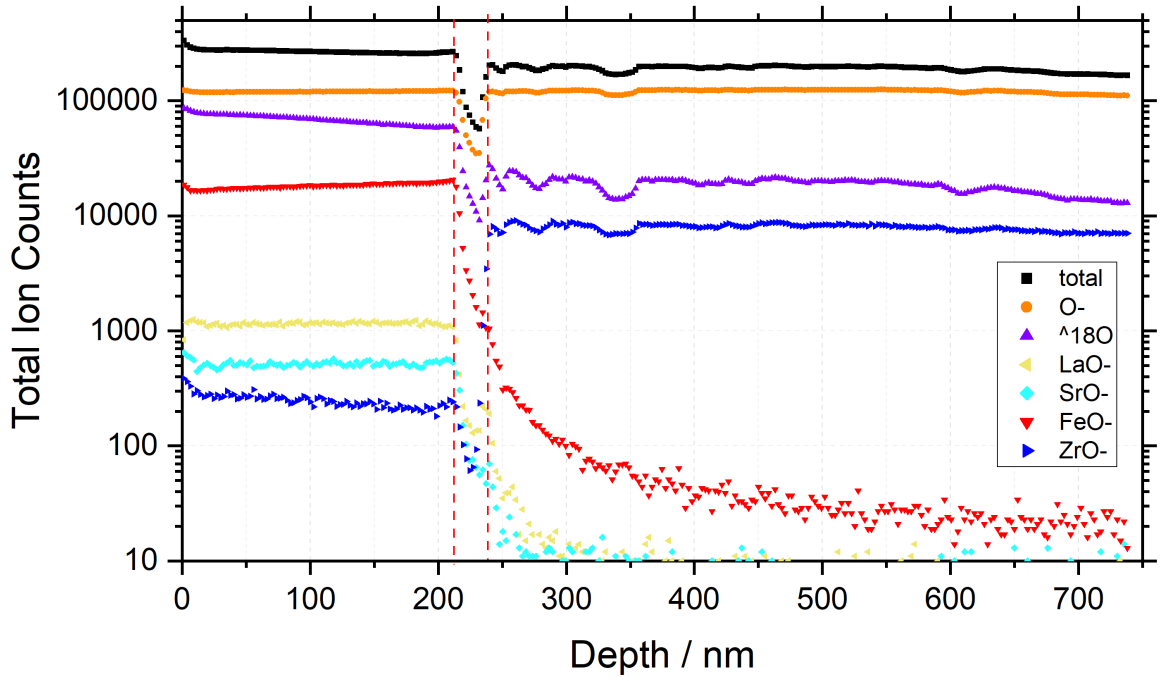

Figure 5.20: Signals of various ion species obtained from a LSCF-YSZ PLD multi-layer sample heat treated at **700 °C**. In addition to the same interface transition information from the previous samples, this data shows the way in which the shape of the individual ion counts mirror that of the total ion counts, enabling the distinction between artefacts related to the ion species and artefacts originating from the physical sample itself.

The sample treated at 700 °C also shows a total ion count dip at the interface, as well as various artefacts in the bulk that can be seen in the isotope exchange profile data. One further explanation for some of these features could be a degree of microporosity in the substrate. If the ion beam sputters through to an area that contains such a micropore, the total amount of signal that could be obtained would reduce due to the lower amount of overall sputterable material. As the depth profile continues, these sections of density variations come and go, resulting in an overall profile with a clear trend, but variation within it. If these artefacts were related to the sputterability of individual compounds within the material, they would likely not be mirrored by all the other species in the same way.

In the interface region of this sample, a larger interface width compared to the previous samples can be observed. The ion signals from this sample are sharp and contain less uncertainty with regards to the position at which the FeO signal ends and the ZrO signal begins. This is a preliminary indicator of the development of an interface region that was formed through cation interdiffusion, as well as the potential formation of reaction products.

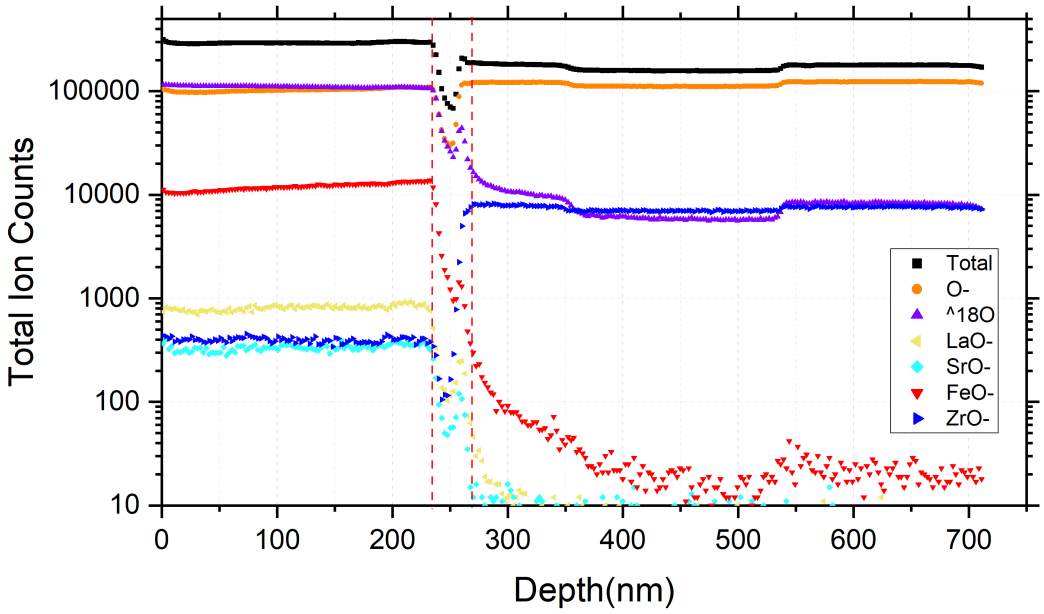

Figure 5.21: Signals of various ion species obtained from a LSCF-YSZ PLD multi-layer sample heat treated at **800 ℃**. The dip in bulk isotopic fraction is mirrored in the total ion counts, indicating that this feature is a result of a locally lower ion yield in the bulk pellet as that point of the depth profile is reached.

Similar to the sample treated at 700 ℃, the ion signals in Figure 5.21 show a total ion count dip at the interface as well as a variation in the bulk of the YSZ that follows an overall trend, potentially explained by a variation in density. The interface width appears to be slightly bigger than the samples heat treated at lower temperatures, which would be consistent with a greater amount of cation diffusion enabled by higher energy availability. This sample in particular shows a relatively smooth ion count curve in the bulk, with little fluctuation. This appears to further indicate that the fluctuations do not originate from an intrinsic electronic property of YSZ relating to its response to the ion beam, but rather from the physical and microstructural properties. This is plausible, as the substrates were fabricated using powder pressing and sintering without the availability of an isostatic press. This makes it possible for local variations in sintering quality and associated micropores or other features.

Figures 5.22-5.25 show the ion signal data obtained from the two samples each heat treated at 900 ℃ and 1000 ℃, respectively.

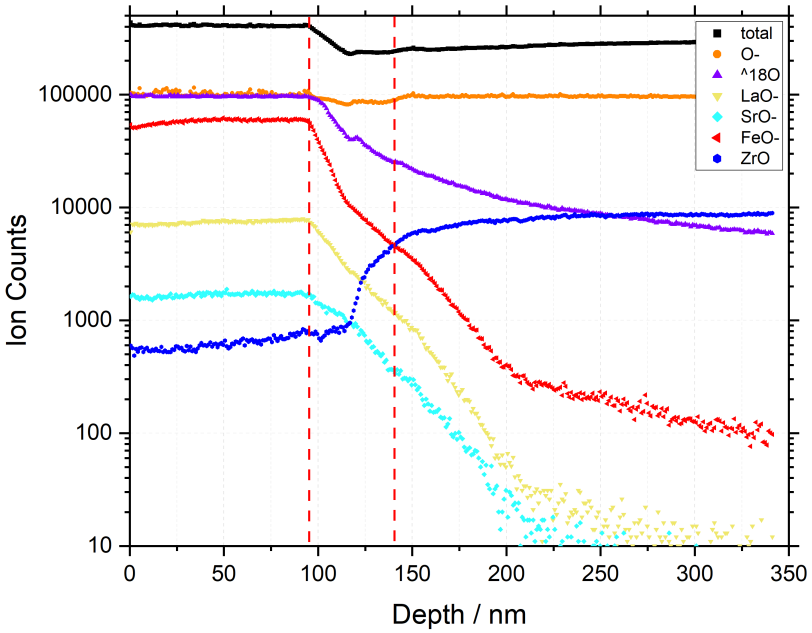

Figure 5.22: Signals of various ion species obtained from the first LSCF-YSZ PLD multi-layer sample heat treated at **900 °C**. The interface region here is extended compared to the previous samples that were heat treated at lower temperatures. It also contains artifacts and features of inconclusive origin, showing the increased complexity of the interface region at higher treatment temperatures.

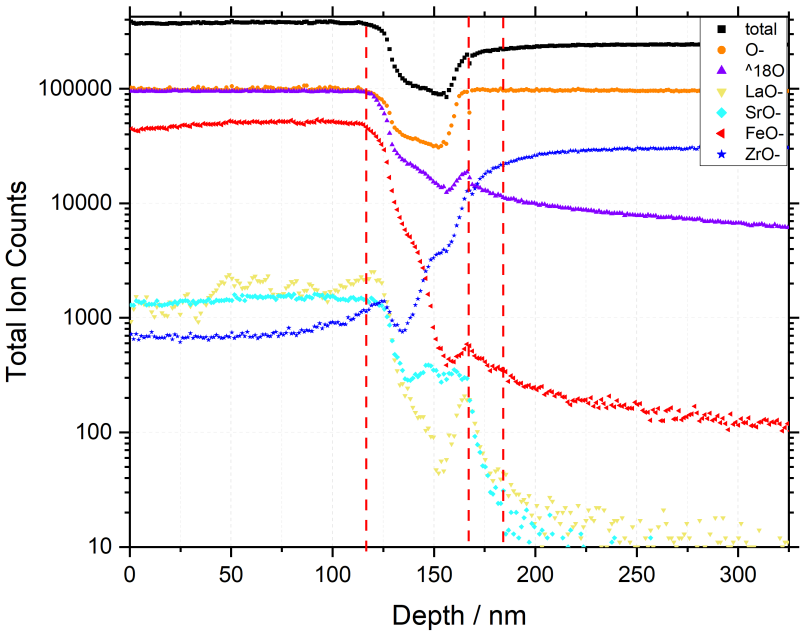

Figure 5.23: Signals of various ion species obtained from the second LSCF-YSZ PLD multi-layer sample heat treated at **900 °C**. Similarly, the interface region is extended and contains different features. While some of them follow the shape of the total ion count curve, others, such as FeO and ZrO, do not. This might indicate a combination of measurement artifacts due to sample quality and the expression of a more intermixed interface region due to high annealing temperatures.

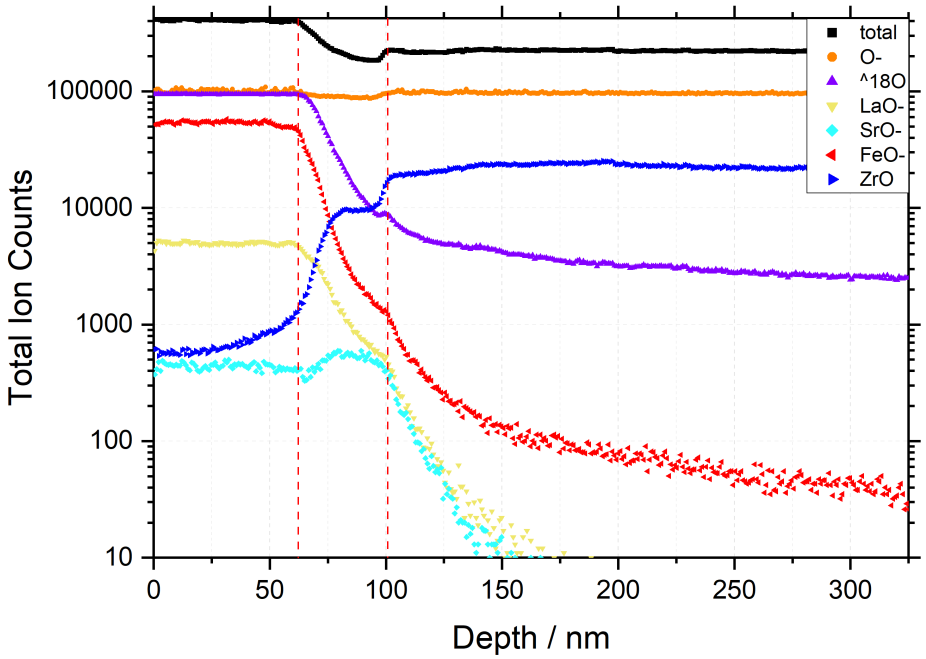

Figure 5.24: Signals of various ion species obtained from the first LSCF-YSZ PLD multi-layer sample heat treated at **1000 °C**. A notable feature that is different from other samples is the slight spike in SrO counts in the interface region, which runs counter to the total ion counts. This might either indicate measurement artifacts or a buildup of strontium in the interface.

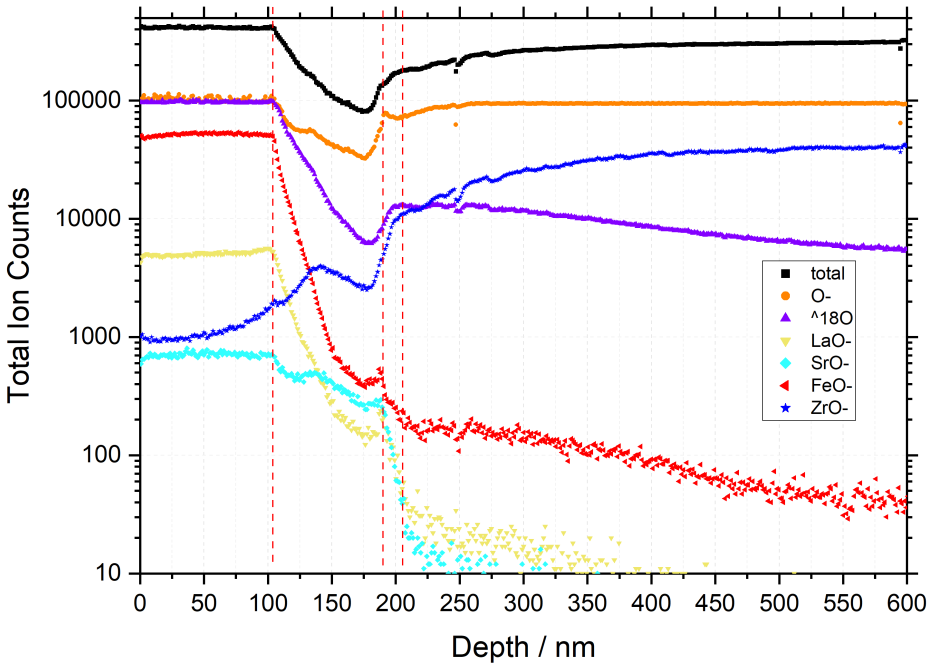

Figure 5.25: Signals of various ion species obtained from the second LSCF-YSZ PLD multi-layer sample heat treated at **1000 °C**, distinct from the previous sample treated at the same temperature. The total ion counts are slightly less consistent compared to other samples, particularly in the bulk region, where they increase steadily until plateauing at around 300-400 nm. This may indicate that the substrate pellet's fabrication quality is lower compared to other samples.

The two samples treated at 900 ℃ show a similar size of the interface region, indicating a broad region of intermixing, as can already be partially deduced from the isotope exchange depth profiles. The first sample treated at 900 ℃ shown in Figure 5.22 shows a relatively smooth drop in ion concentration. The ZrO profile in particular shows a gradual buildup moving away from the interface region, making it difficult to estimate at which point the bulk concentration is convincingly reached. The main distinguishing feature of the other sample treated at 900 ℃ shown in Figure 5.23 is that the interface region itself shows some plateaus and peaks in various ion signals. This variation reflects in the isotopic fraction profile shown in Figure 5.13. While these could potentially be used to identify variations between different species that could be indicative of reaction products, the resolution of the SIMS and the abundance of other possible explanations make this less feasible.

Both samples treated at 1000 ℃ show a wide interface region, as well as some feature variation within the interface region can be observed. The first sample shown in Figure 5.24 contains a peculiar spike in the SrO sample and a plateau in the ZrO signal. Similar features are observed in the other sample shown in Figure 5.25, however given the general uncertainty regarding the shape of the signal in the interface region, it is not reasonable to assume these signals are indicative of any physical mechanism.
Both these samples and the ones treated at 900 ℃ show extended interface regions, while the thickness of the LSCF layer in most cases appears lower than the samples heat treated below these temperatures. This could partially be explained by an uneven thickness of the PLD layer during deposition, creating some variation within the samples. Another plausible mechanism would be the formation of an interlayer that has both reaction products and general species intermixing. Such a layer would reduce the thickness of the LSCF itself relative to the time before heat treatment, explaining why none of the high-temperature samples appear to be close to 200 nm in thickness.

The ion signals shown in this section give some further insight into the behaviour of the samples. Firstly, they provide a method of determining the thickness of the LSCF layer as well as the interface region to some level of precision. They also illustrate the effect of sputtering through multiple layers that respond differently to the incident ion beam, most notably in the dip in total ion counts around the interface region, The variation in total counts in particular has a knock-on effect that explains some of the peculiar fluctuation features seen in the IEDP data. It is noticeable that the fluctuations when observed only occur around the interface and in the YSZ bulk. This suggests that they are related to the substrate microstructure, while the LSCF layer is of reasonable density and quality to never show

an unusual fluctuation. Furthermore, the fact that some samples show no fluctuation while others do implies that this effect can be traced to the microstructure of the physical sample, rather than an intrinsic material property. Finally, the ion signals indicate the width of the interface region quantitatively, implying reactions and interdiffusion taking place at high temperatures. This also decreases the measured length of the LSCF layer. These effects merit a closer look at the concept of interface width.

Interface Width

The ion signals seem to indicate the formation of an extended interface region that progressively increases with higher treatment temperature. The values of interface width obtained from these, as indicated in the SIMS data, is summarised in Figure 5.26. This in principle is logical, as a higher temperature will provide more energy for interdiffusion and chemical reactions that might form new phases.

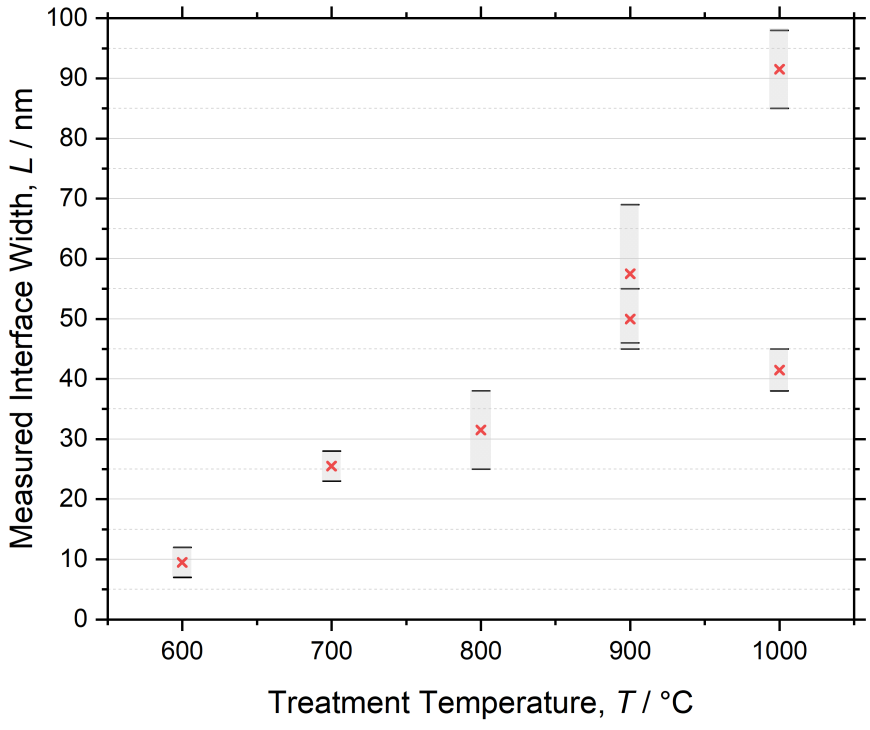

Figure 5.26: Width of the interface region derived from the SIMS data of FeO and ZrO species in a LSCF-YSZ multilayer sample, with associated errors.

This might suggest an effect on the interface resistance depending on the thickness of this intelayer region. While the interface resistance parameter might be able to quantitatively capture the effect this might have on the impedance to ion transport, it does not provide a mechanistic explanation for the

process. Therefore, it makes sense to fit the same isotope exchange data to a triple layer model, which assumes the formation of an interlayer of low diffusivity that progressively increases in thickness. The ion signals might help indicate an approximate value for this thickness, based on the FeO and ZrO signals and when they increase and diminish, and are summarised in Table 5.26.

5.2.6 Triple Layer Model Fit

The previous section discussed fitting the experimental data with the interface resistance model that only assumes a 1D structure that inhibits transport across it. In the following, the same data is fit with the triple layer model instead, describing the interface between LSCF and YSZ as a third layer with a defined thickness and diffusion coefficient. The results of one of these fits is shown in Figure 5.27.

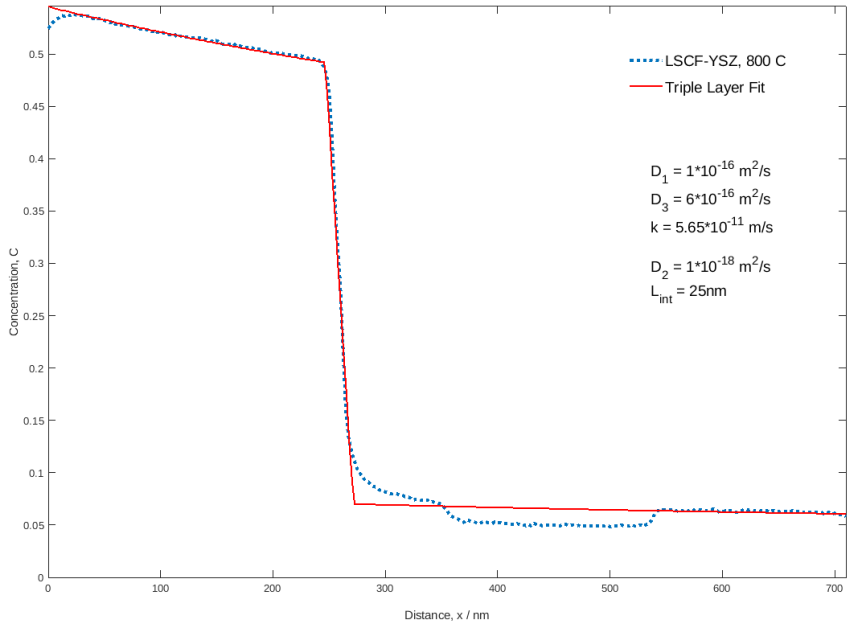

Figure 5.27: LSCF-YSZ PLD sample heat treated at 800 ℃ and fit using the triple layer model.

This result shows that the triple layer model is capable of fitting the data to a better degree of accuracy than the interface resistance model. By setting the interface diffusion coefficient to a value lower than that of each layer by two orders of magnitude, the transport within this layer is inhibited sufficiently to show a near-instantaneous drop. As already outlined in the model description chapter, the size of this drop is dependent on the thickness of the interlayer and its diffusion coefficient, making these two variable the ones determining the shape of the curve. Figures 6.9 and 6.10 show how the variation of each variable affects the overall shape of the curve and by consequence the fit to the

experimental data.

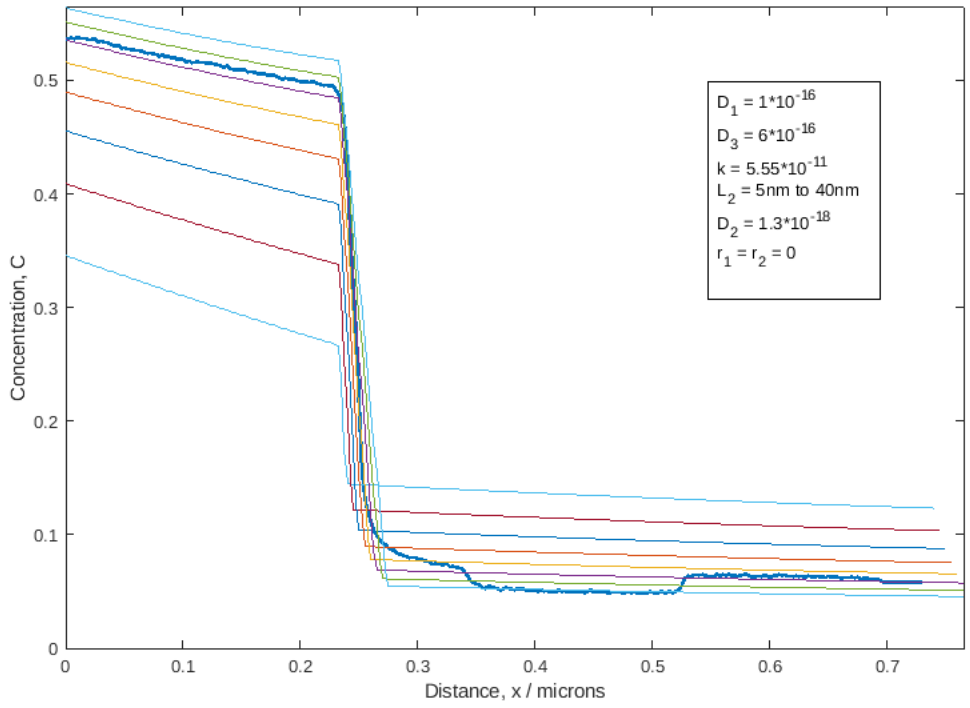

Figure 5.28: Triple Layer Fit of the LSCF-YSZ sample heat treated at 800 ℃ at a constant value of interlayer diffusion coefficient and a thickness varying from 5 to 40nm.

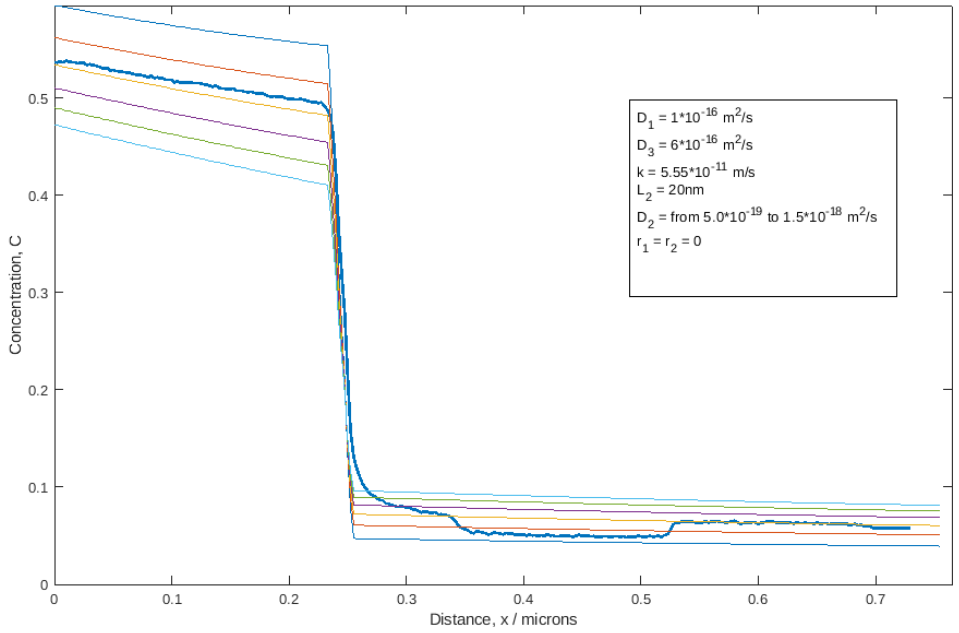

Figure 5.29: Triple Layer Fit of the LSCF-YSZ sample heat treated at 800 ℃ at a constant interlayer thickness of 20nm with a variety of diffusion coefficient values.

The changing diffusion coefficient at a constant thickness results in a significant change in the overall

curve shape. Given that the range of values includes about half an order of magnitude, this makes the accuracy of the diffusion coefficient at a given thickness similar to that of the interface resistance parameter r. Looking at the shape of the fits, a decreasing D_{int} will mean a larger interface drop without affecting other factors. This is in contrast to the simulations with increasing layer thickness. While the interface drop will increase in a similar manner, the thicker interlayer will also change the gradient of this drop. A thicker interlayer will slightly flatten the isotope fraction gradient.
Figure 5.30 investigates this phenomenon more closely. A set of $D_{int} - L_{int}$ combinations is chosen with the aim of fitting the data as accurately as possible, changing from 20 to 35nm in thickness. Each pair produces an interface drop with the same magnitude.

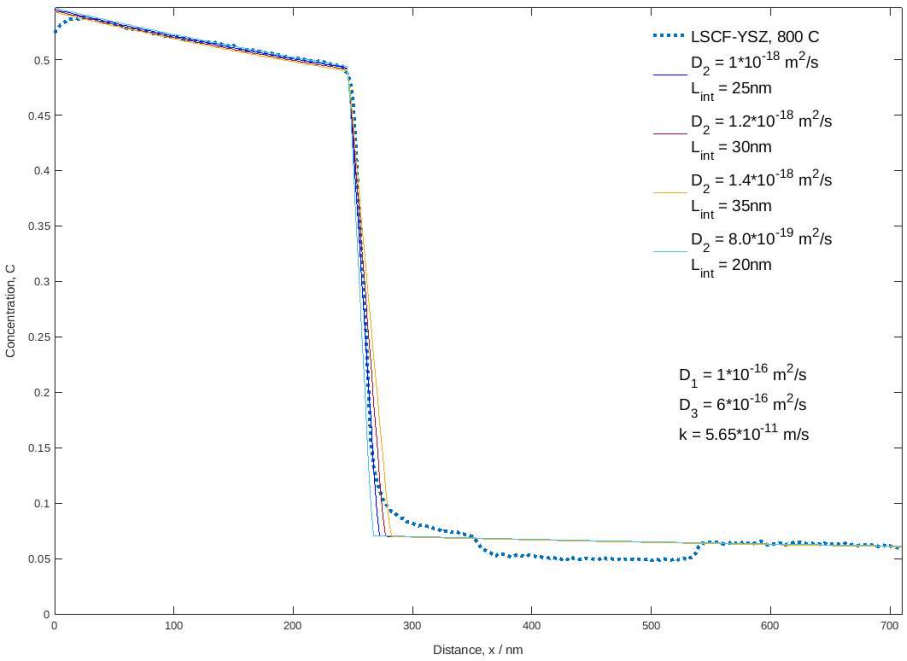

Figure 5.30: Fits of the LSCF-YSZ sample heat treated at 800 °C using the triple layer model where a set of interlayer thicknesses L_{int} and interlayer diffusion coefficients D_{int} are chosen to reproduce an accurate fit. While producing the same magnitude drop with a combination of the two is possible, matching the gradient of the data in the interlayer region narrows the window of L_{int}.

The diffusion coefficient's variation window is narrow, similar to what was established in the error analysis of the interface resistance model. While 20 to 35nm can be considered a quite large variation, the gradient of the interlayer curve might enable further refinement. The gradient of the data is specifically defined, and the gradient of the fit is closely related to the interlayer thickness. This means that if a fit is to be chosen that most closely matches the gradient of the data, the accuracy window of

L_{int} narrows significantly. Comparing the fits with thicknesses from 20 to 30 nm, it becomes clear that the gradient matching will allow for a variation of only a few nm, which also approaches an order of magnitude where it becomes questionable whether such accuracy makes any physical sense.

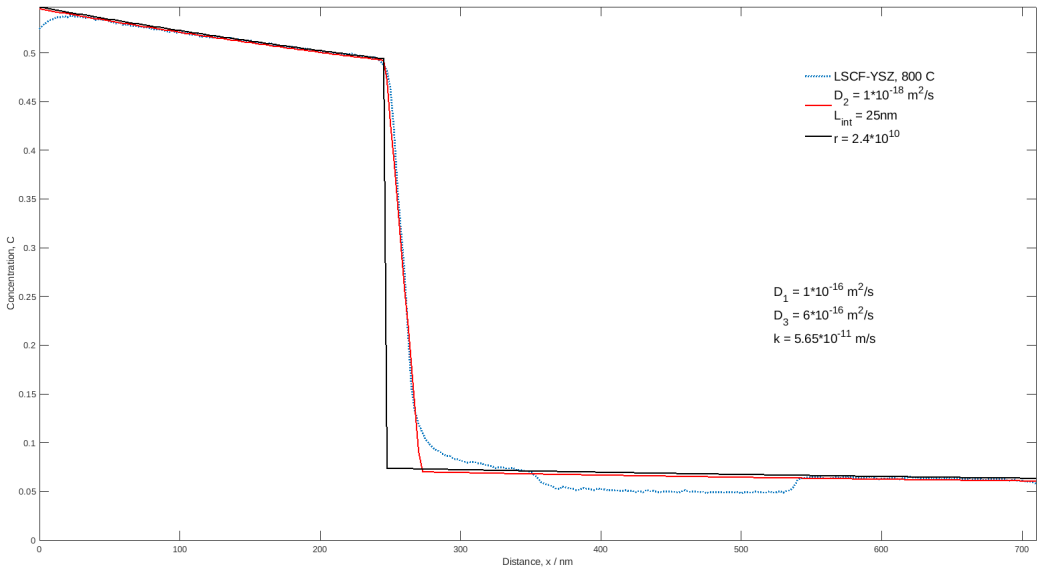

Figure 5.31: Comparison of the fits for the LSCF-YSZ sample heat treated at 800 ℃ obtained via the interface resistance model and the triple layer model. While the size of the drop is the same with both methods, the triple layer fit captures the shape of the broad interface region more accurately.

Figure 5.31 compares the fits obtained with the interface resistance and triple layer models, respectively. Both models capture the overall trends of the data closely, particularly the shape of the curves either side of the interface and the size of the interface drop. However, the triple layer model traces the shape of the data much more closely due to the fact that it is capable of introducing a gradient in the interface region rather than modelling a single drop. The other advantage of the triple layer model is that the two variables it requires, D_{int} and L_{int}, can be matched to known physical properties of materials.

The fitting method outlined here is applied to data obtained from the other samples, as summarised in Figures 5.32-5.35.

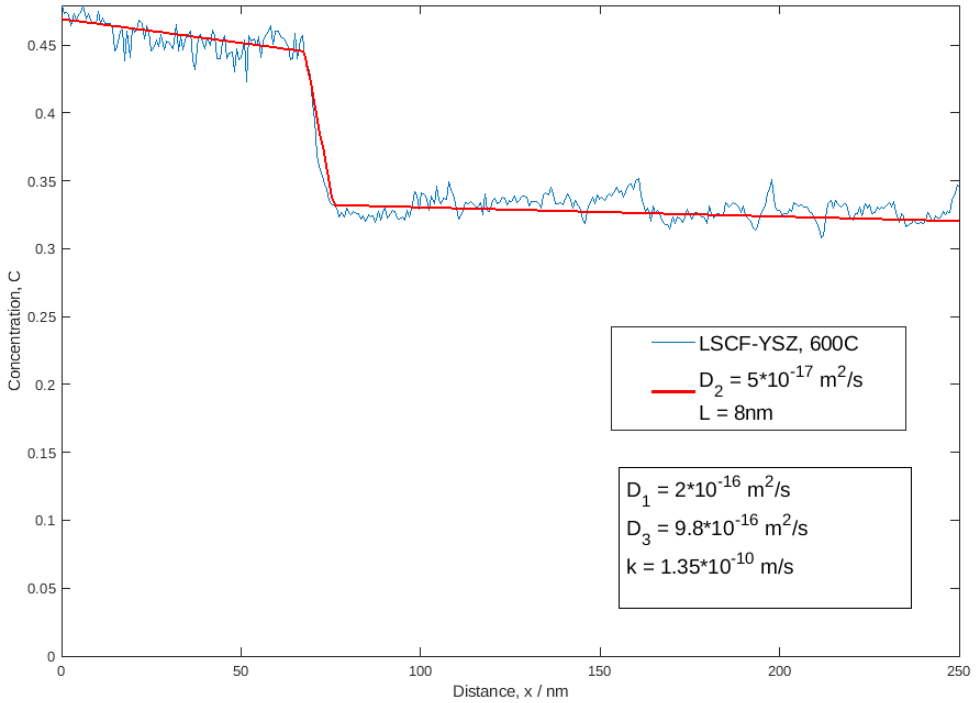

Figure 5.32: Triple Layer Fit of the LSCF-YSZ sample heat treated at 600 ℃.

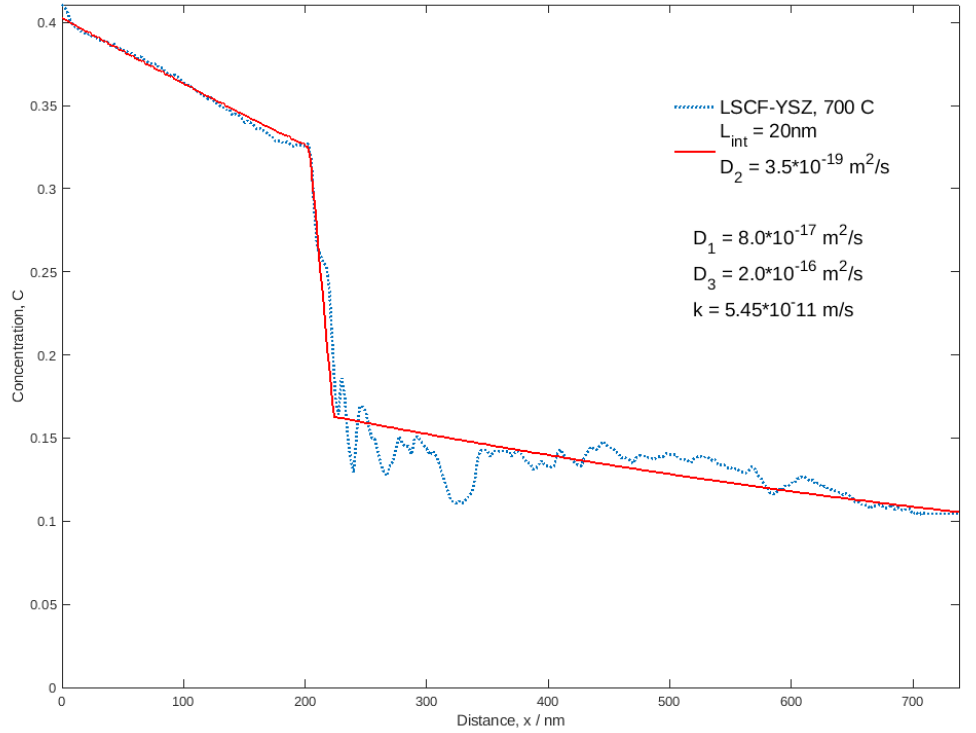

Figure 5.33: Triple Layer Fit of the LSCF-YSZ sample heat treated at 700 ℃.

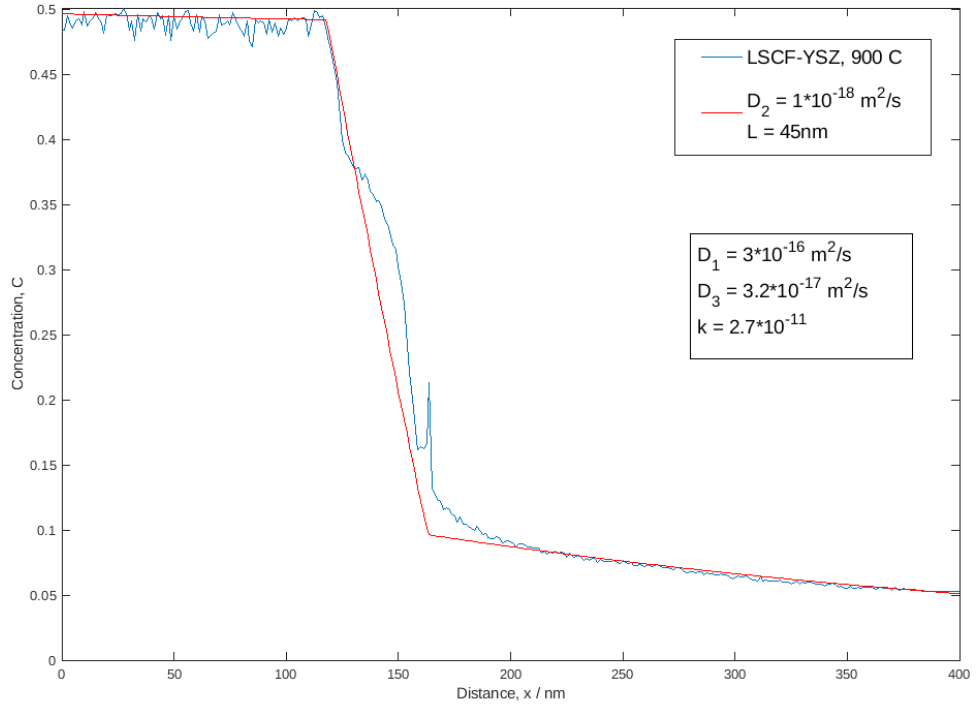

Figure 5.34: Triple Layer Fit of the LSCF-YSZ sample heat treated at 900 ℃.

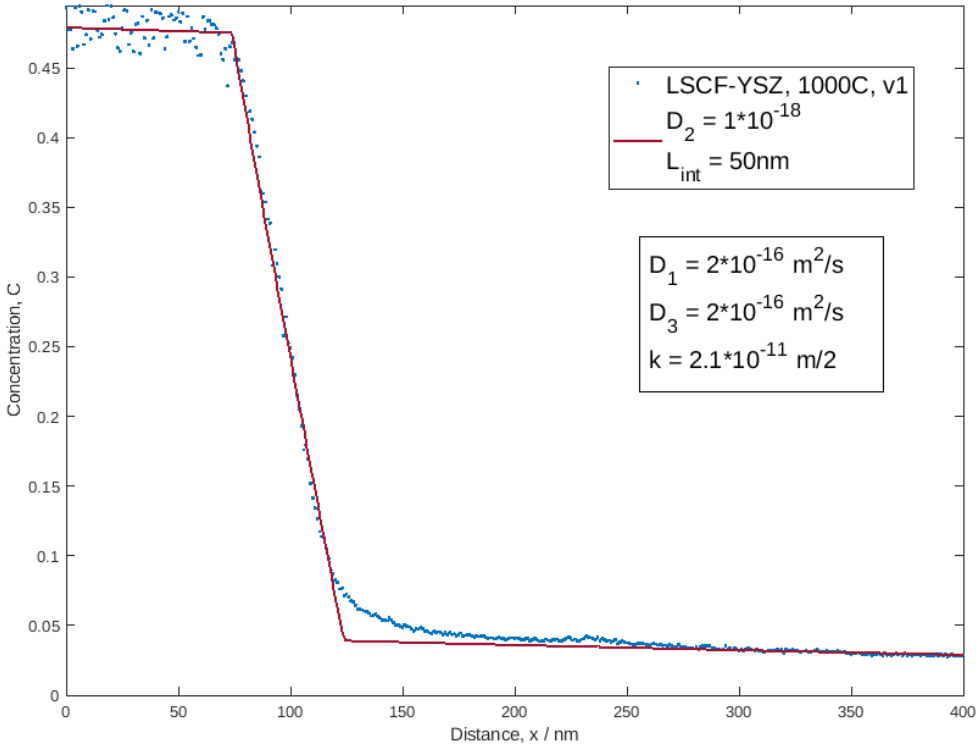

Figure 5.35: Triple Layer Fit of the LSCF-YSZ sample heat treated at 1000 ℃.

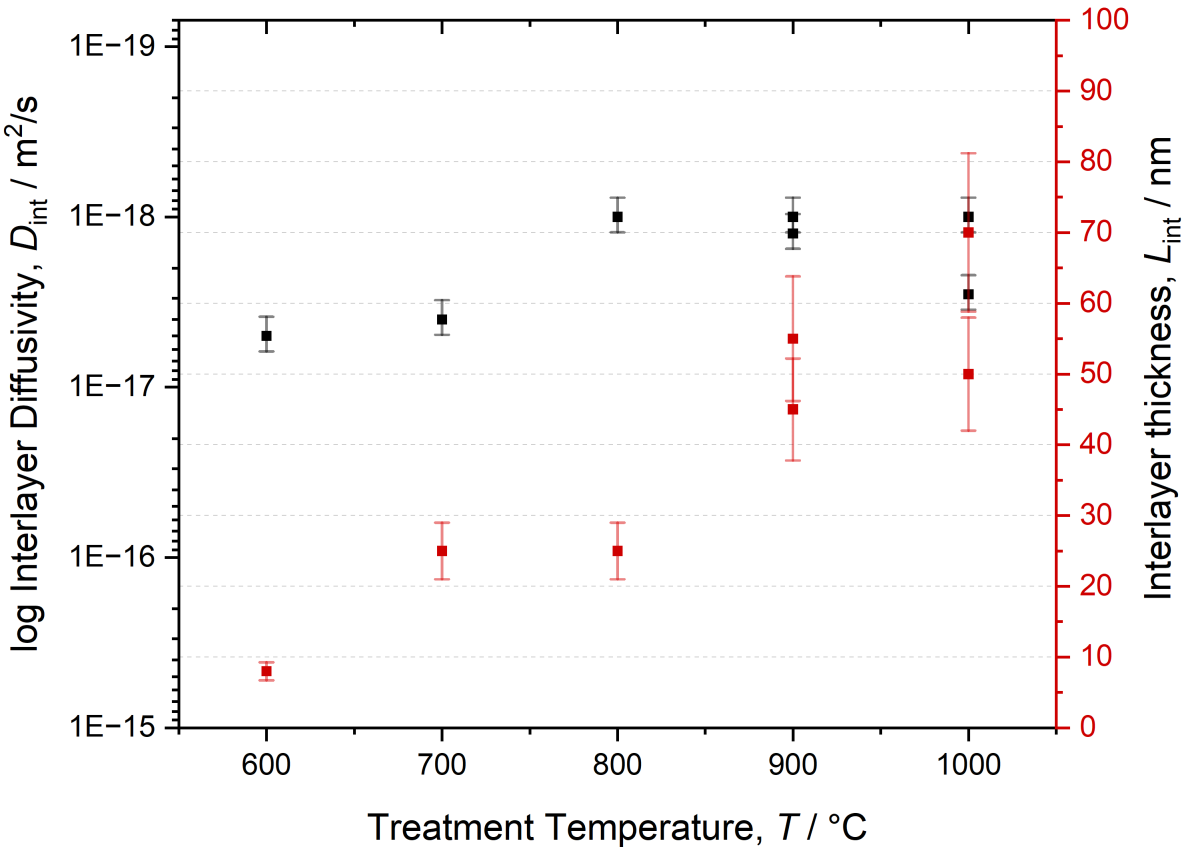

Figure 5.36: Compilation of values for D_{int} and L_{int} obtained using the triple layer fit from the LSCF-YSZ samples heat treated at various temperatures. The black points show the variation of interlayer diffusivity, while the red points show the variation in interlayer thickness.

Figure 5.36 compiles the variables of interest, D_{int} and L_{int}, as obtained from triple layer fits of all the samples. The diffusion coefficient varies inconsistently within an order of magnitude, showing no overall upwards or downwards trend. This indicates a minimal variation of the actual diffusion properties with treatment temperature. Meanwhile, the thickness of the interlayer increases steadily with treatment temperature, indicating that it is the main driver between the increased interface drop as observed in the data.

As both L_{int} in the triple layer model as well as r in the interface resistance model show an increase with treatment temperatures, it is reasonable to consider that the two variables might be related in some way. By analysing the units of the three variables, it can be found that, in theory

$$r\left(\frac{s}{m}\right) = \frac{L_{int}(m)}{D_{int}(\frac{m^2}{s})} \tag{5.1}$$

This relation can be tested by producing a set of r values calculated from the triple layer parameters

and comparing these with the fits from the interface resistance model. The results of this analysis are shown in Figure 5.37.

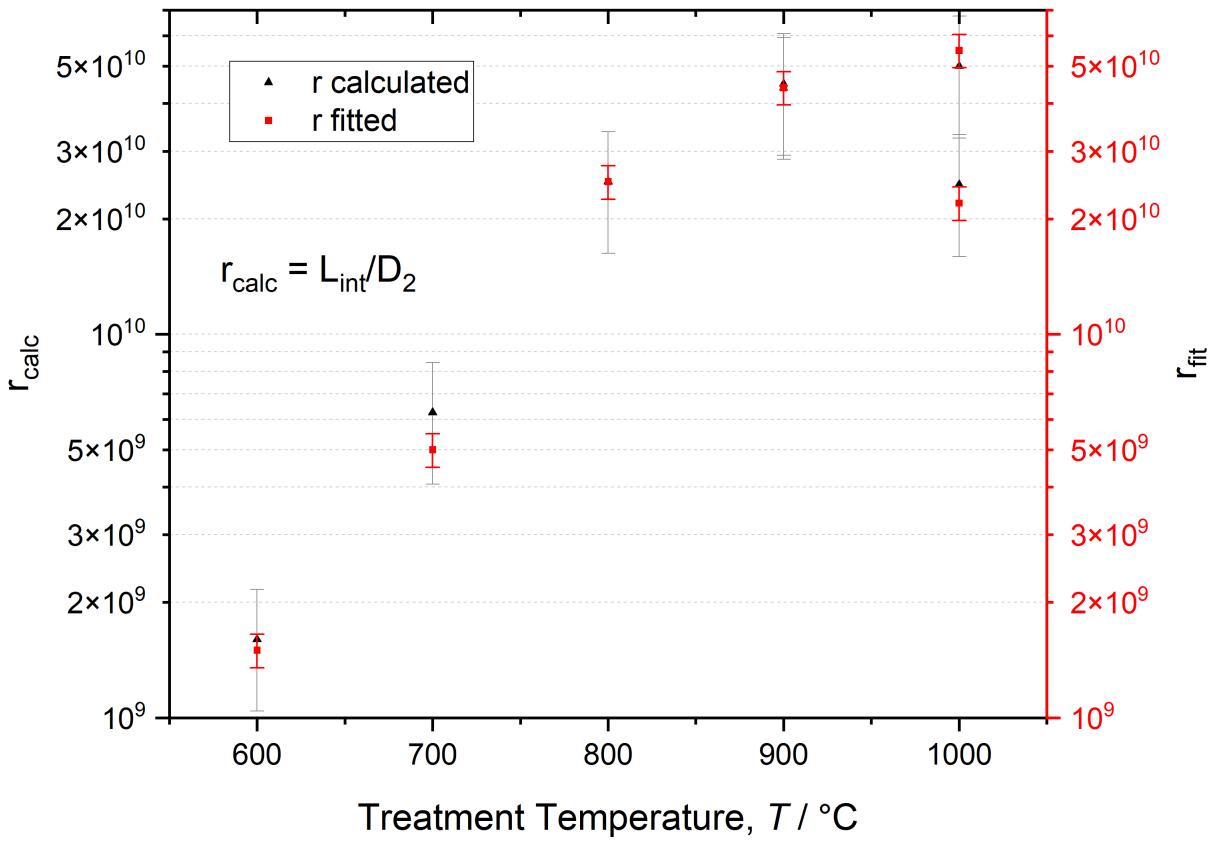

Figure 5.37: Comparison of the values of the interface resistance parameter r as obtained through fitting the data from the model (red) and calculating from the variables in the triple layer model (black).

The error of determination for the calculated interface resistance is significantly higher than that obtained by fitting. This is due to the fact that two separate variables and their associated errors are used to calculate a third value, leading to error propagation. This can be estimated by

$$\frac{\Delta r}{r} = \frac{\Delta D}{D} + \frac{\Delta L}{L} \tag{5.2}$$

Where the relative error of r is composed of the sum of relative errors of the variables used in the calculation. This is how the error bars indicated in Figure 5.37 were obtained. Even with a broad allowance for error in the fit that produces the values used in the calculations, the trends between the two methods follow each other closely. This appears to indicate that r is a simplified, single quantity that captures the ability of a material to allow diffusion across an interface, without providing specific

details about the physical mechanisms.

The triple layer model, by contrast, describes specific physical quantities, but the presence of two variables makes it more complicated to fit. If the quality of the SIMS profile is good enough, the gradient in the interface region is clear enough such that it can be matched to a range of feasible thicknesses, as previously shown in Figure 5.30. In such a case, the triple layer model provides tangible additional information about an interlayer of unknown composition and with an associated diffusivity.

5.2.7 Comparison to Literature Values

To further contextualise the fitting results, literature values for the tracer diffusion and surface exchange coefficients of LSCF6428 and YSZ8 were compared, the results of which are illustrated in Figures 5.38 and 5.39. The values were obtained from [8][9].

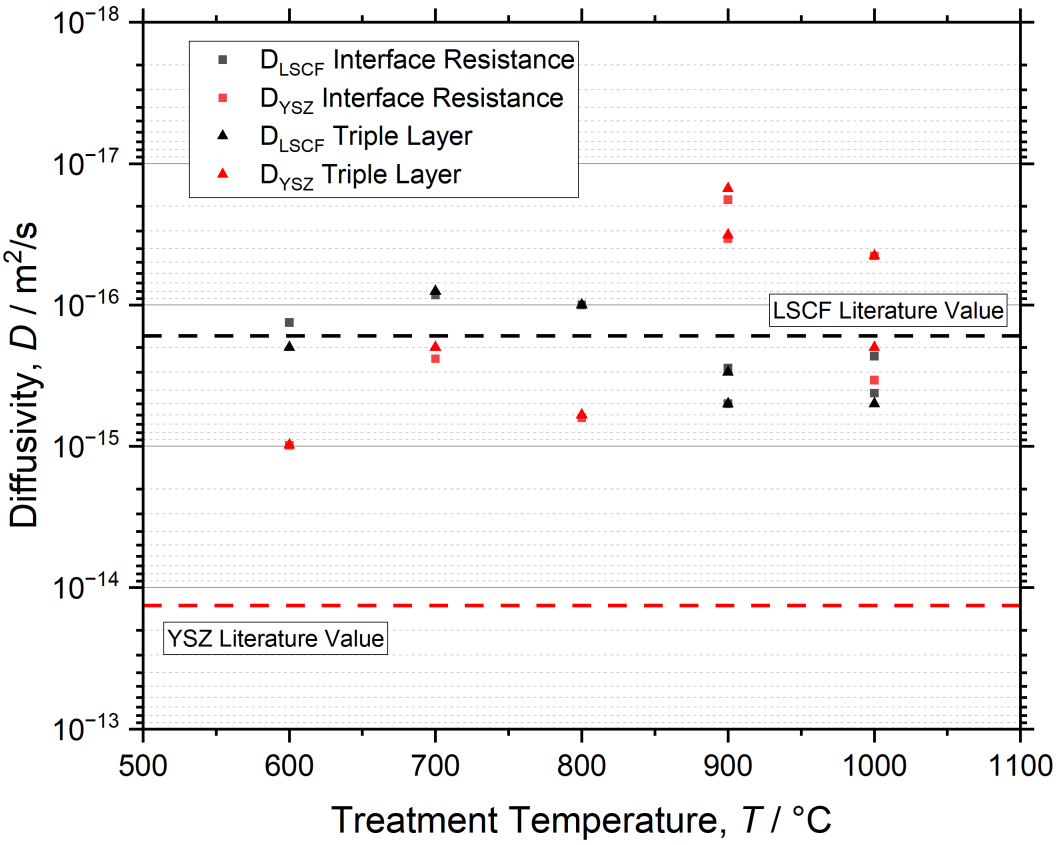

Figure 5.38: Tracer diffusion coefficients obtained from two different fitting methods for LSCF-YSZ samples heat treated at the indicated temperature and compared to the literature values of LSCF and YSZ shown in the dashed lines. The values for 900 and 1000 °C are obtained from two separate samples.

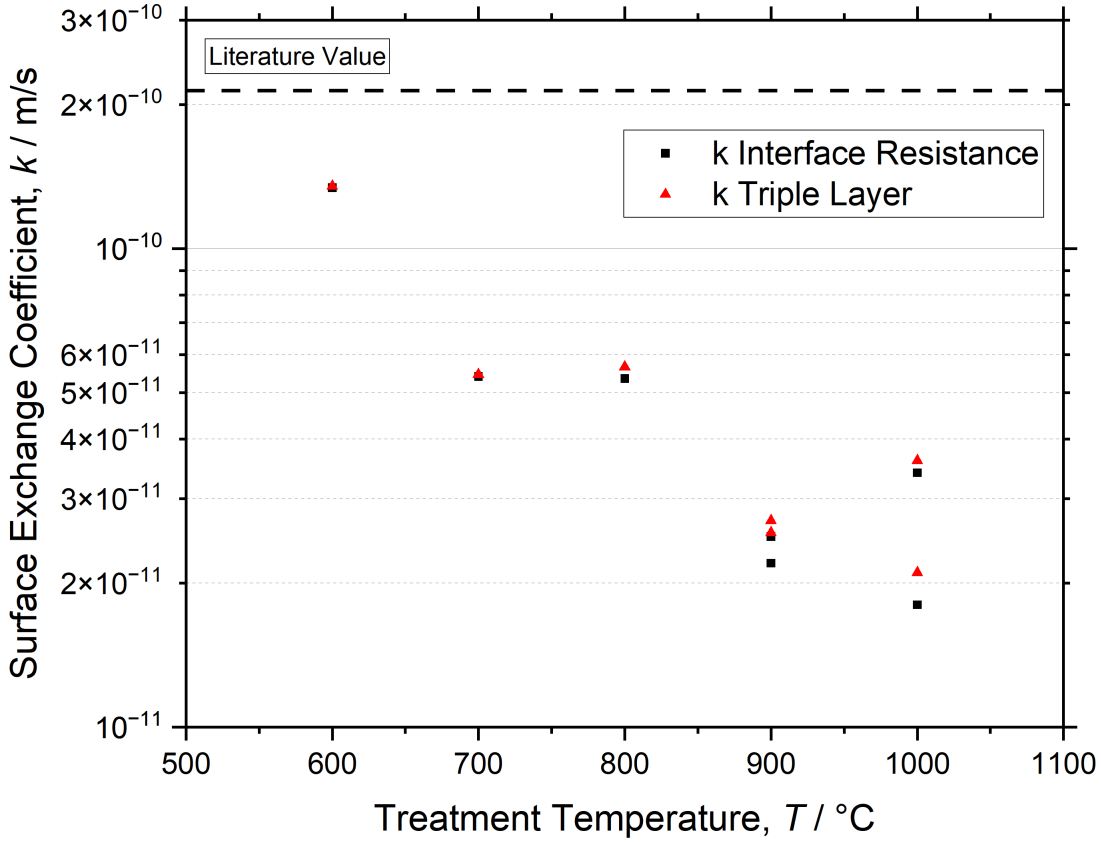

Figure 5.39: Surface exchange coefficients obtained from two different fitting methods for LSCF-YSZ samples heat treated at the indicated temperature and compared to the literature value of LSCF shown in the dashed line. The values for 900 and 1000 °C are obtained from two separate samples.

In general it can be seen that the two fitting methods agree well on the values of both D and k. The diffusion coefficient of LSCF appears to be in the same order of magnitude as the literature value, with both smaller and larger values having been obtained. This could both be due to a small shift in stoichiometry or the error in the fitting process. Inconsistencies induced either during the deposition process or the heat treatment might have slightly altered the oxygen non-stoichiometry of LSCF, which determines its oxygen vacancy concentration and subsequently diffusion properties. The fitting error was discussed in the earlier section and can be higher than 20% in some data. This indicates that the overall diffusion properties of LSCF are as expected and do not significantly change as a result of heat treatment or other factors, and that the model is capable of capturing this behaviour.

The literature value for YSZ is orders of magnitude higher than those obtained from the fit. As was touched upon in the earlier section, this can partially be explained by the nearly horizontal exchange profile that is exhibited by the bulk electrolyte. Such a shape indicates fast diffusion and therefore makes it difficult to determine an upper limit. The fits here were done while trying to capture the

subtle shape changes of the bulk phase as accurately as possible. These features could, however, also result from state changes induced by the elevated temperatures. The samples that underwent higher temperature heat treatment show a gradual transition from the interface region to the bulk. It is possible that some interdiffusion occurred during the heat treatment in the YSZ side of the interface as well, creating a gradual increase in diffusion coefficient until the unaffected bulk of the sample is reached. This could also explain why some of the 900 and 1000 ℃ samples appear to show a D_{YSZ} that is an order of magnitude smaller than the rest.

The values of k are consistently smaller than the literature value. As the surface is the part of the film that is subject to the most change and inconsistencies, the surface exchange coefficient could be affected significantly [10]. The general trend shows a lower value of k with increased treatment temperature. This could indicate some form of surface modification that negatively affects the surface exchange ability. In a system as complex as LSCF, there are many possible ways in which a high temperature could induce processes affecting the surface. One commonly studied mechanism is strontium segregation, i.e. the diffusion of strontium cations toward the surface of LSCF [11][12][13]. This process can create a SrO layer near the surface, which could also induce local changes in the crystal structure, diminishing the surface exchange properties. This effect was found to occur even at 400 ℃ and to increase with higher treatment temperatures [14]. Based on how common this mechanism is in LSCF, it is not unreasonable to assume that an increased post-deposition heat treatment temperature will induce increasingly higher levels of strontium segregation. This may explain the steadily decreasing surface exchange coefficient at higher treatment temperatures, which could be further investigated using LEIS analysis. While this could further elucidate the processes occurring in the material, a reduced surface exchange coefficient due to strontium segregation would likely not have a significant effect on the processes at the solid-solid interface. This is because strontium segregation only occurs near the surface atomic layers and therefore should not affect the bulk LSCF layer, as is further indicated by the relatively consistent values of the diffusion coefficient as summarised in Figure 5.38. While the inconsistency in the surface exchange coefficient slightly diminish the full comparability between samples, the fitting model is able to clearly quantify each layer's material properties, allowing for the separate treatment of the variables. The goal of this series of experiments is to investigate and quantify the interface resistance effects as represented by the variables introduced in the model approaches. A more consistent k^* would strengthen the consistency of the fits, but ultimately is not relevant to the quantification process.

References

[1] H Yokokawa, N Sakai, T Kawada, and M Dokiya. Thermodynamic stabilities of perovskite oxides for electrodes and other electrochemical materials. *Solid State Ionics*, 52(1-3):43–56, 1992.

[2] L Kindermann. Chemical compatibility of the $LaFeO_3$ base perovskites $(La_{0.6}Sr_{0.4})_zFe_{0.8}M_{0.2}O_3$ (z = 1, 0.9; M = Cr, Mn, Co, Ni) with yttria stabilized zirconia. *Solid State Ionics*, 89(3-4):215–220, 1996.

[3] F. Poulsen and N. Van Der Puil. Phase relations and conductivity of Sr- and La-zirconates. *Solid State Ionics*, 53-56:777–783, 1992.

[4] P. Plonczak, A. Bieberle-Hütter, M. Søgaard, T. Ryll, J. Martynczuk, P. Hendriksen, and L. J. Gauckler. Tailoring of La $_x$ Sr $_{1-x}$ Co $_y$ Fe $_{1-y}$ O $_{3-}$ Nanostructure by Pulsed Laser Deposition. *Advanced Functional Materials*, 21(14):2764–2775, 2011.

[5] S.J. Cooper. *PhD Thesis*. PhD thesis, Imperial College London, 2015.

[6] A Benninghoven, F G Rudenauer, and H W Werner. Secondary ion mass spectrometry: basic concepts, instrumental aspects, applications and trends.

[7] J. C. Vickerman and Ian S. Gilmore, editors. *Surface analysis: the principal techniques*. Wiley, Chichester, U.K, 2009. OCLC: ocn254529018.

[8] B Steele. Properties of $La_{0.6}Sr_{0.4}Co_{0.8}Fe_{0.2}O_3$ (LSCF) double layer cathodes on gadolinium-doped cerium oxide (CGO) electrolytes II. Role of oxygen exchange and diffusion. *Solid State Ionics*, 106(3-4):255–261, 1998.

[9] M. Kilo, C. Argirusis, G. Borchardt, and R. A. Jackson. Oxygen diffusion in yttria stabilised zirconia—experimental results and molecular dynamics calculations. *Phys. Chem. Chem. Phys.*, 5(11):2219–2224, 2003.

[10] M. J. Pietrowski, R. A. De Souza, M. Fartmann, R. Ter Veen, and M. Martin. Oxygen Isotope Transport Properties of Yttria-Stabilized Zirconia (YSZ) in O $_2$ - and H $_2$ O-Containing Atmospheres. *Fuel Cells*, 13(5):673–681, 2013.

[11] K. Szot and W. Speier. Surfaces of reduced and oxidized SrTiO 3 from atomic force microscopy. *Physical Review B*, 60(8):5909–5926, 1999.

[12] M. Hervieu. The Surface Science of Metal Oxides. By V. E. Henrich and P. A. Cox, Cambridge University Press, Cambridge 1994, ISBN 0–521–44389-X. *Advanced Materials*, 7(1):91–92, 1995.

[13] H Dulli, P. A. Dowben, S.-H. Liou, and E. W. Plummer. Surface segregation and restructuring of colossal-magnetoresistant manganese perovskites $La_{0.65}Sr_{0.35}MnO_3$. *Physical Review B*, 62(22):R14629–R14632, 2000.

[14] J. Druce, T. Ishihara, and J. Kilner. Surface composition of perovskite-type materials studied by Low Energy Ion Scattering (LEIS). *Solid State Ionics*, 262:893–896, 2014.

Chapter 6

Other interfaces and analysis techniques

The previous chapter outlined the experimental investigation of LSCF deposited on YSZ pellets and analysed using isotope exchange depth profiling, as well as the fitting of the data obtained from these samples to the model developed in chapter 3. This chapter will discuss further experimental results obtained as part of this larger project, with the goal of investigating interfaces in different contexts in order to potentially obtain more information about their nature and behaviour. including depositing LSCF on GDC substrates, as well as some additional characterisation using SEM-EDX and EIS. These were done in order to better understand the potential mechanistic processes and chemical reactions that can take place in multi-layer materials.

6.1 LSCF-GDC multilayer samples fabricated with PLD

The same sample fabrication procedures as discussed in the previous chapter were applied to the LSCF on GDC samples. This means that PLD was used to ablate the same LSCF target as used previously, with the same deposition conditions, the only difference being a GDC substrate pellet instead of YSZ. The powder pressing and sintering procedure to fabricate the substrates were also performed at the same sintering times and temperatures, with the only difference being that GDC powder is denser than YSZ, meaning a slightly higher (around 0.1g) amount of powder was needed to achieve substrates with roughly the same dimensions. The same post-deposition annealing temperatures and times were used in order to investigate the potential formation of an interface. The depth profiles from these samples are shown in Figure 6.1.

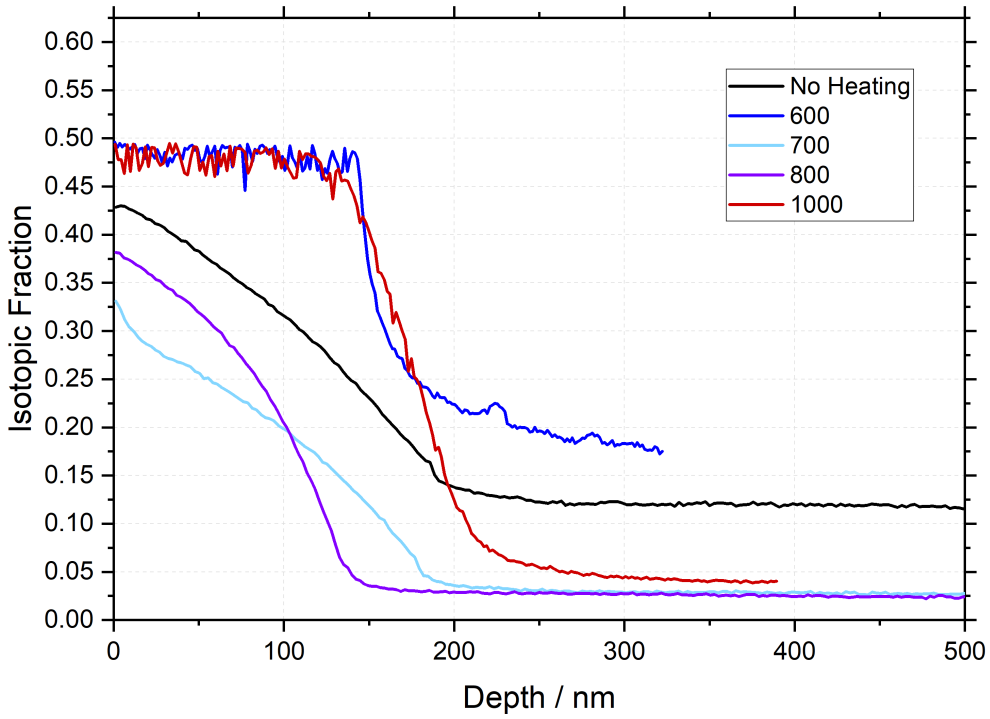

Figure 6.1: Isotopic fraction data obtained from a series of samples containing LSCF deposited on a YSZ substrate and subsequently heat treated at the indicated temperatures. As with the LSCF-YSZ samples, isotope exchanges were performed at 460 ℃ for 90 minutes.

The first notable feature in this series is the differing shape between the samples treated at 600 and 1000 ℃ and the rest. These samples show a flat profile in the first layer, followed by a drop akin to the interface resistance observed in the YSZ samples. This would suggest the formation of an interlayer region, which is supported by the fact that the magnitude of the interface drop is larger for the sample treated at 1000 ℃. There is some work in literature discussing the effects of interdiffusion, suggesting that the migration of species, without the formation of reaction products, can negatively affect diffusion across the interface. Investigating these effects could be future work building on this project.

The sample with no heat treatment and the samples treated at 700 and 800 ℃ show no apparent interface drop, but show a significantly higher downwards gradient in the first layer. This suggests that there is not an interlayer formation, but that the diffusion properties of the LSCF layer deteriorated significantly. It is not possible to fit this first layer to a diffusivity value, as the gradient of the profile in this section changes in a way that cannot be captured by the diffusion model. While the higher temperature heat treatment does diminish the isotopic fraction in the overall profile, suggesting further deterioration of diffusion and surface exchange properties, it is difficult to assign a specific phenomenon to this behaviour. It is possible that there were issues during the PLD process, producing an imperfect LSCF layer with diminished diffusion and exchange properties.

6.2 EDX Analysis

One characterisation method that might give more insight into the mechanics at the interface is SEM-EDX. By mapping the cross-section around the interface region, the distribution of individual species can be visualised. To do this, the LSCF-YSZ ceramics processing samples from the initial approach can be used. These samples underwent high-temperature co-sintering at 1400 ℃ and therefore should show ample evidence of reaction products forming. The cross-section SEM-EDX data from one such sample is shown in Figure 6.2.

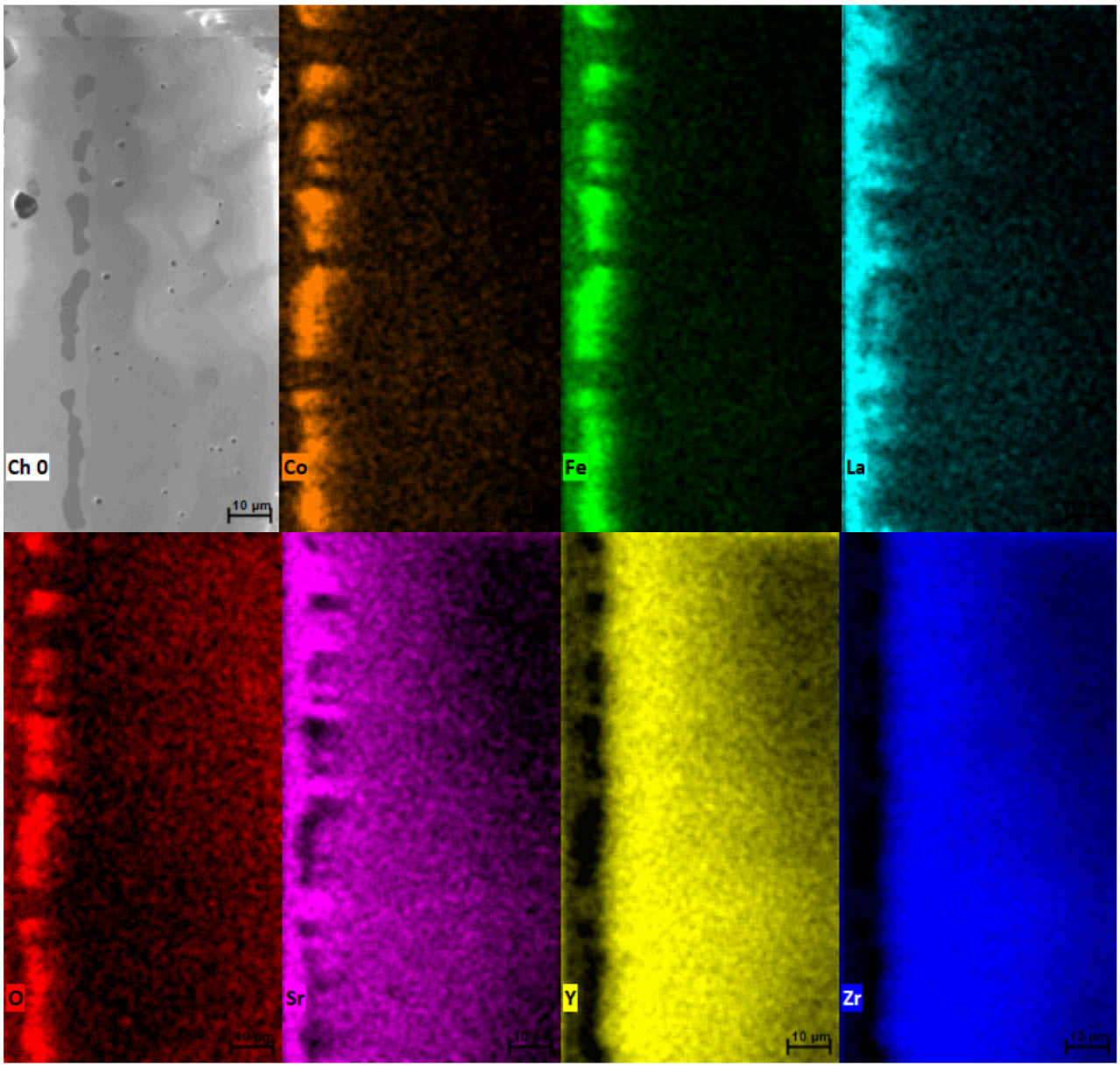

Figure 6.2: EDX images obtained from the cross-section of a sample consisting of LSCF deposited onto a YSZ substrate using the drop casting method. The cross-section focuses on the interface region between the two materials, displaying darker spots with distinct elemental characteristics.

The secondary electron image shows the appearance of slightly darker, rounded spots around the interface region. When the same regions are then analysed using EDX, the visually darker spots reproduce in the ion signals in several ways. The most notable feature is the clear segregation of cobalt and iron signals in the spots, the shape of which roughly reproduces the dark spots from the secondary electrons. Conversely, the remaining cation signals show empty regions around the same spots, both the Zr and Y and the La and Sr signals. Interestingly, the oxygen signals appears to be concentrated in the same places as the Co and Fe signals, even though oxygen is expected to be present throughout the whole sample. In the first instance, this would appear to suggest the formation of a cobalt ferrite species that is physically segregated from the surroundings. The XRD data from Figure 5.1 does hint at the formation of Co_2FeO_4, although the SZO signal dominates. To further investigate this, the darker spots seen in the figures were analysed relative to their surroundings using point EDX analysis, the results are shown in Figure 6.3 and Table 6.1.

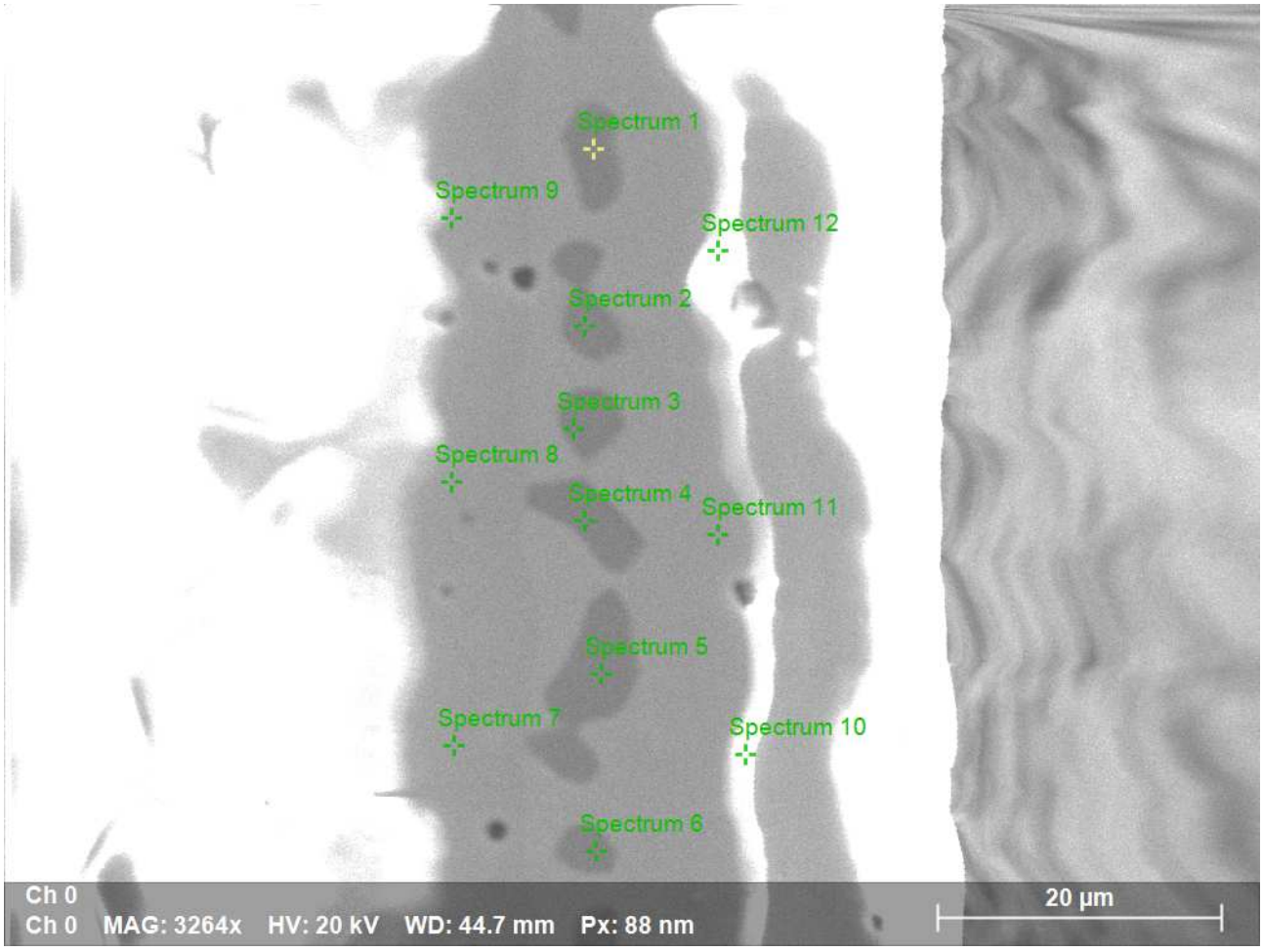

Figure 6.3: EDX analysis obtained from a series of points along the interface of a sample consisting of LSCF deposited onto a YSZ substrate using the drop casting method. The points were chosen to fall within and between the darker spots, as well as away from the region.

Table 6.1: Table compiling the atomic percentage of the listed elements obtained from each point of the cross-section EDX analysis. The columns marked in blue represent the points from the darkened spots around the interface, while the columns marked in yellow were taken from the YSZ side.

Spectrum (at%)	**1**	**2**	**3**	**4**	**5**	**6**	**7**	**8**	**9**	**10**	**11**	**12**
Oxygen	56.2	55.1	69.6	62.7	54.3	64.0	69.7	71.6	71.1	67.9	68.3	69.6
Iron	25.8	26.8	10.3	18.5	28.5	11.9	4.1	3.6	3.2	11.4	11.3	10.4
Cobalt	11.3	11.8	1.4	7.5	12.6	2.4	1.4	0.7	0.41	1.7	1.5	1.4
Lanthanum	1.11	0.5	7.0	2.3	0.3	6.6	0	0	0	7.3	7.5	7.0
Strontium	2.8	3.2	5.7	4.9	2.4	7.6	1.6	1.45	1.5	6.1	5.7	5.7
Zirconium	2.7	2.6	5.7	4.2	1.8	7.5	23.2	22.6	23.7	5.7	5.7	5.7

The point probes confirm the higher presence of cobalt and iron signals in the darker areas. Furthermore, the atomic percent ratio of cobalt to iron in most probes approaches 1:2, in reality being closer to 1:2.25. This matches the stoichiometric ratio of the $CoFe_2O_4$ phase (CFO). The oxygen signal in general is difficult to match with quantification of stoichiometry, as it would be present in basically any phase that might form. While this is not a confirmation of this specific $CoFe_2O_4$ phase being present, it is an indicator of a cobalt and iron containing phase segregating out.

6.2.1 Properties of potential reaction products

The EDX and XRD results give an indication of the species that form between LSCF and YSZ. Table 6.2 summarises some of these phases and their properties as obtained from various literature sources.

Table 6.2: Table summarising the conductivity and, where available, diffusivity at 460 °C of potential reaction products between LSCF and YSZ.

	$SrZrO_3$	**$CoFe_2O_4$**	**$La_2Zr_2O_3$**
Conductivity at 460 °C (S/m)	$5 \cdot 10^{-8}$ [1][2][3]	$5 \cdot 10^{-7}$[4]	$4 \cdot 10^{-7}$ [5][1][6]
Oxygen diffusion coefficient (m^2/s)	10^{-20} at 460 °C calculated from [7] 10^{-16} for grain boundaries [7]	-	12 times lower than YSZ [8]

$SrZrO_3$

Strontium zirconate has a long history of being investigated as a proton conductor [3][9] and other applications such as magnetohydrodynamics [10]. While the principal phase follows the $SrZrO_3$ stoichiometry, polymorphism in this system has been reported [1]. Many SZO species doped with different cations have been investigated, showing the potential for the diffusion of yttrium ions into the SZO lattice. Develos-Bagarinao *et al.* suggested that this diffusion-driven Y-doping could act as a

precipitation site for yttrium oxides, inhibiting conductivity significantly [11]. The conductivity studies suggest a lower value compared with YSZ and LSCF, and this further reflects in the tracer diffusion measurements undertaken by Nivot *et al.* [7]. The calculations obtained from the experimental values would suggest a low value of D in the range of 10^{-19} or lower, however it must be pointed out that this is based on an extrapolation of the high-temperature behaviour rather than a direct measurement. The same study investigated the potential effect of grain boundary diffusion in SZO, which was determined to be four orders of magnitude higher. This means that grain boundary diffusion could potentially be a viable path in an SZO-containing interlayer.

$\mathbf{CoFe_2O_4}$

The spinel-structure CFO has undergone intense investigations as a thin film for its magnetic properties and as nanoparticles for catalysis. The presence of cobalt and iron enable high catalytic activity and tunable magnetic properties. Not much work has been done on the oxygen ionic conductivity of this material. Its catalytic properties have, however, inspired studies into the engineering of oxygen vacancy concentration [12][13]. Given this, it is unlikely that the oxygen ionic conductivity would be significantly lower than that of other potential reaction products such as SZO. The SEM-EDX results show a visible phase separation of CFO relative to the other parts of the layer structure, but this is less likely to occur at the lower temperatures of the PLD sample. The XRD results also indicate that the formation of CFO can begin at 800 ℃ or even lower. This appears to suggest that the formation of CFO in a structure where LSCF and YSZ are in contact is possible.

$\mathbf{La_2Zr_2O_7}$

LZO exhibits a pyrochlore structure and has been investigated for thermal barrier coatings due to its good properties at high temperatures [14]. Its defect structure and effect on oxygen ionic conductivity have also been investigated [15]. It seems to operate at similar total conductivity levels to SZO. However, the formation of LZO could not be verified in the XRD data. This could be either because it does not form at all, or because it forms in smaller quantities relative to CFO and SZO.

6.2.2 Phase formation

The phases that could form as a result of a reaction between the LSCF thin film and the YSZ substrate appear to show a consistently lower ionic conductivity and tracer diffusivity compared with LSCF and YSZ. While the exact composition, crystal structure and properties of the interlayer are unclear, a

simplified model with an average diffusivity and ionic conductivity could be applied.
Since the interface is isolated from surface gases and all the potential processes that could come with this, it can be assumed that the cations present in LSCF and YSZ participate in phase formation reactions. It remains open whether one of these new phases (such as SZO) could form while leaving the rest of the crystal in some sort of disordered state, or whether the formation of new phases out of this is inevitable. The formation of SZO, CFO and LZO account for the presence of all of these species. Since strontium is known to diffuse easily through the LSCF lattice, it is plausible that SZO is the phase that forms first. This would entail the gradual removal of strontium from the A-site in order to react with the zirconia from the YSZ. This leaves the LSCF with increasing A-site deficiency that could eventually lead to the decomposition of the perovskite structure. Due to this decomposition, CFO could plausibly form out of the B-site structure. This, in turn, may enable the leftover lanthanum to react itself and form LZO.

Regardless of the specific reaction mechanisms, the interlayer has to contain all of the species that were present before the reaction occurred. This means that the interlayer cannot be modelled as a single material with a specific ability to diffuse oxygen (and compared to literature values). It could be a solid solution or composite of the reaction products mentioned. The value of ionic conductivity and tracer diffusion (where available) of the potential reaction products are several orders of magnitude below that of LSCF and YSZ. If the interlayer is a combination of these materials, it would be plausible to assume that the ionic conductivity would be of a similar order of magnitude to the reaction products. While the ionic conductivity of the materials consistently appear to be around 2 order of magnitude lower, the tracer diffusion data for SZO suggests an even bigger gap [7]. The combination of low diffusivity and potential ability to diffuse along grain boundaries could offer an explanation for the higher interlayer diffusivity as determined by the triple layer model when compared to the literature tracer diffusion of SZO. Finally, tracer diffusion and ionic conductivity properties are often sensitive to slight stoichiometry changes, making it particularly difficult to precisely obtain quantification from a sample as complex as the multi-layer structures investigated in this project.

6.3 EIS Experiments and Results

Impedance Spectroscopy measurements of the same samples that were analysed with the Isotope Exchange method were taken in order to further study the behaviour observed. The samples were the same samples that were analysed using SIMS depth profiling as detailed in the earlier section; LSCF deposited on YSZ using PLD and heat treated at the indicated temperatures for 4 hours. The

Table 6.3: Table summarising the ohmic and polarisation resistance as well as capacitance values obtained from the EIS data. The resistance values are inferred from the start and end point of the semicircles, while the capacitance is calculated from the peak frequencies at each semicircle.

Sample	Peak frequency (Hz)	R_{Ohm} (Ωcm^{-2})	R_{pol} (Ωcm^{-2})	Capacitance (Fcm^{-2})
460	13600	103.35	79.65	$1.47 \cdot 10^{-7}$
	0.1	193	17	$9.36 \cdot 10^{-2}$
700	13600	118.27	85.73	$1.37 \cdot 10^{-7}$
	0.1	212.5	25.5	$6.24 \cdot 10^{-2}$
800	25000	127.4	55.6	$1.14 \cdot 10^{-7}$
	0.1	190	25	$6.37 \cdot 10^{-2}$
900	40000	152	43	$9.25 \cdot 10^{-8}$
1000	63000	1200	38800	$6.51 \cdot 10^{-11}$

temperature in the impedance rig was set to 460 ℃, the same temperature that the isotope exchange experiments were performed at. All of the temperatures henceforth refer to the post-deposition heat treatment temperature, with the EIS rig being at the same 460 ℃ for every sample tested. The overview in Figure 6.4 shows a significant increase in impedance at 1000 ℃ while the other samples are in a similar order of magnitude to each other.

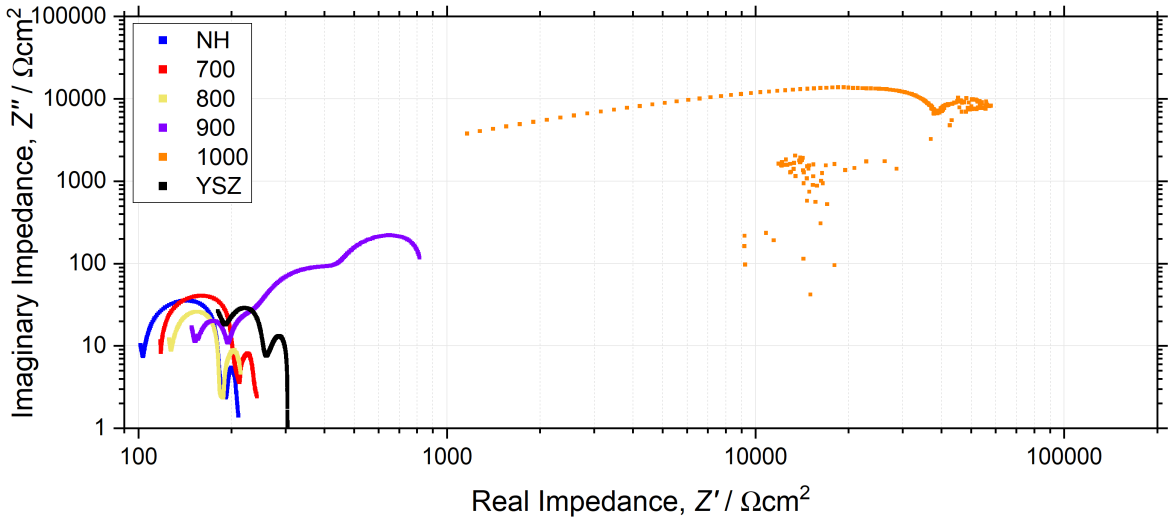

Figure 6.4: Nyquist plots of all the multi-layer LSCF-YSZ samples fabricated with PLD and heat treated at the labelled temperatures. Note the logarithmic scale on both axes for the purpose of global comparison.

The 1000 ℃ sample also shows degeneration in the low frequency range, producing resistance values that are too high for the machine to properly capture. The 900 ℃ sample diverges from the others in that it contains low frequency semicircles which appear not to be present in samples treated below this temperature. These latter samples all show similar orders of magnitude and shapes to each other.

6.3.1 Low Temperature

Figures 6.5 and 6.5 show the EIS data obtained from the sample without heat treatment, as well as the ones treated at 700 and 800 ℃.

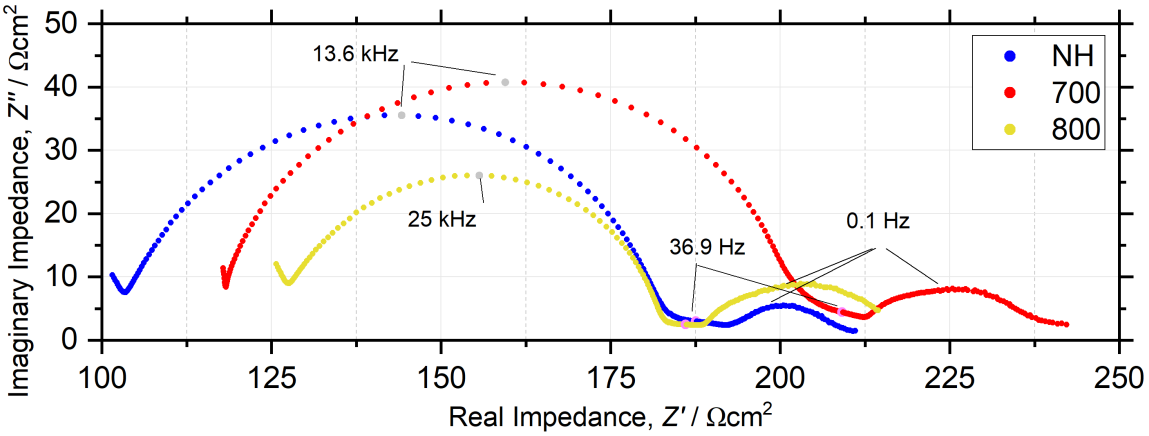

Figure 6.5: Impedance spectra comparing the response of the LSCF-YSZ PLD samples, one without additional heat treatment, the others heat treated at 700 and 800 ℃.

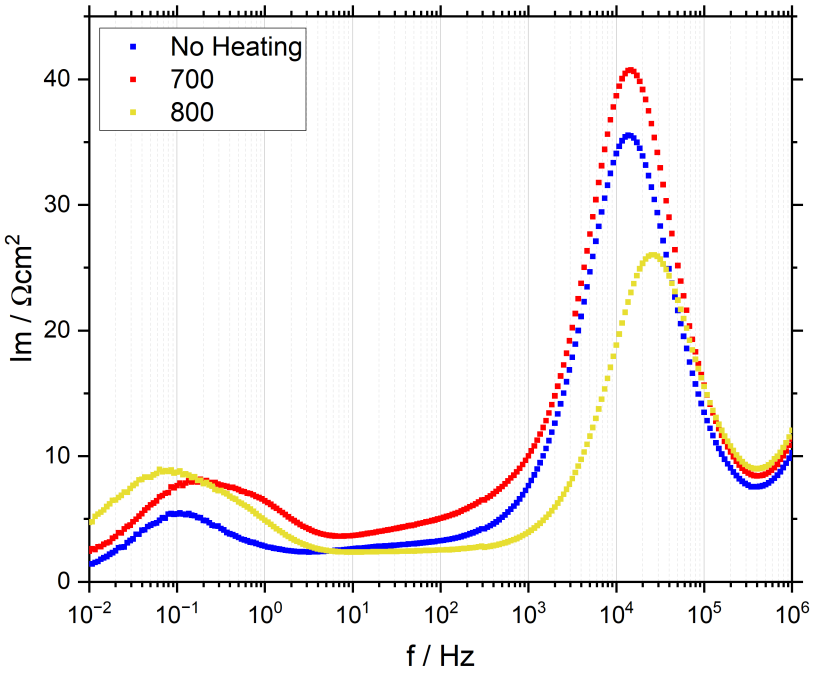

Figure 6.6: Bode plot comparing the imaginary response of the LSCF-YSZ PLD samples, one without additional heat treatment, the others heat treated at 700 and 800 ℃.

The low temperature heat treated samples all show similar behaviour in the magnitude of impedance as well as the general shape. They contain a high-frequency semi-circle with peak frequencies in the kHz range, another smaller semicircle at 0.1 Hz, and an intermediate region in between the circles.

Furthermore, the beginning of the spectra show a distinct tail, which might indicate the remainder of a further, high frequency semicircle.
The samples consist of mostly polycrystalline YSZ with a very thin layer of LSCF on one side, which is unlikely to have a significant effect on the overall sample resistance. It contains ionic conductivity on a similar order of magnitude as YSZ, and as such would likely contribute insignificant amounts to the Ohmic resistance.

Based on the capacitance values in Table 6.3, calculated from the peak frequencies of each semi-circle, indicate that the high frequency semicircle can be assigned to the grain boundary processes, with the bulk conductivity being indicated in the tail at the beginning of the spectra. This would require the samples to be re-measured with a larger frequency range in order to decisively confirm the assignment.
The second, low frequency semi-circle, meanwhile, likely describes the silver paste painted onto the samples and acting as electrodes. The peak frequencies of all these regions are in the approximately correct order of magnitude to be described by the processes mentioned [16][17][14]. Furthermore, there is a gradual increase in ohmic resistance with increased treatment temperature. This trend continues into the higher treatment temperature samples, although the response from these is qualitatively significantly different.
It is likely that small variations in preparation and experimental conditions of the sample explain some of the inconsistencies in the data, such as the shape and magnitude of the semicircles. The area of the silver paste painted onto each side of the sample is subject to experimental inconsistency, as this is manually applied on each side. Repeat experiments and investigations into the effects of the sample preparation is needed to confirm the evolution of behaviour between the samples.

6.3.2 High Temperature

Looking at the high-temperature samples more closely in Figures 6.8 and 6.7 shows the shape more clearly. The 900 ℃ sample shows an initial high-frequency semi-circle that exists in a similar order of magnitude to the samples treated at lower temperatures, albeit with a slightly higher apparent resistance. The main difference is the existence of multiple, high-impedance responses at decreasing frequencies. The two semicircles with the most clear shape exist in the high and low frequency ends at 40 kHz and 0.05 Hz, respectively. The area between these semicircles is characterised by an increase in imaginary impedance that could be interpreted as a combination of various other processes.

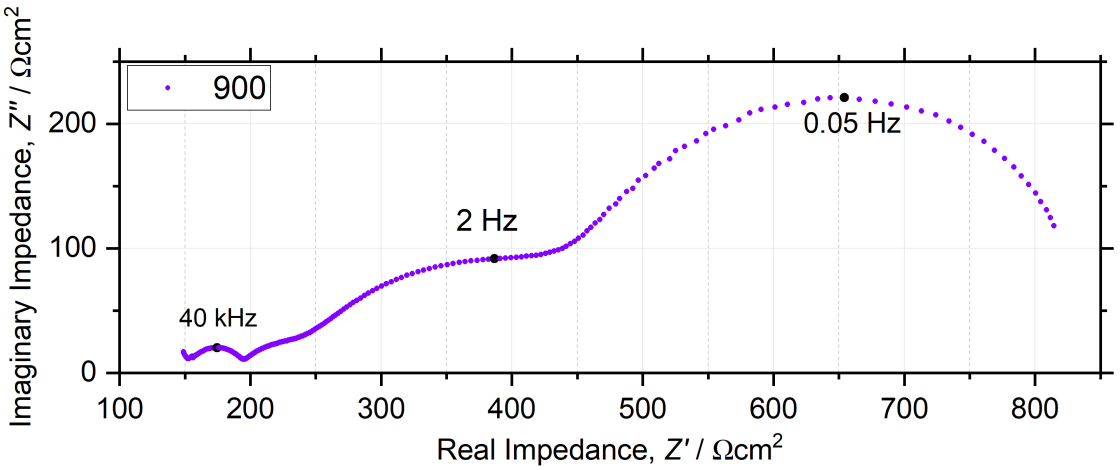

Figure 6.7: Impedance spectrum of the LSCF-YSZ PLD sample heat treated at 900 ℃.

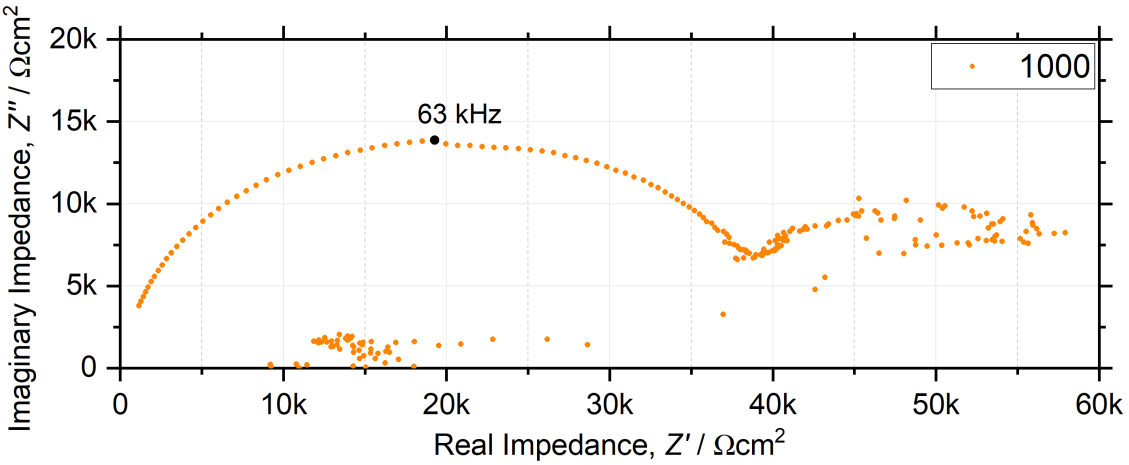

Figure 6.8: Impedance spectrum of the LSCF-YSZ PLD sample heat treated at 1000 ℃.

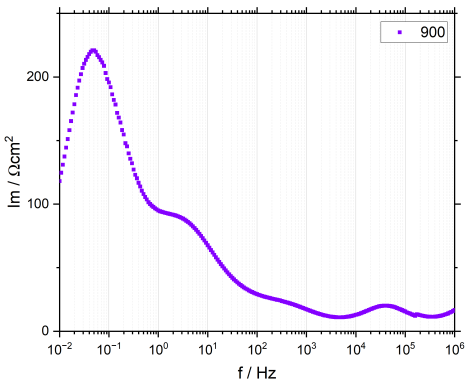

Figure 6.9: Bode plot of the imaginary imedance by the LSCF-YSZ PLD sample heat treated at 900 ℃

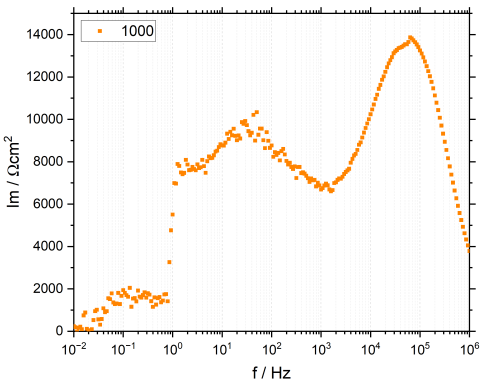

Figure 6.10: Bode plot of the imaginary imedance by the LSCF-YSZ sample heat treated at 1000 ℃.

The 1000 ℃ sample shows only one clear semi-circle at high frequencies, while any lower frequency

processes could not be captured by the machine. Any low frequency processes in this sample cannot be interpreted with this EIS data. Another unique feature observed here is that this spectrum does not contain the high frequency tail that may be indicative of the bulk processes. Looking further at the capacitance value obtained from this semicircle shows it to be several orders of magnitude below the other data, indicating that this may be the semicircle associated with the bulk transport processes. The 900 ℃ sample shows further behaviour that might indicate further potential mechanisms taking place. In particular, the semi-circle at 0.05 Hz indicates a process that did not take place in samples that underwent lower temperature heat treatment. The peak frequency is very low and below the processes normally associated with SOFC material. The closest process commonly found in literature at such frequencies is the inductive loop often seen in battery materials, which cannot describe what is happening in this data, as it does not show the 'looping' behaviour typical of this process [18]. This may indicate that this data does not follow regular behaviours for samples of this type and therefore repetition and further tests are required.

6.4 Conclusion

The experimental results presented in this section explore the formation of diffusion-blocking interfaces in LSCF-YSZ multilayers. The SIMS data reconfirmed the existence of a drop in isotopic fraction at the interface region. This drop was fitted using two models, an interface resistance model and a triple layer model. Both show consistency in fitting the material properties found in the multi-layer. The triple layer model suggests the formation of an interlayer with defined thickness and diffusion coefficient. The reaction products of the LSCF-YSZ reaction at high temperatures were further investigated using SEM-EDX and XRD, suggesting the presence of $SrZrO_3$ and $CoFe_2O_4$. Comparison to literature values for conductivity and diffusion behaviour suggests the diffusivity value obtained by the triple layer model could be plausible. Impedance spectroscopy was applied to the samples, showing an increasing ohmic resistance with higher treatment temperature. These results are compared to theoretical calculations of series resistance in a multi-layer sample with an interlayer of increasing thickness. These results indicate that a layer consisting of some combination of SZO, CFO and other species with increasing length could explain some the behaviour observed. This is based on conductivities and diffusion coefficients from literature being in the right order of magnitude as the D obtained for the interlayer by the triple layer model.

References

[1] F. Poulsen and N. Van Der Puil. Phase relations and conductivity of Sr- and La-zirconates. *Solid State Ionics*, 53-56:777–783, 1992.

[2] P. Huang and A. Petric. Electrical conduction of yttrium-doped strontium zirconate. *Journal of Materials Chemistry*, 5(1):53, 1995.

[3] T. Higuchi, T. Tsukamoto, N. Sata, K. Hiramoto, M. Ishigame, and S. Shin. Protonic Conduction in the Single Crystals of SrZr $_{0.95}$ M $_{0.05}$ O $_{3}$ (M=Y, Sc, Yb, Er). *Japanese Journal of Applied Physics*, 40(6R):4162, 2001.

[4] L. Ajroudi, N. Mliki, L. Bessais, V. Madigou, S. Villain, and Ch. Leroux. Magnetic, electric and thermal properties of cobalt ferrite nanoparticles. *Materials Research Bulletin*, 59:49–58, 2014.

[5] G. Ou, W. Liu, L. Yao, H. Wu, and W. Pan. High conductivity of La $_{2}$ Zr $_{2}$ O $_{7}$ nanofibers by phase control. *J. Mater. Chem. A*, 2(6):1855–1861, 2014.

[6] Q.A. Islam, S. Nag, and R.N. Basu. Study of electrical conductivity of Ca-substituted $La_2Zr_2O_7$. *Materials Research Bulletin*, 48(9):3103–3107, 2013.

[7] C. Nivot, C. Legros, B. Lesage, M. Kilo, and C. Argirusis. Oxygen diffusion in $SrZrO_3$. *Solid State Ionics*, 180(17-19):1040–1044, 2009.

[8] X.Y. Liu, J.W. Che, H. Yi, Jiacheng Zhang, and G.Y. Liang. Diffusion mechanism of oxygen ions in $La_2Zr_2O_7$/YSZ composite ceramics. *Journal of Alloys and Compounds*, 778:522–531, 2019.

[9] T. Yajima, H. Suzuki, T. Yogo, and H. Iwahara. Protonic conduction in $SrZrO_3$-based oxides. *Solid State Ionics*, 51(1-2):101–107, 1992.

[10] E. A. Slonimskaya and A. V. Belyakov. Ceramics Based on Strontium Zirconate. *Glass and Ceramics*, 58(1/2):54–56, 2001.

[11] K. Develos-Bagarinao, H. Yokokawa, H. Kishimoto, T. Ishiyama, K. Yamaji, and T. Horita. Elucidating the origin of oxide ion blocking effects at GDC/SrZr(Y)O-3/YSZ interfaces. *Journal of Materials Chemistry A*, 5(18):8733–8743, 2017. Type: Journal Article.

[12] Y. Zhang, T. Lu, Y. Ye, W. Dai, Y. Zhu, and Y. Pan. Stabilizing Oxygen Vacancy in Entropy-Engineered CoFe $_{2}$ O $_{4}$ -Type Catalysts for Co-prosperity of Efficiency and Stability in an Oxygen Evolution Reaction. *ACS Applied Materials & Interfaces*, 12(29):32548–32555, 2020.

[13] X. Long, C. Feng, D. Ding, N. Chen, S. Yang, H. Chen, X. Wang, and R. Chen. Oxygen vacancies-enriched $CoFe_2O_4$ for peroxymonosulfate activation: The reactivity between radical-nonradical coupling way and bisphenol A. *Journal of Hazardous Materials*, 418:126357, 2021.

[14] J. Zhang, C. Lenser, N. H. Menzler, and O. Guillon. Comparison of solid oxide fuel cell (SOFC) electrolyte materials for operation at 500 °C. *Solid State Ionics*, 344:115138, 2020.

[15] T. Hagiwara, H. Yamamura, and H. Nishino. Relationship between oxide-ion conductivity and ordering of oxygen vacancy in the $Ln_2Zr_2O_7$ (Ln = La, Nd, Eu) system having a pyrochlore composition. *IOP Conference Series: Materials Science and Engineering*, 18(13):132003, 2011.

[16] C. Ahamer, A. K. Opitz, G. M. Rupp, and J. Fleig. Revisiting the Temperature Dependent Ionic Conductivity of Yttria Stabilized Zirconia (YSZ). *Journal of The Electrochemical Society*, 164(7):F790–F803, 2017.

[17] E. Celik, Y. Ma, T. Brezesinski, and M. T. Elm. Ordered mesoporous metal oxides for electrochemical applications: correlation between structure, electrical properties and device performance. *Physical Chemistry Chemical Physics*, 23(18):10706–10735, 2021.

[18] A. Thapa and H. Gao. Low-frequency Inductive Loop and Its Origin in the Impedance Spectrum of a Graphite Anode. *Journal of The Electrochemical Society*, 169(11):110535, 2022.

Chapter 7

Conclusions

This set of experimental data sought to investigate the behaviour of interfaces that impede diffusion in electroceramic materials commonly used in solid oxide cells. Using isotope exchange depth profiling, multi-layer samples of LSCF deposited onto sintered pellets of YSZ using PLD were characterised. Heat treatments of increasing temperature from 600-1000 ℃ were applied to these samples and resulted in a drop in isotopic fraction at the LSCF-YSZ interface region that increased in samples that underwent heat treatment at higher temperatures. Using a newly developed mathematical model for diffusion behaviour across multiple layers with different properties, this IEDP data was fitted, enabling the quantification of the interface blocking effect. Firstly, a model describing the interface as a single step in space with an associated interface resistance parameter r was applied. This showed an increasing value of r with higher post-deposition heat treatment temperature, while the other fitting parameters remained approximately constant. While this model offers a variable that is capable of quantifying the magnitude of the interface drop, it does not provide a mechanistic explanation for the process. Furthermore, it limits the interface region to an infinitesimally small layer, while the data shows the interface forming a region with a finite thickness, as further underlined by the ion signals from LSCF and YSZ obtained from SIMS.

In order to investigate this further, a triple layer model, which assumes the interface to be a third layer with a given dimension and diffusivity, was applied. The fits remained consistent with the interface resistance model in obtaining diffusivity values for the LSCF and YSZ layers, highlighting the validity of this approach. Furthermore, the combination of interlayer thickness and diffusivity enables the model to capture gradients in the IEDP data from the interface region. This allows the triple layer model to estimate the thickness of the interlayer to a reasonable degree, matching the estimations obtained from the SIMS ion signals. Furthermore, the triple layer model's parameters D and L_{int} can

be mathematically related to r, producing closely matching results. This suggests that both models are mathematically valid in capturing the interface drop behaviour, and offer different approaches to fitting.

SEM-EDX and XRD results suggest the formation of $SrZrO_3$ and $CoFe_2O_4$ in the range of the heat treatment temperatures. Given the two layers are in direct contact, it is likely that the interface would consist of a combination of these species, although it is possible that other compounds are also present. Literature values of conductivity and diffusivity for these species suggest that the triple layer model's obtained value is in a similar order of magnitude. This was further confirmed using impedance spectroscopy results of the multi-layer samples. They showed an increase in ohmic resistance with higher treatment temperatures. This was compared to theoretical calculations of the series resistance of a multi-layer species with an interlayer of thickness and diffusivity in the region obtained from the SIMS experiments. While the results mostly match up with the hypothesis of a compound interlayer with diffusion properties in the range known from the reaction products, repetition of the impedance data would be necessary to confirm this.

In summary, the multi-layer model for diffusion developed in this project was validated using multi-layer SIMS data from PLD samples. The model suggests the formation of an interlayer region of finite thickness and diffusivity that blocks the diffusion of oxygen. While the real diffusion properties of the interlayer region may be significantly more complex and without clear boundaries, the information provided by the model is sufficient to provide information about potential performance issues in a SOC structure caused by this layer. The thickness of this layer was estimated separately using the triple layer model, the FeO and ZrO ion signal SIMS data and the ohmic resistance obtained from EIS. The diffusivity of the layer was initially obtained from the triple layer model and estimated to be around two orders of magnitude lower than that of LSCF and YSZ based on SIMS and the impedance data.

7.1 Future Work

The series of experiments presented in this project validate the ability of the multi-layer diffusion models to capture the diffusion behaviour as observed in isotope exchange depth profiling experiments. The models are able to fit the diffusion coefficient and interface resistance of multiple layers simultaneously. While the number of layers investigated in this project was limited to three, in theory the mathematics could be extended to any number of layers. Future work based on this model could therefore investigate

any multi-layer structures commonly found in practical applications. Many fuel cell architectures include several layers of YSZ and GDC-containing compounds. Such multi-layers could be fabricated and tested with IEDP.

7.1.1 Sample Fabrication

One of the issues that repeatedly presented during the experimental process is the inconsistency in quality of the electrolyte pellets. The sample fabrication methods were chosen based on both proximity to industrial processes and ease of fabrication of many samples. However, for the purposes of scientific investigation, having flatter, more evenly grown layers could yield more useful experimental data. The powder pressed pellets have, even after polishing, an intrinsic roughness that exceeds that of the layer thickness. Furthermore, any micropores or other inconsistent regions of the pellet can affect results. Based on these issues, fabricating multi-layer thin films grown on a substrate is one path for future work that could further elucidate details of the multi-layer system's behaviour. This would lengthen the sample fabrication process, as the electrolyte layer would have to be grown first, and it would still have to be thick enough to provide a semi-infinite diffusion condition in the bulk. The resulting multi-layer would have flat interfaces. This would principally be interesting as a comparison set to see if the interface behaves differently if it is much flatter. It also enables further characterisation, such as X-ray reflectivity to confirm sample thickness and roughness. X-ray diffraction analysis could be done under different higher temperatures in order to study the evolution of phases from an as-deposited PLD sample, clarifying the processes resulting from the heat treatment.

7.1.2 Characterisation Methods

One of the insights lacking from this project is regarding the mechanistic processes occurring at the interface. This is mainly due to a lack of high-quality data from the region itself. In the thin film samples, the interface will be in the order of tens of nanometers, making it unsuitable for conventional high-resolution SEM analysis. Furthermore, cross-section XPS analysis of this region is also difficult due to the inherent spot size of the incident X-ray beam.

The primary method of characterisation at this length scale would be transmission electron microscopy. This method has been used extensively in literature for these types of samples. The main issue and reason why it was not possible to do this in this project is the time required for the sample preparation. TEM would provide more detailed information about the interdiffusion around the

interface through higher-resolution EDX, as well as insights regarding the crystal structures present via electron diffraction. EELS analysis could give information around the changes in valence states around the interface. These techniques could help clarify which species form at which interface. This can then, in turn, lead to more hypotheses regarding the diffusion behaviour in interface regions, and which factors might play a leading role in determining this.

LEIS is a highly surface sensitive technique that can help provide information on the species present in the first few nanometers of the sample. This might help clarify the reduction in surface exchange coefficient with treatment temperature that was observed, potentially confirming the occurrence of processes such as strontium segregation.

7.2 Dissemination

7.2.1 Papers

L. Yasin, A. Atkinson, S. J. Cooper, A. Bertei, *Identifiability of the mechanisms governing the reaction kinetics of MIEC electrodes in solid oxide cells.* Electrochimica Acta, Volume 472, 143418, (2023).

7.2.2 Conference Presentations

L. Yasin and S. J. Cooper, *Quantifying Diffusion Across Solid-Solid Interfaces in Electrochemical Cells.* 243rd ECS Meeting (2023).

Appendix A

Further Experimental Data

This Appendix compiles some of the further experimental data that was obtained during the course of the project, but was not conclusive enough to be included in the main text.

A.1 Topography Data

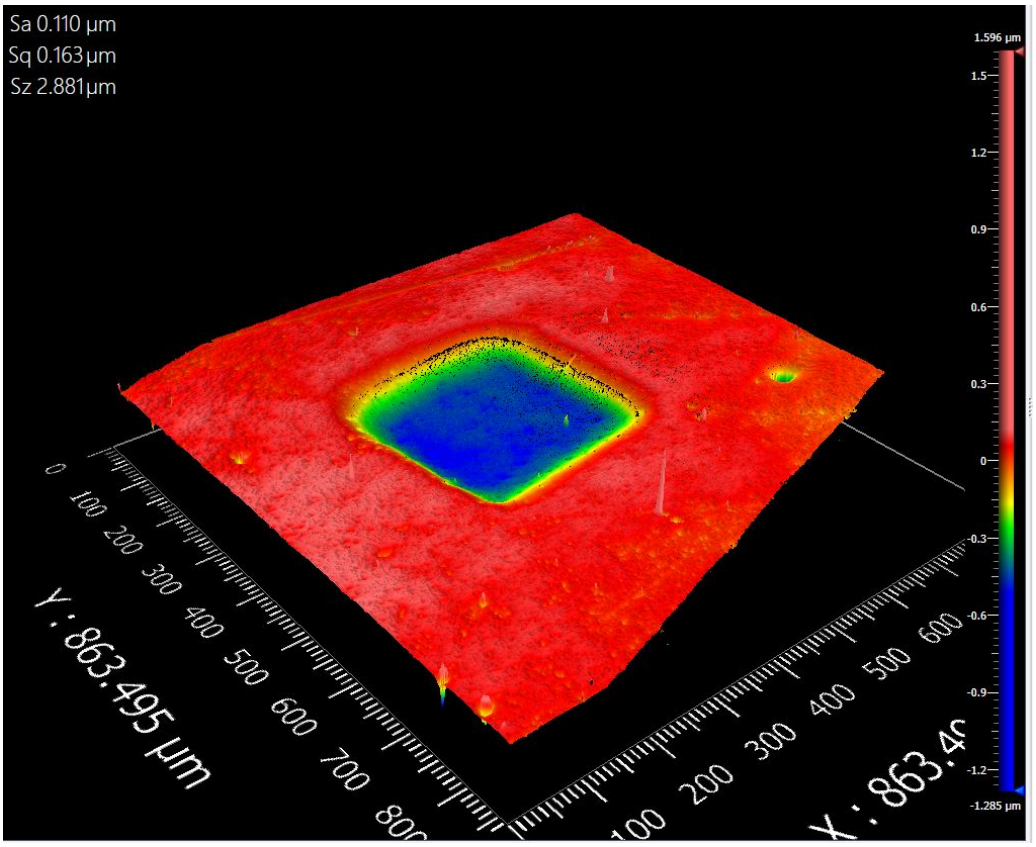

Figure A.1: 3D Zygo topography map of the surface of a multi-layer sample where the LSCF layer was deposited using PLD on a sintered substrate. The crater seen is the result of the sputtering beam in the SIMS.

The Zygo interferometer was used to obtain information about the surface topology, as well as the depth of the sputtering crater, allowing the sputtering time of the SIMS beam to be correlated with the depth that the beam penetrates. The results obtained from a sample 3D map are shown in Figure A.1, with variation in surface position obtained from a linear analysis across the crater area shown in Figure A.2. The data shows the area around the sputtering crater to be flat, with some minor variations. This shows the quality of the PLD process and its ability to create flat and well-defined surfaces, while also highlighting the notable effect of the substrate pellet's microstructure. The topography data shows the overall topology to not be perfectly flat, and the presence of individual artefacts in different parts of the sample. However, given the information in this data, as well as similar results from other samples, a reasonable degree of confidence in the LSCF layer's flatness can be gained.

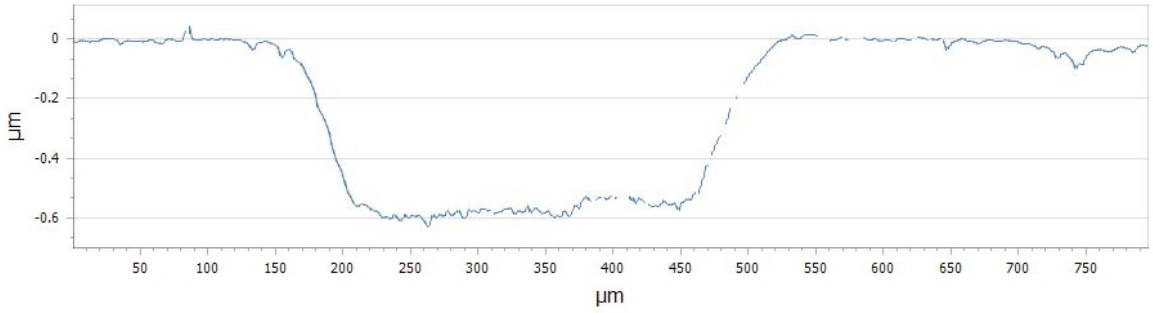

Figure A.2: Variation in surface position as determined by linear analysis of the Zygo surface topography data. The profile shows the depth of the sputtering crater caused by the SIMS.

This information indicates that the area of the sample that is sputtered away and analysed in the SIMS is contained to a sufficiently limited area that variations in surface roughness should not systematically affect the data. Surface isotopic fraction concentrations and interface region widths therefore are not affected in a major way by this. The occasional peaks and troughs around the surface, caused by unevenness in the substrate pellet, might explain some of the artefacts in the SIMS data.

A.2 Grazing incidence XRD data

For the purposes of characterising the thin film samples, grazing incidence XRD was used. All measurements were done at a grazing angle of 1 degree, 0.08 degree step size and 10 seconds dwelling time. The results from these measurements are summarised in Figure A.3.

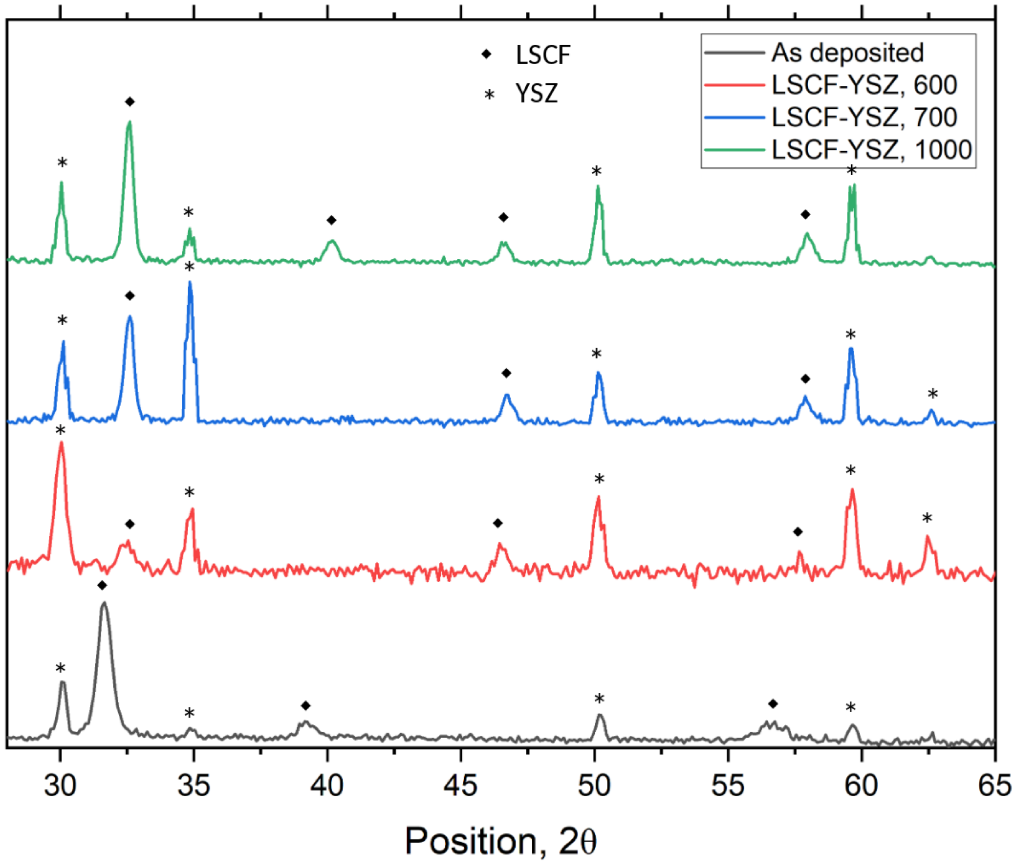

Figure A.3: XRD patterns obtained from LSCF deposited on YSZ substrates and heat treated at different temperatures.

All of the samples consistently show the presence of both LSCF and YSZ, as indicated by the principal peaks of each species. It is notable that there does not appear to be a completely consistent trend in the ratios of the peaks of each species. There are several mechanisms that play a role in influencing the data. Firstly, the penetration depth of the X-ray beam should ideally be consistent due to the same incidence angle being used. Within the same penetration region therefore, variations in thickness of the LSCF layer could influence the peak ratios observed. This thickness can vary both due to the deposition process itself as well as the formation of the interlayer. Furthermore, the X-ray beam is spread across a macroscopic region, where minor variations in surface roughness of the YSZ pellet could influence the relative amount of LSCF to YSZ visible in the peaks. For these reasons, this type of multi-layer sample does not provide enough conclusive information in the GIXRD to gain further insights into the effects of the heat treatment process. This data does, however, confirm the species present in the multi-layer to be as expected.

One notable feature visible from this data is the shift of the LSCF peaks in the as-deposited sample. This sample was analysed directly after the PLD process and before any heat treatment or isotope exchange took place. The peak shifts, which increase in magnitude with higher angle, could indicate

a strain on the LSCF lattice. A residual strain in the LSCF layer after the deposition is plausible, as the stoichiometry might vary slightly due to the laser ablation process as well as the deposition itself on the pre-sintered YSZ pellet with an unlike crystal structure. Exposing this sample to high temperatures under ambient conditions could therefore remove these residual stresses and equilibrate the stoichiometry of the LSCF.

A.3 EIS Data

EIS under Bias

One notable feature of these EIS graphs is the presence of a flat plateau-like region between the two discernible semicircles. This appears to be more noticeable in the multi-layer samples. As the LSCF is only deposited on one side of the sample, there could be some effects that result from this asymmetry. To study this further, impedance analysis that additionally applied a DC bias to the samples was undertaken, the results of which are shown in Figure A.4.

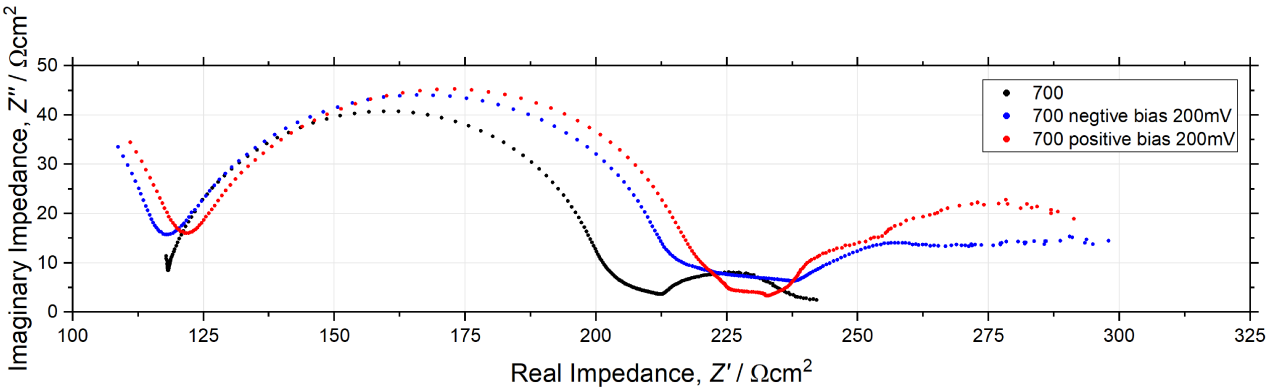

Figure A.4: Impedance spectra collected from a LSCF-YSZ PLD sample heat treated at 700 °C, one without any DC bias and two with a positive and negative DC bias of 200mV, respectively. The spectrum obtained from a pure YSZ pellet is inserted for reference.

The high frequency semicircle changes slightly in both cases, but not sufficiently for deeper analysis. The second semicircle appears to degenerate under bias conditions, potentially splitting up into multiple other contributions. Notably, the plateau region in between the semicircles extends significantly only under negative bias. This effect would warrant further investigation in conjunction with an extended series of EIS experiments.

A.4 Ceramics Processing Samples

The first attempted series of experiments was done by reproducing a multi-layer system that is as close as possible to those found in real fuel cells. The cathode layer in such systems is in the scale of tens of microns, therefore an LSCF layer of this thickness was attempted to be deposited onto a pellet consisting of electrolyte material. This is generally done by means of an ink, consisting of LSCF powder and solvents, which can then be deposited in a controlled manner to adjust the layer thickness.

A.4.1 Ceramics Processing

The general approach to the ink processing samples follows the principle of depositing the ink onto a electrolyte substrate and subsequently sintering the multi-layer, aiming to produce as dense a sample as possible. The two most commonly used methods in industry and research are tape casting and screen printing. Tape casting requires a highly viscous ink that can be spread at a controlled height and dried to form a tape that can be further used. This requires additional care regarding the composition and processing of the ink, as the particles have to form a well-dispersed layer connected by binder material, with minimal agglomerates. Screen printing has similar, albeit less specific requirements, and is generally used to fabricate a large number of samples at once. These requirements introduce complexity to the sample preparation which was chosen to be avoided by instead using a drop casting method for LSCF powder deposition. Furthermore, the inks for these processes are designed with a porous cathode in mind, further reducing the need to use these methods for the purpose of this project

The approach for deposition was based on dropping a dilute ink onto the substrate with a pipette, making the viscosity and structural integrity of the ink less important than it would be in an industrial process such as screen printing or tape casting. The only purpose of the ink was to dissolve the LSCF powder as well as possible such that the particles can evenly distribute and stack on the substrate, forming an even layer.

Using such an initial approach, LSCF ink was drop cast onto a fully sintered GDC pellet (1400 ℃ for 6 h) and then co-sintered at 1250 ℃ for 4 h. GDC was chosen as the electrolyte material at this stage because it is known to be chemically compatible with LSCF and therefore is the system with the least possible other factors (such as chemical reactions) influencing the outcome. This makes it suitable for exploring processing and co-sintering methods. The resulting sample is shown in Figure A.5, where it can clearly be seen that while the LSCF layer has a reasonable flatness and good thickness, its

microstructure is not dense. These results held even with higher sintering temperature and longer sintering times.

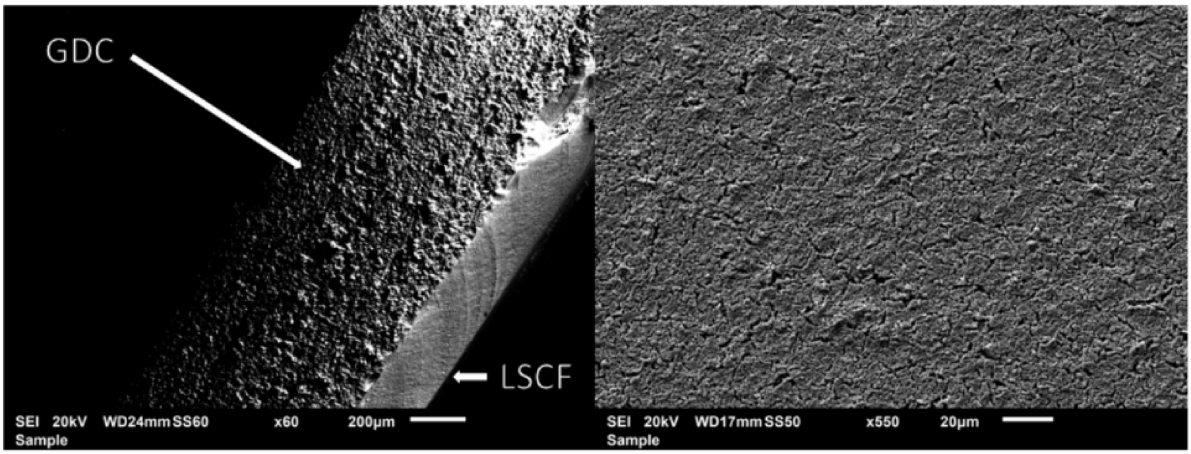

Figure A.5: SEM images obtained from a multilayer samples of LSCF deposited using a terpineol-based ink painted onto a pre-sintered GDC substrate showing a) the cross section and b) a top-down view of the LSCF layer. While a good quality deposition of a layer of approximately 200 µm was achieved, this layer has a clearly porous microstructure, indicating that it has not completed sintering and is therefore not suitable for isotopic exchange experiments.

For comparison, a GDC pellet that was not fully sintered, but rather pre-fired at 800 ℃ for 4 h was used as the substrate. As can be seen in Figure A.6, this created a much denser LSCF layer with clear grains showing the microstructure.

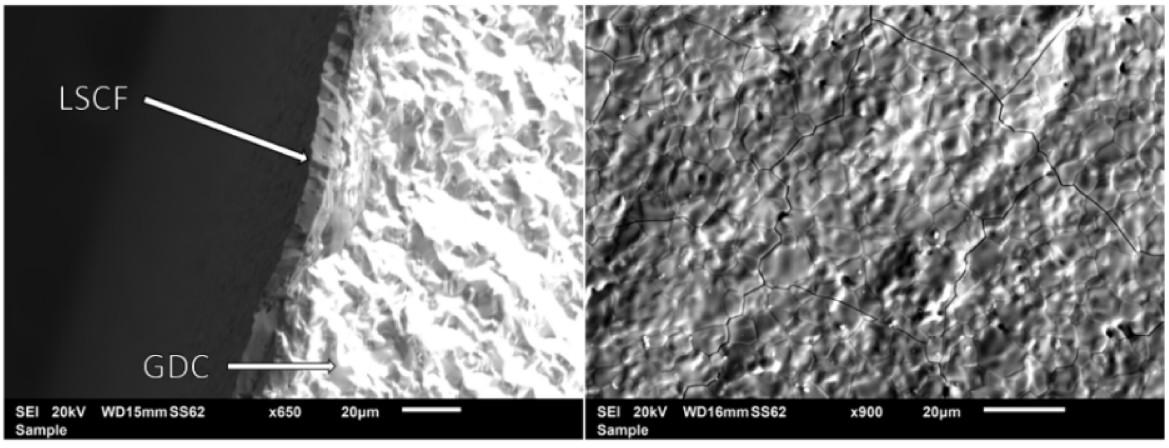

Figure A.6: SEM images obtained from a multilayer samples of LSCF deposited using a terpineol-based ink painted onto a GDC substrate showing a) the cross section and b) a top-down view of the LSCF layer. The GDC substrate was pre-fired at 800 ℃ before ink deposition

This can be explained by the fact that the full sintering of the GDC pellet causes significant shrinkage, particularly in temperatures in excess of 1000 ℃. This fully sintered substrate can therefore

no longer change its dimensions during the co-sintering process. When the LSCF powder layer tries to densify while simultaneously attaching to the GDC substrate, the latter will provide a strain in the opposite direction of the pellet densification. Thereby, the full sintering of the LSCF layer becomes impossible, and the result is a porous microstructure. These concepts are visualised in Figure A.7.

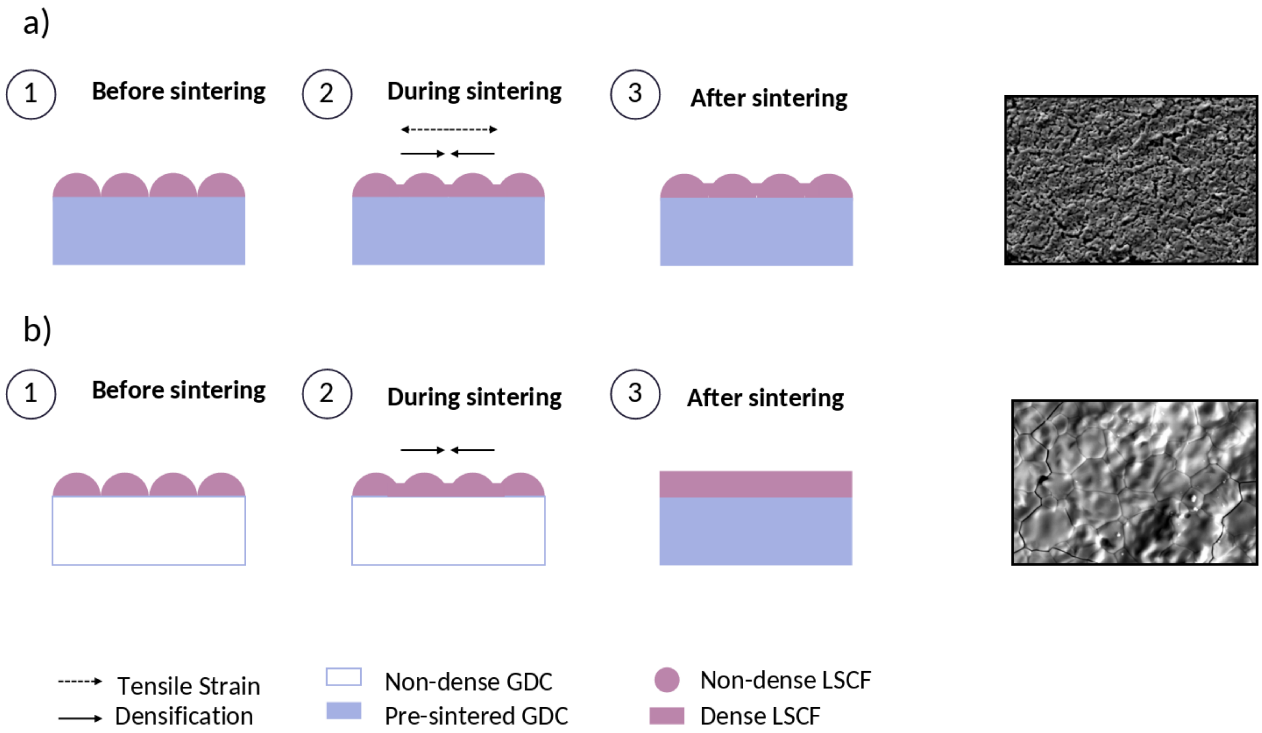

Figure A.7: Simplified respresentation and resulting SEM images of the processes occuring during co-sintering of a) pre-sintered GDC with an LSCF ink deposited on top and b) pre-fired, but not densified GDC with the same ink deposited on top. During the latter process, the intially dispersed layer of LSCF powder densifies along with the electrolyte substrate, whereas in a) the lack of sintering densification in the GDC introduces a tensile strain perpendicular to the interface which prevents full densification of the LSCF powder.

A.4.2 Layer Thickness and Mechanical Stability

Having established the initial concepts for fabricating multi-layer samples, a first SIMS linescan analysis was attempted. As described in the Methods chapter, the samples were exchanged under Oxygen-18 atmosphere and subsequently cut using a diamond saw to reveal the cross-section, which was then polished to a mirror finish.

The isotopic fraction results from this sample are shown in Figure A.8. While this sample does show an evolving diffusion profile across the multi-layer, it is particularly evident that the surface position of the LSCF layer on the left-hand side is unclear. The LSCF surface appears to be rough relative to the length scale of analysis; the start of the surface position varies by a few microns. Given the full length of the layer is lower than 20 microns, this makes it hard to clearly observe and model the diffusion

behaviour.

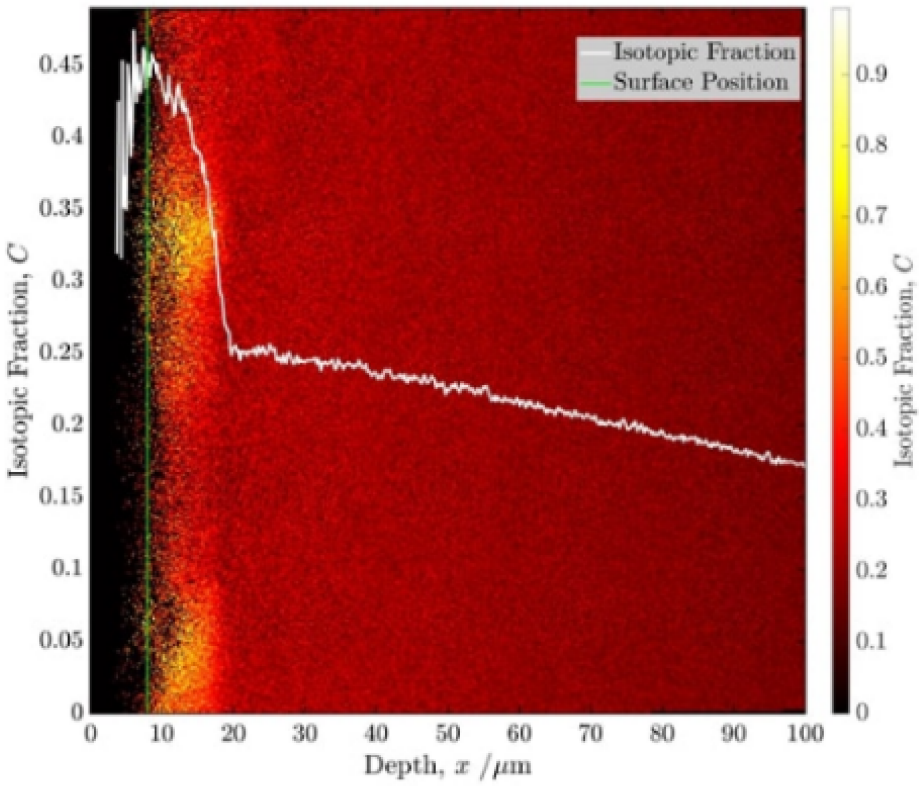

Figure A.8: Oxygen isotopic fraction data of an LSCF layer deposited on a GDC substrate and annealed in Oxygen-18 atmosphere at 650 C for 1h obtained using cross-sectional SIMS

The isotopic fraction also appears to be non-uniform in different areas of the layer. The explanation for this can vary, but is likely to be related to both or either the surface texture (and the influence this has on surface exchange) and the layer uniformity (having variations in density).

This data revealed two major issues that the sample preparation needs to resolve: a thicker LSCF layer and a flatter surface. The thicker layer is necessary to render the surface roughness that is intrinsic to the process less relevant, while any attempt to make the surface more flat directly will play into the same goal.

Initial experiments already showed that, in principle, the layer thickness of LSCF can be infinitely increased by depositing more drops of the ink. However, trying this revealed issues related to the behaviour of the ink as it disperses and dries on the substrate. After a certain number of drops, LSCF particles started to accumulate around the rim of the pellet, which formed a template for subsequent drops of inks to disperse on. This then ultimately results in an uneven layer of LSCF powder that will turn into a multi-layer sample with a rough surface. Furthermore, the rim of the sample will be prone to tears and cracks, as shown in Figure A.9 which has an effect on the overall mechanical properties of the layer, particularly with regards to cutting and polishing the sample.

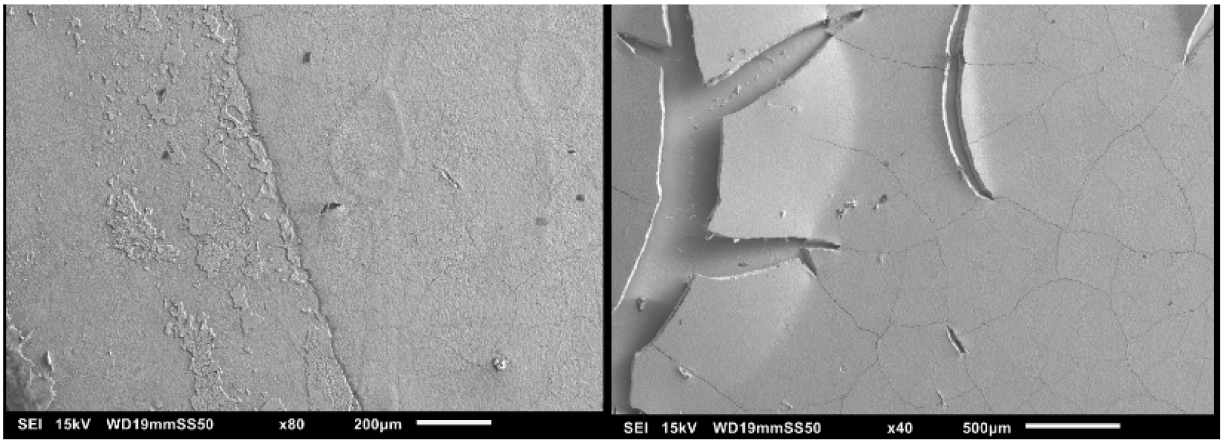

Figure A.9: Top surface images of an LSCF layer deposited onto a GDC pellet using an ink drop casting technique. These images focus in on the edge of the sample pellet, where the accumulation of ink during the deposition of many consecutive layers resulted in the cracks and tears seen.

To mitigate these issues, the ink composition was investigated to potentially improve dispersion, and the limits of how many drops of ink are feasible under such conditions were explored. This would then correspond to a certain LSCF layer thickness which would be feasible. Undertaking the co-sintering process with a weighted alumina plate on top of the LSCF powder in an attempt to flatten the surface was also tried. However, the LSCF ended up reacting with the plates and compromising the overall sample integrity. A thickness of around 30 microns $\pm$ 5 microns was found to be the thickest layer possible with minimal structural issues, shown in Figure A.10.

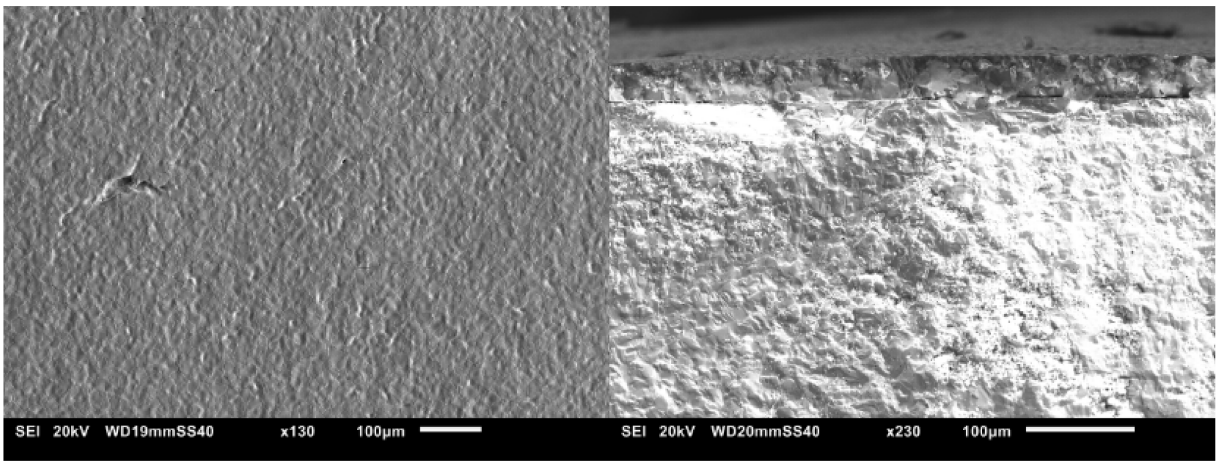

Figure A.10: Top surface and cross-section image of an LSCF layer deposited onto a GDC pellet using ink drop casting. This sample shows minimal cracks and pores, while still having a thickness in the area of 30 microns.

As can be seen, there are still a noticeable number of cracks in the layer. It is likely that the different sintering properties of the materials make it difficult to achieve fully dense multi-layer samples.

While the cracks might provide an alternative diffusion path for oxygen gas and compromise the overall diffusion profile, generally the volume occupied by these cracks is only a small fraction of the layer. Since line scans work by averaging out isotopic fraction across a 2D area, the assumption was made at this stage to accept the state of the samples as is for further analysis.

A final consideration in the linescan preparation is the polishing procedure after isotope exchange. Particularly, LSCF is a significantly softer material when compared with YSZ. LSCF will grind and polish off more easily. While this will mean that the substrate will be the determining factor during the polishing process, it is still possible that the soft properties of LSCF might make the mirror finish imperfect. Initially, the multi-layer cross section sample was fixed by using microscope slides that were cut to shape. Due to the potential issues with the different hardnesses, it was instead decided to embed the sample in an epoxy resin. This will not leave a gap as exists between the sample and the glass slide. Some of the issues encountered regarding the cutting and polishing process are further discussed in the Appendix.

A.4.3 SIMS ANALYSIS

Having established a procedure for substrate presintering, ink deposition and drying, as well as sample polishing, an attempt was then made to investigate interface effects in such samples. The exchange temperature was set at 600 ℃ and the time kept at 90 minutes. Figure A.11 shows the SIMS data from a sample containing an LSCF layer on a YSZ pellet.

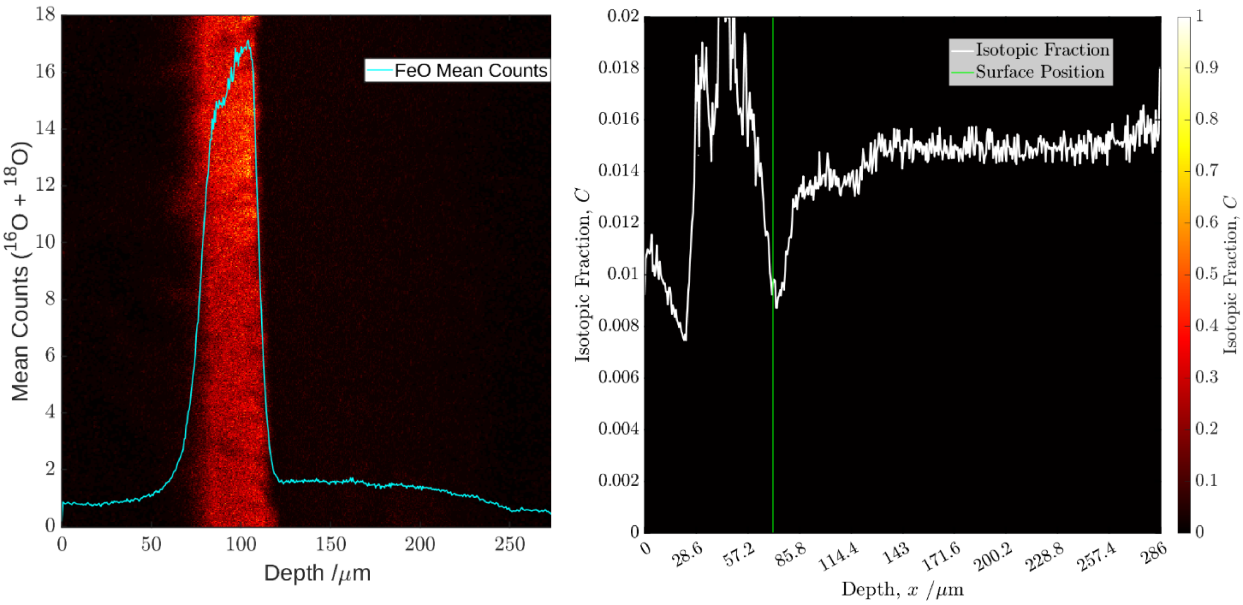

Figure A.11: Oxygen isotopic fraction data of an LSCF layer deposited on a YSZ substrate and annealed in Oxygen-18 atmosphere at 600 C for 1h obtained using cross-sectional SIMS(right) and FeO ion signal data indicating the presence of an LSCF layer (left)

The YSZ data from the SIMS shows that none of the samples was able to exchange a significant amount of Oxygen-18, as shown by the low isotopic fraction that is on the order of the natural background isotope fraction. This can also not be explained by the mechanical delamination of the LSCF layer, as the FeO signal obtained from the SIMS clearly shows the presence of an LSCF layer. The most likely explanation for this is that during the co-sintering process, which takes place at 1400 ℃ reaction products are formed that might act both as an ion blocker and degrade the LSCF itself, compromising its exchange properties. The sintering process lasts for 4 hours and has both heating and cooling processes that exposes the system to temperatures in excess of 800 ℃. This means that the sample is exposed to temperatures capable of forming LSCF-YSZ reaction products, and it appears that these reactions are significant enough to degenerate any ability to exchange and transport oxygen gas. This means the ceramics processing method is fundamentally unsuitable for systematic analysis of interface effects in LSCF-YSZ systems using SIMS. However, the samples can still provide valuable insight into the reaction mechanics in the interface region, as will be discussed in the later section discussing EDX data.

This section illustrated the capabilities and limitations of both multi-layer diffusion models. While the experimental data provides some indication of the physical mechanisms underlying the effects observed, it remains a purely mathematical description that does not detail the actual physical mechanisms occurring at the interface region. While some literature discussed the formation of SZO in triple layer systems and its blocking effect, the direct contact between LSCF and YSZ would produce a range of reaction products beyond SZO. This means that even if the triple layer model's suggested presence of an interlayer of low diffusivity holds true, this interlayer would rather be a solid solution or composite phase of different species. To further study this, various additional characterisation methods are employed.

In the course of the development of the sample fabrication process for ink-based LSCF layers, many different deposition methods, ink compositions and polishing regimes were tried. This resulted in SIMS data that presented a variety of issues that made it impossible to interpret the data. An example of such a result is shown in Figure A.12, illustrating the line scan obtained from an LSCF-GDC multi-layer sample fabricated using drop casting.

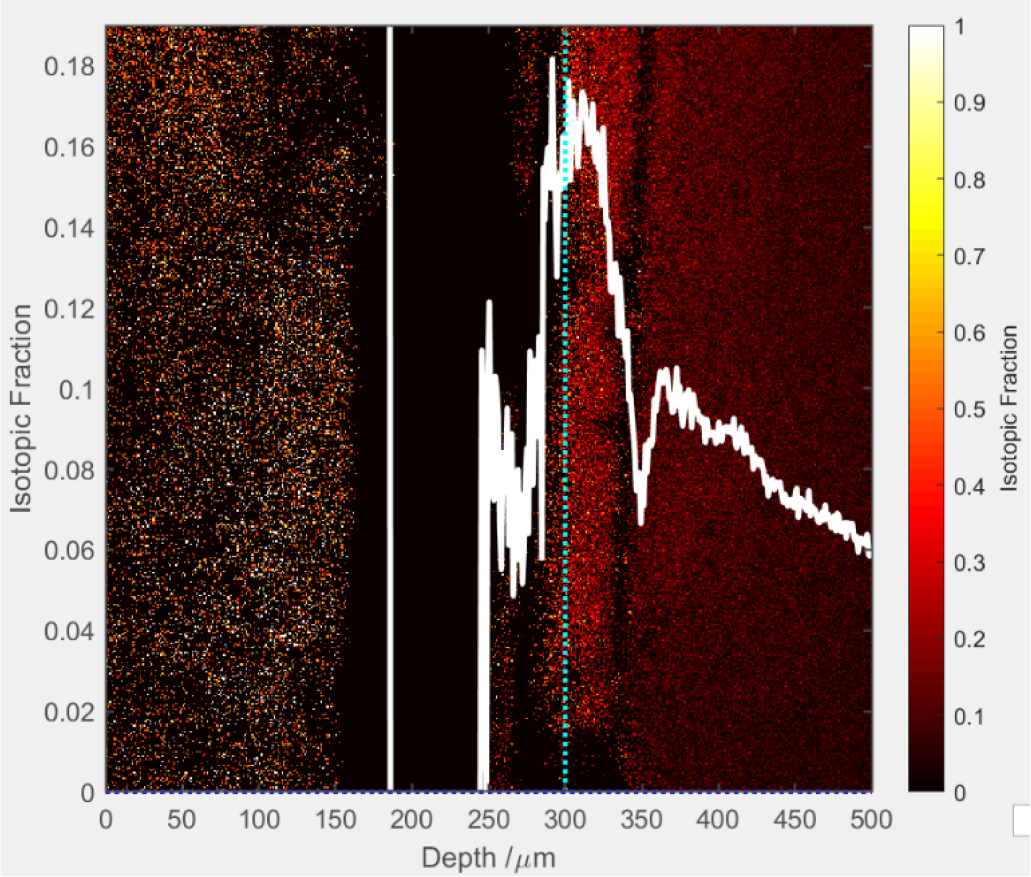

Figure A.12: Cross-section SIMS isotopic fraction data from a LSCF-GDC multi-layer sample fabricated using the drop casting and co-sintering method. The sample was exchanged at 600 ℃ for 90 minutes. The right hand side of the image shows the LSCF layer delaminated from the GDC substrate, while the left hand side represents a different sample pellet glued to the multi-layer.

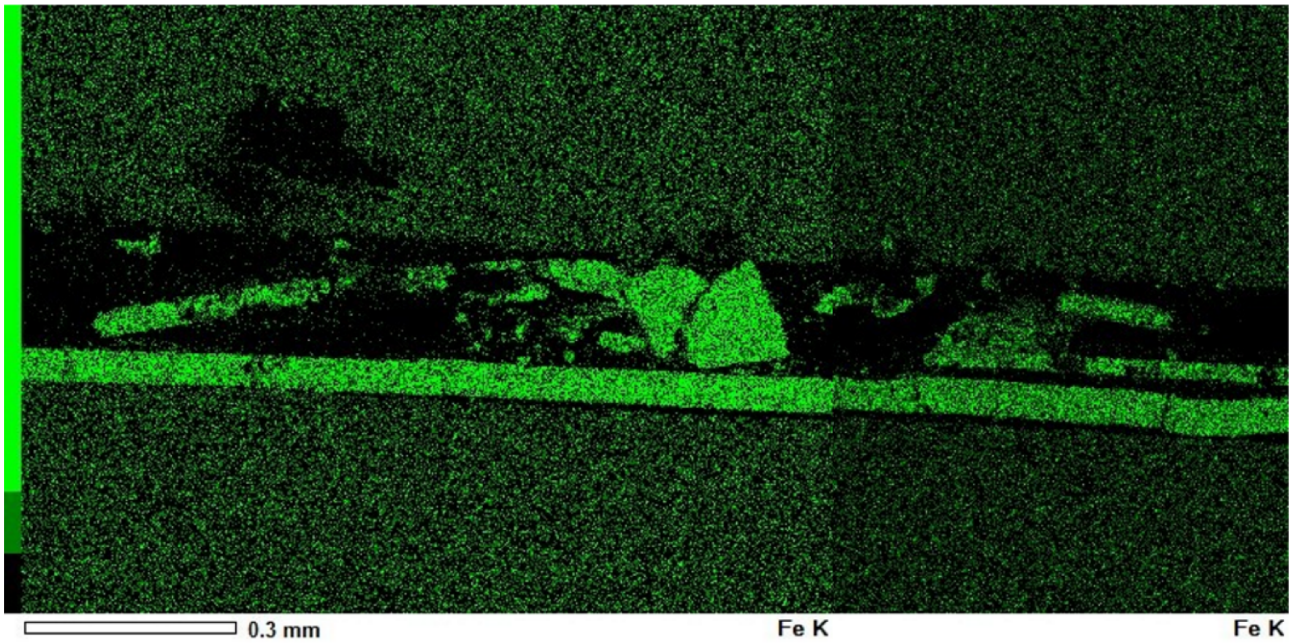

Figure A.13: SEM-EDX compound image of the iron signal in the cross-section of the LSCF-GDC multilayer sample obtained after the full polishing procedure and SIMS analysis. This cross section consists of two multi-layer samples glued to each other along the LSCF surface. The iron signal indicates the presence of LSCF.

This data illustrates several of the recurring issues that emerged when trying to perform line scan analysis on multi-layer samples. Firstly, what appears to be delamination between the LSCF and GDC can be seen. Looking at cross-section SEM, such as the iron signal presented in Figure A.13, gives further clues about what the cause of this delamination could be. The SEM data was obtained after the full polishing procedure for line scans outlined in the Materials and Methods chapter. It shows two samples glued together along the LSCF surface before the mounting and polishing process. While the bottom layer itself appeared to remain mostly intact, delamination can be seen. Furthermore, the top layer of LSCF appears to have been mechanically destroyed, with many fragments of iron-rich phase visible. This destruction and delamination is likely caused by the grinding and polishing process. As alluded to in the Results chapter, LSCF is significantly softer than both GDC and YSZ, making it possible for the SiC paper to induce significant damage to that layer specifically.

Returning to the SIMS data, some level of isotopic fraction that is higher than the natural background can be observed in both the LSCF layer and the GDC bulk, despite the delamination. This further suggests that the delamination occurred during the grinding and polishing process, which takes place after oxygen exchange. Despite this, the uneven surface of the LSCF remains a challenge to the proper determination of a diffusion profile. Much difficulty emerged during the sample fabrication development process with regard to consistently producing good quality multi-layers with no delamination or uneven LSCF surface. The requirement of LSCF to be fully dense was a challenge in particular that ended up not making these methods viable to investigate interface effects.